In-silico investigation of optical and electronic properties of heterocyclic conjugated polymers

A thesis submitted to the Indian Institute of Technology Guwahati for the degree of Doctor of Philosophy

Submitted by:
Harikrishna Sahu
Roll No.: 11612221

Supervisor:
Dr. Aditya N. Panda

Department of Chemistry

Indian Institute of Technology Guwahati
Guwahati - 781039

Declaration

I declare that the thesis entitled "***In-silico* investigation of optical and electronic properties of heterocyclic conjugated polymers**" submitted by me for the degree of Doctor of Philosophy is the record of research work carried out by me during the period from December 2011 to April 2016 under the guidance and supervision of Dr. Aditya N. Panda, associate professor, Indian Institute of Technology Guwahati and has not formed the basis for the award of any degree, diploma, associateship, fellowship, titles in this University or in any other University or other similar institutions of higher learning.

Harikrishna Sahu

Roll No.: 11612221

INDIAN INSTITUTE OF TECHNOLOGY GUWAHATI
Department of Chemistry

Academic Complex, North Guwahati
Guwahati - 781039 India

Certificate

This is to certify that the thesis entitled "*In-silico investigation of optical and electronic properties of heterocyclic conjugated polymers*" submitted for the award of degree of Doctor of Philosophy (Ph.D.) by **Harikrishna Sahu** is the record of research work carried out by him during the period December 2011 to April 2016 under my guidance and supervision, and this work has not formed the basis for the award of any degree, diploma, associateship, fellowship or other titles in this University or in any other University or other similar institutions of higher learning.

Dr. Aditya N. Panda
Thesis supervisor

This dissertation is dedicated to my beloved parents for their endless love, support and encouragement.

"The true laboratory is the mind, where behind illusions we uncover the laws of truth."

Sir Jagadish Chandra Bose

Acknowledgements

Throughout the last five years, many people have dedicated their own time and effort towards helping me, who have made this dissertation possible. First and foremost, I would like to express my sincere gratitude to my advisor **Dr. Aditya N. Panda**, associate professor, IIT Guwahati, Assam, for giving me the opportunity to work on my PhD studies in his group. I have been amazingly fortunate to have an advisor who gave me the freedom to explore on my own, and at the same time the guidance to recover when my steps faltered. His keen interest and encouragement serves as a constant support during all the time of research and writing of this thesis.

Besides my advisor, I would like to thank the rest of my thesis committee members: **Prof. Parameswar Krishnan Iyer**, **Prof. G. Krishnamoorthy**, and **Dr. Kalyanasis Sahu**, for their insightful comments and encouragement.

I am thankful to the centre for development of advanced computing (C-DAC), Pune for providing supercomputing facility, which helps me to carry out computationally expensive calculations. I also thank to IIT Guwahati for providing a HPC cluster, named as ORANG, which is under India's GARUDA grid computing facility. I am grateful to university grants commission (UGC) for financial support.

I thank my fellow labmate **Mr. Debasish Koner** for the countless stimulating discussions we had together. I would also like to thank two new labmates **Ms. Juri Goswami** and **Ms. Sayantani Basu** for extending their helping hands towards me when I needed. I truly appreciate the efforts of few undergraduate students: **Mr. Shashwat Gupta**, **Mr. Priyank Gaur** and **Ms. Swaraj Rashami Pradhan**, who have participated in this study. I would like to take this opportunity to say warm thanks to all my beloved friends, who have been so supportive along the way of doing my thesis.

And last but not least, my heart-felt gratitude goes to my whole family for their unconditional love and support throughout my study. Without them, this thesis would never have been written.

Synopsis

Chapter 1: *Introduction*

Nowadays, heterocyclic conjugated polymers are extensively studied for their applications in organic devices, such as organic light-emitting diodes, organic photovoltaics and organic field-effect transistors. Lack of appropriate optical gap, improper alignment of frontier orbitals with respect to the work function of electrodes, small mobilities of charge carriers, inappropriate hole-electron binding energy, etc., of organic materials often limit the performance of organic devices compared to the inorganic devices. Although a lot of studies have been devoted to find means and methods to improve the performance of these organic devices, designing an appropriate material having required electronic and optical properties is still a challenging task. Computational studies, at this juncture, are of immense help in understanding physical properties of existing conjugated polymers and designing new materials. The objective of the present work is to explore the structure and properties of various heterocyclic conjugated polymers using density functional theory (DFT) and time-dependent DFT (TDDFT) methods.

Chapter 2: *Theoretical methods*

In this chapter, basic concepts of Hartree-Fock theory, DFT and TDDFT are briefly mentioned. Few commonly used functionals and Grimme's dispersion correction terms are emphasized in the discussion.

Chapter 3: *Thiophene–azomethine–pyrrole based conjugated polymers*

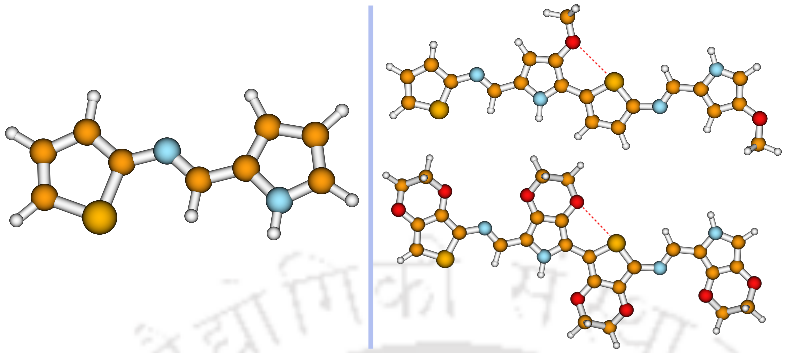

This chapter presents optoelectronic and charge transport properties of a class of conjugated polymers where the basic unit consists of a thiophene and a pyrrole ring linked by a –CH=N– group. The presence of π-spacers in the main chain helps in reducing torsion angle and enhances the π-electron delocalization across the chain. Azomethine-linked oligomers are isoelectronic to their vinylene-linked counterparts. These oligomers are known for the ease of synthesis, effortless purification process and small harmful byproducts. Our results show that sterically demanding substituents induce twisting in the conjugated backbone of oligomers and increase both the HOMO–LUMO and optical gaps, compared to the basic molecule. Properties of the oligomers depend on the positions of the substituents, for both electron donating and withdrawing groups. Two studied oligomers are planar due to the presence of intramolecular O$\cdots$S interactions and optical gaps of these two oligomers are red shifted compared to the values obtained for others. These two planar oligomers and few other azomethines are found to be potential candidates for the absorption layer of an OPV.

After a detailed study of structural and optoelectronic properties, few of these azomethines are carefully selected to study their charge carrier injection and transport properties. Our findings show that the presence of a bulky substituent adversely affects these properties. However, the electronic effect of substituents may be utilized to tune these properties by substitutions at suitable positions. High electron injection barriers and poor stabilities of the anionic forms of these azomethines will prevent them from

being electron transport layer. However, most of the oligomers have excellent hole injection capability. For some of the studied molecules, mobilities of holes and electrons are sufficiently large. Thus, considering both the charge carrier injection and transport properties, it is found that a thiophene–pyrrole azomethine without any substituent and substituted azomethines with a methyl, methoxy or amine group at the 3 position of the pyrrole ring may act as efficient materials for the hole transport layer.

Chapter 4: *Vinylene- and azomethine-linked oligomers: Optoelectronic properties of helical and nonhelical conformers*

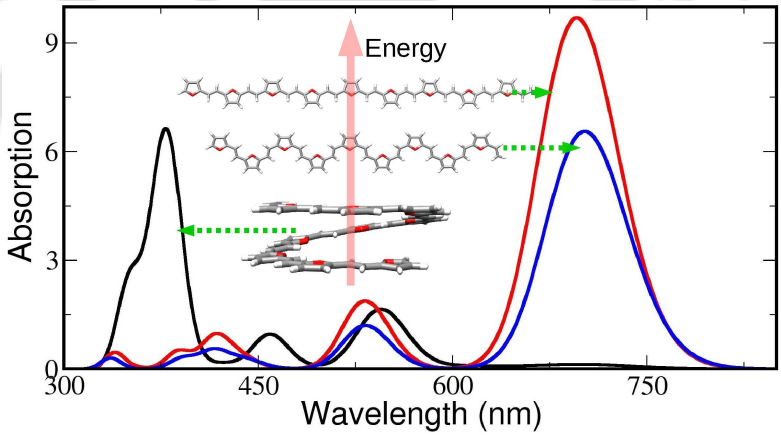

Looking at the possibility of a large number conformers of π-spaced heterocyclic oligomers, this chapter focuses on stabilities and optoelectronic properties of different conformers of an oligomer. Although different conformations of small oligomers are taken care of in several studies, conformations of long oligomers are often neglected. However, order of stability of conformers of an oligomer may change with the increase of chain length due to intramolecular noncovalent interactions, which may lead to change in their optoelectronic properties. To unveil the missing information of structure-property relationships with increase in chain length, a systematic study is carried out for vinylene- and azomethine-based heterocyclic conjugated polymers. For each oligomer, one folding conformer and two linear conformers are considered. B3LYP and B3LYP-D3 functionals are used to observe the effect of dispersion energy, and our results indicate that the B3LYP-D3 functional is suitable for ground-state studies of these systems. In the case

of folding conformers, after a certain chain length, while all vinylene-linked oligomers and thiophene-azomethines form helix-like structures, pyrrole-azomethines and furan-azomethines form irregular foldamers. For long vinylene-linked oligomers, helices are comparatively more stable than their respective linearly conjugated isomers, due to intramolecular noncovalent interactions. In the case of azomethine-linked oligomers, geometries and stabilities of conformers depend on the type of heterocyclic ring in the repeating unit. For linearly conjugated vinylene-linked systems, $S_0 \rightarrow S_1$ transitions have the largest oscillator strengths, and these absorption bands are dominated by the HOMO to LUMO excitation. In the case of a few linear azomethine-linked oligomers, two major electronic transitions, $S_0 \rightarrow S_1$ and $S_0 \rightarrow S_2$, are noticed. However, transitions from S_0 to higher electronic states are the most prominent transitions in cases of foldamers, except azomethine-linked thiophene foldamers. Major absorption bands of these helical oligomers are dominated by transitions from HOMO–N to LUMO+N orbitals.

Chapter 5: *Pyridine–furan/pyrrole/thiophene oligomers: Geometries and optoelectronic properties of helical conformers*

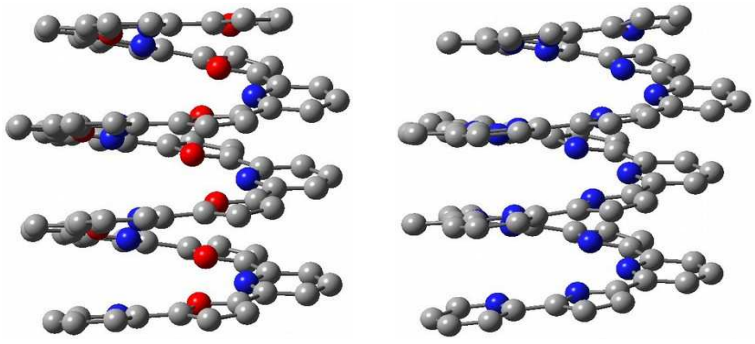

pyridine-furan pyridine-pyrrole

This chapter reveals structural and optoelectronic of pyridine-based helical oligomers. Similar to the above mentioned helical vinylene-linked oligomers, in the case of pyridine–furan, pyridine–pyrrole and pyridine–thiophene oligomers, helix-like structures are also possible even at smaller chain length compared to the vinylene-linked ones. Further,

these pyridine-based oligomers have two different helical conformations, making them suitable candidates to explore the details of structural and optoelectronic properties of helical oligomers. Comparison of results obtained at B3LYP/6-31G(d) and B3LYP-D3/6-31G(d) levels of theories reveals that the inclusion of dispersion correction with the B3LYP functional has a major impact on ground state structures and stabilities of these helical oligomers. Calculation of stabilization energies, gained due to the non-bonding interaction between adjacent helical turns, shows that stabilities of helical oligomers increase with an increase in chain length. Ground state dipole moment values of these helical oligomers fluctuate between a certain range and these values depend on the number of repeating units (n) and the number of repeating units needed to complete one helical turn (u) of a helix. The absorption spectrum of a helical oligomer is composed of multiple electronic transitions having significant oscillator strengths. Furthermore, for the most important electronic transition ($S_0 \rightarrow S_m$) of oligomers with $n > u$, m increases with increasing n. For these helices, excitations involving molecular orbitals other than frontier molecular orbitals significantly contribute to major electronic transitions.

Chapter 6: *Pyridine-pyrrole based cross-conjugated oligomers: Effects of insertion of π-spacers in the main chain on the electronic and optical properties*

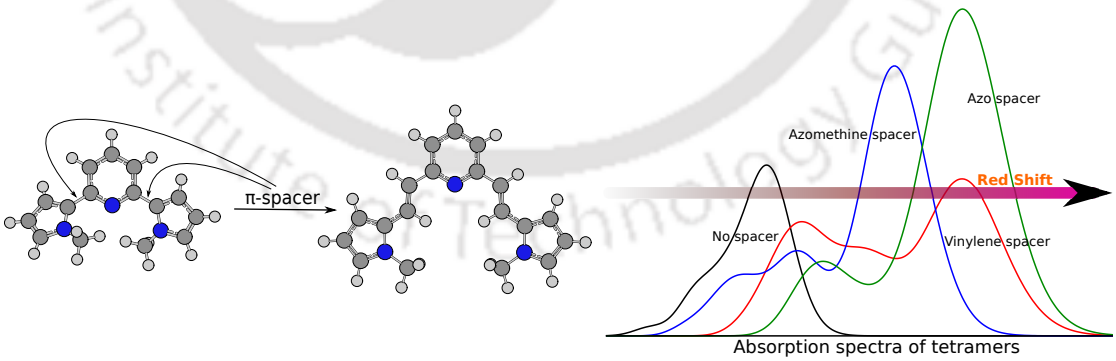

In comparison to through-conjugated systems, electronic and optical properties of cross-conjugated oligomers are difficult to tune. For through-conjugated systems, insertion of π-spacers in the main chain and having copolymers with donor and acceptor units are immensely successful ways to tune their properties. To see the applicability of these

informations in tuning the structure and properties of cross-conjugated systems, in this chapter, pyridine-pyrrole based donor-acceptor oligomers are chosen, and the effect of insertion of π spacers, such as vinylene, azomethine, azo-linkages on the electronic and optical properties are studied. Our results show that major absorption peaks for the π-spaced oligomers are shifted towards the red end compared to those for the basic unit. Optical and fundamental gaps also decrease upon the insertion of π-linkers in the oligomer. Similarly, dipole moment, change in dipole moment upon excitation and hole-electron binding energy of an exciton are significantly altered by the presence of additional π linkages in the main chain. Our results convey that optical and electronic properties of neutral cross-conjugated molecules can be effectively tuned by extending the conjugation length of its two conjugated branches.

Chapter 7: *Summary and conclusions*

In this thesis, structural, electronic and optical properties of various through- and cross-conjugated heterocyclic oligomers are unraveled. Chapter 3 indicates that few thiophene and pyrrole based azomethines have suitable properties for their use in organic devices. Results of Chapter 4 show that the most stable conformer and optoelectronic properties of an oligomer may change with an increase in chain length. In Chapter 5, it is shown that helical conformers of pyridine-furan, pyridine-pyrrole and pyridine-thiophene oligomers are feasible, and this study explores their HOMO-LUMO gaps, optical gaps, absorption spectra and dipole moments. Chapter 6 concludes that properties of a cross-conjugated system can be tuned by the insertion of π-spaces in its main chain.

List of articles published/submitted

1. Harikrishna Sahu and Aditya N. Panda, Computational study on the effect of substituents on the structural and electronic properties of thiophene–pyrrole- based π-conjugated oligomers, *Macromolecules*, **2013**, 46, 844–855.

2. Harikrishna Sahu and Aditya N. Panda, Computational investigation of charge injection, and transport properties of a series of thiophene–pyrrole-based oligoazomethines, *Phys. Chem. Chem. Phys.*, **2014**, 16, 8563–8574.

3. Harikrishna Sahu and Aditya N. Panda, Helical and nonhelical structures of vinylene- and azomethine- linked heterocyclic oligomers: A computational study of conformation-dependent optoelectronic properties, *J. Phys. Chem. C*, **2015**, 119, 22855–22865.

4. Harikrishna Sahu, Shashwat Gupta, Priyank Gaur and Aditya N. Panda, Structure and optoelectronic properties of helical pyridine–furan, pyridine–pyrrole and pyridine–thiophene oligomers, *Phys. Chem. Chem. Phys.*, **2015**, 17, 20647–20657.

5. The contents of Chapter 6 are submitted to a journal.

Contents

Symbols and abbreviations

α	alpha
β	beta
χ	chi
δ	Lowercase delta
Δ	Uppercase delta
$\Delta\mu_{ge}$	Difference in dipole moment of ground and excited states
ϵ	epsilon
η	eta
λ	lambda
μ	mu
μ_g	Ground-state dipole moment
μ_e	Excited-state dipole moment
ν	nu
ρ	rho
σ	sigma
π	pi

ϕ	phi
ψ	psi
Ψ	Psi
%	Percentage
Å	Angstrom
BHJ	Bulk-heterojunction
BLA/Δr/δr	Bond length alternation
CAM	Coulomb-attenuating method
CB	Conduction band
d	Rise per repeating unit
D_{inner}	Inner diameter
D_{outer}	Outer diameter
CD	Circular dichroism
DFT	Density functional theory
DFT-D3	Density Functional Theory including Grimme's D3 version of dispersion
E_{b}^{1}	Hole-electron binding energy = $E_{\text{g}}^{\text{fund}}$–$E_{\text{g}}^{\text{opt}}$
E_{b}^{2}	Hole-electron binding energy = E_{g}^{hl}–$E_{\text{g}}^{\text{opt}}$
E_{H}	Energy of the HOMO
E_{L}	Energy of the LUMO
E_{g}	Excitation energy
E_{g}^{hl}	HOMO-LUMO gap

E_g^{opt}	Optical gap
E_g^{fund}	Fundamental gap
f_{osc}	Oscillator strength
FF	fill factor
FMO	Frontier molecular orbital
H	HOMO
HF	Hartree-Fock
fwhm	Full width at half maximum
GGA	Generalized gradient approximation
HOMO	Highest occupied molecular orbital
I	Current
I_{SC}	Output current at short circuit condition
IP	Ionization potential
ITO	Indium tin oxide
K	Kelvin
kcal	Kilo-calorie
KS	Kohn-Sham
L	LUMO
LUMO	Lowest unoccupied molecular orbital
LDA	Local-density approximation
LSDA	Local spin-density approximation

MO	Molecular orbital
mol	Mole
nm	Nanometer
OFET	Organic field-effect transistor
OLED	Organic light-emitting diode
OPV	Organic photovoltaics
p	Pitch
PBC	Periodic boundary condition
TDDFT	Time-dependent density functional theory
u	Number of repeating units per turn
UV-Vis	ultraviolet-visible
V	Voltage
V_{OC}	Voltage at open circuit condition
VB	Valence band
Vis-NIR	Visible near-infrared

List of Figures

List of Tables

Introduction

For a long time, polymers were known for their electrical insulating properties, and these macromolecules were only used as insulating materials in many applications for their additional suitable chemical and mechanical properties. However, the idea of conductive polymer emerged after a spectacular discovery by three eminent scientists: Alan J. Heeger, Alan G. MacDiarmid and Hideki Shirakawa. In 1977,[1] they revealed the conductive property of halogen doped polyacetylene, which initiated a new field in chemistry by introducing conjugated organic polymers as metals or semiconductors, in contrast to non-conjugated insulators. In 2000,[2] they received the Nobel Prize in chemistry for "*for the discovery and development of conductive polymers*".

With the intrinsic mechanical properties and processing advantages of plastics, the suitable optical and electronic properties of these conjugated polymers enable them as appropriate alternatives for metal/semiconductor materials in electronic devices, which brings an immense hope of development of organic devices, such as organic light emitting diodes (OLEDs),[3] organic photovoltaics (OPVs)[4,5] and organic field-effect transistors (OFETs)[6]. These organic devices have a number of advantages such as cheapness, flexibility, semitransparency, lightweight and easy processability compared to their inorganic counterparts, which amplified the interest in the development of organic electronics. In recent years, as a consequence of the large amount of research carried out by both experimentalists and theoreticians to improve the efficiency and stability,[7–11] few devices

are already at the stage of commercialization[12,13]. Although significant progress has been made in their development in past few years, these devices are still far behind their inorganic counterparts in terms of efficiency and stability. To develop a device, we have to focus on multiple points, such as designing appropriate active materials, device fabrication and interface engineering. In an organic device, active materials are either based on small molecules or conjugated polymers. In this thesis, all studies are based on conjugated polymers. The physics of these polymers are still ill-understood, and understanding the relationship between the structure of an oligomer and their electronic and optical properties is vital for the optimization of active materials.

1.1 Types of conjugated polymers

Conjugated polymers of many different varieties are known which include polymers based on non-hetero atoms,[14] heterocyclic rings,[14] fluorene rings,[15] fused-rings,[16] backbone having π-spacers[17–19] and donor-acceptor systems[20,21], which highlight their structural versatility, and it creates a library of π-conjugated systems. They can be classified in multiple ways based on different factors, and out of them, few important types related to the thesis work are discussed below.

1.1.1 Homopolymers and copolymers

There are two types of polymers based on the types of monomer present in the backbone chain, i.e., homopolymers and copolymers. In homopolymers, only one type of monomer units are involved in polymerization, while two different types are involved in copolymers. Further, copolymers are categorized into different groups depending on the arrangement of two types of repeating units (suppose A and B units), such as random copolymers, block copolymers and alternating copolymers. In random copolymers, the two types monomers are arranged in any possible order. In block copolymers, two types monomers are grouped as homopolymers, and these two homopolymers are joined together by a

covalent bond, i.e., (-A-A-B-B-). In the case of alternating copolymers, two different types of monomers are arranged in regular -A-B-A-B- fashion.

1.1.2 Through-conjugated and cross-conjugated polymers

Based on the connectivity pattern, linearly π-conjugated polymers are divided into two types, i.e., through- and cross-conjugated polymers. In through-conjugated systems, all unsaturated atoms present in the backbone chain are conjugated with each other. In cross-conjugated systems, three unsaturated groups are present (namely **A**, **B** and **C**), while **A** and **C** are conjugated individually to **B**, **A** and **C** are not conjugated to each other.[22]

1.2 Electronic structure and properties

Drastic differences in electrical conductivity and light absorption properties between conjugated and non-conjugated oligomers can be explained by the Peierls distortion and molecular orbital theory. Polyethylene, a nonconjugated polymer, can be represented as a structure of equally spaced CH_2 units having only paired electrons. This forms a completely filled band, making polyethylene to behave as an insulating material. However, the situation is different in the case of a conjugated polymer, such as polyacetylene. Polyacetylene can be represented as a chain containing N carbon atoms with N electrons in $2p_z$-orbitals. This may result in a half filled band, similar to those for the conducting metal. However, as a result of Peierls distortion, the structure of equally spaced carbon atoms in polyacetylene are comparatively less stable than the structure with alternating single and double bonds in the backbone chain.[23] The chain gains electronic energy by separating the half filled band to a valence band and a conduction band with a forbidden zone, called the band gap. This gain in energy exceeds the energy of deformation resulting modification from a structure of equally spaced carbon atoms to a chain of alternate single and double bonds. Thus, bond length alternation (BLA), which is the

difference of the average carbon-carbon single and double bond lengths in the backbone chain, is a crucial parameter for tuning the band gap.[24]

In a molecule, a carbon atom forms four bonds with neighboring atoms due to its electronic structure of $1s^2\ 2s^2\ 2p^2$. In the case of non-conjugated polymers, such as polyethylene, all carbon atoms are sp^3 hybridized. Thus, they form four σ bonds with neighboring atoms resulting a large gap between the highest bonding σ molecular orbital (MO) and the lowest anti-bonding σ^* MO, which lead them to behave as insulators and made them insensitive to the visible light. On the other hand, in the case of conjugated polymers, valence orbitals of carbon atoms are involved in sp^2 (or sp) hybridization. For example, in polyacetylene, all carbon atoms are sp^2 hybridized, resulting three sp^2 hybrid orbitals and a free $2p_z$-orbital on each atom. Thus, in addition to σ bonds, bonding π and anti-bonding π^* MOs are formed by the overlap of the remaining $2p_z$-orbitals of carbon atoms. Compared to the σ electrons, π-electrons are loosely bound by carbon atoms resulting delocalization across the chain. As the number of unsaturated carbon atom increases with increasing chain length, number of $2p_z$-orbitals involved in π MOs also increases which forms more delocalized orbitals and subsequently, this leads to decrease in the energy gap (E_g) between π and π^* orbitals. In an conjugated polymer of infinite chain length, interactions of large number of $2p_z$-orbitals broaden the molecular energy levels into electronic bands, which results in the formation of a fully occupied π-valence band (VB) and an empty π^*-conduction band (CB). In comparison to the lowest allowed electronic transition $\sigma \rightarrow \sigma^*$ for a non-conjugated polymer, energy of the lowest $\pi \rightarrow \pi^*$ transition of a conjugated polymer is smaller, and for many systems it drops to the visible region. This results in drastic change of the properties of conjugated polymers such as absorption of small energetic photons, semiconducting behavior, easy oxidization and reduction, good charge carrier mobilities, etc., which are not seen in the case of non-conjugated polymers.

However, it is important to mention that undoped polyacetylene is a non conductive material. To increase its conductivity, it must be doped to either partially fill the CB by addition of electrons through the reduction process or partially vacate the VB by

the oxidation process. These processes certainly improves its electrical conductivity, but with a cost of air stability, which urges us to search new conjugated polymers those are stable upon doping or conductive without doping. It is observed that electron rich heterocyclic conjugated polymers and their derivatives are quite stable upon oxidation, with good electrical conductive properties. Thiophene and pyrrole rings are examples of such heterocycles which are widely mentioned in the literature.[14]

1.2.1 Band gap

The band gap is defined as the energy difference between the top of the VB and the bottom of the CB, i.e., the energy range where no electron state exist. It determines the conductivity and wavelength of interacting light, while the positions of the band edges determine the ease of doping, stability of the doped state compared to its neutral state and the ease of carrier injection from an electrode. While metals have zero band gaps, a band gap of 3 eV is considered as a border line between the insulating and semiconducting materials. In particular, small band gap (less than 1.5 eV) polymers are in focus of recent research due to their many interesting applications. In order to investigate an infinite system, band gaps of conjugated polymers are often calculated by applying the periodic boundary condition (PBC) to the repeating unit, which is the most stable conformer of the monomer. However, in organic thin films, often disordered structures are found, which results in localization of the wavefunction over a small chain length. Further, stability of conformers of an oligomer may change with increasing chain length due to the intramolecular non-covalent interactions between different parts of the chain. For these reasons, oligomer extrapolation approach is nowadays widely adopted compared to the cost effective PBC calculations. It is important to mention that the linear extrapolation approach often fails to predict the properties of polymers, and therefore other extrapolation techniques (such as the Kuhn formula[25]) are generally used for the calculation.[26–28]

1.2.2 IP, EA and orbital energies

The ionization potential (IP) and electron affinity (EA) are the amount of energy needed to remove the most loosely bound electron from a neutral molecule and the amount of energy released upon addition of an electron to a neutral molecule, respectively. Experimentally observed IP/EA is the the difference between the energy of the N-electron neutral ground state and that of the (N±1)-electron ionized state. The energy is adiabatic if the geometric relaxation is considered after the ionization; otherwise it is diabatic/vertical. The adiabatic IP and EA are calculated as follows:

$$\mathrm{IP}(a) = E^{+}(\mathrm{M}^{+}) - E^{0}(\mathrm{M}^{0}) \tag{1.1}$$

and

$$\mathrm{EA}(a) = E^{0}(\mathrm{M}^{0}) - E^{-}(\mathrm{M}^{-}). \tag{1.2}$$

Vertical IP and EA are calculated as

$$\mathrm{IP}(v) = E^{+}(\mathrm{M}^{0}) - E^{0}(\mathrm{M}^{0}) \tag{1.3}$$

and

$$\mathrm{EA}(v) = E^{0}(\mathrm{M}^{0}) - E^{-}(\mathrm{M}^{0}). \tag{1.4}$$

Here, $E^{X}(\mathrm{M}^{Y})$ represents the energy of M with charge 'X' at 'Y' charged geometry of a molecule.

As an approximation, the vertical IP and EA are calculated by the Koopmans' theorem. As per the Koopmans' theorem, assuming identical orbitals for both ionized and neutral states of a molecule, negative of energies of the highest occupied MO, denoted as HOMO, (E_{H}) and the lowest unoccupied MO, denoted as LUMO, (E_{L}) obtained at the close-shell Hartree-Fock (HF) level of theory are the first vertical IP and EA of the system.[29] This theorem neglects errors obtained from the orbital relaxation and electron correlation in an ion, and the cancellation of these two errors often provide good

gas-phase IP from the -E_{H}.[30] However, in the case of EA, these two errors add up which results an unreliable value. Further, LUMO is a virtual orbital and E_{L} is very sensitive to the the basis set used in the calculation, resulting in uncertainty in the EA value. Applicability of the Koopmans' theorem in the DFT level of theory is even more complected compared to the HF theory. In DFT, the energies of orbitals strongly depends on the approximation employed for the exchange correlation functional.[30] It is thought that an exact DFT functional will be able to calculate appropriate IP and EA values, which is still unknown.

1.2.3 Fundamental and optical gaps

Fundamental gap ($E_{\mathrm{g}}^{\mathrm{fund}}$) is the difference between IP(v) and EA(v),[29]

$$E_{\mathrm{g}}^{\mathrm{fund}} = \mathrm{IP}(v) - \mathrm{EA}(v). \tag{1.5}$$

This is also calculated as $E_{\mathrm{L}} - E_{\mathrm{H}}$, written as $E_{\mathrm{g}}^{\mathrm{hl}}$. The reliability of $E_{\mathrm{g}}^{\mathrm{hl}}$ depends on the method used for the calculation. Further, it is found that $E_{\mathrm{g}}^{\mathrm{hl}}$ of a small oligomer is relatively smaller compared to the $E_{\mathrm{g}}^{\mathrm{fund}}$, and upon extrapolation, these two meet at the infinite chain length.[31] In contrast, optical gap ($E_{\mathrm{g}}^{\mathrm{opt}}$) is the energy required to excite an electron from the ground state (S_0) to the first optically allowed excited state (S_1). It is important to mention that the $E_{\mathrm{g}}^{\mathrm{hl}}$ calculated by a DFT functional having 20-30% HF exchange (such as B3LYP) is close to the $E_{\mathrm{g}}^{\mathrm{opt}}$ and therefore, the comparison between these two are often found in the literature.[30] However, these two are completely different quantities by definition, and only the $E_{\mathrm{g}}^{\mathrm{fund}}$ and $E_{\mathrm{g}}^{\mathrm{opt}}$ are relevant for finite oligomers.

For most of the conjugated polymers, in the presence of light of appropriate wavelength, an electron is excited to the LUMO and a hole is created in the HOMO, which are electrostatically bound resulting a hole-electron pair, called exciton. The energy required to dissociate an excited electron-hole pair into free charge carriers is called the exciton binding energy (E_{b}) and is calculated as $E_{\mathrm{b}} = E_{\mathrm{g}}^{\mathrm{fund}} - E_{\mathrm{g}}^{\mathrm{opt}}$.[29]

1.2.4 Dipole moment

Dipole moment is a measure of charge distribution and its value in the ground state (μ_g) affects molecular aggregation, solubility of a molecule and solid state morphology. As a result, μ_g becomes an important parameter to be considered while developing efficient organic devices.[32–35] For an oligomer, for which there are various possible conformations, different μ_g values are obtained for different conformers.[33,35] Change in dipole moment ($\Delta\mu_{ge}$) upon excitation of an electron from the ground state to an excited state is linearly related to the degree of separation of a hole and an electron in an exciton, and thus affects the power conversion efficiency of an organic device.[36–38] However, a very large $\Delta\mu_{ge}$ value may adversely affect the device performance.[39]

1.2.5 Absorption spectrum and oscillator strength

Under illumination, a molecule absorbs electromagnetic radiation of appropriate energy resulting transition of an electron from an occupied orbital in the ground state to an unoccupied orbital, and an excited state is formed. The Beer–Lambert Law states that the absorbance (A) is proportional to the concentration (c) of a substance dissolved in a solvent and measured at a wavelength (λ), which is written as

$$\mathrm{A} = \varepsilon \mathrm{cL}, \tag{1.6}$$

where L is the path length. The molar absorption coefficient (ε) is directly related to the intensity of each band and its value for a particular compound is a constant at the specified wavelength. Oscillator strength (f_{osc}) which describes the strength of a particular transition is related to ε as[40]

$$f_{osc} = \frac{2303 m_e c_0^2}{\pi N_{av} e^2 n} \int \varepsilon(\overline{\nu}) d\overline{\nu} = \frac{4.32 \times 10^{-9}}{n} \int \varepsilon(\overline{\nu}) d\overline{\nu}, \tag{1.7}$$

where c_0 is the velocity of light, n is the index of refraction, N_{av} is the Avogadro number, $\overline{\nu}$ is the wavenumber (in cm^{-1}), and m_e and e are the mass and the charge of an electron, respectively. The term $\int \varepsilon(\overline{\nu})d\overline{\nu}$ represents the area of the absorption band under consideration.

Quantum mechanically, the f_{osc} associated with an electronic transition from the ground state ψ_i to an excited state ψ_f is written in terms of transition dipole moment, μ_{if}, as

$$f_{osc} = \frac{8\pi^2 m_e E_{fi}}{3he^2}|\mu_{if}|^2, \tag{1.8}$$

where $E_{fi} = E_f - E_i$ is the difference of energies between the ground and excited states, and m_e and e are the mass and charge of an electron. The transition moment μ_{if} is expressed as

$$\mu_{if} = \langle \psi_i \chi_i | \widehat{\mu} | \psi_f \chi_f \rangle, \tag{1.9}$$

where $\widehat{\mu}$ is the dipole moment operator. Here, the wave function of a molecule is described by the product of the electronic wave function (ψ) and its associated vibrational wave function (χ), while ignoring the rotational contribution. According to the Franck-Condon principle, the electronic transition occurs on a short time scale compared to the nuclear motion, so the $\widehat{\mu}$ depends only on the electronic coordinates, and the above integral can be written as $\langle \psi_i | \widehat{\mu} | \psi_f \rangle \times \langle \chi_i | \chi_f \rangle$. The square of the second term, $|\langle \chi_i | \chi_f \rangle|^2$, is called the Franck-Condon factor and measures the expected intensity of a transition.

1.3 Photophysical and electronic process in organic devices

The designing of efficient active materials requires a fundamental understanding of photophysical and electronic processes involved in a device, and their relation to the electronic and optical properties of organic materials. In the subsections below, working principles of OPV, OLED and OFET are described, focusing on the matters related to

organic materials. However, there are many other factors such as the device configuration, which affects the efficiency and stability of an organic device.

1.3.1 Working principle of organic devices

1.3.1.1 OPV

OPVs are organic devices which produce electricity from the sunlight by the photovoltaic effect. Unlike inorganic solar cells, organic materials are used as active materials in OPVs. Depending on the type of junction present in OPVs, they are categorized in to different types, such as single layer, bilayer and bulk-heterojunction (BHJ) solar cells. In the case single layer OPVs, only one organic layer is sandwiched between two electrodes. However, due to the large hole-electron binding energy of the organic layer, most of the photogenerated charge carriers often recombine, resulting in poor output current. To solve this issue, instead of one layer, a combination of donor and acceptor layers are used as the active material. In this bilayer architecture, a major problem remains due to the small exciton diffusion length in organic materials, leading to small output current as excitons often fail to reach the bilayer junction.

Nowadays, the single layer and bilayer device architectures are replaced by the BHJ solar cell. To demonstrate its architecture and working principle, a model of BHJ solar cell is shown in Figure 1.1 (a). BHJ is a blend of the donor and acceptor materials in nanoscale to form the absorption layer, where each interface is within a distance less than the exciton diffusion length from the absorbing site. When light of appropriate wavelength falls on the active layer, it absorbs photons and excitons are formed by excitations of electrons from occupied to unoccupied orbitals. These excitons migrate towards the donor-acceptor interface, where the charge separation takes place to form the individual charge carriers. These separated holes and electrons travel towards anode and cathode, respectively, and finally these charge carriers are collected at the respective electrodes, which leads to the generation of electric current. With consideration of

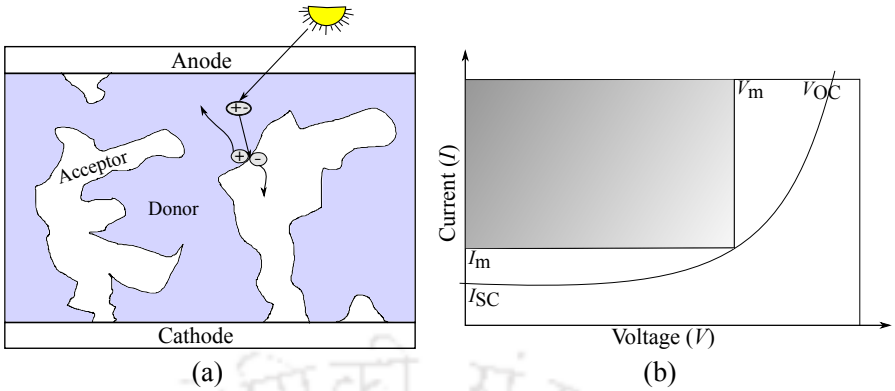

FIGURE 1.1: (a) Structure of a bulk-heterojunction solar cell and (b) current (I)-voltage (V) curve of an OPV.

number of processes involved, power conversion efficiency (η) of a BHJ solar cell can be written as[41]

$$\eta = \eta_{\mathrm{A}} \times \eta_{\mathrm{ED}} \times \eta_{\mathrm{CT}} \times \eta_{\mathrm{CC}}, \tag{1.10}$$

where η_{A}, η_{ED}, η_{CT} and η_{CC} are efficiencies of light absorption by the active layer, exciton dissociation, charge transfer and carrier collection by electrodes, respectively.

Electric power is the rate at which the electrical energy is transferred by an electric circuit. So, work done per unit time is

$$P = \frac{V \times Q}{t} = V \times I, \tag{1.11}$$

where V, Q and I are electric potential/voltage, electric charge and electric current, respectively. A representative diagram showing the relation between current and voltage of an organic solar cell under illumination is shown in Figure 1.1 (b). At a particular point of the I-V curve, the maximum power (P_{m}) is generated with the corresponding current I_{m} and voltage V_{m}. Power conversion efficiency is calculated as[41]

$$\eta = \frac{P_{\mathrm{m}}}{P_{\mathrm{in}}} = \frac{V_{\mathrm{m}} \times I_{\mathrm{m}}}{P_{\mathrm{in}}} = \frac{V_{\mathrm{OC}} \times I_{\mathrm{SC}} \times \mathrm{FF}}{P_{\mathrm{in}}}, \tag{1.12}$$

where P_{in} is the incident light intensity. V_{OC}, I_{SC} and FF are the voltage at open circuit condition, the output current at short circuit condition and the fill factor of the device,

respectively. V_{OC} is related to the difference of energies of HOMO of the donor and LUMO of the acceptor materials.[5] Short circuit indicate a circuit having no resistance or with negligible resistance. In the light absorption layer, each absorbed photon creates a hole-electron pair, and without any resistance all charge carriers will be collected by the electrodes. Thus, I_{SC} is directly related to the absorption of light. FF represents the ease of extraction of charge carriers in a solar cell. In the ideal case, FF is unity (100%). In reality, it is 50-70% for the organic solar cells, while $\sim$ 90% for the inorganic solar cells. So, there is a large amount of efficiency drop due to the resistance called parasitic resistance. There are two types of parasitic resistances: series resistance and shunt resistance. Series resistances in metal electrodes are very small compared to that in the organic layers. Also, the resistance at the interface of a metal electrode and an organic layer can be avoided by a careful selection of materials having proper energy levels,[42] which may lead to an ohmic contact. Thus, the resistance in the organic layer dominates the series resistance, which depends upon the product of resistivity and thickness of the organic layer. Resistivity (ρ) is inversely related to the mobility (μ) of charge carriers as

$$\rho = \frac{1}{\sigma} = \frac{1}{nq\mu}. \tag{1.13}$$

Here, n and q are the density of free carriers in the organic material and the elementary charge, respectively. Although η is directly related to the μ of a charge carrier, unbalanced μ values for holes and electrons results in accumulation of charge carriers in the organic material, leading to a substantial reduction of η.[41] In addition, current leakage can take place by the shunt resistance, mainly caused by three reasons, (a) pinhole in the cell, (b) edge of the device and (c) traps. Another major reason for the small FF is the large intrinsic hole-electron binding energy in the organic materials, which results in more recombinations of holes and electrons compared to what happens in the inorganic materials.

1.3.1.2 OLED

OLEDs are light-emitting diodes composed of thin films of organic molecules, which emits light in the response to electric current. Figure 1.2 shows a representative model of an multilayer OLED. It consists of three organic layers embedded between the anode

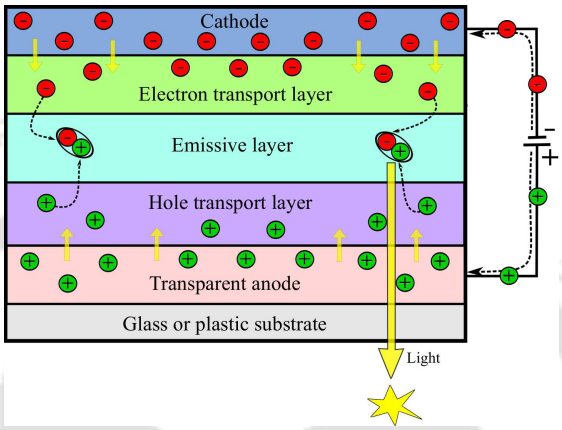

FIGURE 1.2: Structure of a multilayer OLED

and cathode. Out of three organic layers, the emissive electroluminescent layer is sandwiched between two distinct carrier transport layers for holes and electrons. When a voltage is applied to the electrodes, electrons are injected from the cathode to the electron transport layer, while holes are propelled from the anode to the hole transport layer. Driven by the applied electric field, holes and electrons travel in opposite directions and combine in the emissive layer to form excitons. In excitons, spins of holes and electrons can be combined in four different ways, i.e., one combination of antiparallel spin and three combinations of parallel spins. Therefore, 25% singlet and 75% triplet excitons are generated. Singlet and triplet excitons are primarily decayed *via* fluorescence and thermal relaxation, respectively, which limits the maximum output of a fluorescent OLED to 25%. Further, the efficiency of an OLED depends upon the ease of charge carrier injection from metal electrodes to transport layers and mobilities of these charge carriers in organic layers, which can be monitored by designing appropriate organic materials. Furthermore, band gap of the organic molecule present in the emissive layer determines the wavelength of emitted light, and the intensity of light is related to the current.

1.3.1.3 OFET

OFETs are field effect transistors where semiconducting materials are organic molecules. It is composed of three terminals named as the source, drain and gate, in which the current flows between the source and drain controlled by the voltage applied to the gate electrode. The source and drain electrodes are connected through an organic semiconducting layer, and an insulating layer is placed between the semiconducting layer and the gate electrode which forms a capacitor. In the case of zero gate voltage, charge carriers are not present in the organic semiconducting layer. The only way to drive current between the source and drain electrodes is the direct carrier injection from the source/drain electrodes to the semiconductor, which produces a small current due to large resistance of the organic semiconducting layer. When a voltage is applied on the gate electrode, like in any capacitor, charge carriers are formed at the interface of the insulating and semiconducting layers. This increases the conductivity of the semiconducting layer which enhances the current flow between the source and drain electrodes. Therefore, the gate voltage controls the current flow between the two terminals, and this enables the device to behave as a microelectric switch. The efficiency of an OFET is mainly determined by the mobilities holes and electrons in the organic semiconducting layer.[9,43,44] Besides that, the resistances at the contact surface between organic materials and electrodes also affect the device efficiency.

1.3.2 Key properties of organic materials for the development of devices

Conjugated polymers of specific properties are required for a specific purpose in organic devices. For example, polymers having different optical gaps are needed for the emission layer of an OLED compared to that for the absorption layer of an OPV. I_{SC} of an OPV is directly related to the amount of photon absorbed under the illumination, and thus, for the absorption layer, the optical gap in Vis-NIR range is a prime requirement.[5] In OPV, V_{OC} can be approximately calculated as the difference between HOMO and LUMO

energies of the organic material, and thus it directly affects the efficiency of a device.[5] In the interface of electrode and organic layer of all devices, polymers having appropriate HOMO and LUMO levels are required for the easy charge carrier injection/extraction from/to an electrode.[45] Small mobilities of holes and electrons in organic layers often limit the device efficiency, and it is a challenge to design a material having good charge carrier mobilities, for both holes and electrons. Balance in the mobilities of these two charge carriers is also important to avoid charge accumulation in the material.[41] In the case of OPV and OLED devices, the binding energy (E_b) between a hole and an electron in an exciton is a crucial parameter,[41] as it determines the ease of hole-electron separation. For a polymer, small E_b is a necessary requirement of an OPV, while the opposite enhances the efficiency of an OLED device. This binding energy can be effectively tuned by altering the fundamental and optical gaps, as discussed in subsection 1.2.3. It is also known that there is a correlation between the E_b and the $\Delta\mu_{ge}$, and thus, the $\Delta\mu_{ge}$ is a useful parameter to tune the E_b.[36,37] Further, the donor-acceptor interface morphology and the ease of hole-electron separation in the interface are also important factors for the development of an OPV. Furthermore, suitable IP and EA values of organic polymers are required to enhance the environmental stability of organic materials in devices. Thus, a large number of factors related to the active materials affect the efficiency and stability of an organic device, and all these properties are related to the chemical structures of the active materials.

1.4 Motivation

Conjugated polymers are center of attraction these days due to their possible use in organic devices.[5,6,46,47] A clear understanding of the optical and electronic processes occurring in conjugated polymers is vital to build a material of specific need. Chemical structures of the conjugated polymers are affected by the presence of electron donating and withdrawing groups, and this result in alternation of the geometries as well as their optical and electronic properties.[14] Even the effects of the same group present at

different positions in the main chain are quite different. Further, the configurational and conformational isomers of the same polymer have different properties.[33,48] To get an understanding of this multiple complexity, arduous studies on this topic are of urgent need. Further, the focus of the majority of research community is on the through-conjugated polymers, while helical shaped conjugated polymers[49,50] and linearly cross-conjugated polymers[51] are suffering from the lack of attention. This clearly points at the gap in understanding the relationship between the chemical structure and the properties, and there is a long path to achieve a full grasp over it, which is a very difficult task for the experimentalists. Here, computational studies play a key role in exploring varieties of conjugated polymers and gaining an understanding of the properties of the conjugated polymers in a faster and efficient way.

Recently, the interest in heterocyclic conjugated polymers has increased considerably.[52–58] In these polymers, as a result of the presence of hetero-atoms (S, N and O) in the main chain, the orbitals of these atoms also contribute to the electronic structure of the polymer. This leads to drastic change of their geometries and stabilities of various electronic states, resulting in different electronic and optical properties.[59–61] The presence of hetero-atoms in a polymer helps to regulate its own geometry and the bulk geometry by the intramolecular and intermolecular interactions, respectively, with the formation of hydrogen-bonds and other noncovalent bonds (e.g., S$\cdots$S, S$\cdots$N and S$\cdots$O). This leads to change in packing motifs of the organic materials, resulting alternation in charge transport, light absorption and other properties. Many heterocyclic polymers composed of thiophene, pyrrole, furan rings and their derivatives are widely studied for the search of a new conjugated polymer. Especially, polythiophene and their derivatives have gained considerable attention due to their chemical stability and suitable optoelectronic properties.[14,62] Chemical modification of these oligomers is of great interest for further development, which may lead to novel conjugated oligomers having better performance in devices than the existing ones.

One promising strategy to develop a suitable organic material is the introduction of vinylene and azomethine linkages in the main chain of an oligomer.[17,63–66] Introduction

of these π-spacers in the main chain of a conjugated polymer reduces dihedral angles between the repeating units and increases the π-electron delocalization over the main chain.[64,66] However, preparations of vinylene-linked oligomers require stringent reaction conditions, and these reactions often release lots of harmful byproducts.[67,68] The situation is completely different for azomethine-linked oligomers, which are isoelectronic with their vinylene counterparts. Besides the ease of synthesis and modification of their structures, these azomethine-linked oligomers have numerous advantages in optical and hole/electron transport properties.[17,69,70] Looking at the advantages of these linkages, a number of experimental studies have been carried out to explore the structural details and usability of these azomethine-linked heterocyclic polymers.[17] However, few computational studies are devoted to these systems,[19,71] and their properties are still unexplored.

For these π-spaced heterocyclic oligomers, a large number of conformations are possible,[65] and it is known that optoelectronic properties of a molecule are dependent on its conformation.[33,48] Stabilities of different conformers may vary with an increase in chain length, as for larger oligomers intramolecular noncovalent interactions affect the geometries of conformers.[50,72] As a result, optoelectronic properties of a molecule may also change with an increase in chain length. However, in the literature, optoelectronic properties of long oligomers have been calculated mostly either by applying the periodic boundary condition or by increasing the chain length of the most stable conformer out of the various possible conformations for a small oligomer. These methods may miss the picture of the conformation-optoelectronic properties relationship for large chain oligomers. Hence, systematic studies on conformational analyses, starting from small to large oligomers, are necessary to be carried out, and subsequently their optoelectronic properties are needed to be explored.

Out of large number of conformers of long oligomers, helical conformers are of immense interest as the understanding of their structural and stereochemical aspects paves ways to control and design the architecture of devices, in addition to gaining more knowledge about naturally occurring helices. These systems have extra stabilization

which arises from noncovalent interactions between adjacent turns in a helix. This, in conjunction with the inherent extended π-conjugation, has generated a lot of interest in this area of research. In addition to having good electronic and optical properties, these π-conjugated helical polymers are also optically active[73], and are potential candidates as chiral materials for applications like in circularly polarized electroluminescent devices[47,74–78] and may be used as chiral templates and chiral sensors[79,80]. Furthermore, π-conjugated helices may behave like molecular solenoids enabling them to act as potential candidates for high density data storage materials.[2,49,81–83] Various experimental studies[73,84–89] performed on helical conjugated polymers reveal that solute-solvent, π-π and H-bonding interactions affect the formation of a helical system. Many theoretical/computational studies have also been carried out to have structural information of π-conjugated helices[49,50,82,85,90–93] and in a few cases, to access the performance of computational methods (e.g. DFT functionals) in reproducing experimental observables. Some of these theoretical investigations have utilized the B3LYP functional in their studies.[49,82] However, theoretical studies on difluorinated thienylfurans[50] and *ortho*-phenylenes[85] have stressed on the importance of noncovalent interactions on the stability of their helical conformations. It is well known that hybrid *meta* density functionals and dispersion-corrected functionals are well suited for hydrogen bonding and other weak interactions, while poor results are observed for some traditional functionals like B3LYP[50,94–97]. This indicate that choosing a suitable functional becomes vital for theoretical investigations of helical oligomers. Further, to date, the optoelectronic properties of heterocyclic helical oligomers are not properly investigated.

Similar to helical oligomers, relatively less number of studies have been devoted to cross-conjugated polymers, and their electronic and optical properties with regard to their usage in organic devices are still largely unexplored.[51,98–100] Indeed, these properties are dependent on electron delocalization, and moderate electron delocalization in the main chain of these cross-conjugated polymers compared to their through-conjugated

analogues finds limited applications in advanced materials.[51] As mentioned in literature,[51,101] due to interleaving π-conjugation path in a cross-conjugated polymer, excitation energies, ionization potentials and electron affinities do not change much with respect to chain length, making it difficult to tune their optoelectronic properties. Further, compared to through-conjugated systems, quite different absorption spectra are observed due to small oscillator strengths of the first excitations of these oligomers.[102,103] On the other hand, cross-conjugated systems are known for their stability.[104,105] Also, after ionization, significant improvement is seen in π-electron delocalization near the bifurcation point of two conjugated branches, and this results in substantial change in absorption and conduction properties.[51,106] Owing to these unique advantages, attention on cross-conjugated oligomers is growing each day, and several important features of these oligomers are being explored.[51,104,106–112] These oligomers are now thought as suitable candidates for devices like molecular switches and molecular transistors.[51] However, more attention is needed to reveal their concealed properties, especially the ways to tune of the electronic and optical properties of neutral molecules.

1.5 Outline of the thesis

In this thesis, results of computational studies on various types of heterocyclic polymers are presented and discussed. In chapter 2, theoretical methods are briefly discussed. In chapter 3, the optoelectronic and charge transport properties of thiophene–azomethine–pyrrole-based oligomers are explored. Few of these azomethines are found to be suitable for light absorption, hole injection and hole transport in organic devices. This is followed by a study of the dependence of optoelectronic properties on different conformers of vinylene- and azomethine-linked oligomers with increasing chain length, which is presented in chapter 4. A clear deviation in the trend is seen in the energy profile of folding conformers with the increase of chain length, and optoelectronic properties of these folding conformers are quite different than those for their respective linearly conjugated oligomers. Chapter 5 explores the ground state geometries and optoelectronic properties

of pyridine-furan, pyridine-pyrrole and pyridine-thiophene based helical oligomers. In the absorption spectra of these helical oligomers, multiple electronic transitions other than the first excitation contribute significantly, and these major transitions are mainly dominated by HOMO$-N$ to LUMO$+N$ excitations. Finally, optical and electronic properties pyridine-pyrrole based cross-conjugated systems are presented in chapter 6. Here, three different π spacers, such as, vinylene-, azomethine-, azo-groups are utilized to enhance the electron delocalization in two conjugated branches of each pyridine–pyrrole-based cross-conjugated unit. Our study reveals that electronic and optical properties of a neutral cross-conjugated oligomer can be tuned effectively by introducing π-spacers in the main chain.

Theoretical methods

2.1 Many-electron system and Hartree-Fock theory

The time-independent Schrödinger equation for a system of N electrons and M nuclei is written as

$$\hat{H}\Psi_i(\mathbf{x}_1, \mathbf{x}_2, \ldots, \mathbf{x}_N, \mathbf{R}_1, \mathbf{R}_2, \ldots, \mathbf{R}_M) = E_i\Psi_i(\mathbf{x}_1, \mathbf{x}_2, \ldots, \mathbf{x}_N, \mathbf{R}_1, \mathbf{R}_2, \ldots, \mathbf{R}_M), \quad (2.1)$$

where $\hat{H}$ is the Hamilton operator representing the total energy of the system. Ψ is the wave function of the i'th state of the system which depends of $3N$ spacial and N spin coordinates of electrons, jointly denoted as $\mathbf{x}_i$, and $3N$ spacial coordinates of nuclei denoted as $\mathbf{R}_i$. E_i is the energy of the state i described by the wave function Ψ_i. In atomic units, the Hamiltonian is

$$\hat{H} = -\sum_{i=1}^{N}\frac{1}{2}\nabla_i^2 - \sum_{A=1}^{M}\frac{1}{2M_A}\nabla_A^2 - \sum_{i=1}^{N}\sum_{A=1}^{M}\frac{Z_A}{\mathbf{r}_{iA}} + \sum_{i=1}^{N}\sum_{j>i}^{N}\frac{1}{\mathbf{r}_{ij}} + \sum_{A=1}^{M}\sum_{B>A}^{M}\frac{Z_A Z_B}{\mathbf{R}_{AB}}. \quad (2.2)$$

Here, M_A is the ratio of the mass of nucleus A to the mass of an electron, and Z_A is the atomic number of nucleus A. $\mathbf{R}_A$ and $\mathbf{r}_i$ are position vectors of the nucleus A and electron i, respectively. The distances between two electrons i and j, electron i and nucleus A, and two nuclei A and B are denoted by $\mathbf{r}_{ij}$, $\mathbf{r}_{iA}$ and $\mathbf{R}_{AB}$, respectively. First and second terms are operators for kinetic energies of electrons and nuclei, respectively. Last three

terms constitute the potential energy operator for the electron-nucleus attraction, the electron-electron repulsion and the nucleus-nucleus repulsion, respectively.

Invoking the Born-Oppenheimer approximation at this point, kinetic energy of the nuclei can be neglected and nucleus-nucleus repulsion term can be made constant. Thus, the electronic Hamiltonian operator for N electrons moving under M fixed nuclei is written as

$$\hat{H}_{\text{elec}} = -\sum_{i=1}^{N} \frac{1}{2}\nabla_i^2 - \sum_{i=1}^{N}\sum_{A=1}^{M} \frac{Z_A}{\mathbf{r}_{iA}} + \sum_{i=1}^{N}\sum_{j>i}^{N} \frac{1}{\mathbf{r}_{ij}}, \tag{2.3}$$

and the electronic wave function as

$$\Psi_{\text{elec}} = \Psi_{\text{elec}}(\mathbf{r}_i; R_A). \tag{2.4}$$

Here, Ψ_{elec} depends explicitly on electronic coordinate, but parametrically on the nuclear coordinate. The corresponding Schrödinger equation is

$$\hat{H}_{\text{elec}}\Psi_{\text{elec}} = E_{\text{elec}}\Psi_{\text{elec}}, \tag{2.5}$$

where E_{elec} is the corresponding electronic energy. The total energy of a fixed nuclei system is

$$E = E_{\text{elec}} + \sum_{A=1}^{M}\sum_{B>A}^{M} \frac{Z_A Z_B}{\mathbf{R}_{AB}}. \tag{2.6}$$

From now onwards, only electronic terms will be discussed, and so the subscript 'elec' is removed for simplicity. For a N electron system, the wave function is $\Psi(\mathbf{r}_1, \mathbf{r}_2 \ldots \mathbf{r}_N)$, where $\mathbf{r}_i$ represents position coordinates of the electron i, and it depends on all the electron present in the system. This complex many electron wave function can be simplified to a product of one-electron orbitals by the orbital approximation and it is written as

$$\Psi(\mathbf{r}_1, \mathbf{r}_2 \ldots \mathbf{r}_n) = \Phi_1(\mathbf{r}_1)\Phi_2(\mathbf{r}_2)...\Phi_n(\mathbf{r}_N). \tag{2.7}$$

Introducing spin of electrons in to the one-electron orbital, $\Phi_1(\mathbf{r}_1)$, it can be expressed as $\Phi_1(1)\sigma(1)$, where σ is the spin wave function which is either α or β depending on

the orientation of the electron. Indistinguishability of electrons and Pauli principle of antisymmetric wave function can be satisfied by a Slater determinant, and for a N-electron system it can be written as,

$$\Psi(1,2\ldots3) = \frac{1}{\sqrt{N!}} \begin{vmatrix} \Phi_1(1)\alpha(1) & \Phi_1(1)\beta(1) & \ldots & \Phi_M(1)\beta(1) \\ \Phi_1(2)\alpha(2) & \Phi_1(2)\beta(2) & \ldots & \Phi_M(2)\beta(2) \\ \ldots\ldots\ldots\ldots\ldots\ldots\ldots\ldots\ldots\ldots\ldots\ldots\ldots\ldots\ldots\ldots\ldots\ldots\ldots\ldots\ldots\ldots \\ \Phi_1(N)\alpha(N) & \Phi_1(N)\beta(N) & \ldots & \Phi_M(N)\beta(N) \end{vmatrix}, \tag{2.8}$$

where M equals to $N/2$ and $(N+1)/2$ for even and odd N, respectively.

A single Slater determinant that gives the ground-state can be obtained by the Hartree-Fock (HF) method. The orbital approximation allows to express an n-electron Schrödinger equation as n one-electron Schrödinger equation, thus each electron correspond to $\Phi_i(r)$ satisfies the following equation,

$$\left(-\frac{1}{2}\Delta_i^2 - \sum_{A=1}^{M} \frac{Z_A}{\mathbf{r}_{iA}} + v^{\mathrm{HF}}(i) \right) \Phi_i(\mathbf{r}) = \varepsilon_i \Phi_i(\mathbf{r}), \tag{2.9}$$

where $i = 1, 2 \ldots, n$. The operator is an effective one-electron operator, named as Fock operator. $v^{\mathrm{HF}}(i)$ is the average interaction potential experienced by the ith electron in the presence of other electrons. The resulting set of equations is referred to as the HF equations, and the iterative self-consistent field procedure is used to solve them.

In the HF method, electron-electron correlation effects are not taken into account, as a consequence the calculated band gap for a conjugated polymer is too large. To incorporate electron-electron correlation effect, various post-HF methods are developed, such as Möller-Plesset perturbation theory, algebraic diagrammatic construction method, and approximate coupled cluster approach of second order (CC2). These methods are used for many systems,[113–118] and obtained results are quite impressive. However, these methods are not cost-effective to handle macromolecules, such as conjugated polymers similar to our systems, and due to the excellent accuracy-to-computational costs ratio,

DFT and TDDFT methods are generally used to obtain the structure and properties of conjugated polymers.[30,119]

2.2 Density functional theory

Electron probability density function or simply electron density, denoted as $\rho(x, y, z)$, is extracted from the electronic wave function. It is a function of only three variables (x, y, z), while an N-electron wave function depends on $4N$ variables, i.e., 3 spacial and one spin coordinates of each electron. The single-particle probability density corresponding to a normalized ground-state N-electron wave function is given by,

$$\rho(\mathbf{r}) = N \int |\Psi(\mathbf{r}, \mathbf{r}_2, \ldots, \mathbf{r}_N)|^2 d^3\mathbf{r}_2 \ldots d^3\mathbf{r}_N. \tag{2.10}$$

Electron density $\rho(\mathbf{r})$ have some specific properties, mentioned below, which enable it as a useful physical observable for the prediction of energy and other properties instead of complicated N-electron wave function.

- Integrated over all space, it gives the total number of electrons N, i.e.,

$$\int \rho(\mathbf{r}) d\mathbf{r} = N. \tag{2.11}$$

- Position of the nuclei leads to local maxima in the electron density.

- Nuclear atomic numbers can be obtained from the electron density by the following equation,

$$\left.\frac{\partial \overline{\rho}(\mathbf{r}_A)}{\partial \mathbf{r}_A}\right|_{\mathbf{r}_A=0} = -2Z_A\rho(\mathbf{r}_A) \tag{2.12}$$

  where Z is the atomic number of A, $\mathbf{r}_A$ is the radial distance from A, and $\overline{\rho}$ is the spherically averaged density.

Many early attempts have been made to deduce an energy functional for the electron density, for example, Thomas-Fermi-Dirac model. However, all produce inadequate results, as a consequence, these methods are not generally used in modern computations.

2.2.1 The Hohenberg-Kohn theorems and the Kohn-Sham approach

In 1964, two important theorems[120] were published by Hohenberg and Kohn which formed the platform of the modern Kohn-Sham (KS) approach. The Hohenberg-Kohn existence theorem says that all the properties of a molecule in a ground electronic state can be determined by the ground-state electron density function. The Hohenberg-Kohn variational theorem states that any trial electron density function will give an energy higher than or equal to the true ground-state energy, which is only true for the exact functional.

The Hohenberg-Kohn theory is valid for both interacting and non-interacting electrons. The realization by Kohn and Sham[121] that a system of non-interacting electrons can be taken as reference that have their ground state density the same as that of the real system made the major breakthrough. The non-interacting part can be treated easily which constitutes a major portion of the electronic energy, and relatively small portion is associated with the interacting part which can be calculated by a density functional.

The ground-state energy of a real molecule is

$$E_0 = T_s[\rho_0] - \sum_A Z_A \int \frac{\rho_0(\mathbf{r}_1)}{\mathbf{r}_{1A}} d\mathbf{r}_1 + \frac{1}{2}\int\int \frac{\rho_0(\mathbf{r}_1)\rho_0(\mathbf{r}_2)}{\mathbf{r}_{12}} d\mathbf{r}_1 d\mathbf{r}_2 + E_{\mathrm{XC}}[\rho_0], \qquad (2.13)$$

where the terms on the r.h.s indicate the kinetic energy of the noninteracting electrons, the nuclear-electron interaction, the classical electron-electron repulsion and the exchange-correlation energy, respectively. $T_s[\rho_0]$ in terms of the KS orbitals, ψ_i^{KS}, can be expressed as

$$T_s[\rho_0] = -\frac{1}{2}\sum_{i=1}^{N} \langle \psi_i^{\mathrm{KS}} | \nabla_i^2 | \psi_i^{\mathrm{KS}} \rangle. \qquad (2.14)$$

The orbitals ψ_i^{KS} used in equation 2.14 to minimize the energy E are obtained by the KS pseudo eigenvalue equations,

$$\hat{h}_i^{\mathrm{KS}}\psi_i^{\mathrm{KS}} = \varepsilon_i^{\mathrm{KS}}\psi_i^{\mathrm{KS}}, \tag{2.15}$$

where $\hat{h_i^{\mathrm{KS}}}$ is the KS one-electron operator defined as

$$\hat{h}_i^{\mathrm{KS}} = -\frac{1}{2}\nabla_i^2 - \sum_A^{\text{nuclei}} \frac{Z_A}{\mathbf{r}_{1A}} + \int \frac{\rho(\mathbf{r}_2)}{\mathbf{r}_{12}} d\mathbf{r}_2 + V_{\mathrm{XC}}. \tag{2.16}$$

The exchange correlation potential V_{XC} is a functional derivative of the exchange-correlation energy, E_{XC}, as mentioned in the following equation,

$$V_{\mathrm{XC}}(\mathbf{r}) = \frac{\delta E_{\mathrm{XC}}[\rho(\mathbf{r})]}{\delta\rho(\mathbf{r})}. \tag{2.17}$$

The $E_{\mathrm{XC}}[\rho_0]$ term, a functional of the electron density function associated with two terms, originating from the difference between the real and fictitious noninteracting reference systems is given by

$$E_{\mathrm{XC}}[\rho_0] = \Delta\langle T[\rho_0]\rangle + \Delta\langle V_{\mathrm{ee}}[\rho_0]\rangle. \tag{2.18}$$

Here, $\Delta\langle T\rangle$ term represents the correction to the kinetic energy deriving from the interacting nature of electrons called the kinetic correlation energy, and $\Delta\langle V_{\mathrm{ee}}\rangle$ term represents the non-classical corrections to the electron-electron repulsion energy, i.e., the potential correlation and exchange energies.

2.2.2 Approximate exchange-correlation functionals

The exact functionals for the exchange and correlation are unknown and, therefore, many approximations are employed to calculate the E_{XC}. In the local-density approximation (LDA), at each point $\mathbf{r}$ in space, the $E_{\mathrm{XC}}(\mathbf{r})$ is approximated as that of a homogeneous electron liquid of density $\rho(\mathbf{r})$, and it is computed exclusively from the value of $\rho(\mathbf{r})$.

The LDA functional which includes electron spin is called the local spin-density approximation (LSDA) functional. As the electron density is far from the spatially uniform model in a molecular system, the functional is further improved by including the first derivative or the gradient in addition to the $\rho(\mathbf{r})$, called generalized gradient approximations (GGA). In the *meta*-GGA functionals, in addition to the spin densities and their gradients, additional terms, such as Laplacians of the spin density, are also included to construct the functional. Nowadays, the most popular functionals are hybrid functionals, which are constructed by mixing a fraction of the exact exchange energy functional to the LDA/LSDA or GGA functional, and it is computed similar to HF calculations with KS orbitals. A hybrid functional can be written as,

$$E_{\mathrm{XC}}^{\mathrm{hybrid}} = aE_{\mathrm{X}}^{\mathrm{exact}} + (1-a)E_{\mathrm{X}}^{\mathrm{DFT}} + E_{\mathrm{C}}^{\mathrm{DFT}}, \tag{2.19}$$

where $E_{\mathrm{X}}^{\mathrm{exact}}$ is the nonlocal HF exchange energy, a is the percentage of HF exchange in the hybrid functional, $E_{\mathrm{X}}^{\mathrm{DFT}}$ is the local DFT exchange energy, and $E_{\mathrm{C}}^{\mathrm{DFT}}$ is the local DFT correlation energy. The Becke's three-parameter Lee–Yang–Parr (B3LYP) exchange-correlation functional[122] is a well known hybrid functional, and it can be expressed as

$$E_{\mathrm{XC}}^{\mathrm{B3LYP}} = 0.80E_{\mathrm{X}}^{\mathrm{LSDA}} + 0.20E_{\mathrm{X}}^{\mathrm{exact}} + 0.72E_{\mathrm{X}}^{\mathrm{B88}} + 0.81E_{\mathrm{C}}^{\mathrm{LYP}} + 0.19E_{\mathrm{C}}^{\mathrm{LSDA}}. \tag{2.20}$$

The PBE0[123,124] functional is given by

$$E_{\mathrm{XC}}^{\mathrm{PBE0}} = 0.25E_{\mathrm{X}}^{\mathrm{exact}} + 0.75E_{\mathrm{X}}^{\mathrm{PBE}} + E_{\mathrm{C}}^{\mathrm{PBE}}, \tag{2.21}$$

where $E_{\mathrm{X}}^{\mathrm{PBE}}$ and $E_{\mathrm{C}}^{\mathrm{PBE}}$ are the Perdew-Burke-Ernzerhof exchange and correlation functionals, respectively. M06-2X[125] is a hybrid *meta*-GGA functional, written as

$$E_{\mathrm{XC}}^{\mathrm{M06-2X}} = 0.54E_{\mathrm{X}}^{\mathrm{exact}} + 0.46E_{\mathrm{X}}^{\mathrm{M05}} + E_{\mathrm{C}}^{\mathrm{M06}}, \tag{2.22}$$

The exchange ($E_{\rm X}^{\rm M05}$) and correlation ($E_{\rm C}^{\rm M06}$) functionals are the same as for M05 and M06, respectively. PW6B95[126] is a hybrid *meta* exchange-correlation 6-parameter functional based on reoptimized Perdew-Wang-91 (PW) GGA-exchange and Becke-95 (B95) *meta*-GGA correlation,

$$E_{\rm XC}^{\rm PW6B95} = 0.28E_{\rm X}^{\rm exact} + 0.72E_{\rm X}^{\rm PW} + E_{\rm C}^{\rm B95}. \tag{2.23}$$

The functional can be further improved by the inclusion of many-body perturbation (MP) term, called double hybrid (DH) functionals. The exchange-correlation energy of a DH-functional can be expressed as

$$E_{\rm XC}^{\rm DH} = (1-a)E_{\rm X}^{\rm DFT} + aE_{\rm X}^{\rm exact} + (1-c)E_{\rm C}^{\rm DFT} + cE_{\rm C}^{\rm MP2}. \tag{2.24}$$

B2PLYP[127] is an example of such functional which has a correlation term at the MP2 level, written as

$$E_{\rm XC}^{\rm B2PLYP} = 0.53E_{\rm X}^{\rm exact} + 0.47E_{\rm X}^{\rm B88} + 0.73E_{\rm C}^{\rm LYP} + 0.27E_{\rm C}^{\rm MP2}. \tag{2.25}$$

The PWPB95[128] functional is a well-known DH-*meta*-GGA density functional, containing reoptimized parameters of 50% of each HF and PW exchange, 73.1% B95 correlation and 26.9% of spin-opposite scaled perturbative (SOS-PT2) correlation functionals, given by

$$E_{\rm XC}^{\rm PWPB95} = 0.50E_{\rm X}^{\rm exact} + 0.50E_{\rm X}^{\rm PW} + 0.731E_{\rm C}^{\rm B95} + 0.269E_{\rm C}^{\rm SOS-PT2}. \tag{2.26}$$

These DH-types functionals are computationally expensive, limiting their use in electronic structure calculations of large molecules.

2.2.3 CAM-B3LYP functional

Although DFT functionals are successful for a number of applications, these are still unsuccessful in many important applications, such as the polarizability of long chains

and excitations using TDDFT.[129,130] This problem is overcome to a large extent by the the long-range (LR) scheme,[129] where the electron repulsion operator $1/r_{12}$ splits into short-range and long-range parts by using the error function (erf). In consequence, the correct asymptotic $r_{12} \rightarrow \infty$ behavior is retained, where the Coulomb and exchange potentials cancel each other. The equation is

$$\frac{1}{r_{12}} = \frac{1 - erf(\mu r_{12})}{r_{12}} + \frac{erf(\mu r_{12})}{r_{12}}, \tag{2.27}$$

where μ is a range separating parameter. While the first term of this equation accounts to the short range, the second term accounts to the long-range part. For the exchange energy term, the short-range and long-range parts are treated by the DFT and exact HF exchange, respectively. However, the electron correlation term is the same as the DFT functional.

Yanai et al.[130] have generalized the equation 2.27 by introducing two additional parameters (α and β) in the equation as,

$$\frac{1}{r_{12}} = \frac{1 - [\alpha + \beta\ erf(\mu r_{12})]}{r_{12}} + \frac{\alpha + \beta\ erf(\mu r_{12})}{r_{12}}, \tag{2.28}$$

where $0 \leq \alpha + \beta \leq 1$, $0 \leq \alpha \leq 1$, $0 \leq \beta \leq 1$. The terms α and $\alpha + \beta$ represent the HF-exchange in short- and long-range limits, respectively. This Coulomb-attenuating method (CAM) with three parameters is more flexible than the LR-method. In the case of CAM-B3LYP functional,[130] the standard α, β and μ parameters are 0.19, 0.46 and 0.33, respectively.

2.2.4 DFT with London dispersion corrections

Conventional DFT functionals which do not contain the physics of dispersion interactions often fail in cases where the dispersion interaction plays a vital role, such as in the case of determination of the geometries and thermodynamic properties of systems.[131,132] Out of various methods developed to incorporate the dispersion interaction, Grimme's DFT-D

methods are well-established, and at present, the DFT-D3 method is the most successful one. Addition of a small dispersion correction term significantly improves the accuracy at the expense of a small computational cost. The wavefunction does not change with the addition of this correction term, and thus other molecular properties are unaffected. However, as the dispersion correction alters the force acting on the atoms, optimizations with DFT and DFT-D levels lead to different geometries.

In 2004, DFT-D1[133] was introduced with only sixth-order dispersion term, and it is slightly modified in DFT-D2[134] version. In DFT-D3, the dispersion correction term incorporate sixth- and eighth-order terms with modified dispersion coefficients and damping function, and the details of this method are mentioned below. The dispersion corrected total energy is given by

$$E_{\mathrm{DFT-D3}} = E_{\mathrm{DFT}} + E_{\mathrm{disp}}, \tag{2.29}$$

where E_{DFT} is the energy obtained by the original DFT functional, and E_{disp} is the dispersion energy, which is the addition of two- and three-body terms, written as

$$E_{\mathrm{disp}} = E^{(2)} + E^{(3)}. \tag{2.30}$$

Out of these two, the $E^{(2)}$ is the most important term. To avoid near singularities in the case of small internuclear distance of two atoms, the dispersion contribution is damped at short distances. The $E^{(2)}$ term with the standard zero damping formula, leading to zero contribution at short ranges, is given by,[95]

$$E_{\mathrm{disp}}^{\mathrm{D3ZERO}} = -\sum_{n=6,8} s_n \sum_{i,j>i}^{N_{\mathrm{at}}} \frac{C_n^{ij}}{(R_{ij})^n} f_{\mathrm{damp}}(R_{ij}), \tag{2.31}$$

where C_n^{ij} is the average nth-order dispersion coefficients for atom pair ij, R_{ij} is their inter-atomic distances, and s_n is the overall scaling factor, optimized for each DFT

functional. $f_{damp}(R_{ij})$, the damping function, is expressed as

$$f_{\text{damp}}(R_{ij}) = \frac{1}{1 + 6(R_{ij}/(s_{r,n}R_0^{ij}))^{-\alpha_n}}. \tag{2.32}$$

Here, parameters $s_{r,6}$ and s_8 are fitted for individual functionals. α_ns are the steepness parameters, which is adjusted such that the dispersion correction is $< 1\%$ of $\max(|E_{\text{disp}}|)$ for typical covalent bond distances. The $E^{(2)}$ term with the Becke-Johnson (BJ) damping function, leading to finite values for small interatomic distances, is expressed as[135]

$$E_{\text{disp}}^{\text{D3BJ}} = -\sum_{n=6,8} s_n \sum_{i,j>i}^{N_{\text{at}}} \frac{C_n^{ij}}{(R_{ij})^n + (f_{\text{damp}})^n}, \tag{2.33}$$

where the damping function is

$$f_{\text{damp}} = a_1 \sqrt{\frac{C_8^{ij}}{C_6^{ij}}} + a_2. \tag{2.34}$$

Here, s_n, a_1 and a_2 parameters are fitted for each DFT functional. The three-body dispersion contribution, $E^{(3)}$, is written as

$$E^{(3)} = \sum_{\text{ABC}} f_{\text{d},(3)}(\overline{r}_{\text{ABC}}) E^{\text{ABC}}, \tag{2.35}$$

where the sum is over all atom triples ABC in the system, and the equation 2.32 with $\alpha = 16$, $s_r = 4/3$ and geometrically averaged radii $\overline{r}_{\text{ABC}}$ is used as damping function. The term E^{ABC} is expressed as

$$E^{\text{ABC}} = \frac{C_9^{\text{ABC}}(3\cos\theta_{\text{a}}\cos\theta_{\text{b}}\cos\theta_{\text{c}} + 1)}{(r_{\text{AB}}r_{\text{BC}}r_{\text{CA}})^3}, \tag{2.36}$$

where θ_{a}, θ_{b} and θ_{c} are the internal angles of the triangle formed by r_{AB}, r_{BC} and r_{CA}. C_9^{ABC} is the triple-dipole constant defined by

$$C_9^{\text{ABC}} \approx -\sqrt{C_6^{\text{AB}}C_6^{\text{AC}}C_6^{\text{BC}}}. \tag{2.37}$$

The third body term is small for medium sized molecules, and therefore, this term is ignored in all the calculations reported in the thesis.

2.3 Time-dependent density functional theory

Time-dependent DFT (TDDFT) is an extension of DFT, which is used to investigate the properties and dynamics of many body systems in the presence of time-dependent potential. This method is widely used to investigate the excited-state properties of conjugated polymers.[30] Here, the basic ideas behind the TDDFT are presented. Runge-Gross theorem[136] is the foundation of the TDDFT and it conveys an important message which states that, for all many-body systems evolving from a fixed initial state, a one-to-one mapping exists between the time-dependent external potential ($v(\mathbf{r},t)$), and the time-dependent density ($\rho(\mathbf{r},t)$). Similar to the DFT, the time-dependent KS (TDKS) equation is also developed by replacing the interacting system with a fictitious noninteracting system. However, in most of the cases of our interest, under the small external perturbation, the system does not deviate much from the ground-state, and a full solution of the TDKS equation is often not required. For such weakly perturbed systems, linear response TDDFT has now become one of the most widely used methods.

Let us assume that at $t < t_0$, the time-dependent potential is zero and the system is in its ground-state density, $\rho_0(\mathbf{r})$. At t_0, a small time-dependent perturbation, $v_1(\mathbf{r},t)$, is turned on, which induces a change in the density, and it can be written as,

$$\rho(\mathbf{r},t) - \rho_0(\mathbf{r}) = \rho_1(\mathbf{r},t) + \rho_2(\mathbf{r},t) + \rho_3(\mathbf{r},t) + \dots \ . \tag{2.38}$$

Here, $\rho_1(\mathbf{r},t)$ is the linear response, $\rho_2(\mathbf{r},t)$ is the second-order response, etc. For weak perturbation, only the linear term can be considered, while ignoring higher order terms. The first order term is given by

$$\rho_1(\mathbf{r},t) = \int dt' \int d^3r' \ \chi(\mathbf{r},t,\mathbf{r}',t')v_1(\mathbf{r}',t'), \tag{2.39}$$

where χ is the linear density-density response function of the system. According the TDKS framework, we can calculate the linear change in density using the fictitious noninteracting system by the following equation,

$$\rho_1(\mathbf{r},t) = \int dt' \int d^3r' \; \chi_s(\mathbf{r},t,\mathbf{r}',t')v_{s1}(\mathbf{r}',t'), \tag{2.40}$$

where χ_s is the density-density response function for the noninteracting KS electrons. The term $v_{s1}(\mathbf{r},t)$ is the linear change of the effective potential, $v_s(\mathbf{r},t)$, of the time-dependent KS system, and it can be explicitly written as,

$$v_{s1}[\rho](\mathbf{r},t) = v_1(\mathbf{r},t) + \int d^3r' \frac{\rho_1(\mathbf{r}',t)}{|\mathbf{r}-\mathbf{r}'|} + v_{XC1}(\mathbf{r},t), \tag{2.41}$$

where $v_1(\mathbf{r},t)$ is the external perturbation, the next term is the linearized time-dependent Hartree potential. The last term is the linearized XC potential and it can be expressed as,

$$v_{XC1}(\mathbf{r},t) = \int dt' \int d^3r' \; \frac{\delta v_{XC}[\rho](\mathbf{r},t)}{\delta\rho(\mathbf{r}',t')} \; \rho_1(\mathbf{r}',t'). \tag{2.42}$$

The XC kernel is defined by,

$$f_{XC}(\mathbf{r},t,\mathbf{r}',t') = \frac{\delta v_{XC}[\rho](\mathbf{r},t)}{\delta\rho(\mathbf{r}',t')}. \tag{2.43}$$

Finally, by comparing the response equations of the KS and real systems, and combing equations 2.41, 2.42 and 2.43, it yields the Dyson equation,

$$\begin{aligned}\chi(\mathbf{r},t,\mathbf{r}',t') =& \chi_s(\mathbf{r},t,\mathbf{r}',t') + \int d\tau \int d^3x \int d\tau' \int d^3x' \chi_s(\mathbf{r},t,\mathbf{x},\tau) \\ & \left\{ \frac{\delta(\tau-\tau')}{|\mathbf{x}-\mathbf{x}'|} + f_{XC}(\mathbf{x},\tau,\mathbf{x}',\tau') \right\} \chi(\mathbf{x}',\tau',\mathbf{r}',t').\end{aligned} \tag{2.44}$$

The above equation is useful to calculate the properties of many body systems under small perturbation. Other variants of TDDFT are also available, such as the Casida formalism, which can be found in the book.[137]

2.4 Methods used in the thesis

Nowadays, DFT and TDDFT methods are widely used to obtain geometries and properties of conjugated polymers, as these theories provide better results than the HF theory and the calculations are computationally feasible for a system of 200-500 atoms, which is an impossible task for the high level post-HF methods.[30,119,138] The DFT method has been very popular for the optimization of the ground-state geometry, and calculations of properties, such as, E_{H}, E_{L}, IP, EA, transport rates and mobilities of charge carriers, etc.[54,139–142] For conjugated systems, excited-state geometry, transition energies, and their corresponding oscillator strengths are well predicted by the TDDFT method with reasonable accuracy at affordable computational costs.[30] Accuracy of these two methods primarily depends upon the quality of the *XC*-functional used for the calculation,[137,143] and hybrid functionals are often preferred for this purpose. For these functionals, although the calculated results are not exactly equal to the experimental results, the trend has been found to be the same. A large number of hybrid functionals are developed, out of them, the B3LYP functional in combination with a split valence double or triple zeta basis sets with the polarization and/or diffuse functions is the most widely used level of theory for these type of calculations.[54,139,144–146] However, DFT and TDDFT methods have been less successful in cases like charge transfer excitations, excited states with a multiple-excitation character, and geometries and excitation energies of long conjugated polymer.[143] As mention in the subsection 2.2.3, the problem for the charge transfer excitation is considerably resolved by the long-range corrected hybrid functionals. The reason for failure in the case of multiple excitations is the adiabatic approximation used in the linear-response TDDFT, and many attempts has been made to circumvent the issue and few of them succeed to some extent.[147,148] With the increase in chain length of a conjugated oligomer, B3LYP and other standard functionals strongly underestimate the optical gap because of the overestimation of the extent of conjugation.[143] The amount delocalization error is directly related to the proportion of HF-exchange used in the *XC*-functional. At present, no clear solution exists for this problem. However,

in conjugated polymers, breaks in conjugation caused by conformational and chemical defects often lead to spectroscopic segments in the main chain. Thus, computational calculations mostly deal with oligomers up to a finite chain length, and for a small oligomer, the error associated with the result will be small. Further, as the differences in errors for similar systems are small, these errors will not hamper in the qualitative analysis of a particular system and their derivatives.

Thiophene–azomethine–pyrrole based conjugated polymers

In this chapter, structural, optoelectronic and charge transfer properties of azomethine-based heterocyclic oligomers are investigated. Alternation in these properties due to the presence of various electron donating and withdrawing groups in the main chain are explored. The contents of this chapter are published in the following two papers:

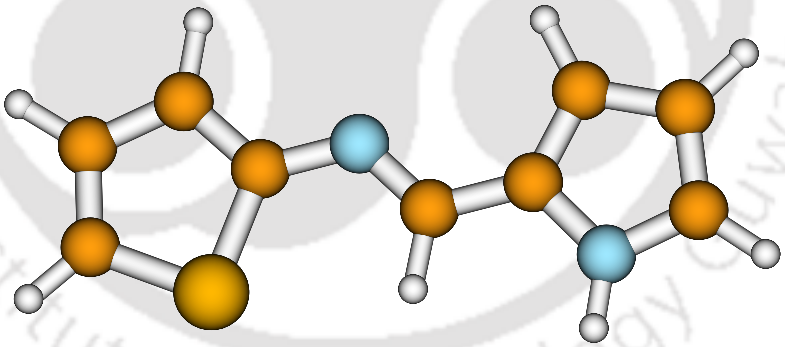

Figure: Thiophene–azomethine–pyrrole system

- H. Sahu and A. N. Panda, *Macromolecules*, **2013**, 46, 844.
- H. Sahu and A. N. Panda, *Phys. Chem. Chem. Phys.*, **2014**, 16, 8563.

The presence of bulky groups in conjugated polymers often results in a nonplanar structure due to the steric effects. This hampers the electron delocalization across the chain, which affects the electronic and optical properties of the polymer. Insertion of π spacers, such as vinylene, in the main chain of π-conjugated systems is an effective strategy to enhance the conjugation length by eliminating torsional strains.[64–66] This helps in reducing the band gap and broadening the absorption spectrum, in comparison to the polymers made up of monomers connected *via* single bonds. However, unfavorable synthesis technique and processability limit their practical use.[67,68]

Azomethine-linked polymers are isoelectronic to their vinylene counterparts. In contrast to vinylene-linked polymers, polyazomethines are easy to synthesize with high purity and yield,[70,149–151] liberating exclusively water as byproduct.[70] Easy modification of their structures by hydrogen bonding, complex formation with lewis acid[152] and conventional substitution makes them further attractive and proficient materials for the recent research. But the associated problems of being nonfluorescent and insoluble in organic solvents have been a hindrance to their applications. The problem with solubility has recently been overcome[153,154] and fluorescent polymers are prepared.[155,156] Many of the recent experimental studies[17] have focused on heterocyclic-based azomethines as the heterocyclics help in planarizing the system leading to greater conjugation. Further, few azomethines are also known for the mutual hole and electron transport properties.[157,158] Charge transport properties of thiopheno–azomethines have been investigated by Işik et al.[70] and a hole mobility of $\sim 3 \times 10^{-5}$ cm^2/Vs was found for an azomethine triad. Furthermore, the presence of pyrrole ring in a polymer uplifts frontier molecular orbitals, and improves redox properties of the polymers.[159–161] However, there are only few studies reported on thiophene-pyrrole based azomethines[152,154,162–165] and most of them are experimental works.

Keeping in mind the recent progress in the experimental side, the optoelectronic, charge injection and transport properties of thiophene-pyrrole based azomethines are studied using DFT and TDDFT methods. Theoretical methodology and computational

details are discussed in sections 3.1 and 3.2, respectively. This is followed by the result and discussion in section 3.3 and finally, conclusions are in 3.4.

3.1 Theoretical methodology for charge transport properties

The stability of holes and electrons, and the energy barriers for the injection processes, affect the device performance. Recently, extensive studies have been carried out to estimate the E_{H}, E_{L}, IP and EA of molecules, and to study their effect on the injection ability.[45,141,166–172] Suitable HOMO level (or IP) of a hole transport layer, and a suitable LUMO level (or EA) of the electron transport layer, are required for the efficient hole and electron injection from an anode and a cathode, respectively.[45]

Charge transfer processes are usually explained either by the coherent band theory or the incoherent hopping model.[173–177] Band theory is used for highly ordered systems where the charge carrier is delocalized over the entire system. However, at room temperature or in less ordered systems, charge transport is described predominately by the hopping model.[173,174] In the hopping model, charge carrier is considered as localized and hops between adjacent molecules. Here, from a practical point of view, the hopping mechanism is considered. At high temperatures, the charge hopping rate (k_{ct}) between two adjacent molecules **a** and **b** can be expressed by the Marcus theory[178,179] as

$$k_{\mathrm{ct}} = \left(\frac{\pi}{\lambda k_{\mathrm{B}} T}\right)^{\frac{1}{2}} \frac{V_{\mathrm{ab}}^2}{\hbar} exp\left(-\frac{\lambda}{4k_{\mathrm{B}}T}\right). \tag{3.1}$$

Here, λ is the reorganization energy accompanying geometric relaxation associated with the charge transfer, V_{ab} is the electronic coupling between neighboring molecules **a** and **b**, T is the absolute temperature, and k_B and $\hbar$ are the Boltzmann and Planck constants, respectively. It is clear that the charge transfer rate depends upon two factors, the charge transfer integral and the reorganization energy. Hence, these two need to be properly tuned based on the requirement.

Total reorganization energy is the sum of the internal and external reorganization energies. Intramolecular vibrations and polarization of surrounding medium are responsible for the internal and external components of the reorganization energy, respectively. In the present study, only internal reorganization energies induced either by a hole or an electron are considered. The hole (or electron) reorganization energies, λ_h (or λ_e), can be expressed as follows:

$$\begin{aligned}\lambda_h &= \lambda_1 + \lambda_2 \\ &= [E^+(M^0) - E^+(M^+)] + [E^0(M^+) - E^0(M^0)] \\ &= [E^+(M^0) - E^0(M^0)] - [E^+(M^+) - E^0(M^+)] \\ &= IP(v) - HEP \end{aligned} \tag{3.2}$$

and

$$\begin{aligned}\lambda_e &= \lambda_3 + \lambda_4 \\ &= [E^0(M^-) - E^0(M^0)] + [E^-(M^0) - E^-(M^-)] \\ &= [E^0(M^-) - E^-(M^-)] - [E^0(M^0) - E^-(M^0)] \\ &= EEP - EA(v). \end{aligned} \tag{3.3}$$

HEP and EEP are the hole and electron extraction potentials, calculated as the energy differences between charged and neutral states of molecules at the optimized geometries of the charged species.

Charge transfer integral (V_{ab}) describes the strength of electronic coupling between two neighboring molecules **a** and **b**. Koopmann's theorem[180] can be used to calculate V_{ab} values by considering the interacting molecules as identical and symmetrically equivalent and having the same site energies by the following equation

$$V_{ab} = \frac{E_{H/L+1} - E_{H-1/L}}{2}, \tag{3.4}$$

where $E_{\mathrm{H/L+1}}$ and $E_{\mathrm{H-1/L}}$ are the energies of the HOMO/LUMO+1 and HOMO-1/LUMO, respectively, obtained from the close–shell configuration of the neutral state of two stacked molecules. Once charge transfer rate is obtained by equation 3.1, the hopping mobility can be estimated by the relation

$$\mu_{\mathrm{hop}} = \frac{eD}{k_{\mathrm{B}}T}. \tag{3.5}$$

Here, T is the temperature, k_{B} is the Boltzmann constant and D is the diffusion coefficient. The relation between D and k_{ct} for a one dimensional system is given by $D = l^2 k_{\mathrm{ct}}$, where l is the spatial distance between two interacting molecules.

3.2 Computational details

3.2.1 Optimizations of ground state geometries and optoelectronic properties

All the calculations were performed with ORCA 2.9 package.[181] The ground state geometries of the monomers were fully optimized using different functionals such as B3LYP, PBE0, PW6B95 and B2PLYP in combination with the 6-31G(d) basis set. Single point calculations using PWPB95 functional were performed for the optimized geometries obtained at the PW6B95/6-31G(d) level. To check the effect of basis sets, the monomers were also optimized using the 6-311++G(d,p) basis set. Optimizations of all the oligomers were carried out at the B3LYP/6-31G(d) level. No symmetry constraints were enforced in the calculations. HOMO and LUMO levels were examined and $E_{\mathrm{g}}^{\mathrm{hl}}$ values were evaluated.

Excited state calculations were carried out using the TDDFT method at the ground state optimized geometries, and the transition energies and oscillator strengths (f_{osc}) were computed. The $E_{\mathrm{g}}^{\mathrm{hl}}$ and $E_{\mathrm{g}}^{\mathrm{opt}}$ are linearly extrapolated to infinite chain length in order to get polymer value. As it is well known[28,182,183] that the linear extrapolation

is not best suited for computing the excitation energy of conjugated polymers, extrapolations of the E_g^{hl} and E_g^{opt} are also carried out using the Kuhn's formula[25] based on coupled oscillators,

$$E_N = E_0\sqrt{1 - 2\alpha\ \cos\frac{\pi}{N+1}}, \tag{3.6}$$

where N is the number of linearly conjugated double bonds. E_N, E_0, and α refer to the energy at infinite chain length, energy of an isolated oscillator and the coupling strength between neighboring oscillators, respectively.

3.2.2 Optimizations of neutral and charged states geometries, and charge transport properties

The optimization of molecular geometries of the neutral and charged states for all the azomethines was performed with the B3LYP functional and a split valence 6-31G(d,p) basis set as implemented in the Orca 2.9 package.[184] Unrestricted DFT (UDFT) method is applied for all the open shell calculations. All the optimizations were performed without any symmetry constraints. On the basis of the above calculations, various properties such as IP(a,v), EA(a,v), and reorganization energies for holes (λ_h) and electrons (λ_e) of all the studied compounds were calculated. Reorganization energies are extrapolated to the polymer limit using the Kuhn's formula (see equation 3.6). A basis set with diffuse functions is a better option for the above calculations than the 6-31G(d,p) basis set. However, to keep the computational cost under control, basis sets with diffuse functions were not used.

V_{ab} of all the dimers and pentamers were calculated using the equation 3.4. In the absence of any experimental results, two different methodologies have been used to compute the V_{ab} values. In the first case, two dimers of each compound are cofacially placed at a distance of $\sim$ 3.5 Å as the starting geometry. These structures are then optimized and energies of orbitals required for the charge transfer integral calculation are obtained from the optimized geometries. In the second case, pentamers are considered. Single point calculations are carried out for two cofacially placed pentamers at 3.5 Å π-stacking

distance to evaluate the strength of the electronic coupling. As conventional functionals of DFT do not contain the physics of the dispersion interaction, B3LYP–D3 was applied for the electronic coupling calculations.[95,135] Charge transfer rates and hopping mobilities were estimated by using the equations 3.1 and 3.5, respectively.

3.3 Results and discussion

In this chapter, the steric and electronic effects of various groups on the geometries and properties of the thiophene-pyrrole based azomethines are taken into consideration. While geometries and optoelectronic properties are presented in subsection 3.3.1, charge injection and transport properties are explored in subsection 3.3.2.

3.3.1 Effects of substituents on the optoelectronic properties

The sketch maps of the fifteen thiophene and pyrrole based copolymers considered in this work are shown in Figure 3.1. Compound **1** is the basic unit, where thiophene and pyrrole rings are connected through a –CH=N linkage. Carbon–carbon bond numbering scheme of the basic monomer unit is shown in Figure 3.2. Various groups like $-CH_3$, $-CF_3$, $-OCH_3$, *tert*-butyl (*t*-Bu), $-NH_2$, $-NO_2$, and $-OC_2H_4O-$ are attached in different positions of the basic unit, in order to understand their effect on the geometry and optoelectronic properties of the compounds. For compounds **2**–**5**, substituents are attached only at the pyrrole nitrogen positions. In compounds **6** and **7**, in addition to the substitution at the pyrrole nitrogen position, 3 and/or 4 positions of the pyrrole and thiophene rings are also substituted. For compounds **8**–**14**, substituents are attached only at the 3 positions of the pyrrole rings and in the compound **15**, both 3 and 4 positions of the pyrrole and thiophene rings are substituted. To keep computational cost under control, oligomers up to trimers are considered for all the studied molecules.

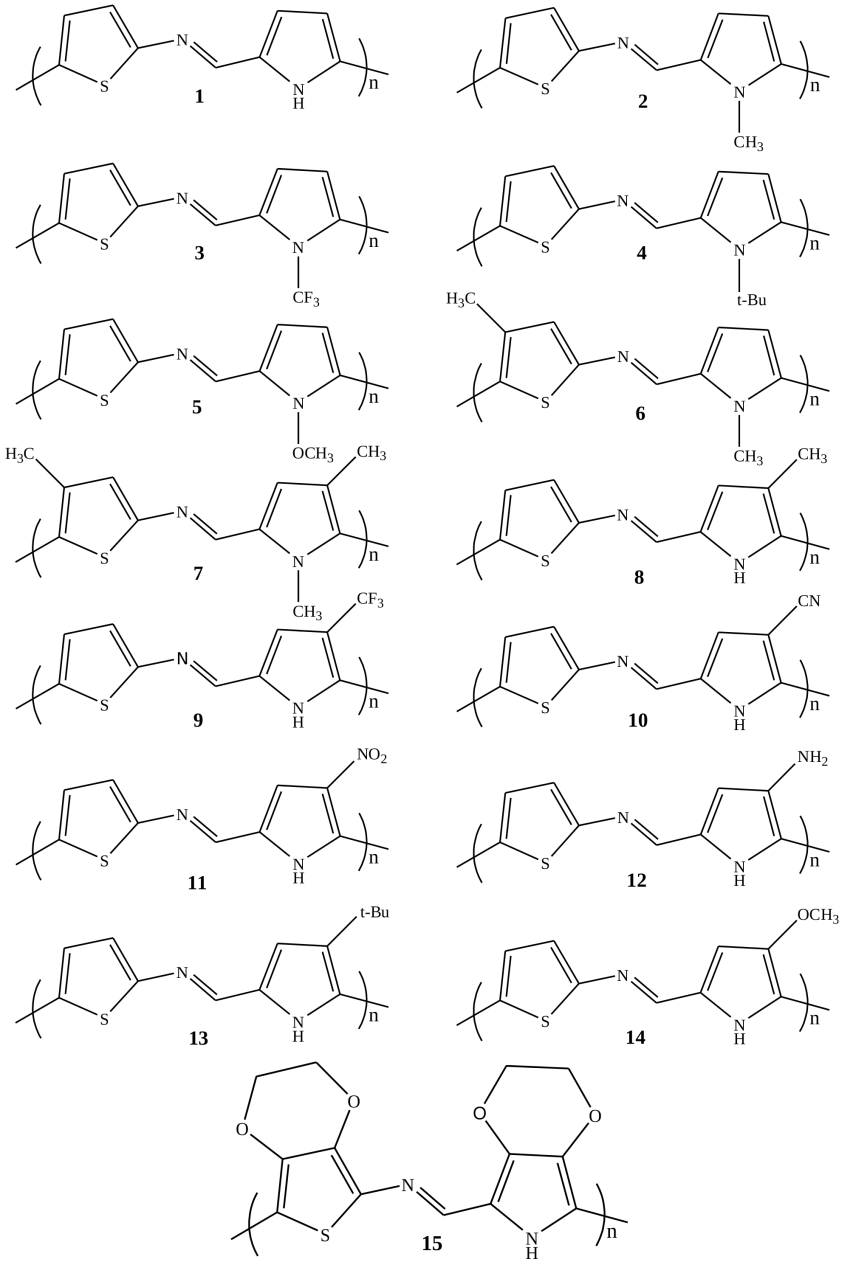

FIGURE 3.1: Sketch maps of the structures of thiophene- and pyrrole-based oligomers.

3.3.1.1 Ground state electronic structure and effect of functionals and basis sets

The optimized geometries of all the monomers are perfectly planar. All the carbon–carbon bond lengths calculated at the B3LYP/6-31G(d) level are listed in Table 3.1. It is observed that all the carbon–carbon single bonds are shorter than those in ethane (1.54

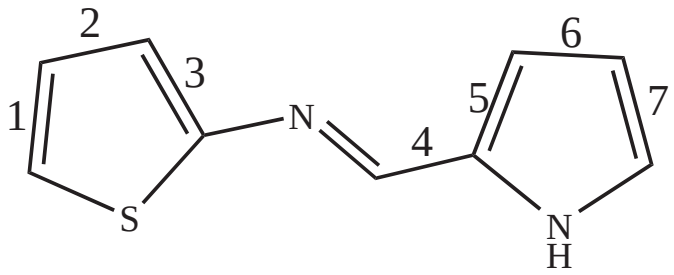

FIGURE 3.2: Numbering scheme of carbon–carbon bonds in the monomer **1**.

TABLE 3.1: Calculated bond lengths for the B3LYP/6-31G(d) optimized geometries of monomers. All bond lengths are in Å.

monomers	carbon-carbon bonds						
	1	2	3	4	5	6	7
1	1.37	1.42	1.38	1.44	1.39	1.41	1.39
2	1.37	1.42	1.38	1.44	1.40	1.41	1.39
3	1.37	1.42	1.38	1.44	1.39	1.42	1.38
4	1.37	1.42	1.38	1.44	1.40	1.40	1.38
5	1.37	1.42	1.38	1.44	1.40	1.41	1.39
6	1.37	1.43	1.38	1.44	1.40	1.41	1.39
7	1.37	1.43	1.38	1.44	1.40	1.41	1.39
8	1.37	1.42	1.38	1.44	1.39	1.42	1.39
9	1.37	1.42	1.38	1.44	1.39	1.42	1.39
10	1.37	1.42	1.38	1.44	1.39	1.42	1.39
11	1.37	1.42	1.38	1.44	1.39	1.41	1.39
12	1.37	1.42	1.38	1.43	1.40	1.41	1.39
13	1.37	1.42	1.38	1.44	1.39	1.42	1.39
14	1.37	1.42	1.38	1.44	1.39	1.41	1.39
15	1.36	1.43	1.38	1.43	1.40	1.41	1.38

Å) at the same level of theory. On the contrary, all the double bond (C=C) lengths are longer than that of the C=C double bond in ethylene (1.33 Å). This shows that the bond distances are between C=C and C–C bond lengths, indicating electron delocalization across the molecule.

The arrangement of monomer units in oligomers can modify their conformational features. A representative structure for the dimers is presented in Figure 3.3 showing the interunit dihedral angle D_{NCCC}. Table 3.2 shows the calculated dihedral angles of all the oligomers, and it is observed that dimer **4** has the largest dihedral angle of

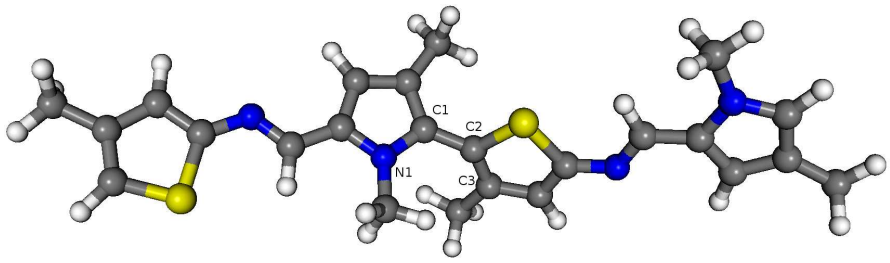

FIGURE 3.3: Representative structure showing dihedral angle between monomers where D_{NCCC} = N1–C2–C3–C4.

127.9° among the studied compounds. The presence of the bulky *t*-Bu group distorts the geometry and increases the torsional angle. The $-CH_3$ and $-CF_3$ groups are smaller than the *t*-Bu group. This results in smaller dihedral angles for the dimers **2** and **3** than that in the dimer **4**. The $-CF_3$ group is bigger than the $-CH_3$ group, but the D_{NCCC} of dimer **3** is 2.1° less than in the dimer **2** as shown in Table 3.2. This anomalous behavior

TABLE 3.2: Calculated dihedral angles (in degree) for all the studied oligomers at the B3LYP/6-31G(d) level of theory. "D" and "T" denote dimers and trimers, respectively.

compounds		D^1_{NCCC}	D^2_{NCCC}	compounds		D^1_{NCCC}	D^2_{NCCC}
1	D	13.5		**9**	D	26.6	
	T	11.5	−11.2		T	25.3	−25.2
2	D	35.6		**10**	D	10.4	
	T	35.0	−35.3		T	9.4	−8.7
3	D	33.5		**11**	D	17.3	
	T	33.2	−33.6		T	16.8	−17.0
4	D	127.9		**12**	D	22.2	
	T	53.8	−54.6		T	17.2	−21.4
5	D	17.6		**13**	D	42.8	
	T	17.4	16.8		T	41.6	−43.2
6	D	55.4		**14**	D	0.5	
	T	55.3	−55.7		T	0.2	−0.2
7	D	62.6		**15**	D	−0.2	
	T	62.8	−62.8		T	0.5	0.3
8	D	15.6					
	T	15.0	−14.9				

can be explained in terms of the C–F and C–H bond distances. The C–F bond distance in the $-CF_3$ group is 1.34 Å which is much larger than the C–H bond distance (1.09 Å) of the $-CH_3$ group, and this results in less repulsion between the $-CF_3$ group and the thiophene ring of the adjacent monomer unit. In the dimers **6** and **7**, the presence of

large number of $-CH_3$ groups results in more electronic repulsion between the monomer units and hence, large dihedral angles are found.

The dihedral angle of dimer **9** is larger than in dimer **8**. This is due to the presence of the $-CF_3$ group in dimer **9**, which is bulkier than the $-CH_3$ group in dimer **8**. These results are found to be different in comparison to the geometries of dimers **2** and **3**. In the present case, the C–F bond distance does not affect the dihedral angle as the substitution occurs at different position of the monomer unit. Even though the dimers of compounds **2** and **8** bear the same $-CH_3$ group, the dihedral angle of dimer **8** is 17.9° smaller than in the dimer **2**. Furthermore, dimer **13** shows a dihedral angle of 42.8°, but this is much smaller (by 85.1°) than the angle in dimer **4**. The above results show that the presence of substituent in the pyrrole nitrogen position causes more repulsion between the monomer units than at the 3 position of the pyrrole ring.

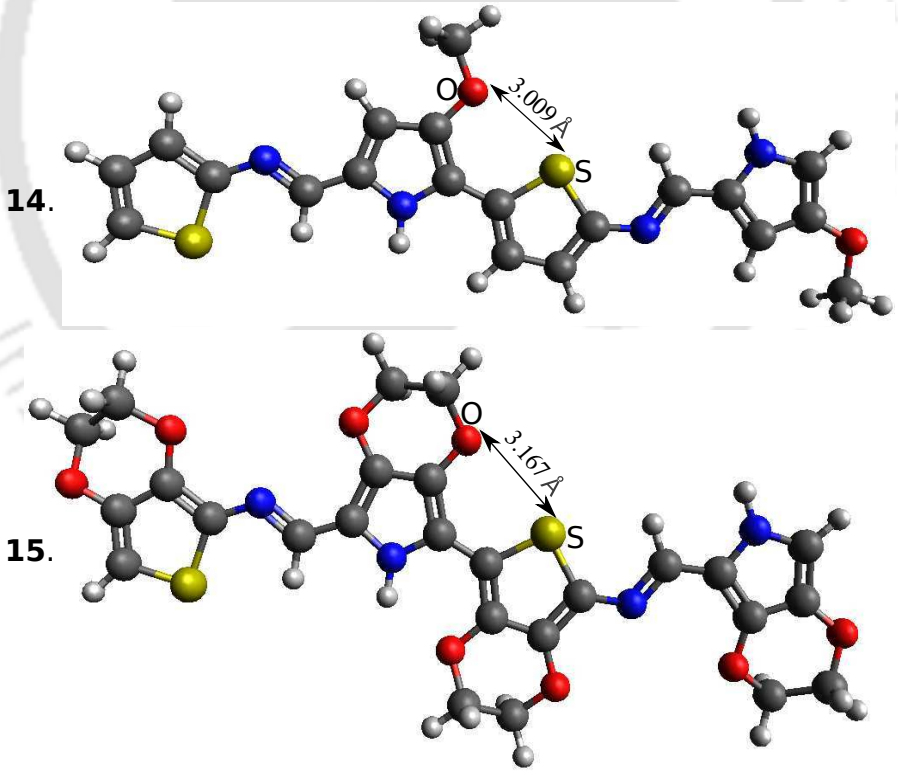

FIGURE 3.4: Structures of the dimers **14** and **15**. These two structures are planar owing to the noncovalent O···S interactions.

Dimers **14** and **15** are shown in Figure 3.4. Both the oligomers are planar due to the presence of intramolecular O···S interaction. The intramolecular O···S distances are 3.01 and 3.17 Å in dimers **14** and **15**, respectively. These distances are shorter than the sum of van der Waals radii of sulfur and oxygen.[185] This indicates a noncovalent interaction between the sulfur and oxygen atoms.[60,186–191]

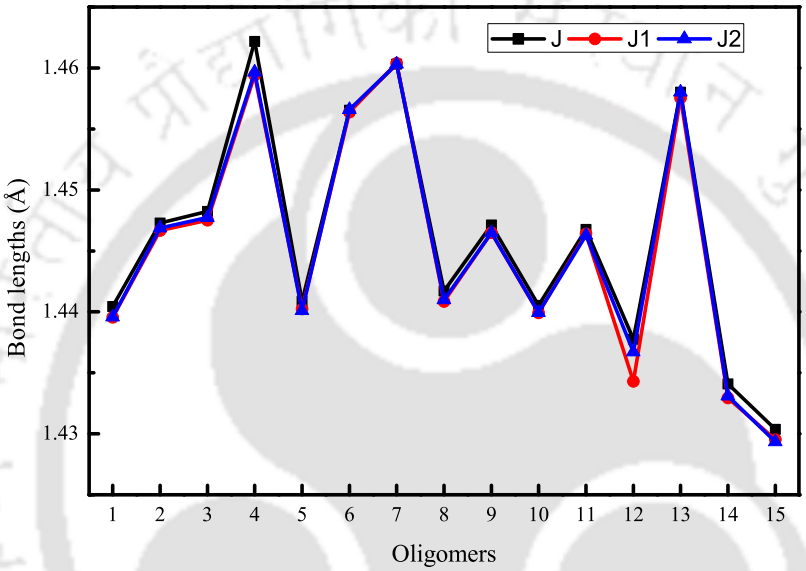

FIGURE 3.5: Comparison of calculated junction bond distances of all the studied oligomers. J stands for the junction bond distances of the dimers, and J_1 and J_2 are two junction bond distances of the trimers.

A comparison of various bond lengths between adjacent monomer units shows very small differences. The main structural changes happen at the junctions of adjacent monomer units. For all the studied oligomers, bond lengths between two adjacent monomer units are calculated and plotted in Figure 3.5. Bonds are denoted as J for dimers, and J_1 and J_2 for trimers. The variation in these junction bond lengths are related to the dihedral angles between the monomer units. Dimer **4** shows the largest J value because of its largest dihedral angle. A comparison of dimers **2** and **8** shows that dimer **8** has a smaller J value than dimer **2**, owing to the larger junction dihedral angle in dimer **2** than in dimer **8**. As discussed earlier, dimer **2** has a larger dihedral

angle than in the dimer **3** whereas the J values of these dimers are in the opposite order. This is because of electron withdrawing nature of the $-CF_3$ group in dimer **3**. Although dimer **10** contains electron withdrawing –CN groups, the J value is small due to a small junction dihedral angle. The presence of strong electron donating $-NH_2$ group in dimer **12** results small junction bond distance. The interring torsion angles of the dimers **14** and **15** are found to be 0°, which makes these dimers to exhibit shorter junction distances than in other dimers. Overall, the dimers having large dihedral angle or bearing electronic withdrawing groups have large junction bond distances whereas comparatively smaller J values are found for those dimers which are planar or have electron donating groups.

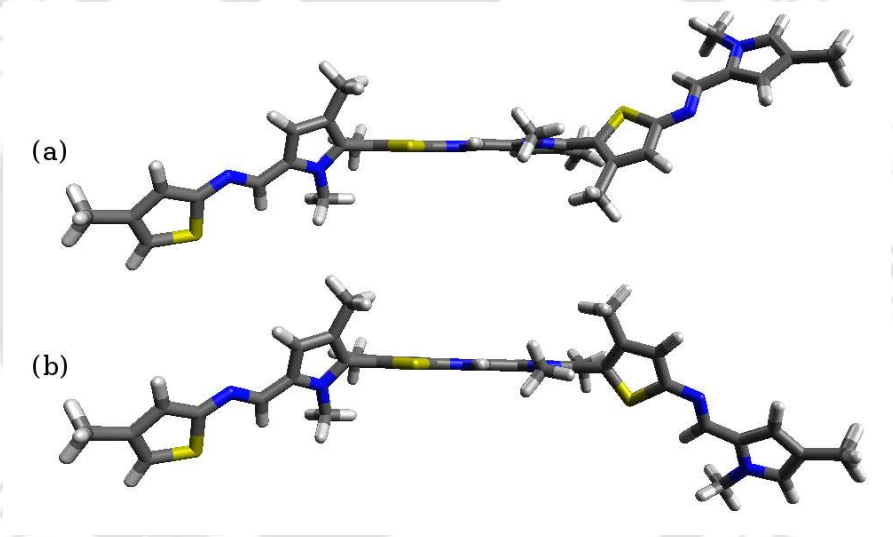

FIGURE 3.6: Optimized geometries of trimer 7: (a) d+d+ configuration and (b) d+d– configuration.

In trimers, there are two junction dihedral angles, D^1_{NCCC} and $\mathrm{D}^2_{\mathrm{NCCC}}$. So, two types of conformations are possible for each trimer: (1) both dihedral angles are positive (denoted as d+d+) and (2) one angle is positive and the other is negative (denoted as d+d–). From the optimized structures, it is found that these two types of conformations for all the trimers have similar energies. Figure 3.6 shows both these conformations for trimer **7**, and the energy difference between these two is 0.003 kcal/mol. In trimers, the trends of dihedral angle are found to be similar to those in the dimers except that in

trimer **4**. The dihedral angles of the trimer **4** are found to be smaller than in the trimers **6** and **7**. With increase in repeating units, small changes take place in the bond lengths of the trimers. As shown in Figure 3.5, the trimer **7** has the highest J_1 and J_2 values unlike the case of dimers where compound **4** has the highest interunit bond length.

Two different types of BLA values are calculated for all the compounds. First one is the difference between the average carbon–carbon single and double bond lengths along the π conjugated path[192,193] and it is denoted as Δr. Other one is the junction BLA (δr) of the repeating unit, i.e., the average difference between the C–C bond lengths, located between the –C=N–linkage and pyrrole ring, and the C=N bond length. Both the Δr and δr are plotted in Figure 3.7. For all the compounds except monomers **3** and

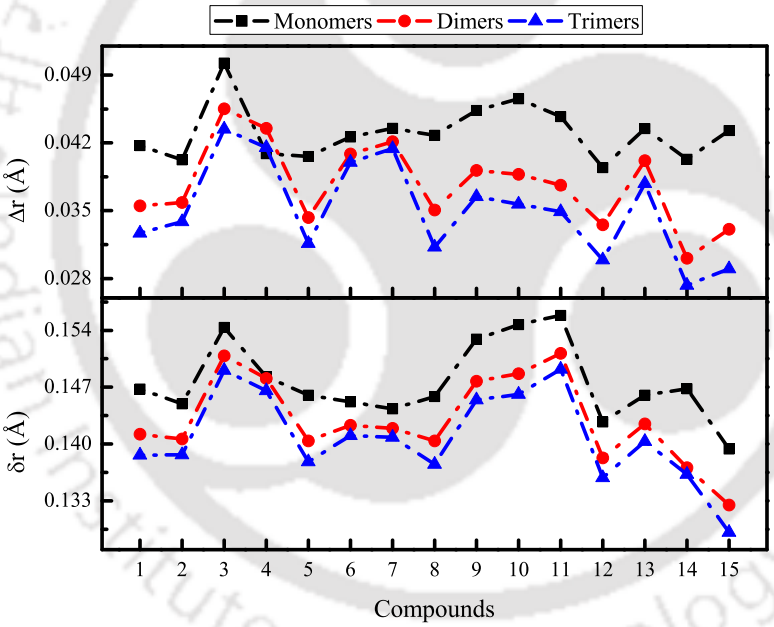

FIGURE 3.7: BLA values, Δr and δr, of the studied compounds. See text for the definitions of Δr and δr.

10, Δr values are smaller than the Δr values of the thiophene and pyrrole rings (For thiophene and pyrrole, Δr values are 0.062 and 0.047 Å, respectively at the B3LYP/6-31G(d) level of theory). It indicates that the monomers **3** and **10** are less conjugated than the individual thiophene and pyrrole rings. As shown in Figure 3.7, compound **3**

has the highest Δr value. For all the compounds, Δr decreases from the monomer to the corresponding trimer except in the compound **4**. Δr value of the dimer **4** is larger than in monomer **4**, and this result shows that the presence of *t*-Bu groups in the pyrrole nitrogen positions decrease the conjugation length upon dimerization of the compound **4**. It is also observed that the magnitude of Δr for the trimers **14** and **15** are smaller than for other trimers indicating more delocalization over the oligomer chains. Overall, small dihedral angles or the presence of electron donating groups in a compound results a small Δr value whereas the opposite happens for the compounds having large dihedral angles or electron withdrawing groups. The δr is less affected by the dihedral angle as compared to the Δr, and in most of the cases, electronic effects of the substituents are predominant over the steric effect. Among all the monomers and oligomers, compound **11** has the largest δr value because of the presence of a strong electron withdrawing $-NO_2$ group. The δr value of the compounds **3**, **9**, **10** are also large because of the electron-withdrawing effect of the substituents. The presence of two electron-donating $-OC_2H_4O-$ groups in the repeating unit of compound **15** causes the smallest δr values. All the compounds (i.e., compounds **2**, **5**, **6**, **7**, **8**, **12**, **14**) containing electron-donating groups have small δr values except in compounds **4** and **13**. This is due to the presence of bulky *t*-Bu group. For all compounds, the δr value decreases from the monomer to the corresponding trimer.

To check the effect of different DFT functionals on the electronic structures, extra calculations were performed using B2PLYP, PBE0, PW6B95 and PWPB95 functionals, for all the monomers. The energies of the monomers calculated by different functionals are plotted in Figure 3.8, with respect to the energies obtained by the B3LYP functional. The energies obtained follow the order, PBE0 > B2PLYP > PWPB95 > B3LYP > PW6B95. It is also observed that the energies of the monomers follow the same order, for all the functionals.

The C–C bond lengths and Δr values obtained by different functionals and basis sets are listed in Table 3.3, and the bond lengths are plotted in Figure 3.9. The C–C single and double bond lengths derived using PBE0 and PW6B95 functionals are slightly

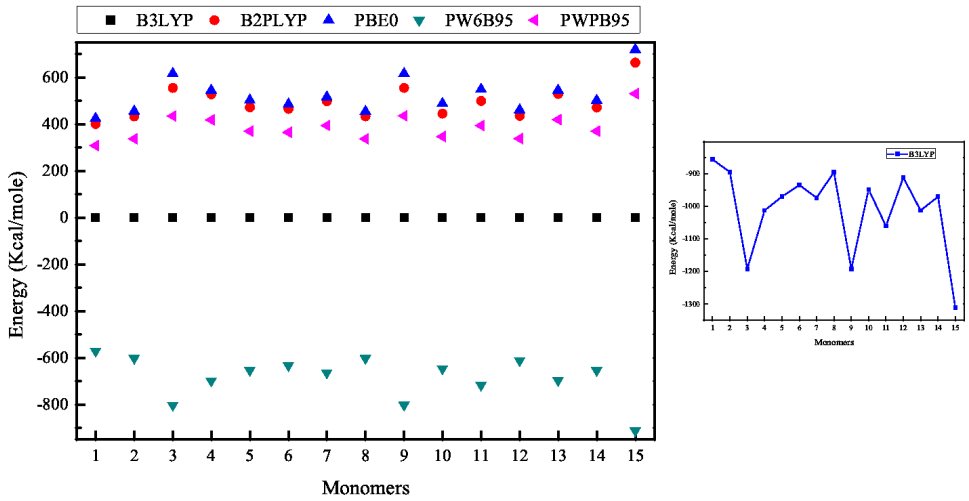

FIGURE 3.8: Comparisons of energies of monomers calculated by different functionals with respect to the B3LYP functional.

TABLE 3.3: Bond lengths and Δr values of the basic monomer unit obtained using different functionals and basis sets.

	bond lengths (Å)				
bonds	B3LYP		B2PLYP	PBE0	PW6B95
	6-31G(d)	6-311G++(d,p)		6-31G(d)	
1	1.37	1.37	1.37	1.37	1.36
2	1.42	1.42	1.42	1.42	1.42
3	1.38	1.38	1.38	1.38	1.37
4	1.44	1.44	1.44	1.43	1.43
5	1.40	1.39	1.39	1.39	1.39
6	1.41	1.41	1.41	1.41	1.41
7	1.39	1.39	1.39	1.38	1.38
Δr (Å)	0.04	0.04	0.04	0.04	0.04

smaller than those obtained using the B3LYP functional. While the calculated Δr values using B2PLYP and PBE0 functionals are smaller than the one obtained using the B3LYP functional, the value obtained using the PW6B95 functional is larger. Extra calculations were also carried out to see the effect of basis sets, and the results are shown in Figure 3.9. Bond lengths obtained at the B3LYP/6-311++G(d,p) level are slightly smaller than those at the B3LYP/6-31G(d) level. Also the Δr obtained at the B3LYP/6-311++G(d,p) level is larger than the result at the B3LYP/6-31G(d) level.

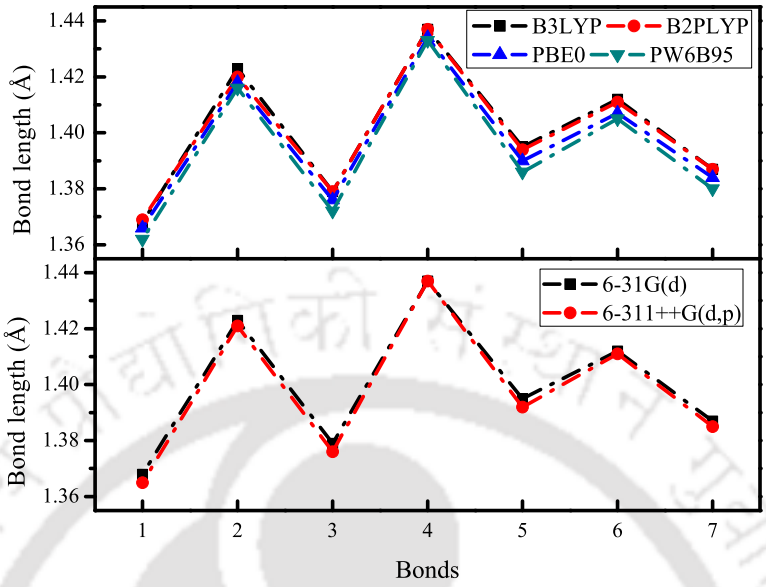

FIGURE 3.9: Bond lengths of basic monomer unit calculated by different functionals and basis sets.

3.3.1.2 HOMO–LUMO gaps, excitation energies, and oscillator strengths

E_H, E_L and the corresponding E_g^{hl} values of all the compounds are listed in Table 3.4. From the table, it can be observed that the E_H and E_L of the monomers **2** and **4** are larger than those of the monomer **1**. The observed red shift in the E_g^{hl} for both the monomers compared to that of monomer **1** is due to the electron donating nature of the group attached to the pyrrole ring, i.e., $-CH_3$ in monomer **2** and *t*-Bu in monomer **4**. The change in the position of substitution also affects the E_g^{hl} values as seen in cases of monomers **3** and **9**. Both have the same $-CF_3$ group, but the E_g^{hl} of monomer **3** is smaller than that of monomer **9**. This is because of the presence of $-CF_3$ group in the pyrrole nitrogen position in monomer **3**. In monomers **6** and **7**, the increase in the number of $-CH_3$ substituents and their positions in the pyrrole and thiophene rings decrease the magnitude of the E_g^{hl} values. The HOMOs of the monomers **11** and **15** are the most and the least stable, respectively. The presence of an electron withdrawing nitro group in the monomer **11** and two electron donating $-OC_2H_4O-$ groups in the

TABLE 3.4: Calculated E_H, E_L and E_g^{hl} at the B3LYP/6-31G(d) level for all the studied compounds. For the monomers, the values inside the brackets indicate the E_g^{hl} at the B3LYP/6-311++G(d,p) level. All the energies are in eV and 'M', 'D' and 'T' stand for monomer, dimer and trimer, respectively

compounds		E_H	E_L	E_g^{hl}	compounds		E_H	E_L	E_g^{hl}
1	M	−5.14	−1.52	3.62(3.56)	**9**	M	−5.53	−1.86	3.67(3.62)
	D	−4.71	−2.03	2.68		D	−5.19	−2.35	2.84
	T	−4.56	−2.25	2.32		T	−5.07	−2.55	2.52
2	M	−5.07	−1.51	3.56(3.48)	**10**	M	−5.69	−2.02	3.66(3.61)
	D	−4.70	−1.96	2.74		D	−5.34	−2.60	2.74
	T	−4.58	−2.15	2.42		T	−5.22	−2.81	2.41
3	M	−5.43	−1.84	3.59(3.52)	**11**	M	−5.78	−2.17	3.61(3.49)
	D	−5.06	−2.33	2.72		D	−5.49	−2.72	2.77
	T	−4.93	−2.54	2.39		T	−5.40	−2.89	2.51
4	M	−4.98	−1.45	3.53(3.48)	**12**	M	−4.84	−1.44	3.40(3.34)
	D	−4.82	−1.76	3.07		D	−4.42	−1.93	2.50
	T	−4.64	−1.95	2.70		T	−4.25	−2.12	2.14
5	M	−5.18	−1.56	3.62(3.54)	**13**	M	−5.09	−1.50	3.59
	D	−4.73	−2.05	2.69		D	−4.81	−1.89	2.92
	T	−4.58	−2.25	2.34		T	−4.70	−2.05	2.65
6	M	−5.02	−1.46	3.56(3.47)	**14**	M	−5.06	−1.52	3.54(3.48)
	D	−4.76	−1.81	2.95		D	−4.44	−1.97	2.47
	T	−4.68	−1.96	2.72		T	−4.27	−2.15	2.11
7	M	−4.96	−1.43	3.53	**15**	M	−4.65	−1.22	3.43
	D	−4.76	−1.74	3.02		D	−4.09	−1.65	2.44
	T	−4.69	−1.88	2.82		T	−3.88	−1.82	2.06
8	M	−5.08	−1.49	3.59(3.52)					
	D	−4.63	−1.98	2.65					
	T	−4.47	−2.17	2.30					

monomer **15** is the cause of the above results. Both monomers **12** and **15** have small E_g^{hl} values. While the presence of an amino group in monomer **12** helps in decreasing the E_g^{hl} by 0.22 eV compared to monomer **1**, the presence of two $-OC_2H_4O-$ groups in monomer **15** results in a value smaller by 0.19 eV than in monomer **1**. Monomer **9** shows the maximum E_g^{hl} of 3.67 eV, and monomer **12** exhibits the lowest E_g^{hl} of about 3.40 eV.

The E_g^{hl} values of oligomers are directly proportional to the torsional angles at the junctions.[15,21,71,194–196] A large torsional deviation from the coplanarity leads to a large E_g^{hl} value. Thus, the arrangement of monomers in the backbone of oligomers plays a vital role in determining the optoelectronic properties of oligomers. Analysis of the results obtained for the dimers shows that the compounds **4** and **15** exhibit the highest and the lowest E_g^{hl} values, respectively. As already discussed, the D_{NCCC} is the largest

for dimer **4**. This results in the reduction in conjugation length and makes the dimer **4** to exhibit the highest E_g^{hl} value. For compounds **1**–**7**, the order of E_g^{hl} is consistent with the order of the dihedral angle.

By the dimerization of monomers **2** and **8**, the E_g^{hl} increases and decreases respectively, with respect to dimer **1**. As discussed above, $-CH_3$ groups in dimer **2** produce a larger dihedral angle than that in dimer **8**. In compound **2**, the steric influence of the substituent is more effective than the electronic effect whereas the reverse happens in the dimer **8**. Both the dimers **14** and **15** are planar and have small E_g^{hl} values, i.e., 2.47 eV and 2.44 eV, respectively.

In the case of trimers, the trimer of compound **7** is shown to have the highest E_g^{hl} value of about 2.82 eV unlike the case of dimers where the dimer of compound **4** is found to have the highest E_g^{hl}. As listed in Table 3.2, the dihedral angles in the trimer of compound **4** are 53.8° and -54.6°, smaller than in the dimer. The effect of change in the dihedral angle on the E_g^{hl} value is seen in Table 3.4. The dihedral angles in the trimer **7** are larger than the ones in the trimer of compound **4**. Larger dihedral angles decrease the degree of $\pi - \pi$ conjugation between the adjacent units resulting in a larger E_g^{hl} value in compound **7**.[64,197–200] On the other hand, highly conjugated π-bonding systems have smaller E_g^{hl} values, like in the case of trimers of compounds **14** and **15**. Planar structures of these compounds help in increasing the E_Hs while stabilizing the LUMOs, thus increasing the coupling between the neighboring units. As listed in Table 3.4, the calculated E_g^{hl} values for these trimers are smaller than in the other trimers.

The E_H, E_L and E_g^{hl} values of the basic monomer unit obtained by different functionals are shown in Figure 3.10. Compared to the B3LYP functional, all the functionals produce larger E_g^{hl} values. The E_g^{hl} calculated by B2PLYP and PWPB95 functionals are very large compared to the other functionals. This is due to more stabilization of the HOMO orbitals and destabilization of the LUMO orbitals at B2PLYP/6-31G(d) and PWPB95/6-31G(d) levels. The E_g^{hl} values of all the studied monomers obtained by different functionals are plotted in Figure 3.11. As seen in the figure, for all the

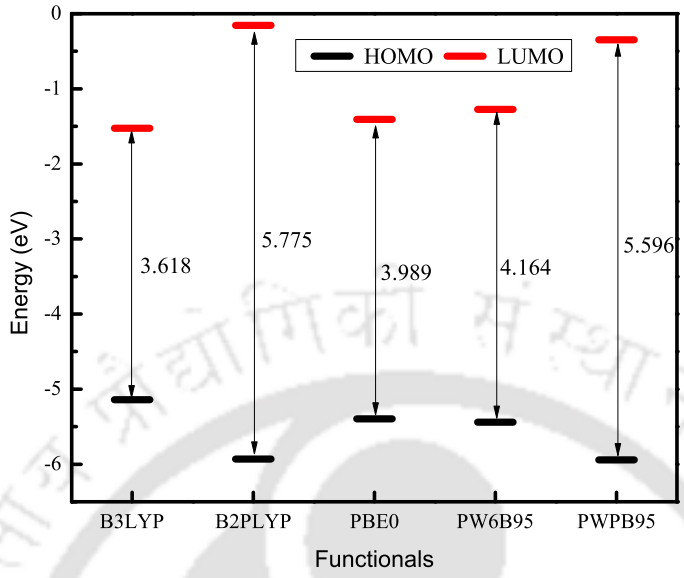

FIGURE 3.10: E_{H}, E_{L}, and $E_{\mathrm{g}}^{\mathrm{hl}}$ values of the basic monomer unit calculated by different functionals.

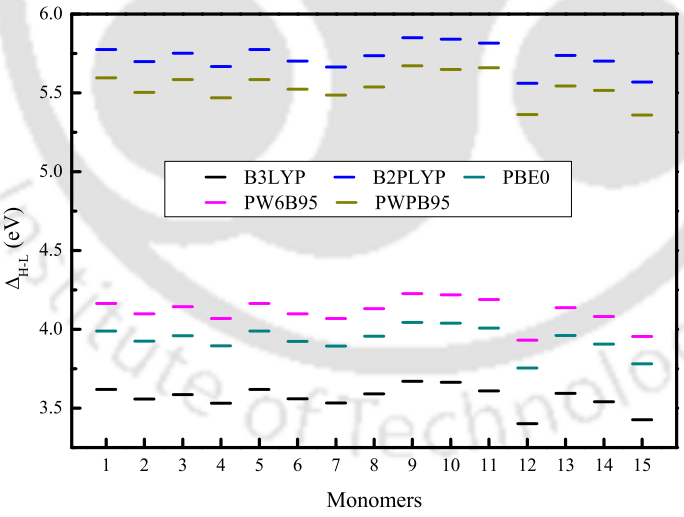

FIGURE 3.11: Comparison of $E_{\mathrm{g}}^{\mathrm{hl}}$ values calculated by using five different functionals as mentioned in the figure.

monomers, the $E_{\mathrm{g}}^{\mathrm{hl}}$ values are overestimated by B2PLYP and PWPB95 functionals. But all the functionals have the same trend in our studied systems. The $E_{\mathrm{g}}^{\mathrm{hl}}$ values of

the monomers by different basis sets are listed in Table 3.4. Compared to the 6-31G(d) basis set, the 6-311++G(d,p) basis set results in slightly smaller E_g^{hl}, but the trend is the same for both the basis sets.

TABLE 3.5: Electronic transition data obtained by TDDFT method for trimers at the B3LYP/6-31G(d) level.

trimers	transitions	E_g(eV)	f_{osc}	configurations	trimers	transitions	E_g(eV)	f_{osc}	configurations
1	$S_0 \rightarrow S_1$	2.24	3.58	H→L(98%)	**2**	$S_0 \rightarrow S_1$	2.29	3.03	H→L(98%)
	$S_0 \rightarrow S_2$	2.55	0.17	H→L+1(53%)		$S_0 \rightarrow S_2$	2.61	0.41	H→L+1(52%)
	$S_0 \rightarrow S_3$	3.00	0.05	H→L+2(62%)		$S_0 \rightarrow S_3$	2.96	0.03	H→L+2(45%)
3	$S_0 \rightarrow S_1$	2.27	3.10	H→L(98%)	**4**	$S_0 \rightarrow S_1$	2.46	2.50	H→L(98%)
	$S_0 \rightarrow S_2$	2.58	0.41	H→L+1(49%)		$S_0 \rightarrow S_2$	2.75	0.24	H→L+1(48%)
	$S_0 \rightarrow S_3$	2.96	0.01	H→L+2(41%)		$S_0 \rightarrow S_3$	2.97	0.01	H→L+2(28%)
5	$S_0 \rightarrow S_1$	2.24	3.45	H→L(98%)	**6**	$S_0 \rightarrow S_1$	2.48	2.01	H→L(98%)
	$S_0 \rightarrow S_2$	2.57	0.29	H→L+1(53%)		$S_0 \rightarrow S_2$	2.80	0.62	H→L+1(52%)
	$S_0 \rightarrow S_3$	2.99	0.03	H→L+2(54%)		$S_0 \rightarrow S_3$	2.95	0.07	H−1→L(30%)
7	$S_0 \rightarrow S_1$	2.54	1.44	H→L(97%)	**8**	$S_0 \rightarrow S_1$	2.22	3.69	H→L(98%)
	$S_0 \rightarrow S_2$	2.85	0.82	H→L+1(63%)		$S_0 \rightarrow S_2$	2.53	0.06	H→L+1(53%)
	$S_0 \rightarrow S_3$	2.89	0.16	H−1→L(49%)		$S_0 \rightarrow S_3$	2.98	0.06	H→L+2(67%)
9	$S_0 \rightarrow S_1$	2.36	2.97	H→L(98%)	**10**	$S_0 \rightarrow S_1$	2.27	3.12	H→L(98%)
	$S_0 \rightarrow S_2$	2.69	0.32	H→L+1(52%)		$S_0 \rightarrow S_2$	2.60	0.30	H→L+1(53%)
	$S_0 \rightarrow S_3$	3.04	0.05	H→L+2(38%)		$S_0 \rightarrow S_3$	2.97	0.07	H→L+2(35%)
11	$S_0 \rightarrow S_1$	2.31	2.41	H→L(98%)	**12**	$S_0 \rightarrow S_1$	2.09	3.64	H→L(98%)
	$S_0 \rightarrow S_2$	2.56	0.32	H→L+1(82%)		$S_0 \rightarrow S_2$	2.36	0.00	H→L+1(53%)
	$S_0 \rightarrow S_3$	2.80	0.21	H−1→L(60%)		$S_0 \rightarrow S_3$	2.83	0.10	H→L+2(66%)
13	$S_0 \rightarrow S_1$	2 429	2 24	H→L(98%)	**14**	$S_0 \rightarrow S_1$	2.10	3.98	H→L(97%)
	$S_0 \rightarrow S_2$	2.76	0.51	H→L+1(54%)		$S_0 \rightarrow S_2$	2.39	0.16	H→L+1(54%)
	$S_0 \rightarrow S_3$	2.96	0.11	H−1→L(30%)		$S_0 \rightarrow S_3$	2.89	0.09	H→L+2(64%)
15	$S_0 \rightarrow S_1$	2.04	3.76	H→L(97%)					
	$S_0 \rightarrow S_2$	2.33	0.42	H→L+1(51%)					
	$S_0 \rightarrow S_3$	2.82	0.03	H→L+2(50%)					

Excitation energies, f_{osc}s, and the important configurations involved for first three singlet-singlet electronic transitions are listed in Table 3.5. For trimers of compounds **14** and **15**, the E_g^{hl} values (see Table 3.4) are close to the E_g^{opt}s. The relationships between the calculated E_g^{hl} values and E_g^{opt} with the inverse number of double bonds are plotted in Figure 3.12, for compounds **7**, **14**, and **15**. The properties of polymers are determined by extrapolation to infinite chain length, and in the present studies, the linear extrapolation technique and the Kuhn's formula (see equation 3.6) are used for computing the energies of a polymer. Figure 3.12 shows that linearly extrapolated E_g^{hl} values for **7** and **15** polymers are the highest (2.42 eV) and the lowest (1.31 eV) as shown in Figure 3.12(a), which is due to the largest and the smallest dihedral angles, respectively. The corresponding results obtained using the equation 3.6 are 2.71 and 1.78 eV. Excitation energies plotted in Figure 3.12(b) show that while the extrapolated

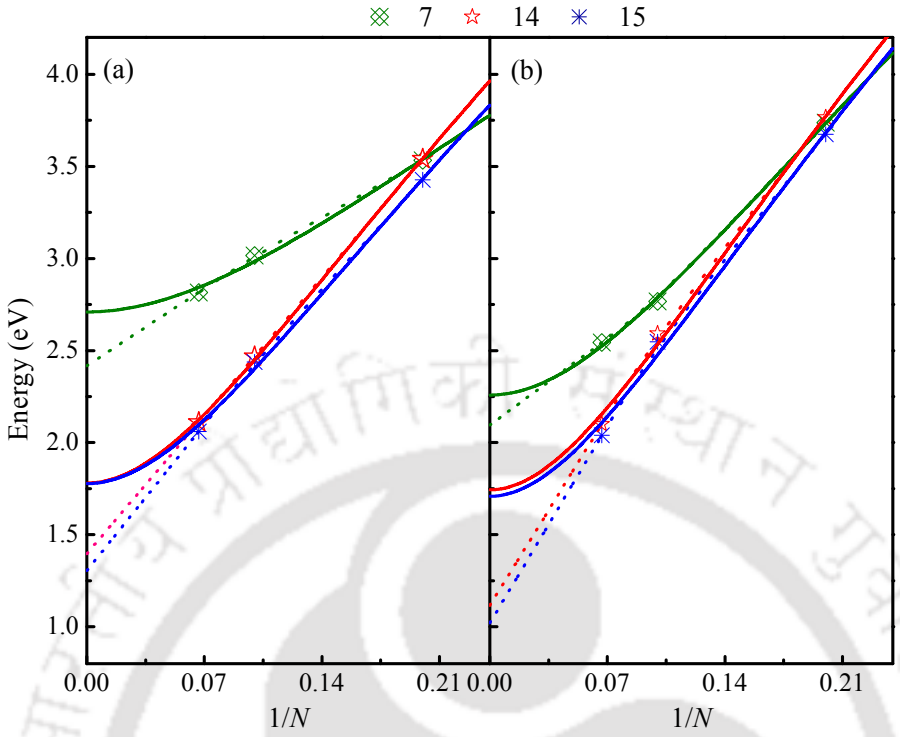

FIGURE 3.12: Variation of E_g^{hl} (a) and E_g^{opt} values (b) against the reciprocal of N, where N is the number of linearly conjugated double bonds. The Figure shows the results for compounds **7**, **14**, and **15**. Both the E_g^{hl} and the E_g^{opt} values are extrapolated to infinite chain length. Linear extrapolated results are shown as dotted lines and the results obtained using the Kuhn's formula (see equation 3.6) are shown as solid lines.

E_g^{opt} values of the compounds **7** and **15** are 2.26 and 1.71 by using the Kuhn's formula, values of 2.09 and 1.02 are obtained by the linear extrapolation. These results clearly indicate the failure of the linear extrapolation approach, similar to other studies.[26,27] The small E_g^{hl} and E_g^{opt} values of compounds **14** and **15** signify that those can be interesting materials with good conduction and light absorption properties. In the case of trimers, the orders of the E_g^{hl} and E_g^{opt} values are similar except that of trimer **12**. As reported in Tables 3.4 and 3.5, the E_g^{hl} for trimer **14** is smaller than the E_g^{hl} in trimer **12**, while the order reverses for the E_g^{opt}.

Table 3.5 also shows that the lowest optically allowed electronic transition (i.e. $S_0 \rightarrow S_1$) has the largest intensity for all cases. The first absorption bands can be assigned to HOMO $\rightarrow$ LUMO transitions predominantly. The f_{osc} values for the transitions to higher excited states are much smaller than that for the lowest energy transition. As

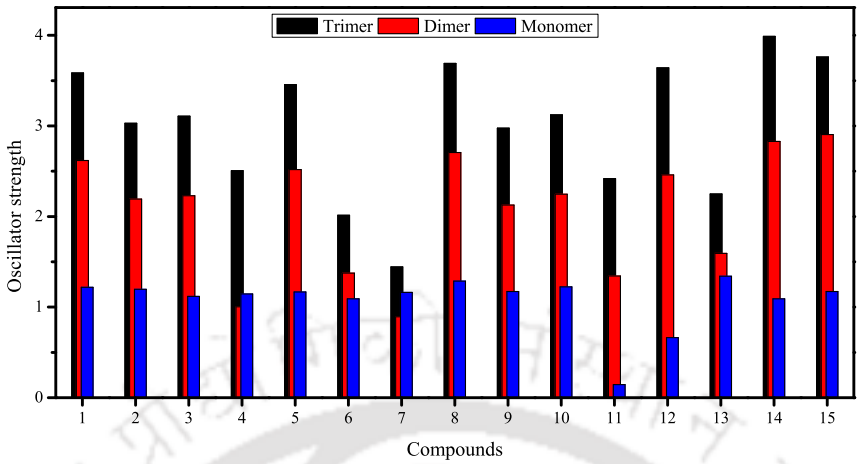

FIGURE 3.13: f_{osc} values of the first vertical transition for all the studied compounds.

shown in Figure 3.13, the f_{osc}s of the $S_0 \rightarrow S_1$ transitions of all the compounds are found to increase with an increase in chain length except that in the compounds **4** and **7**. For these two, the f_{osc} for the lowest excitation in monomer is larger than that in dimer. The oscillator strengths are found to decrease with increase in the dihedral angles. In accordance with the excitation energies, the oscillator strength is the smallest in the case of trimer **7** while it is the largest in cases of trimers **14** and **15**, for the $S_0 \rightarrow S_1$ transition. The presence of strong π electron withdrawing groups in the main chain of trimer **11** results in a small oscillator strength of 2.41 for the first excitation.

It is instructive to look at the frontier molecular orbitals to get a reasonable qualitative indication of the excitation properties. The electron densities of these orbitals are shown in Figure 3.14, for compounds **7**, **11**, **14** and **15**. For **14** and **15**, π electrons are delocalized over the entire molecule in their frontier orbitals. Maximal absorption wavelengths of 590.5 nm and 607.9 nm with large oscillator strengths of 3.98 and 3.76 are found for the trimers **14** and **15**, respectively. On the other hand, for the trimers of **7** and **11**, the conjugation does not extend over the entire backbone of the oligomers. In **7**, this is again due to the large interunit dihedral angles which distorts the structure. In trimer **11**, the electron density in the LUMO is not homogeneously distributed due

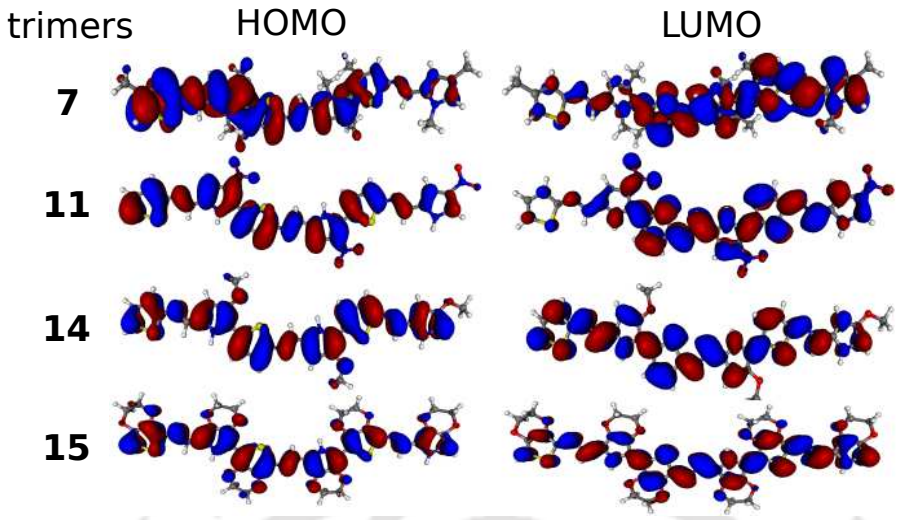

FIGURE 3.14: Electron density plots of the HOMO and LUMO orbitals of the trimers **7**, **11**, **14** and **15**.

to the presence of strong electron withdrawing $-NO_2$ group.

3.3.2 Effect of substituents on the charge carrier injection and transport properties

After a thorough analysis of ground state structures and optoelectronic properties of thiophene–pyrrole-based oligo-azomethines in the previous subsection, this subsection pays attention to their charge carrier injection and transport properties. Our study mainly focuses on the steric and electronic effects of different types of substituents on both the hole and electron injection/transport properties. Out of fifteen azomethines studied in the previous subsection, eight are carefully selected for this study, namely **1**, **7**, **8**, **9**, **11**, **12**, **14** and **15**. Sketch maps of these eight oligo–azomethines are shown in Figure 3.1. Studied compounds have varied interunit dihedral angles: from ladder type planar structures to nonplanar structures having large torsional angles are considered. Electron donating and/or withdrawing substituents having strong/weak effect are attached at different positions of the repeating units to get a complete understanding of the substitution effect on the charge injection and transport properties for our studied systems.

The structural parameters of the neutral and charged states of all the studied molecules are obtained at the B3LYP/6-31G(d,p) level of theory. Irrespective of the type of substituent, the monomer unit is planar for all cases. The effect of substituents on the geometries of the neutral forms is discussed in subsection 3.3.1. This subsection focuses on the geometrical changes occurring in the oligomers while carrying a charge (hole/electron) in comparison to their neutral counterparts.

3.3.2.1 Comparison of geometries of the $(N \pm 1)$-charged oligomers with their neutral counterparts

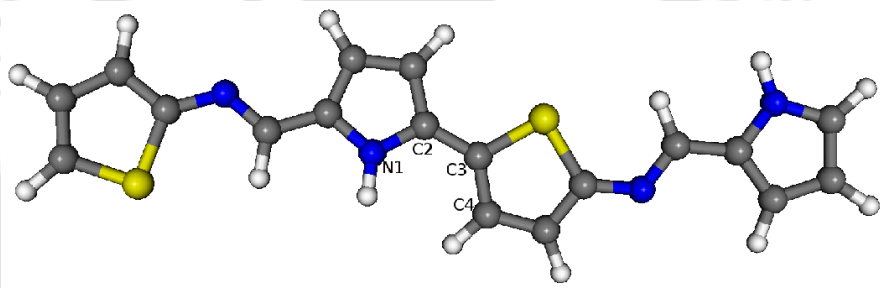

FIGURE 3.15: Representative structure showing dihedral angle between two repeating units. Here ϕ = N1–C2–C3–C4.

Dihedral angles between the repeating units contribute significantly to the reorganization energy in the hole/electron transport process for a π–conjugated polymer.[201,202] Thus, comparison of interunit dihedral angles between the neutral and charged forms of an oligomer is very informative. A representative structure of an interunit dihedral angle is shown in Figure 3.15. The calculated dihedral angles of all the pentamers are listed in Table 3.6. For all the studied compounds, reductions in the dihedral angles are observed after the injection of charge. Pentamer of the compound **1** has an interunit dihedral angle of about $\sim 11.5°$ in neutral form, whereas it is planar in its charged states. In the case of pentamer of **8**, four repeating units are in one plane for both the charged states, whereas one terminal–unit in each of the charged molecule produces a noticeable dihedral angle with the adjacent one. Compound **7** has the largest dihedral angles for all the states because of large steric hindrance arising due to the presence of three alkyl

TABLE 3.6: Calculated dihedral angles (in degrees) of all the eight pentamers at the B3LYP/6-31G(d,p) level. +1, 0 and -1 designate the monocation, neutral and monoanion forms of the pentamers. ϕ_{1-4} represent the four interunit dihedral angles in a pentamer.

pentamers	charge	dihedral angles				pentamers	charge	dihedral angles			
		ϕ_1	ϕ_2	ϕ_3	ϕ_4			ϕ_1	ϕ_2	ϕ_3	ϕ_4
	+1	0.1	0.2	0.2	1.2		+1	9.7	8.5	11.0	12.9
1	0	11.6	10.6	12.7	11.8	**11**	0	17.2	16.7	17.2	17.2
	–1	0.0	0.0	0.0	0.0		–1	14.4	10.3	9.7	11.2
	+1	47.0	47.3	49.1	53.1		+1	11.6	10.5	11.4	14.8
7	0	62.6	63.9	63.0	62.7	**12**	0	16.9	16.1	15.5	16.9
	–1	55.0	50.0	48.1	49.5		–1	15.6	11.7	10.2	11.8
	+1	0.9	0.2	0.6	6.3		+1	0.1	0.0	0.1	0.0
8	0	15.0	13.3	12.8	15.2	**14**	0	1.0	0.3	0.2	0.3
	–1	9.3	0.4	2.2	1.1		–1	0.1	0.0	0.1	0.1
	+1	16.2	13.7	15.6	19.9		+1	0.4	0.7	0.7	0.4
9	0	25.5	24.8	25.2	25.7	**15**	0	0.3	0.3	0.2	0.3
	–1	21.6	17.5	16.4	18.3		–1	0.3	0.5	0.3	0.3

groups. Compounds **14** and **15** are planar in their charged and neutral states because of O$\cdots$S interaction between oxygen atom of the methoxy substituent of one repeating unit and the sulfur atom of thiophene ring of an adjacent unit as described in section 3.3.1.

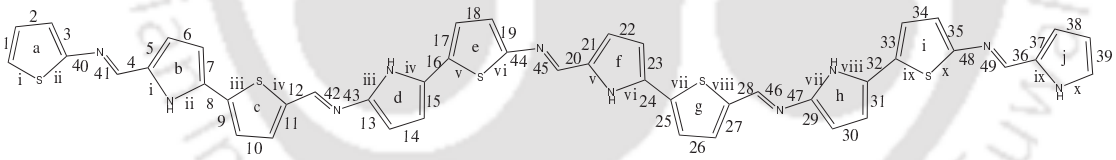

FIGURE 3.16: Labeling of various bonds and heterocyclic rings of a pentamer. Lower case letters, numbers and Roman numerals represent heterocyclic rings, C–C and C–N bonds along the conjugation path, and C–S and C–N bonds of the heterocyclic rings, respectively. H atoms and substituents are not shown in the Figure for clarity.

Bonds and heterocyclic rings of the pentamer **1** are labeled in Figure 3.16 and important bond length parameters are plotted in Figures 3.17 and 3.18. Changes in carbon–heteroatom bond lengths of the heterocyclic rings introduced by the injection of a hole or an electron are represented by d_{nc} and d_{na}. These are calculated by subtracting carbon–heteroatom bond lengths of monocationic and monoanionic forms, respectively, from the carbon–heteroatom bond lengths of the neutral state. d_{nc} and d_{na} values for the

C–S and C–N bonds of both the heterocyclic rings of pentamer **1** are plotted in Figure 3.17. Figure 3.17(a) shows that all C–S bonds of the monoanion are longer than those

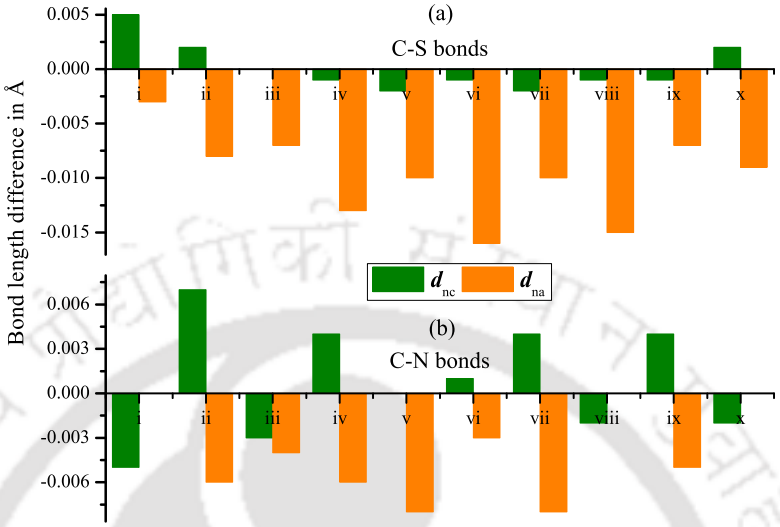

FIGURE 3.17: Difference between carbon–heteroatom bond lengths of heterocyclic rings in neutral and charged states, where $\boldsymbol{d}_{\rm nc} = (C-S/C-N)_{neutral} - (C-S/C-N)_{cation}$ and $\boldsymbol{d}_{\rm na} = (C-S/C-N)_{neutral} - (C-S/C-N)_{anion}$. $\boldsymbol{d}_{\rm nc}$ and $\boldsymbol{d}_{\rm na}$ for the thiophene rings and for the pyrrole rings of the pentamer **1** are shown in (a) and (b), respectively.

in the neutral form. Also the central bonds are more distorted than the terminal bonds of the chain. For the C–S bonds, $d_{\rm nc}$ values are relatively smaller than the $d_{\rm na}$ values. In the monocationic state, the terminal C–S bonds (***i***, ***ii*** and ***x*** bonds) are shorter and the central C–S bonds are longer than those in the neutral state. Introduction of a hole affects both the C–N bonds in many of the pyrrole rings, but to different degrees. Except in the ***c*** pyrrole ring, one C–N bond is longer and the other one is shorter than the two in the neutral form in all the rings. In the ***c*** ring, while the length of bond ***v*** remains unchanged, bond ***vi*** is shorter than in the neutral form. Compared to the neutral form, the C–N bond lengths of the monoanion are slightly larger as in the case of the C–S bonds of thiophene rings, except for bonds ***i***, ***viii*** and ***x***. The lengths of these bonds are equal for both the neutral and the monoanionic forms. In the presence of a hole or an electron, the C–S and C–N bonds of all other pentamers behave similarly to those of pentamer **1**.

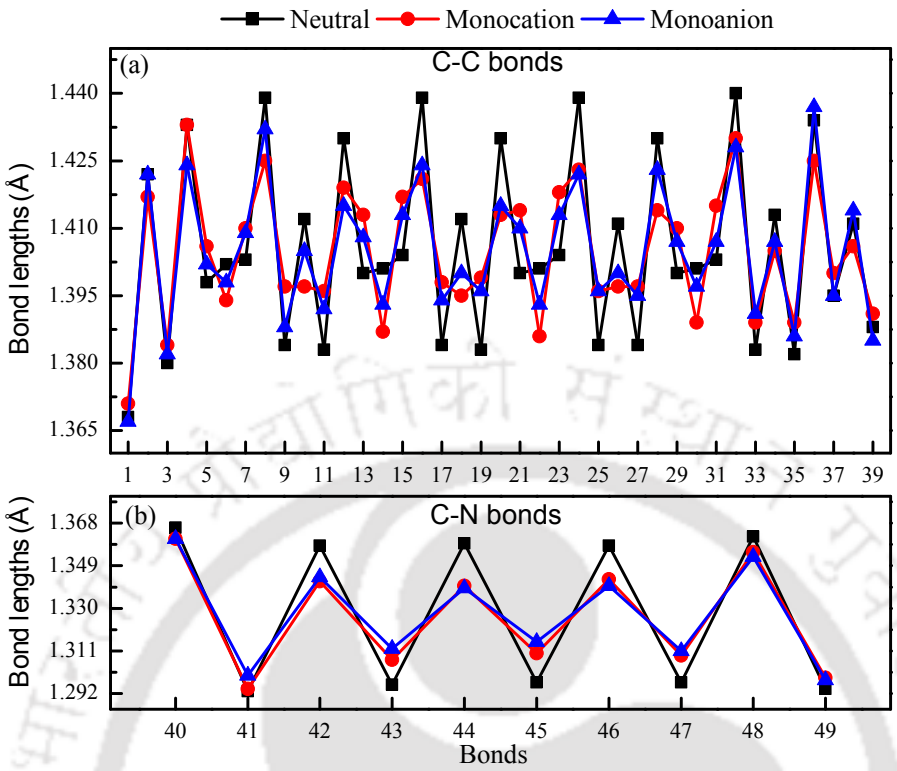

FIGURE 3.18: Bond lengths of (a) carbon–carbon and (b) carbon–nitrogen bonds along the conjugation path of pentamer **1** for the neutral and charged states.

Lengths of C–C and C–N bonds along the conjugation path of pentamer **1** for all the states are calculated and plotted in the Figure 3.18. It is clear from the figure that the deviations in the bond lengths of the charged states from the neutral states are more pronounced in the central part of the oligomer. The single bonds become shorter and the double bonds become longer in the charged states compared with the bonds in the neutral form. In the case of pentamer **1**, BLA values of the individual rings (denoted as δr) are also calculated for the neutral and charged states geometries. These are evaluated by dividing the sum of two C–C double bonds by 2 × C–C single bond of each heterocyclic ring.[203] Hence, a value of 1 for the BLA indicates the boundary between the aromatic- and quinoid-like structures. The results for the thiophene and pyrrole rings are shown in Figure 3.19. This shows that the pyrrole rings, apart from the terminal pyrrole ring, are at the boundary position of aromatic- and quinoid-like structures in the neutral form. So, a small distortion of the bonds renders them quinoid-like structures. However, in the case of the thiophene ring the situation is completely different, and a

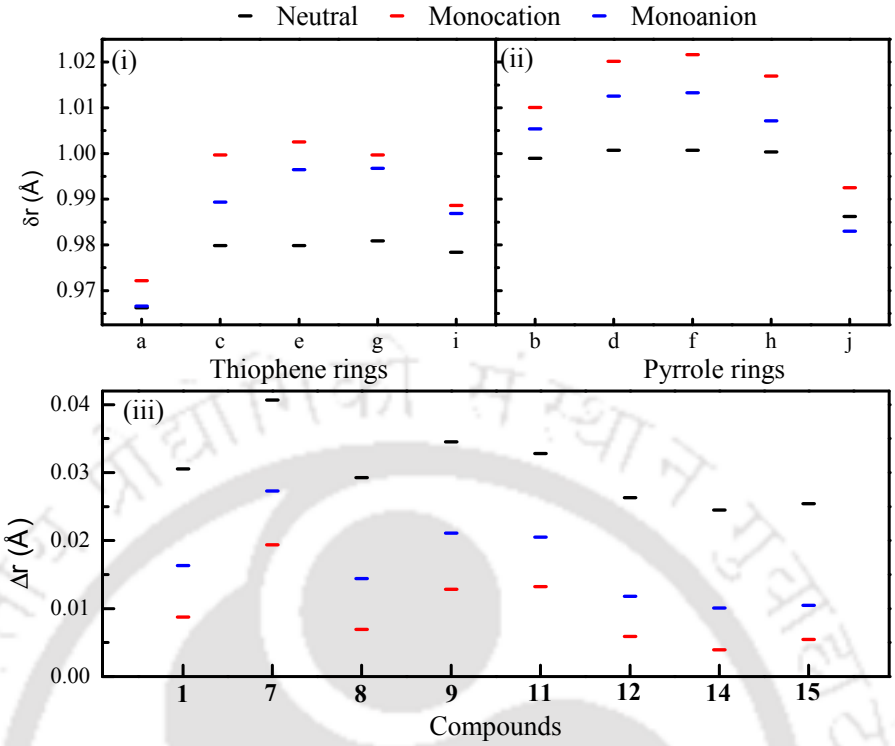

FIGURE 3.19: δr values of (i) thiophene rings and (ii) pyrrole rings of the pentamer **1**, and (iii) Δr values of all the studied compounds. Where δr = (sum of two C=C bonds)/(2×C–C bond) and Δr = C–C_{avg} – C=C_{avg}

large distortion is needed to form a quinoid–like structure. Hence, between the two types of heterocyclic rings in pentamer **1**, quinoid–like structures are mostly found in pyrrole rings. Another important observation that can be made from Figure 3.19(i) and (ii) is that the presence of a hole causes more distortion than an electron. Differences of δr between the neutral and charged states of both the heterocyclic rings are comparatively smaller for pyrrole rings than for thiophene rings. A small change in δr value may lead to less reorganization energy and, hence, introduction of pyrrole rings in a polymer may enhance the charge transfer rate. Carbon–carbon BLAs (denoted as Δr) for pentamers of all the compounds are plotted in Figure 3.19(iii). It is calculated as the difference of average C–C single and double bonds.[193] It is noticed that compound **7** has the largest Δr value, while compound **14** has the smallest Δr value for all the states. This may occur because of large dihedral angles between adjacent repeating units leading to poor conjugation in pentamer **7**, and the highly conjugated planar structure of pentamer **14**.

TABLE 3.7: Values of E_H, E_L, IP and EA of all the studied pentamers calculated at the B3LYP/6-31G(d,p) level of theory. Work functions of some metal electrodes are also tabulated for comparison.

pentamers	frontier orbitals (eV)		IPs (eV)		EAs (eV)	
	E_H	E_L	adiabatic	vertical	adiabatic	vertical
1	−4.47	−2.42	5.07	5.18	1.80	1.71
7	−4.65	−1.98	5.17	5.36	1.40	1.26
8	−4.37	−2.36	4.95	5.06	1.75	1.66
9	−5.00	−2.71	5.59	5.71	2.09	2.00
11	−5.36	−3.03	5.95	6.04	2.42	2.32
12	−4.12	−2.29	4.68	4.80	1.70	1.60
14	−4.12	−2.30	4.69	4.80	1.71	1.62
15	−3.72	−1.96	4.24	4.36	1.42	1.31
metal electrodes	Au	ITO	Ag	Al	Mg	Ca
work function (eV)	5.10[45,205]	4.70[206]	4.26[205]	3.70[206]	3.66[205]	2.87[205]

Pentamer **15** is also planar, while its Δr values (for all the three forms) are slightly larger than the values for **14**. A large electronic effect of the $–OC_2H_4O–$ groups in pentamer **15** may be a cause of the above result. For all the studied compounds, it is observed that the Δr values of pentamers are in accordance with interunit dihedral angles, and are largely affected by the nature of substituents. An electron withdrawing effect of the substituents causes an increase in Δr, while an electron donating effect causes a decrease in Δr value compared to the values for pentamer **1**.

3.3.2.2 Charge injection properties

As holes/electrons are either injected from a metal electrode to a polymer or discharged from a polymer to a metal electrode in any optoelectronic device, it is important to maintain a balance between the work function (ϕ_m) of metals and the ionization potential and electron affinity (or energies of frontier orbitals) of polymers at the metal–polymer interface.[45,204] The zero–field barrier height is often calculated as $|E_H| - \phi_m$ (for hole injection) or $\phi_m - |E_L|$ (for electron injection).[45,166,169] For all the studied compounds, values of E_H, E_L, IP(v,a) and EA(v,a) are reported in Table 3.7. ϕ_m values of some metals (high work function metals such as Au, Ag and Indium Tin Oxide (ITO) and

low work function metals such as Al, Mg and Ca) are also listed in the same table to compare their ϕ_m values with the energies of the frontier orbitals of the studied oligomers. Adiabatic and vertical EAs and IPs are plotted in Figure 3.20. As reported in the Table, $|E_H|$ of the studied pentamers are smaller than the work function of the Au metal electrode (5.1 eV), except for that of pentamer **11**. This negative potential barrier may facilitate hole injection from the metal electrode to these oligo–azomethines, and space charge distribution in the polymer network may be the only hindrance for the injection.[207–210] Even pentamer **11** has an injection barrier of only 0.255 eV. However,

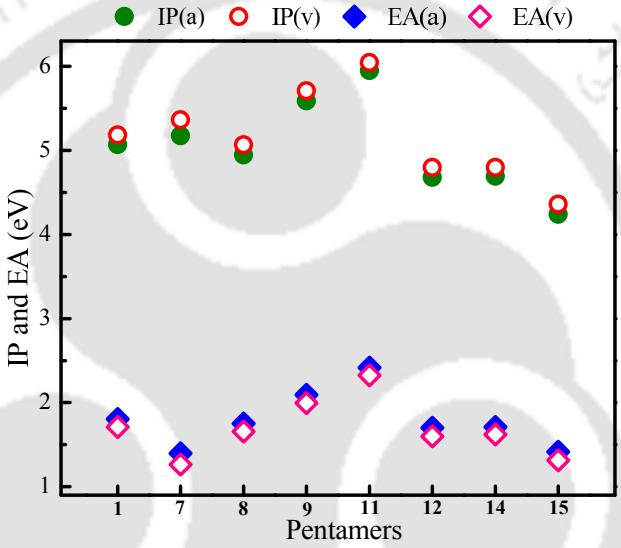

FIGURE 3.20: Vertical and adiabatic EA and IP values for all the studied pentamers.

the comparison of IP(v) and ϕ_m of electrodes indicate that the injection barrier exist for pentamers **1**, **7**, **9** and **11**, and the barrier height is the largest for pentamer **11**.

Pentamers **11** and **15** have the largest and the smallest IP values, respectively, as shown in Figure 3.20. The strong electron donating nature of $–OC_2H_4O–$ groups and the strong electron withdrawing nature of $–NO_2$ groups dictate this variation in IPs. The planar structure of pentamer **15** provides further support for the small IP value. Although the $–NH_2$ group is a stronger electron donor than the $–OCH_3$ group, the planarity of the pentamer **14** compensates for this, and equal IP values are obtained for both pentamers **12** and **14**. Both pentamers **8** and **7** have larger dihedral angles than

pentamer **1**, but the IP values of **8** and **7** are smaller and larger, respectively, compared to that of **1**. It clearly shows that the electronic effect of the alkyl substituents in pentamer **8** and the steric effect in **7** are the most dominant factors for the prediction of IP values. As the $-CF_3$ is a weaker electron withdrawing group than the $-NO_2$, the IP value of pentamer **9** is slightly smaller than that of pentamer **11**. The above discussion of the IPs seems to suggest that compound **15** may be the most suitable candidate for the hole injection. But it is also possible that such a small IP may lead to unintentional doping in the presence of oxygen.[171,211] Pentamer **14** has almost the same IP value as polyacetylene (4.7 eV[212]), and is expected to have similar environmental stability.

Most of our studied materials show large barriers for electron injection as seen in Table 3.7, and thus these compounds may not be suitable for electron injection. Large barriers may be due to the raising of energy of frontier molecular orbitals in the presence of azomethine groups and pyrrole rings in the oligomers.[159–161] However, in the presence of electron withdrawing groups, electron injection may be possible from low work function metals such as Mg and Ca. In contrast to IP, the presence of withdrawing groups increases the EA value, whereas the reverse happens for electron donating groups.[3,213] Compound **11** has the largest EA value due to the strong electron withdrawing effect of $-NO_2$ substituents. But for the studies systems, these smaller values of electron affinities (less than 3.0 eV) may result in poor stabilities of these anionic compounds. Thus, although pentamers **9** and **11** have comparatively larger EA values than the other studied molecules, their EA values are still smaller than 2.5 eV, which may cause hindrance for electron injection. It is also clear from the figure that, in addition to the electronic effect of a substituent, the steric effect is also an important factor for the determination of EA. As a consequence, pentamer **7** has the smallest EA value. As expected, all the compounds containing electron donating groups have small EA values.

As reported in Table 3.7 and shown in Figure 3.20, IP(v) values are always larger and EA(v) values are always smaller than the adiabatic counterparts because of reorganization of molecules after the Franck–Condon excitations. For pentamers, both IP(v) and EA(v) follow the same order as IP(a) and EA(a). IP(v, a) and EA(v, a) values for all the

oligomers of all the compounds are listed in Table A1 (see Appendix I). As reported in the table, EA(v, a) and IP(v, a) values increase and decrease with the addition of each repeating unit, respectively.

3.3.2.3 Charge transport properties

Internal reorganization energies for the hole and electron carriers of all the compounds are reported in Table 3.8 and plotted in Figure 3.21. As the monomers are completely planar, the electronic effect of the substituents is the dominant factor. Thus, in addition to oligomers, λ_h and λ_e of the monomers are also analyzed to explore the electronic effect of the substituents on the internal reorganization energies. Apart from monomers **8** and **14**, all other monomers have larger λ_h values than monomer **1** (**1** has no substituent). The large distortion of geometries after substitution of strong electron donating/withdrawing group(s) may be the reason for the above result. Monomer **12** has the largest

TABLE 3.8: Intramolecular reorganization energies for holes (λ_h) and electrons (λ_e) calculated at the B3LYP/6-31G(d,p) level of theory of all the studied compounds. Here, "M", "D", "T", "TT" and "P" denote monomer, dimer, trimer, tetramer and pentamer, respectively.

compounds	λ_h in eV							
	1	**7**	**8**	**9**	**11**	**12**	**14**	**15**
M	0.40	0.41	0.39	0.47	0.44	0.49	0.40	0.46
D	0.32	0.46	0.32	0.41	0.37	0.39	0.31	0.34
T	0.29	0.45	0.30	0.36	0.31	0.33	0.27	0.30
TT	0.25	0.40	0.27	0.31	0.25	0.30	0.25	0.27
P	0.22	0.34	0.24	0.26	0.20	0.25	0.22	0.25
polymer (n=∞)	0.21	0.27	0.24	0.24	0.18	0.23	0.21	0.24
	λ_e in eV							
	1	**7**	**8**	**9**	**11**	**12**	**14**	**15**
M	0.35	0.37	0.35	0.39	0.34	0.42	0.37	0.50
D	0.28	0.38	0.28	0.34	0.34	0.32	0.27	0.33
T	0.24	0.36	0.26	0.29	0.27	0.27	0.23	0.28
TT	0.21	0.32	0.22	0.24	0.22	0.23	0.21	0.24
P	0.19	0.26	0.19	0.20	0.18	0.21	0.18	0.21
polymer (n=∞)	0.17	0.19	0.19	0.18	0.15	0.18	0.17	0.19

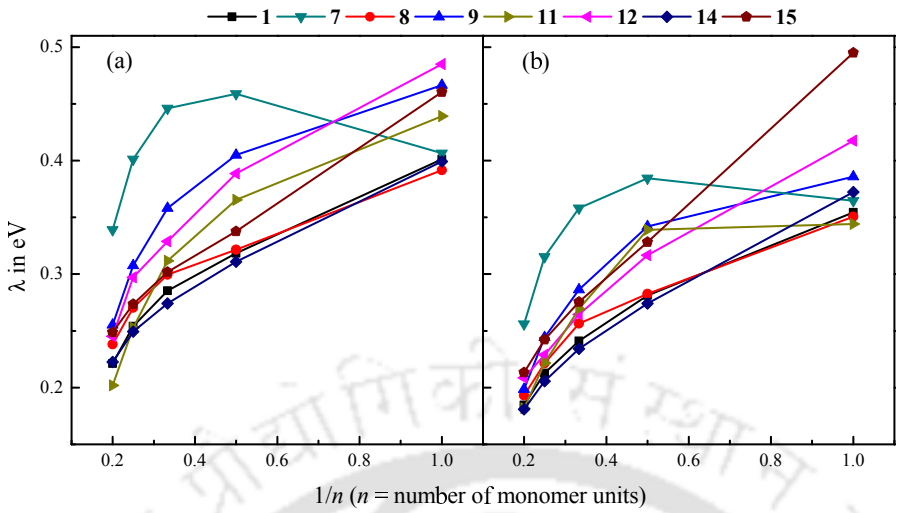

FIGURE 3.21: Internal reorganization energies induced by (a) a hole and (b) an electron for all the studied compounds.

and monomer **8** has the smallest λ_h values. However, in the case of λ_e, monomer **15** has the largest and **11** has the smallest value. This may be due to the presence of strong electron donating (–OC_2H_4O–) and withdrawing (–NO_2) groups in **15** and **11**, respectively. The steric effect of the substituents on the reorganization energies is clearly noticeable when we move from monomers to dimers and to large oligomers. For all the studied oligomers, λ_h and λ_e values decrease after the addition of each repeating unit, except in the case of compound **7**. In the case of **7**, λ_h and λ_e values for the dimer are larger than those of the monomer. From trimer onwards, the values decrease with the increase of the oligomer size. Compound **7** has large interunit dihedral angles in the neutral form, and it reorganizes towards planar geometry when carrying a charge, leading to a large reorganization energy. The order of λ_h in the monomer is different than in the dimer, and many crosses occur after the addition of another repeating unit, which can be understood by comparing with their dihedral angles listed in Table 3.6. Pentamer **11** has the smallest and **7** has the largest λ_h values. Crossed lines in Figure 3.21(b) again indicate the dominant behavior of the steric effect of the substituents on the λ_e values for the oligomers, as in λ_h. In the case of pentamers, **11** and **14** have the smallest and **7** has the largest λ_e values. The planarity of pentamer **14**, the strong electron withdrawing nature of the –NO_2 substituent in pentamer **11** and the large inter–unit dihedral angles

of **7** are the reasons of the above result.

For all cases, λ_h is larger than λ_e (except monomer **15**). Although pentamers **14** and **15** are planar, both λ_e and λ_h values of **15** are larger than those of **14** because of the presence of a strong electron donating group (–OC_2H_4O–). If we compare pentamers **1** and **14**, the differences between λ values are small (only 0.002 in λ_h and 0.004 in λ_e). Thus, the presence of –OCH_3 groups at the '3' position of the pyrrole rings has little effect on the internal reorganization energy for the studied systems. For all the studied compounds, no sign of convergence is observed for either λ_h or λ_e, even after the addition of five repeating units (each pentamer contains 10 heterocyclic rings and 5 azomethine linkages). λ convergence behavior depends upon delocalization of charge in the π–conjugated backbone of a polymer. In the studied systems, charge (hole/electron) distribution is not restricted to a finite region, rather it spreads all over the pentamers. Thus, the reorganization occurs all over the oligomer chain resulting in a non-convergent behavior of the reorganization energy. Bond lengths and BLA values also support the above explanation. Reorganization energies of the polymers are predicted by the Kuhn's formula and listed in Table 3.8. The results indicate that localization length increases further for long polymers and smaller reorganization energies are obtained compared with their respective pentamers, except λ_h of the compound **8** where similar values are obtained for both of its pentamer and polymer. λ_h values of the polymers **7** and **11**, and λ_e values of the polymers **15** and **11** are the largest and smallest, respectively.

Electronic coupling values of all the dimers are calculated for the optimized structures of two adjacent dimers obtained at the B3LYP-D3/6-31G(d,p) level. Optimized structures of the dimers of compounds **1** and **8** are shown in Figure 3.22. The average intermolecular distance between two dimers of each compound is calculated and listed in Table 3.9. The inter-chain distances are strictly consistent with the steric effect of the substituents. While two neighboring dimers of compound **7** are situated at the average distance of 3.58 Å, the value is 3.23 Å for compound **1**. Except compound **7**, the average intermolecular distances in the optimized structures are smaller than 3.5 Å. Strong intermolecular $\pi - \pi$ interactions and hydrogen bonds between neighboring

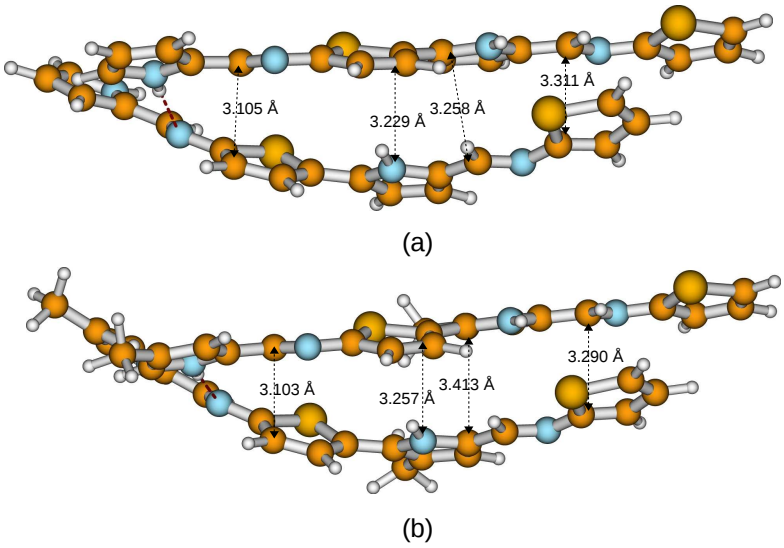

FIGURE 3.22: Optimized structures of two neighboring dimers for dimer **1** (a) and **8** (b), calculated at the B3LYP-D3/6-31G(d,p) level.

TABLE 3.9: Charge transfer integral (V_{ab}), average intermolecular distances, charge transfer rates (k_{ct}), and mobilities (μ_{hop}) calculated for the optimized structures of two closely spaced dimers of each compound at the B3LYP-D3/6-31G(d,p) level.

compounds	V_{ab} (eV)		distance (Å)	$k_{ct} \times 10^{-13}/s^{-1}$		$\mu_{hop}/cm^2V^{-1}s^{-1}$	
	hole	electron		hole	electron	hole	electron
1	0.18	0.20	3.23	4.53	8.58	1.84	3.48
7	0.11	0.15	3.58	0.34	1.44	0.17	0.72
8	0.20	0.20	3.27	5.08	8.30	2.11	3.45
9	0.07	0.03	3.38	0.27	0.09	0.12	0.04
11	0.08	0.05	3.44	0.57	0.25	0.26	0.12
12	0.10	0.09	3.36	0.59	1.08	0.26	0.47
14	0.18	0.18	3.33	4.50	6.95	1.94	3.00
15	0.10	0.09	3.28	1.13	0.95	0.47	0.40

molecules control the morphology of adjacent dimers, and such close packed structures are obtained.

Charge transfer integrals, charge transfer rates, and hopping mobilities calculated from equations 3.4, 3.1 and 3.5, respectively, for all the studied dimers are reported in the same table. The above calculations are performed at room temperature (298 K). As reported in the table, the smallest V_{ab} values for holes (0.07 eV) and electrons (0.03 eV) are estimated for compound **9**. For both holes and electrons, compounds **1**, **8** and **14**

have large V_{ab} values. Estimated charge transfer rates and hopping mobilities of all the dimers using their λ and V_{ab} values are plotted in Figure 3.23. As shown in the figure,

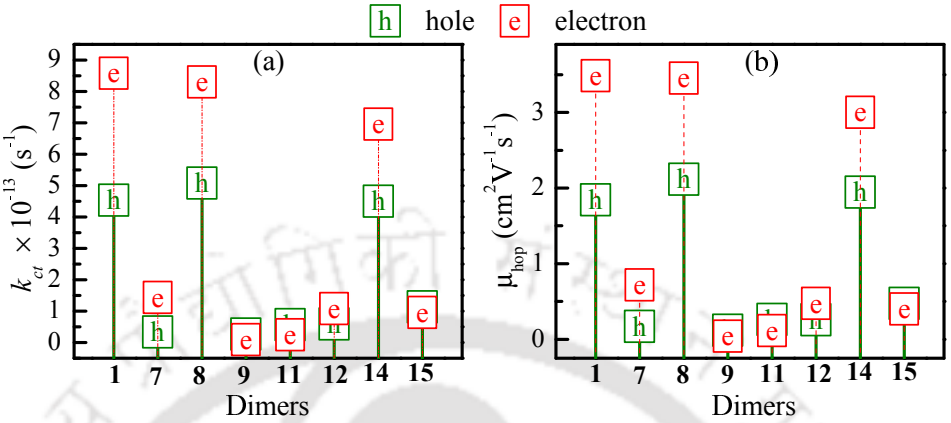

FIGURE 3.23: Charge transfer rates (a) and hopping mobilities (b) of all the studied dimers.

both the charge transfer rate and the mobility have the same trend. Both are larger for electrons compared to holes, except for dimers **9**, **11** and **15**. Among all the studied molecules, the k_{ct} and μ_{hop} values of dimers **1**, **8** and **14** are quite large because of small reorganization energies and large transfer integrals. Although both dimers **14** and **15** are planar, dimer **15** has smaller k_{ct} and μ_{hop} values than those of **14**, as it suffers from large reorganization energy and small electronic coupling. k_{ct} and μ_{hop} values of dimer **9** are the smallest among all the studied compounds.

As mentioned in subsection 3.2.2, single-point calculations were also carried out at the B3LYP-D3/6-31G(d,p) level to calculate the V_{ab} values of pentamers. In these calculations, two pentamers of each compound were cofacially placed at a distance of 3.5 Å, except in the case of pentamer **7**. As pentamer **7** has large interunit dihedral angles with three bulky $-CH_3$ substituents, two chains were placed at a 6.0 Å center to center distance in the above calculation. The coplanar position of the chains is not considered here as their charge transfer integrals are negligible compared to the cofacially stacked ones.[166,214] The dimer of pentamer **1** is shown in Figure 3.24 as a representative structure. Inter-chain distances, electronic coupling values, charge transfer rates and

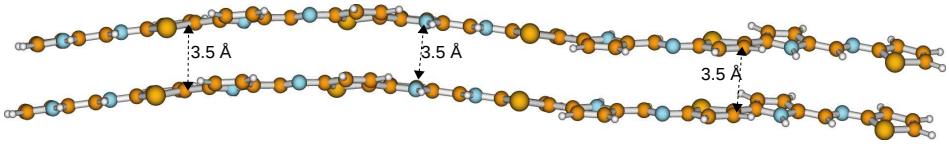

FIGURE 3.24: Representative structure of two stacked pentamers. Interchain distances are 3.5 Å for all the studied pentamers other than **7**. For **7**, the distance is 6 Å.

mobilities are listed in Table 3.10. Estimated k_{ct} and μ_{hop} values for the pentamers at 298 K are plotted in Figure 3.25.

TABLE 3.10: Charge transfer integral (V_{ab}), average intermolecular distances, charge transfer rates (k_{ct}), and mobilities (μ_{hop}) calculated for two stacked pentamers of each compound at the B3LYP-D3/6-31G(d,p) level.

compounds	V_{ab} (eV)		distance (Å)	$k_{ct} \times 10^{-13}/s^{-1}$		$\mu_{hop}/cm^2V^{-1}s^{-1}$	
	hole	electron		hole	electron	hole	electron
1	0.16	0.12	3.5	10.05	9.92	4.80	4.73
7	0.06	0.07	6.0	0.42	1.33	0.59	1.86
8	0.16	0.15	3.5	8.28	13.20	3.95	6.30
9	0.04	0.10	3.5	0.34	5.41	0.16	2.58
11	0.10	0.10	3.5	5.25	7.26	2.51	3.47
12	0.17	0.17	3.5	8.81	14.36	4.20	6.85
14	0.16	0.15	3.5	9.80	15.27	4.68	7.28
15	0.17	0.17	3.5	8.09	12.92	3.86	6.16

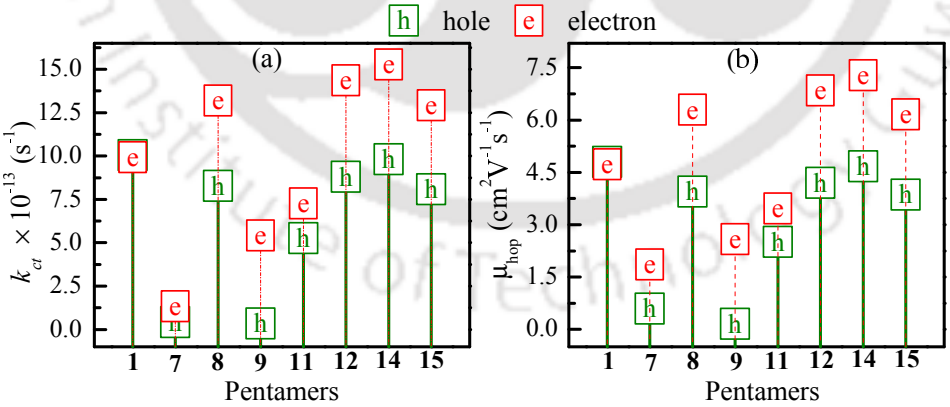

FIGURE 3.25: Charge transfer rates (a) and hopping mobilities (b) of all the studied pentamers.

As listed in the table, V_{ab} values for holes and electrons are the largest in the case of pentamers **12** and **15**. Pentamers **9** and **7** have the smallest coupling values for

the hole and electron, respectively. It is also noticed that for the dimer of pentamers having the same internuclear distance, small coupling values are obtained for compounds containing electron withdrawing groups (i.e., **9** and **11**) compared to other pentamers. For both holes and electrons, V_{ab} values are also small for compound **7**. As shown in Figure 3.25, electron transport rates and mobilities are always larger than those for holes, except for pentamer **1**. In the case of pentamer **1**, values for the hole transport rate and mobility are slightly larger than those for electrons. Pentamers **1** and **9** have the largest and the smallest hole transport rate and mobility, respectively. On the other hand, pentamers **7** and **14** have the smallest and the largest electron transport rate and mobility, respectively. In comparison to the optimized dimers of dimers, significant changes are noticed in the k_{ct} and μ_{hop} values for the dimers of pentamers **12** and **15** (k_{ct} values are increased from $< 1.5 \times 10^{-13} s^{-1}$ to $> 8.0 \times 10^{-13} s^{-1}$ and, μ_{hop}s are increased from $< 0.5\ cm^2V^{-1}s^{-1}$ to $> 3.5\ cm^2V^{-1}s^{-1}$). The reason for the above result is that V_{ab} values of these compounds for the optimized structures of the dimers are much smaller than the values for pentamers. In addition to this, the reorganization energies for the pentamers are also smaller than those for dimers. Both for holes and electrons, k_{ct} and μ_{hop} for pentamers **1**, **8**, **12**, **14** and **15** are sufficiently large, and these compounds may act as efficient charge transport materials. Although pentamer **11** has a small λ value, its small V_{ab} value results in poorer hole and electron transport rates and mobilities, compared to the values obtained for the above compounds. As the anionic forms of these materials are not stable enough, these material are mostly favorable for the hole transport layer. As discussed in the subsection 3.3.2.2, the small IP value of pentamer **15** may cause hindrance for the hole transport process.

3.4 Salient findings

Our study on the geometric and optoelectronic properties of fifteen pyrrole and thiophene based oligo-azomethines shows that the geometric structure is very much dependent on the steric influence of the bulky substituents and their positions. Torsional angle plays

a major role in determining the localization and delocalization of wave functions and hence, any deviation from planar structure affects the optoelectronic properties of the π-conjugated polymer. All the compounds with large torsional angles have large E_g^{hl} and E_g^{opt} values and small oscillator strengths for the $S_0 \rightarrow S_1$ transition. The largest E_g^{hl} and E_g^{opt} values was found for compound **7**. For this system, the oscillator strength for the lowest electronic transition is also the smallest. Oligomers of compounds **14** and **15** are found to be planar due to intramolecular O $\cdots$ S interactions, and these two have significantly smaller E_g^{hl} and E_g^{opt} values and larger oscillator strengths for the lowest electronic transition than the other compounds.

After a detail investigation on the optoelectronic properties of these heterocyclic azomethines, eight out of fifteen azomethines are selected for the study of their charge injection and transport properties. Our results show that these properties are largely dependent on the electronic and steric effects of the substituents, and it can be tuned according to requirements. These azomethines are favorable for the hole injection process from a high work function metal electrode (such as Au), while large electron injection barriers make them unfavorable for the electron injection process. For the optimized dimer of dimers **1**, **8** and **14**, hole and electron mobilities are larger than 1.5 $cm^2V^{-1}s^{-1}$ and 3.0 $cm^2V^{-1}s^{-1}$, respectively. For pentamers, compounds **1**, **8**, **12**, **14** and **15** have carrier mobilities greater than 3.5 $cm^2V^{-1}s^{-1}$. Although these compounds show good charge carrier mobilities for holes and electrons, they have certain limitations. The possibility of unintentional doping in **15** may hamper its use in practical applications. Large electron injection barriers and low stabilities of the anionic forms are disadvantages of these compounds, and these may hinder the behavior of the oligomers as ambipolar materials. However, these compounds are promising candidates for the hole transport layer.

Vinylene- and azomethine-linked oligomers: Optoelectronic properties of helical and nonhelical conformers

This chapter reveals the structural and optoelectronic properties helical and nonhelical conformers of vinylene- and azomethine-linked heterocyclic oligomers. The contents of this chapter are published in the following paper:

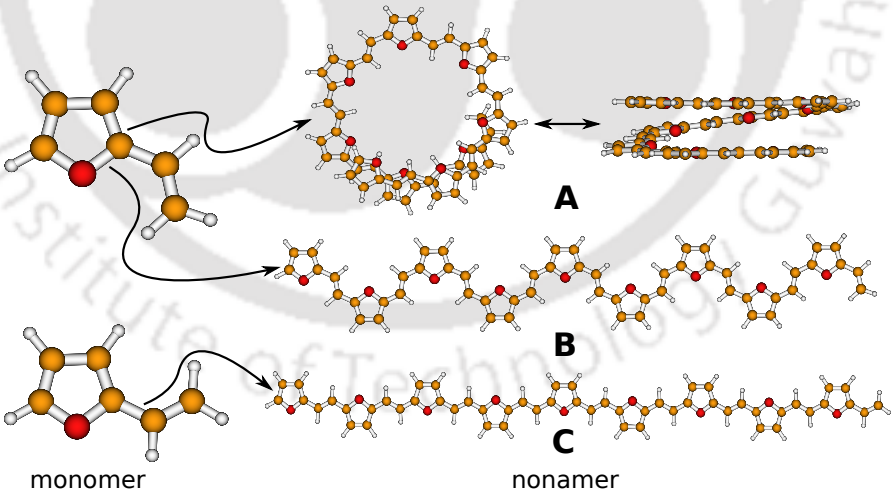

Figure: Different conformers of furan-vinylene monomer and nonamer.

- H. Sahu and A. N. Panda, *J. Phys. Chem. C*, **2015**, 119, 22855.

Nowadays, vinylene- and azomethine-based heterocyclic conjugated polymers are in the focus of the recent research[17,18,48,63–65,69], as these π-spacers reduces dihedral angles between the repeating units and increases the electron delocalization over the main chain. Many different conformations are possible for these oligomers, and stabilities of these conformations are discussed in literature[48,65], but all the results are from studies on small (2 to 4 repeating units) linear oligomers. However, it is known that the intramolecular noncovalent interaction has a major impact on secondary structures like helices for a large π-conjugated oligomer. In addition to other helical polymers[73,215,216], heterocyclic conjugated helical polymers like substituted polythiophene and polypyrrole have already been synthesized.[217–219] These helices are either in the form of nonaggregated intrachain helical conformations or the aggregated form of planar oligomers. Few studies show that helices of substituted polythiophenes are formed due to intermolecular helical packing of planar polythiophene chains in aggregated states.[220–222] On the other hand, many researchers have synthesized polythiophene derivatives having nonaggregating folded structures.[223,224] Computational studies based on the semiempirical method[225] and density functional theory[49] also support intrachain helical conformations of these polymers. In cases of fluorinated thienylfurans[50] and phenylene-ethylene foldamers[72], computational investigations show that hydrogen bonding and π-π stacking interactions between adjacent helical turns lead to folding structures. These studies and their results raise the possibilities of formation of similar looking folding structures for vinylene- and azomethine-linked heterocyclic oligomers. However, this issue has not been addressed yet, and the structural aspects of these type of polymers are yet to be revealed.

In cases of heterocyclic ring-vinylene/azomethine polymers, the absence of informations on the structural, energetics and absorption properties of different conformers, especially for long chains, in the literature motivates us to investigate these types of oligomers. In this chapter, the conformation-dependent optoelectronic properties of vinylene/azomethine-linked heterocyclic π-conjugated oligomers are presented and discussed. In section 4.1, computational aspects are briefly discussed. This is followed by

results and discussion in section 4.2 and conclusions in 4.3.

4.1 Computational details

All calculations were carried out with the Orca 3.0 program.[184] B3LYP and B3LYP-D3 functionals[95] in combination with the 6-31G(d,p) basis set are used to optimize the ground-state geometry of all the studied compounds. In B3LYP-D3, the Becke-Johnson damping[226] was used with the D3 version of dispersion, as mentioned in the subsection 2.2.4. No constraint was applied during the above optimization processes. To calculate vertical excitation energies and oscillator strengths, single point TDDFT calculations were performed using the B3LYP functional with the same basis set at the optimized ground-state geometries obtained by the B3LYP-D3/6-31G(d,p) level. To comment on the optical activity of the folded conformers, electronic circular dichroism (CD) spectra have also been computed. Maximum number of repeating units considered varied from system to system, and the largest oligomer in this study consists of 14 units to keep the computational cost under control. In fact, optimizations of ground state geometries were stopped once a helix/foldamer is formed and the size was not increased further. IP(v) values are calculated for the longest oligomers of all the studied conformers at the B3LYP-D3/6-31G(d,p) level using the equation 1.3.

4.2 Results and discussion

Sketch map representations of the repeating units for studied oligomers are shown in Figure 4.1. Furan, pyrrole and thiophene rings substituted at their "2" positions by either a vinylene or azomethine linkage are taken as repeating units. In each of these oligomers, two adjacent heterocyclic rings are trans to each other with reference to either C=C or C=N linkages. Three different types of conformers, **A**, **B** and **C**, of each oligomer are considered in this work. In **A**, hetero atoms of adjacent heterocyclic rings are in the same side, and in **B** and **C**, these are in the opposite sides of the linkages. However, the

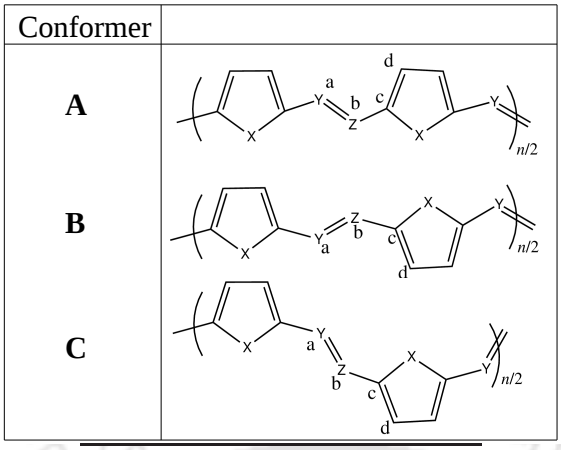

compounds	X	Y	Z
FV	O	CH	CH
PV	NH	CH	CH
TV	S	CH	CH
FAm	O	CH	N
PAm	NH	CH	N
TAm	S	CH	N

FIGURE 4.1: Sketch map representations of the repeating units of the studied heterocyclic oligomers, where n starts at 1 and goes up to 14. Three different conformers (**A**, **B** and **C**) of oligomers are shown in the figure. Furan, pyrrole, and thiophene rings are represented by F, P and T, and vinylene and azomethine linkages are represented by V and Am, respectively. The dihedral angle (ϕ) between two repeating units of these conformers is also depicted as $\phi = \angle$ a-b-c-d.

difference between **B** and **C** is that the heterocyclic rings are attached at two possible different trans positions of the linkage. Denoting furan, pyrrole and thiophene by F, P and T, and vinyl and azomethine as V, Am, respectively, the studied oligomers can be identified by the following abbreviation: conformation-(heterocyclic ring linkage type)$_n$, where n is the number of repeating units. All the studied compounds were fully optimized at B3LYP/6-31G(d,p) and B3LYP-D3/6-31G(d,p) levels. Frequency calculations were carried out for all **A**, **B** and **C** conformers of a few selected small oligomers. The absence of any imaginary frequency showed that all are minima in the potential energy hypersurface.

4.2.1 Ground-state: geometries, diameter of helices, bond length alternation and dipole moment

Monomers of all the compounds obtained using both the functionals are found to be planar. Bond lengths of C=C linkages of optimized structures of dimers for the **C** conformer obtained at these levels are in good agreement with the previous work.[65] Angles between heterocyclic rings and these linkages obtained at the B3LYP/6-31G(d,p) level are the same as the results of the previous work,[65] while little deviations ($\leq 0.5°$) are noticed for the results obtained at the B3LYP-D3/6-31G(d,p) level. All these dimers are planar, which matches with the previous results.[65] Keeping in mind the above results for dimers, these combinations of functionals and basis sets have been chosen to study the structures of large oligomers (up to 14-mer).

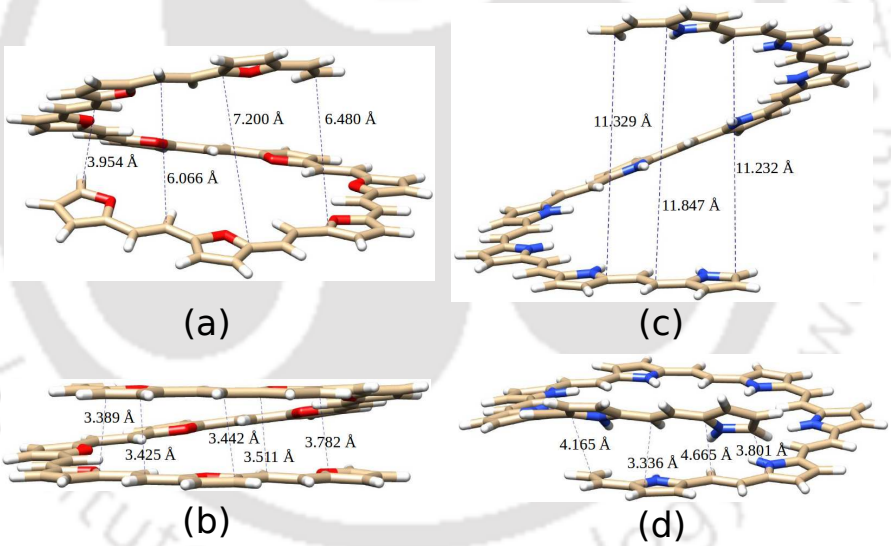

FIGURE 4.2: Ground-state structures of **A**-$(FV)_9$ and **A**-$(PV)_9$ optimized at B3LYP/6-31G(d,p) (a, c) and B3LYP-D3/6-31G(d,p) (b, d) levels. Distances between the atoms of two adjacent helical turns are given in Å.

Optimized structures of **A**-$(FV)_9$ and **A**-$(PV)_9$ oligomers obtained by B3LYP and B3LYP-D3 functionals in combination with the 6-31G(d,p) basis set are shown in Figure 4.2. Ground state geometries of **A**-$(TV)_{14}$ are shown in Figure A1 (see Appendix II). As shown in these figures, all are helix-like structures. The π-stacking distance between two adjacent helical turns of all these helical oligomers is shown in the same figure. As shown,

the optimized structure of **A**-$(FV)_9$ obtained using the B3LYP functional is slightly bent at the terminal units of the oligomer, while two adjacent helical turns reside parallel to each other for the B3LYP-D3 functional. For all these vinylene-linked helical oligomers, distances between the adjacent helical turns obtained by the B3LYP functional are comparatively larger than the distances obtained by the B3LYP-D3 functional. In **A**-$(PV)_9$, shown in Figure 4.2 (d), hydrogen bonds are formed between the nitrogen and hydrogen atoms of two adjacent helical turns, and this results in a bent structure in the case of B3LYP-D3. Ground-state structures of **A**-$(FAm)_9$ and **A**-$(PAm)_9$ obtained

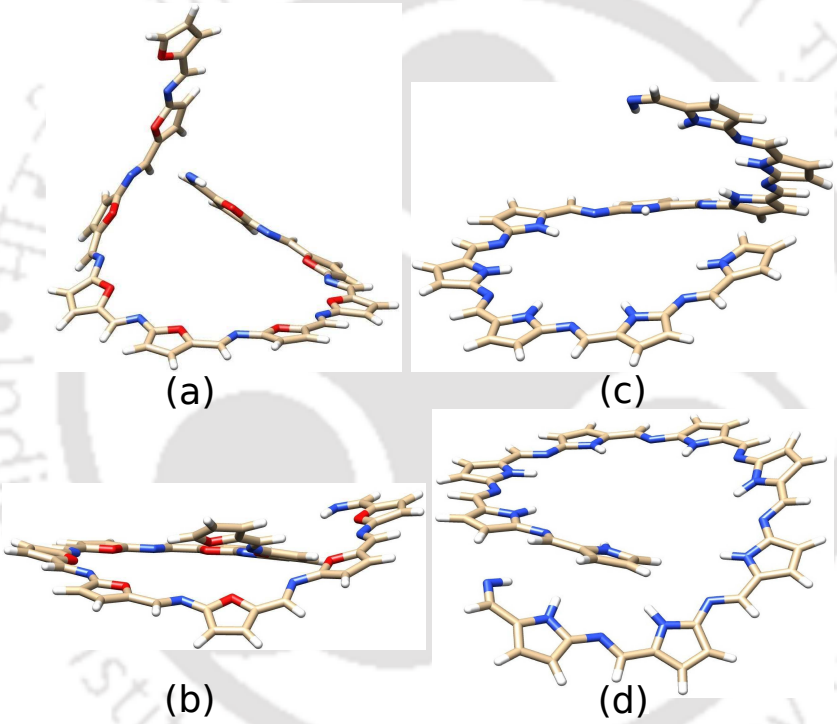

FIGURE 4.3: Ground-state structures of **A**-$(FAm)_9$ and **A**-$(PAm)_9$ optimized at B3LYP/6-31G(d,p) (a, c) and B3LYP-D3/6-31G(d,p) (b, d) levels.

by the two different functionals are shown in Figure 4.3. None of the structures for **A**-$(FAm)_9$ and **A**-$(PAm)_9$ obtained by either of the functionals are helical, unlike the vinylene-linked compounds. This is due to noncovalent interactions between different parts of these oligomers. A representation of the interunit dihedral angle of conformer **A** is shown in Figure 4.1. For **A**-$(TAm)_2$, the dihedral angle (ϕ) between the two monomers is $\sim$ -25.7° for both the functionals. As a result, successive addition of repeating units

leads to a helix-like structure, similar to the helical conformer of polythiophene[225]. Figure 4.4 shows that helical structures of **A**-$(TAm)_{10}$ obtained by both the functionals

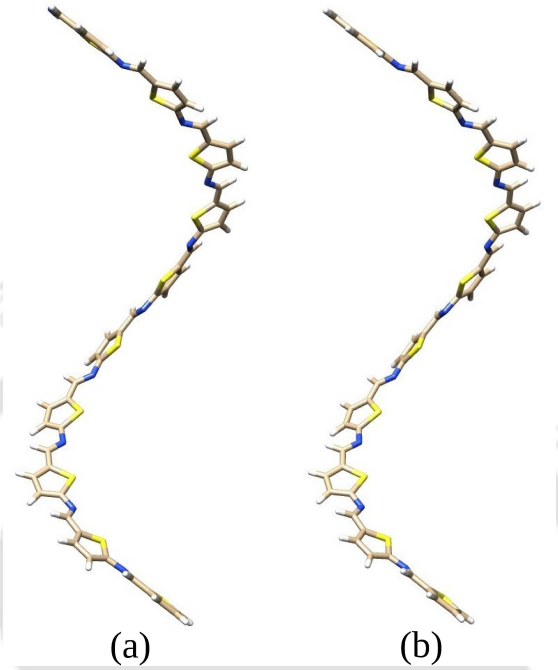

FIGURE 4.4: Ground-state structures of **A**-$(TAm)_{10}$ optimized at B3LYP/6-31G(d,p) (a) and B3LYP-D3/6-31G(d,p) (b) levels.

are similar. Interunit dihedral angles of **A**-$(TAm)_5$ and **A**-$(TAm)_{10}$ obtained at the B3LYP-D3/6-31G(d,p) level are listed in Table 4.1. As reported in the table, interunit dihedral angles of these two oligomers are $\sim$ 25-27°, which are close to the value for **A**-$(TAm)_2$. Although not shown, dihedral angles of B3LYP optimized structures are similar to those for B3LYP-D3 results. From the above, except in the case of TAm oligomers, it is clear that B3LYP-D3 and B3LYP functionals behave very differently from each other while predicting the structures for conformer **A**, and this may be a result of noncovalent interactions[227,228] that is taken care of in the B3LYP-D3 functional.

All the linearly conjugated oligomers obtained by B3LYP and B3LYP-D3 functionals are planar, except those of **B**-TAm oligomers. Structures of planar oligomers are similar to those for **B**-$(FV)_9$ and **C**-$(FV)_9$ shown in Figure 4.5(a,b). The structure of **B**-$(TAm)_{10}$ obtained at the B3LYP-D3/6-31G(d,p) level is shown in the same Figure. For **B**-TAm oligomers, noticeable interunit dihedral angles are observed. The dihedral angle

TABLE 4.1: Calculated interunit dihedral angles (ϕ_{1-9}) of **A**-(TAm)$_n$ and **B**-(TAm)$_n$ at the B3LYP-D3/6-31G(d,p) level, where $n = 5$ and 10. All angles are in degrees.

dihedral angles	**A**-(TAm)$_5$	**A**-(TAm)$_{10}$	**B**-(TAm)$_5$	**B**-(TAm)$_{10}$
ϕ_1	−27.3	−27.6	23.7	24.3
ϕ_2	−25.5	−25.9	−20.8	−21.6
ϕ_3	−25.4	−26.2	21.0	21.6
ϕ_4	−25.0	−26.3	−23.2	−21.5
ϕ_5		−26.3		21.8
ϕ_6		−26.1		−21.5
ϕ_7		−26.0		21.5
ϕ_8		−25.8		−21.6
ϕ_9		−25.2		23.4

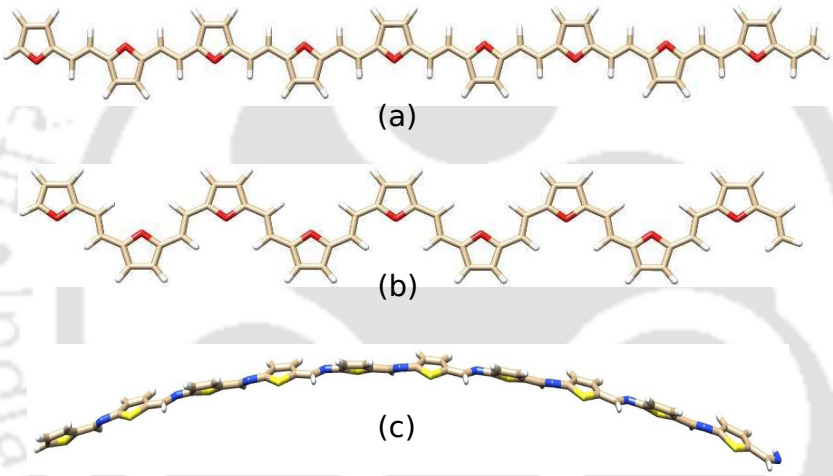

FIGURE 4.5: Ground-state structures **B**-(FV)$_9$, **C**-(FV)$_9$, and **B**-(TAm)$_{10}$ optimized at the B3LYP-D3/6-31G(d,p) level.

between two adjacent repeating units for **B**-(TAm)$_2$ is 24.9°, for both the functionals. The existence of similar dihedral angles in the structures of other **B**-TAm oligomers makes these nonplanar. A careful inspection of interunit dihedral angles of **B**-(TAm)$_5$ and **B**-(TAm)$_{10}$ in Table 4.1 shows that terminal dihedral angles are comparatively larger than other dihedral angles.

Stabilities of different conformers were calculated with respect to the conformer **A**, and the results obtained for vinylene and azomethine-linked oligomers are depicted in Figures 4.6 and 4.7, respectively. In Figure 4.6, B3LYP results show that **C** is the most preferred conformer for all the vinylene-linked oligomers. The stability of this conformer

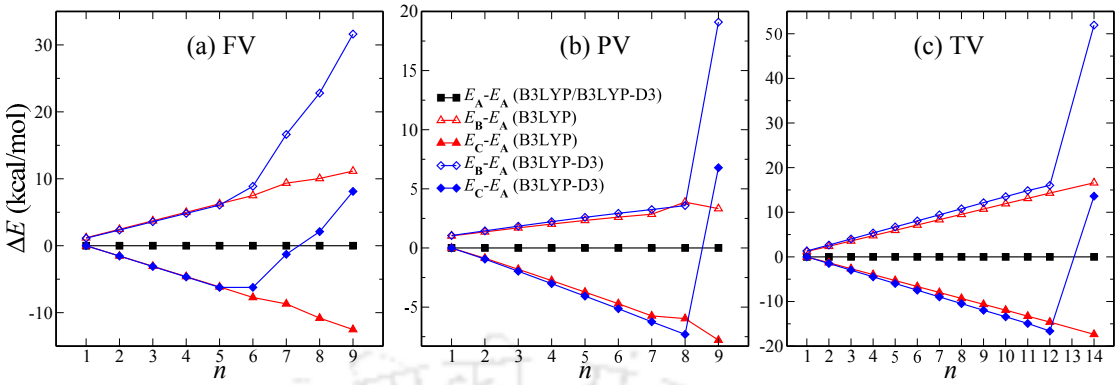

FIGURE 4.6: Energies of different conformers with respect to that of conformer **A**. (a), (b) and (c) show the results for $(FV)_n$, $(PV)_n$ and $(TV)_n$, respectively. Results are shown for B3LYP and B3LYP-D3 functionals. Here, n is the number of repeating units.

gradually increases with the increase in chain length. For B3LYP-D3, similar results are obtained for $(FV)_{1-7}$, $(PV)_{1-8}$ and $(TV)_{1-12}$. However, unlike the B3LYP results, the helical structures of $(FV)_{8-9}$, $(PV)_9$ and $(TV)_{14}$ are found to be the most stable conformers. Figure 4.7 shows that **C** and **A** conformers of FAm and PAm, respectively, are the most stable conformers for both the functionals. Stabilities of these conformers do not vary regularly with the size of oligomers. For TAm oligomers, results are similar for both the functionals. Conformer **C** is the most stable structure, and its stability gradually increases with the increase of chain length.

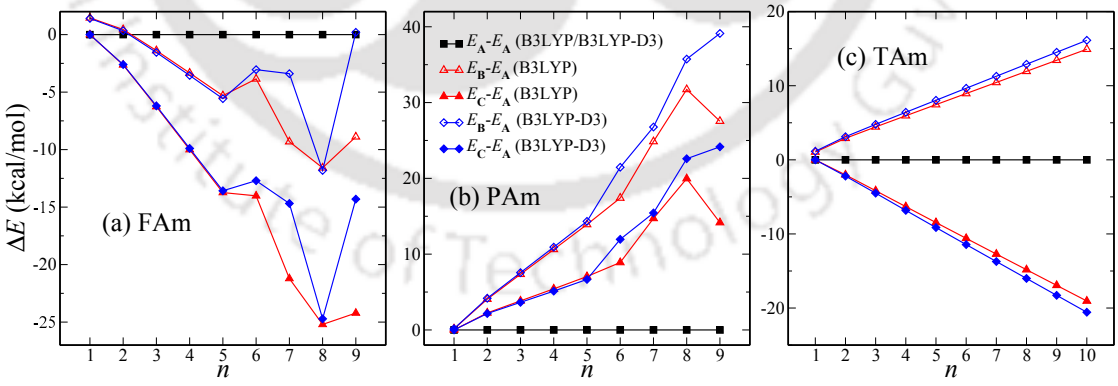

FIGURE 4.7: Energies of different conformers with respect to that of conformer **A**. (a), (b) and (c) show the results for $(FAm)_n$, $(PAm)_n$ and $(TAm)_n$, respectively. Results are shown for B3LYP and B3LYP-D3 functionals. Here, n is the number of repeating units.

Noncovalent interactions play an important role in stabilizing the folding of oligomers.[50]

To check the performance of the two DFT functionals considered in this work, interaction energies between the overlapping regions of the helix are calculated at B3LYP-D3 optimized geometries for all the studied helical oligomers. The rest of the oligomer was ignored during this calculation. Single point calculations were carried out for this overlapping region which can be considered as a "π-stacked" system, in addition to computing the single point energies of the individual fragments. Interaction energies were calculated using the supermolecular approach as $E_{\text{int}} = E_{\text{AB}}^{\text{AB}}$ - ($E_{\text{A}}^{\text{A}} + E_{\text{B}}^{\text{B}}$) and these were later corrected for the basis set superposition error (BSSE) to give $E_{\text{int}}^{\text{CP}} = E_{\text{AB}}^{\text{AB}}$ - ($E_{\text{A}}^{\text{AB}} + E_{\text{B}}^{\text{AB}}$). E_{X}^{Y} is the energy of fragment X with basis set of Y. These energies calculated using both the B3LYP and B3LYP-D3 functionals in combination with the 6-31G(d,p) basis set are reported in Table 4.2. Negative and positive values of E_{int} and $E_{\text{int}}^{\text{CP}}$ indicate stabilization and destabilization of this π-stacked system in comparison to the individual entities, respectively. This, as a result, points at the effect of noncovalent interaction between adjacent helical turns of a helix. Results of the B3LYP-D3 functional for all the systems, except **A**-$(\text{TAm})_{10}$, exhibit the fact that the π-π interaction between adjacent helical turns helps in stabilizing the systems. In the case of **A**-$(\text{TAm})_{10}$, there is no interaction between the adjacent helical turn due to its large pitch (32.7 Å). It is to be mentioned that basis set used in this study is not very large, and uncorrected results show strong noncovalent interactions between helical turns for all the systems. Compared to the B3LYP-D3 results, interaction energies obtained by the B3LYP functional are either very small or even positive. The poor performance of the B3LYP functional on the prediction of the dispersion interaction is already mentioned in the literature.[50,94,96] From now onwards, all the discussion will be based on the optimized structures predicted at the B3LYP-D3/6-31G(d,p) level.

Diameter, pitch (p), number of repeating units needed to complete one helical turn (u) and rise per repeating unit (d) of the largest helical oligomer of each compound are listed in Table 4.2. Diameters of **A**-$(\text{FV})_9$ and **A**-$(\text{PV})_9$ are nearly the same, i.e., 16.47 and 17.64 Å, respectively. For this reason, both have the same number of repeating units in one helical turn. **A**-$(\text{TV})_{14}$ and **A**-$(\text{TAm})_{10}$ oligomers have the largest and the

TABLE 4.2: Interaction energies between the overlapping regions and geometrical parameters of helical oligomers. E_{int} and E_{int}^{CP} represent the uncorrected and BSSE corrected interaction energies, respectively. Values of interaction energies calculated at B3LYP-D3/6-31G(d,p) and B3LYP/6-31G(d,p) levels are shown. p, u and d represent pitch, number of repeating units per turn and rise per repeating unit, respectively.

helices	E_{int}/E_{int}^{CP} (kcal/mol)		diameter (Å)	pitch (Å)	u	$d = (p/u)$
	B3LYP-D3	B3LYP				
A-$(FV)_9$	-34.87/-11.41	-9.81/13.81	16.47	3.5	7	0.50
A-$(PV)_9$	-25.97/-11.43	-12.28/2.37	17.64	4.0	7	0.57
A-$(TV)_{14}$	-46.41/-24.77	1.44/23.21	25.55	3.4	11	0.31
A-$(TAm)_{10}$	-0.01/-0.07	-0.01/-0.07	11.18	32.7	8	4.09

smallest diameters having values of 25.55 and 11.18 Å, respectively. Requirement of 11 repeating units to complete one helical turn leads to a large diameter for **A**-$(TV)_{14}$. The helix pitch is the largest for **A**-$(TAm)_{10}$ and is the smallest for **A**-$(TV)_{14}$. Accordingly, rise per repeating unit (d), defined as p/u, is the largest for **A**-$(TAm)_{10}$ and is the smallest for **A**-$(TV)_{14}$.

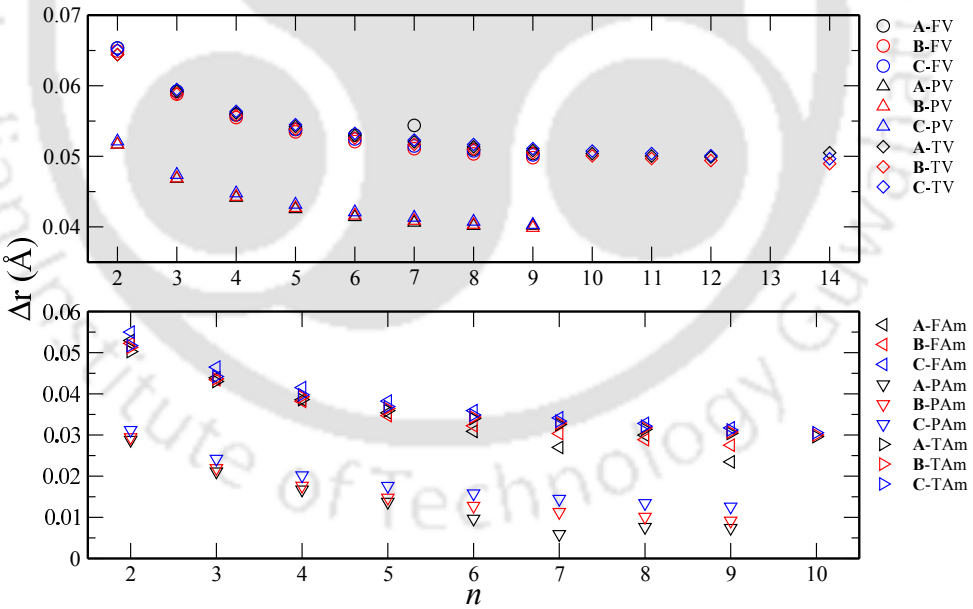

FIGURE 4.8: Δr values of all the studied oligomers. Here, Δr = C-C_{avg} – C=C_{avg} and n is the number of repeating units.

Δr values are calculated for all the studied compounds and plotted in Figure 4.8. Δr is the difference between the average of carbon-carbon single and double bond lengths along

the π-conjugation path. Pyrrole based oligomers connected by different linkages have smaller Δr values compared to the values obtained for respective furan and thiophene carrying oligomers. Δr values for furan and thiophene based oligomers are nearly the same. Further, differences in Δr values between different conformers of an oligomer are not significant.

TABLE 4.3: μ_g values of **A**, **B** and **C** conformers for FV, PV and TV oligomers calculated at the B3LYP-D3/6-31G(d,p) level.

	FV			PV			TV		
n	**A**	**B**	**C**	**A**	**B**	**C**	**A**	**B**	**C**
1	0.79	0.65	0.79	1.36	1.83	1.36	0.79	0.62	0.79
2	1.29	0.35	0.37	2.33	0.91	1.01	1.50	0.23	0.30
3	1.53	0.72	0.87	2.95	2.01	1.62	2.15	0.64	0.86
4	1.46	0.44	0.49	3.19	1.18	1.31	2.71	0.29	0.40
5	1.12	0.76	0.92	3.01	2.10	1.76	3.12	0.66	0.90
6	0.22	0.48	0.54	2.43	1.29	1.43	3.38	0.31	0.45
7	1.38	0.78	0.94	1.53	2.15	1.82	3.44	0.66	0.91
8	1.38	0.49	0.57	2.97	1.33	1.48	3.33	0.32	0.47
9	1.64	0.79	0.95	2.54	2.16	1.85	3.03	0.67	0.92
10							2.58	0.32	0.48
11							1.98	0.67	0.93
12							2.13	0.33	0.48
14							2.56	0.32	0.49

To check the dependency of dipole moment on three different conformers considered in this work, values of μ_g calculated at the B3LYP-D3/6-31G(d,p) level for all the studied compounds are listed in Tables 4.3 and 4.4. In the case of our studied systems, heteroatoms of adjacent rings are either on the same side (as in **A**) or on the opposite sides (as in **B** and **C**) of the linkage. Hence, it is expected that **B** and **C** conformers would have smaller μ_g values as a result of cancellation of oppositely oriented bond dipole moments than that of **A**. The same is observed in the Table 4.3 for the longest chain of vinylene-linked conformers, although the differences between the μ_g values are small. However, as has been discussed, **A** adopts a folded form after a certain chain length, and this structure may decide the trend of variations of μ_g between **A**, **B** and **C**. Apparently, a clear correlation is obtained between the chain length and μ_g values for **A** conformers as reported in Table 4.3. In cases of **A** oligomers, the μ_g value increases up

to certain n, and then it starts to decrease. The dipole moment becomes the smallest once a folded structure is formed. This decrease is certainly the result of cancellation of individual bond dipole moments because of the adoption of a folding structure. After completion of a helical turn, μ_g values of these oligomers again start to increase as is observed in cases of $(FV)_9$, $(PV)_9$ and $(TV)_{14}$ in Table 4.3. In these systems, there are more repeating units than needed to complete one helical turn. In cases of **B** and **C** conformers reported in Table 4.3, μ_g values for oligomers with odd n are larger compared to that for the oligomer with even n. The presence of extra rings and extra heteroatoms in the case of odd n structures explains this trend. Variations of the μ_g as a function of chain length for azomethine-linked oligomers are reported in Table 4.4. Form the

TABLE 4.4: μ_g values of **A**, **B** and **C** conformers for FAm, PAm and TAm oligomers calculated at the B3LYP-D3/6-31G(d,p) level.

	FAm			PAm			TAm		
n	**A**	**B**	**C**	**A**	**B**	**C**	**A**	**B**	**C**
1	3.45	3.31	3.45	3.05	3.39	3.06	3.30	3.13	3.30
2	6.16	5.21	3.27	4.08	5.82	3.85	6.00	5.14	4.15
3	8.21	7.45	4.91	5.14	8.09	4.90	8.74	7.40	5.85
4	9.00	10.20	5.62	5.69	11.08	6.07	11.04	10.23	7.38
5	8.57	13.25	7.47	5.43	14.09	7.37	12.74	13.24	9.41
6	1.99	16.64	8.74	1.74	17.53	8.74	13.83	16.55	11.35
7	1.99	20.23	10.74	1.41	20.98	10.15	14.74	19.98	13.61
8	8.25	24.04	12.34	3.16	24.69	11.61	15.78	23.53	15.80
9	6.79	28.00	14.46	3.63	28.38	13.11	17.47	27.12	18.20
10							19.84	30.75	20.51

table, it is observed that folding conformers have the smallest μ_g values, while the μ_g values for **B** and **C** are very large in these cases. The presence of azomethine linkages in the main chain results in large dipole moment values in the case of linearly conjugated oligomers, while cancellation of bond dipole moments in cases of folded structures leads to a smaller μ_g values than those for **B** and **C**. It is worth mentioning that in cases of FAm and PAm oligomers, results similar to those for vinylene-linked species are observed for the **A** conformers, although **A** conformers of these compounds are not strictly helical as mentioned before. However, in contrast to other helical oligomers, the μ_g value of TAm oligomers increases with increasing n. As a consequence of larger pitch, the cancellation

of individual bond dipole moments effectively gets reduced, and this leads to an increase of the μ_g value per addition of a repeating unit. For **B** and **C** oligomers, μ_g values increase with an increase in chain length in most of the cases.

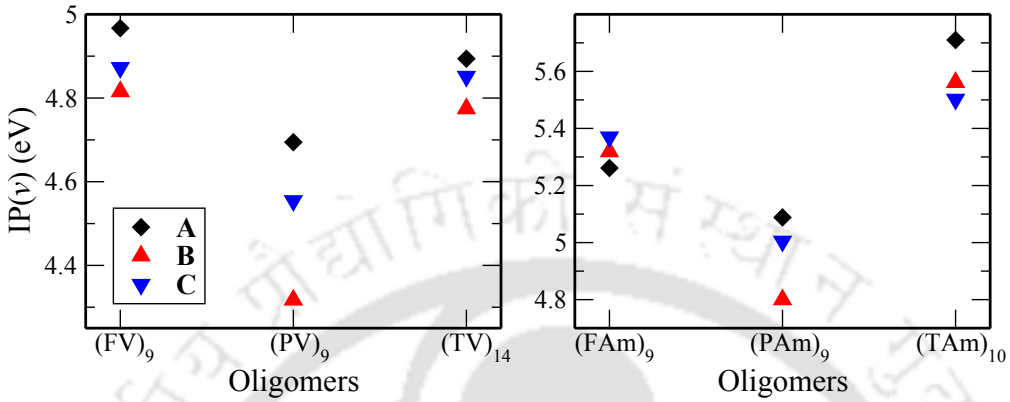

FIGURE 4.9: IP(v)s of the longest oligomers of studied vinylene- and azomethine-linked compounds calculated at the B3LYP-D3/6-31G(d,p) level.

Figure 4.9 shows the variation of IP(v) with the change of conformer for the longest chain of the studied vinylene- and azomethine-linked heterocyclic oligomers. It can be seen from the figure that for the vinylene-linked compounds, the IP(v)s of the helical conformers are larger compared to the other conformers. The IP(v) increases in the order: **B** < **C** < **A**. But the differences between the IP(v) values are very small in cases of $(FV)_9$ and $(TV)_{14}$. However, the IP(v) of $(PV)_9$ seems to depend strongly upon the conformation, and comparatively larger differences between the IP(v)s of different conformers are noticed. As shown, azomethine-linked compounds do not have any general trend. **C**, **A** and **A** have the largest, and **A** , **B** and **C** have the smallest IP(v) values for $(FAm)_9$, $(PAm)_9$ and $(TAm)_{10}$, respectively.

4.2.2 Frontier orbitals, excitation energies, absorption and CD spectra

Values of E_g^{hl} and E_g^{opt} of vinylene- and azomethine-linked oligomers are plotted in Figures 4.10 and A2, respectively. Figures show that there is a gradual decrement in the values of E_g^{hl} and E_g^{opt} with increase in chain length for all the conformers, except for E_g^{opt} of **A**-$(FV)_8$ and E_g^{hl} of **A**-$(TV)_{14}$. For almost all **A** conformers, it is noticed that

deviations in slopes of E_g^{opt} and E_g^{hl} occur when an oligomer starts to form a folding structure. To elucidate this interruption in E_g^{hl}, HOMO and LUMO energies of $(FV)_{6-9}$ are plotted in Figure 4.11. It is observed that E_H and E_L for **B** and **C** conformers follow a certain trend: E_H increases and E_L decreases with increase in the size of chain. However, for **A**, sudden changes in the trends of E_H and E_L occur as the oligomer starts to complete one helical turn. This is a consequence of loss of planarity of the backbone chain as the helix formation starts and this results in breaking the general trend observed for **B** and **C**.

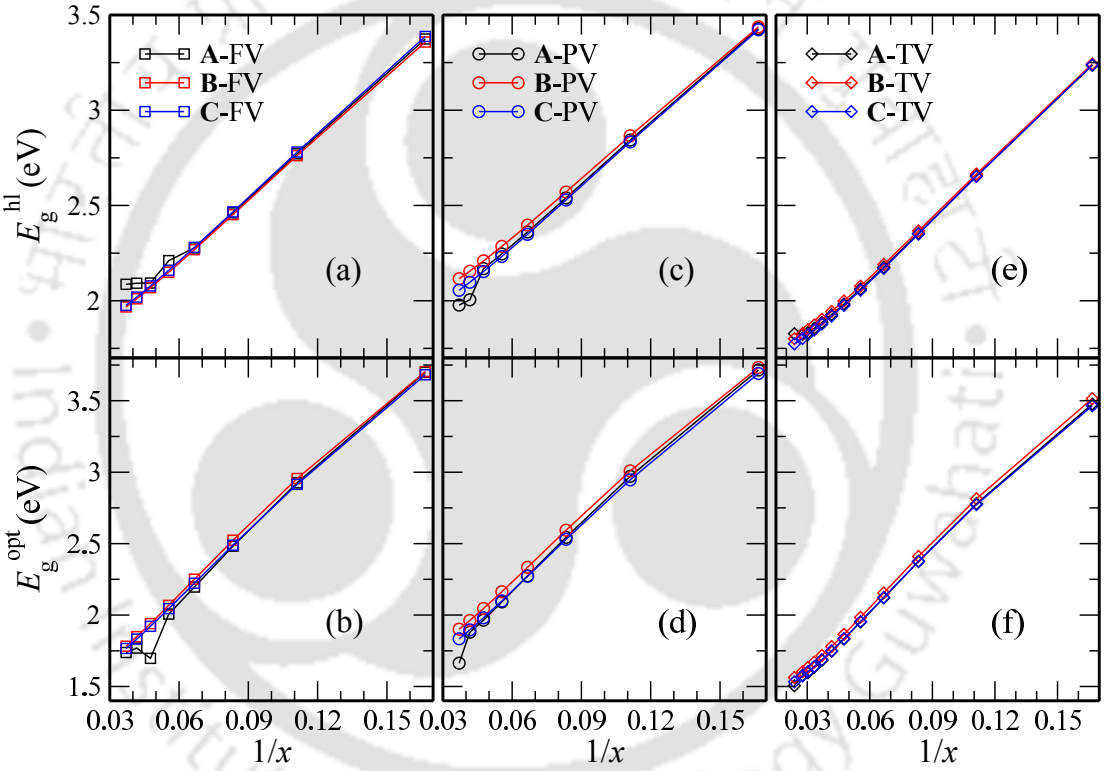

FIGURE 4.10: E_g^{hl} and E_g^{opt} of vinylene-linked oligomers as function of the reciprocal number of the double bonds (x) in oligomers.

Absorption spectra of **A**, **B** and **C** conformers for the longest oligomer of the studied compounds are plotted in Figure 4.12. For each oligomer, the 25 lowest singlet transitions are considered. In these spectra, full-width at half-maximum height (fwhm) is 1500 cm^{-1}. The main feature of these simulated spectra is that the spectra of the **A** conformer are always blue-shifted compared to those of **B** and **C** conformers, in each

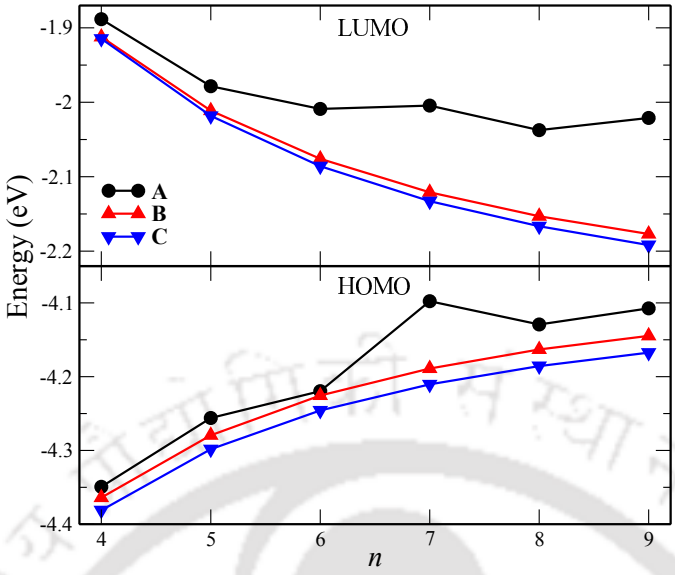

FIGURE 4.11: HOMO and LUMO energies of $(FV)_{4-9}$ of three conformers **A**, **B** and **C**.

case. For all the folding structures, contributions of more than one electronic transitions are significant. In absorption spectra of **B** and **C** conformers, only one electronic transition has the significant contribution in the case of vinylene-linked oligomers. But for most of the azomethine-linked oligomers, contribution of a second electronic transition can not be neglected. The most intense bands of **B** and **C** are very close and in few cases, they overlap.

TABLE 4.5: Electronic transition data for the lowest excitation (S_0 to S_1) obtained by the TDDFT method for **B** and **C** conformers of FV, PV and TV oligomers at the B3LYP/6-31G(d,p) level. The HOMO and LUMO are indicated by H and L, respectively.

conformations	oligomers	E_g (eV)	f_{osc}	configurations
B	$(FV)_9$	1.78	6.70	H $\rightarrow$ L(97%)
	$(PV)_9$	1.90	6.86	H $\rightarrow$ L(96%)
	$(TV)_{14}$	1.56	10.16	H $\rightarrow$ L(89%)
C	$(FV)_9$	1.77	4.53	H $\rightarrow$ L(97%)
	$(PV)_9$	1.83	5.10	H $\rightarrow$ L(96%)
	$(TV)_{14}$	1.53	8.41	H $\rightarrow$ L(89%)

E_gs, f_{osc}s, and configurations involved in all the important transitions for **B** and **C** conformers of $(FV)_9$, $(PV)_9$ and $(TV)_{14}$ are listed in Table 4.5. Similarly, the results

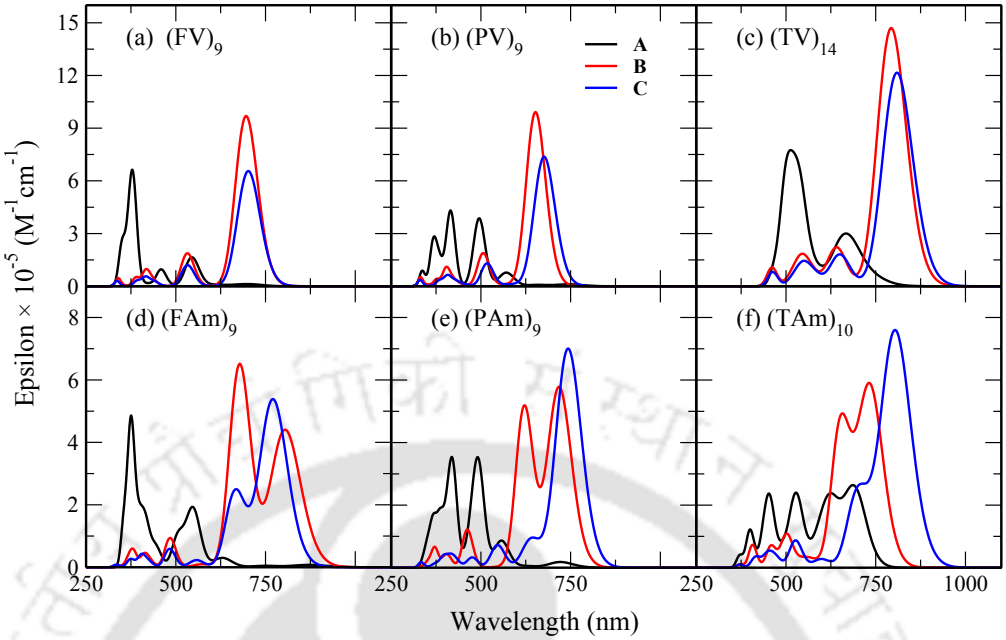

FIGURE 4.12: Simulated UV-Vis spectra of **A**, **B** and **C** conformers for $(FV)_9$ (a), $(PV)_9$ (b), $(TV)_{14}$ (c), $(FAm)_9$ (d), $(PAm)_9$ (e), $(TAm)_{10}$ (f). The fwhm is 1500 cm^{-1}.

for conformers **A** of $(FV)_{n=4,5,9}$, $(PV)_{n=5,6,9}$ and $(TV)_{n=8,14}$ are listed in Table 4.6. These informations for other vinylene-linked oligomers are presented in Tables A2-A5 (see Appendix II). As reported in the Tables 4.5 and A2, for **B** and **C** conformers of vinylene-linked oligomers, the lowest optically allowed electronic transition has the largest oscillator strength. As an example, absorption peaks at 695.9 nm (f_{osc}=6.70) and 702.1 nm (f_{osc}=4.53) for **B** and **C** conformers of $(FV)_9$, respectively, originate from $S_0 \rightarrow S_1$ transitions. All these transitions are dominated by HOMO $\rightarrow$ LUMO excitations. E_g and f_{osc} values decrease and increase, respectively, with an increase in chain length. Additionally, for **B** and **C** conformers of the same chain length, E_g follows the order: $(TV)_n < (FV)_n < (PV)_n$. The results are distinctly different for **A** conformers, as seen in Figure 4.12 and discussed in the previous paragraph. For **A** conformers of $(FV)_{n=1-4}$, $(PV)_{n=1-5}$ and $(TV)_{n=1-8}$, the electronic transition $S_0 \rightarrow S_1$ has the largest oscillator strength. On further addition of repeating units to these oligomers, transitions from the ground-state to higher excited states become prominent transitions. Instead of being HOMO $\rightarrow$ LUMO type excitations, these transitions involve occupied orbitals other than HOMO and unoccupied orbitals other than LUMO. After completion of a helical turn,

TABLE 4.6: Electronic transition data obtained by the TDDFT method for **A** conformers of FV, PV and TV oligomers at the B3LYP/6-31G(d,p) level. The HOMO and LUMO are indicated by H and L, respectively. Electronic transitions are from S_0 to S_m. Transition energies (E_gs) are in eV.

oligomers	m	E_g	f_{osc}	configurations	oligomers	m	E_g	f_{osc}	configurations
$(FV)_4$	1	2.48	1.89	H→L(97%)	$(PV)_5$	1	2.27	2.20	H→L(98%)
	5	3.73	1.83	H−1→L(44%), H→L+1(42%)		5	3.29	2.08	H−1→L(42%), H→L+1(38%)
$(FV)_5$	1	2.20	1.46	H→L(98%)	$(PV)_6$	1	2.09	1.78	H→L(98%)
	5	3.26	2.51	H−1→L(42%), H→L+1(42%)		5	2.97	2.63	H−1→L(40%), H→L+1(37%)
$(FV)_9$	1	1.74	0.07	H→L(86%)		8	3.49	1.04	H−2→L+1(38%), H−3→L(39%)
	16	3.21	1.68	H−2→L+4(21%), H−1→L+5(22%)	$(PV)_9$	1	1.66	0.08	H→L(97%)
	17	3.27	1.78	H−3→L(24%), H→L+3(18%)		5	2.49	1.60	H→L+2(39%)
	19	3.32	1.13	H−4→L+2(23%), H−1→L+5(22%)		11	2.95	1.50	H−4→L(22%), H→L+3(16%)
						13	3.03	1.29	H−4→L(25%)
						19	3.38	1.32	H−4→L+1(39%)

oligomers	m	E_g	f_{osc}	configurations
$(TV)_8$	1	1.75	2.78	H → L(97%)
	5	2.38	2.50	H → L+1(30%), H-1 → L(28%)
	8	2.76	1.22	H-2 → L+1(32%), H-1 → L+2(28%)
$(TV)_{14}$	1	1.51	0.01	H-1 → L(54%), H → L+1(43%)
	14	2.29	1.84	H-4 → L+1(56%)
	15	2.35	1.98	H-2 → L+4(29%)
	18	2.46	2.08	H-4 → L+2(26%)
	19	2.51	1.33	H-4 → L+2(48%), H-2 → L+4(26%)

$S_0 \rightarrow S_1$ transitions have negligible oscillator strengths for **A** conformers of vinylene-linked compounds. The main absorption peaks shown in Figure 4.12(a), (b) and (c) for **A**-$(FV)_9$, **A**-$(PV)_9$ and **A**-$(TV)_{14}$ originate from S_0 to $S_{m=16,17,19}$, $S_{m=5,11,13,19}$ and $S_{m=14,15,18,19}$ transitions, respectively.

E_g, f_{osc}s and configurations for all the important electronic transitions for $(FAm)_{n=4,5,9}$, $(PAm)_{n=4,5,9}$ and $(TAm)_{n=4,5,10}$ are reported in Tables 4.7, 4.8 and 4.9, respectively. Results for other azomethine-linked compounds are listed in Tables A6-A11 (see Appendix II). As is the case with vinylene-linked oligomers, $S_0 \rightarrow S_1$ transitions in cases of **C**-(FAm), **B/C**-(PAm) and **B/C**-(TAm) oligomers have the largest oscillator strengths.

TABLE 4.7: Electronic transition data obtained by the TDDFT method for **A**, **B** and **C** conformers of FAm oligomers at the B3LYP/6-31G(d,p) level. The HOMO and LUMO are indicated by H and L, respectively. Electronic transitions are from S_0 to S_m. Transition energies (E_gs) are in eV.

oligomers	m	E_g	f_{osc}	configurations	oligomers	m	E_g	f_{osc}	configurations
A-$(FAm)_4$	1	2.37	1.35	H→L(93%)	**B**-$(FAm)_4$	1	2.40	2.52	H→L(92%)
	2	2.85	0.92	H→L+1(48%)		2	2.80	1.40	H→L+1(50%)
				H−1→L(44%)					H−1→L(41%)
A-$(FAm)_5$	1	2.073	1.01	H→L(96%)	**B**-$(FAm)_5$	1	2.09	2.71	H→L(94%)
	2	2.52	0.91	H→L+1(50%)		2	2.47	2.09	H→L+1(51%)
				H−1→L(45%)					H−1→L(42%)
	5	3.44	2.50	H→L+2(25%)	**B**-$(FAm)_9$	1	1.54	3.04	H→L(98%)
				H−1→L(24%)					
A-$(FAm)_9$	1	1.42	0.05	H→L(96%)		2	1.83	4.50	H→L+1(52%)
									H−1→L(43%)
	5	2.26	1.28	H→L+2(32%)					
	18	3.27	1.48	H−6→L(19%)					
				H−1→L+4(16%)					
	19	3.32	1.63	H−4→L+1(24%)					

oligomers	m	E_g	f_{osc}	configurations
C-$(FAm)_4$	1	2.44	2.31	H → L(95%)
C-$(FAm)_5$	1	2.14	2.61	H → L(96%)
C-$(FAm)_9$	1	1.61	3.71	H → L(98%)
	2	1.86	1.70	H → L+1(49%)
				H-1 → L(47%)

These transitions are assigned to HOMO → LUMO excitations predominantly. Along with the first excitation, $S_0 \rightarrow S_2$ transitions have noticeable oscillator strengths for few of these oligomers. For example, for **C**-$(FAm)_9$, in addition to the major absorption peak at 770.9 nm (f_{osc}=3.71), another peak of medium intensity appears at 667.9 nm (f_{osc}=1.70). This secondary peak arises due to HOMO → LUMO+1 and HOMO–1 → LUMO transitions. However, transitions from S_0 to higher excited states are major transitions for **A**-$(FAm)_{n\geq5}$, **B**-$(FAm)_{n\geq7}$ and **A**-$(PAm)_{n\geq5}$. In these cases, mainly HOMO–N and LUMO+N orbitals are involved. In the case of **A**-TAm oligomers, unlike other folding oligomers, first electronic excitation is one of the major electronic transitions along with a few other important higher excitations. The major absorption peaks for **A**-$(FAm)_9$, **A**-$(PAm)_9$ and **A**-$(TAm)_{10}$ shown in Figure 4.12(d), (e) and (f) are due to S_0 to $S_{m=5,18,19}$, S_5 and $S_{m=1,2,5,10}$ transitions, respectively.

TABLE 4.8: Electronic transition data obtained by the TDDFT method for **A**, **B** and **C** conformers of PAm oligomers at the B3LYP/6-31G(d,p) level. The HOMO and LUMO are indicated by H and L, respectively. Electronic transitions are from S_0 to S_m. Transition energies (E_gs) are in eV.

oligomers	m	E_g	f_{osc}	configurations	oligomers	m	E_g	f_{osc}	configurations
A-$(PAm)_4$	1	2.45	1.49	H→L(95%)	**B**-$(PAm)_4$	1	2.49	2.80	H→L(95%)
	5	3.86	1.28	H−1→L(25%)		2	2.92	1.11	H→L+1(55%)
				H−2→L(21%)					H−1→L(39%)
A-$(PAm)_5$	1	2.18	1.17	H→L(97%)	**B**-$(PAm)_5$	1	2.204	3.085	H→L(96%)
	5	3.43	2.13	H→L+2(24%)		2	2.60	1.69	H→L+1(56%)
				H−1→L(24%)					H−1→L(40%)
A-$(PAm)_9$	1	1.72	0.13	H→L(93%)	**B**-$(PAm)_9$	1	1.73	3.99	H→L(96%)
	5	2.51	1.61	H→L+2(46%)		2	2.00	3.58	H→L+1(54%)
									H−1→L(39%)

oligomers	m	E_g	f_{osc}	configurations
C-$(PAm)_4$	1	2.46	2.73	H → L(98%)
C-$(PAm)_5$	1	2.17	3.21	H → L(98%)
C-$(PAm)_9$	1	1.67	4.84	H → L(96%)

TABLE 4.9: Electronic transition data obtained by the TDDFT method for **A**, **B** and **C** conformers of TAm oligomers at the B3LYP/6-31G(d,p) level. The HOMO and LUMO are indicated by H and L, respectively. Electronic transitions are from S_0 to S_m. Transition energies (E_gs) are in eV.

oligomers	m	E_g	f_{osc}	configurations	oligomers	m	E_g	f_{osc}	configurations
A-$(TAm)_4$	1	2.36	1.52	H→L(96%)	**B**-$(TAm)_4$	1	2.36	2.21	H→L(95%)
	2	2.86	1.10	H−1→L(49%)		2	2.82	1.22	H→L+1(49%)
				H→L+1(46%)					H−1→L(46%)
A-$(TAm)_5$	1	2.14	1.54	H→L(98%)	**B**-$(TAm)_5$	1	2.11	2.52	H→L(97%)
	2	2.571	1.363	H−1→L(49%)		2	2.520	1.728	H−1→L(46%)
				H→L+1(48%)					H→L+1(49%)
A-$(TAm)_{10}$	1	1.79	1.72	H→L(78%)	**B**-$(TAm)_{10}$	1	1.69	3.97	H→L(86%)
	2	1.978	1.318	H−1→L(33%)		2	1.897	3.259	H→L+1(42%)
				H→L+1(38%)					H−1→L(38%)
	5	2.34	1.28	H−2→L(52%)					
				H→L+2(44%)					
	10	2.71	1.15	H→L+3(38%)					
				H−3→L(29%)					

oligomers	m	E_g	f_{osc}	configurations
C-$(TAm)_4$	1	2.35	2.77	H → L(97%)
C-$(TAm)_5$	1	2.08	3.23	H → L(97%)
C-$(TAm)_{10}$	1	1.54	5.23	H → L(94%)
	2	1.77	1.73	H-1 → L(47%)
				H → L+1(45%)

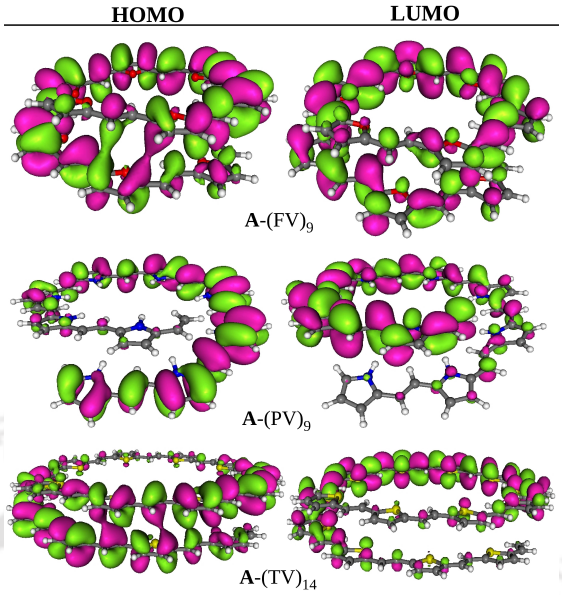

FIGURE 4.13: Electron distributions in HOMOs and LUMOs of **A** conformers of $(FV)_9$, $(PV)_9$ and $(TV)_{14}$.

The magnitude of the oscillator strength of an electronic transition is directly proportional to the degree of spatial overlap of orbitals involved in that transition.[172,229–232] Thus, it is instructive to look at the electron density in molecular orbitals. Electron distributions in HOMOs and LUMOs of few selected vinylene-linked **A** oligomers are shown in Figure 4.13 and those of **B** and **C** conformers are shown in Figure 4.14. As can

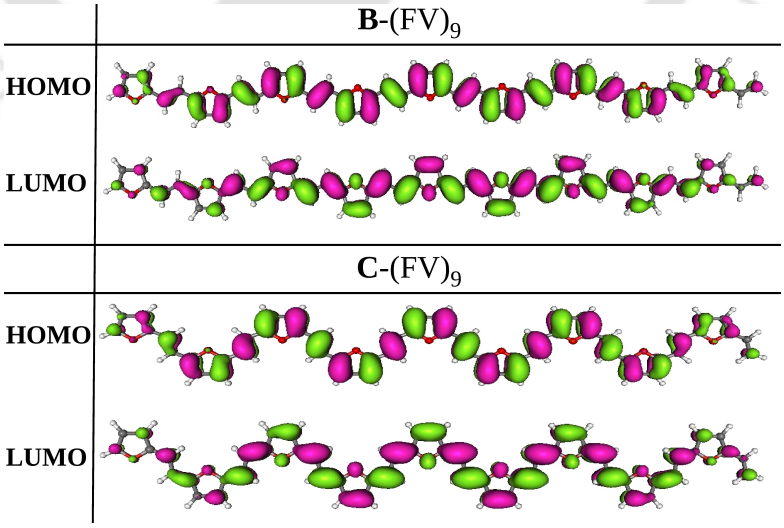

FIGURE 4.14: Electron distribution in HOMO and LUMO of **B**-$(FV)_9$ and **C**-$(FV)_9$.

be seen, in HOMOs and LUMOs of **B** and **C** conformers of $(FV)_9$, π electrons are spread over the entire chain having large electron density in the middle of the oligomer. Similar results are noticed for **B** and **C** conformers of $(PV)_9$ and $(TV)_{14}$. Thus, overlapping of electron density between HOMO and LUMO is quite large for these oligomers and the main absorption peaks are dominated by HOMO $\rightarrow$ LUMO transitions. However, a much different organization is observed for **A** conformers of these oligomers. Although π electrons in HOMO and LUMO of **A**-$(FV)_9$ are spread over the entire helical chain, larger electron density is found at the overlapping region of adjacent helical turns for the HOMO compared to that in the LUMO of the oligomer. In **A**-$(PV)_9$, the HOMO is localized at one end of the helix, while the LUMO localized at the other end of the helix. In the HOMO of **A**-$(TV)_{14}$, the overlapping region has larger electron density than the nonoverlapping region, and in the LUMO, π electrons are mainly accumulated over the nonoverlapping region. Thus, the degree of electron density overlapping between HOMO and LUMO for **A** conformers of these compounds is quite small, in comparison to those for the **B** and **C** conformers. This results in decreasing the involvement of HOMOs and LUMOs toward major absorption peaks in cases of **A** conformers, and contributions of HOMO$-N$ and LUMO$+N$ orbitals become prominent for these transitions.

CD spectra of **A**, **B** and **C** conformers for the longest oligomer of each of our studied compounds are depicted in Figure 4.15. It is observed that all four helical oligomers, **A**-$(FV)_9$, **A**-$(PV)_9$, **A**-$(TV)_{14}$ and **A**-$(TAm)_{10}$ are CD active having strong positive and negative Cotton effects. In addition, **A**-$(PAm)_9$ with an irregular folding structure is also optically active. As expected, all linearly conjugated conformers of the studied oligomers are found to be CD inactive. It is worth mentioning that CD spectra are sensitive to basis sets and DFT functionals, and the present study only highlights the fact that few of the studied oligomers are optically active.

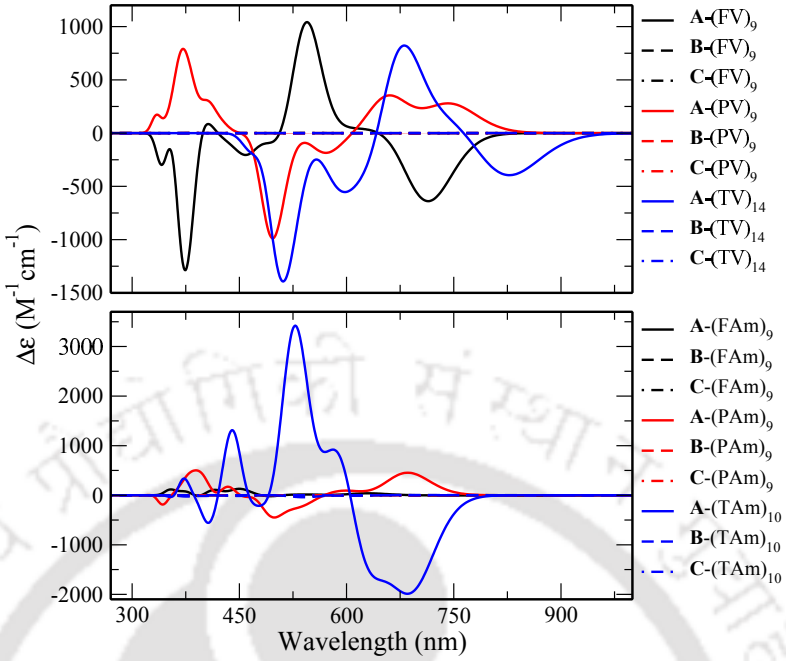

FIGURE 4.15: CD spectra of **A**, **B** and **C** conformers for $(FV)_9$, $(PV)_9$, $(TV)_{14}$, $(FAm)_9$, $(PAm)_9$, $(TAm)_{10}$. Results are obtained at the TDDFT/B3LYP/6-31G(d,p) level.

4.3 Salient findings

In this chapter, structural and optoelectronic properties of vinylene- and azomethine-linked furan-, pyrrole- and thiophene-based oligomers are explored. Three different conformers are considered for each oligomer, and out of these three, one form folded structures. Our results show that the B3LYP functional fails to predict the ground-state geometries of studied foldamers, expect in the case of TAm oligomers. However, the B3LYP-D3 functional is suitable for this purpose as it takes care of the dispersion interactions, while the B3LYP does not. As a result of these interactions, the order of stabilities of conformers change with increasing chain length, and for long oligomers, helices are more stable than the corresponding linear conformers. However, in the case of TAm oligomers, a linear conformer is comparatively more stable than the helical one due to the lack of $\pi - \pi$ interaction between adjacent helical turns. In FAm and PAm,

the formation of hydrogen bonds between two terminal units results in nonhelical structures. Optoelectronic properties of the studied foldamers are quite different from those for linear conformers. Absorption bands of these foldamers are blue-shifted with respect to the absorption bands of the corresponding linear conformers. In the case of linear conformers, the first allowed electronic transition is the prominent transition, and in some cases of azomethine-linked oligomers, transitions other than the S_0 to S_1 transition have significant oscillator strengths. In most of the transitions, HOMO and LUMO orbitals are mainly involved. However, in foldamers, more than one electronic transition has significant contributions in absorption spectra. These electronic transitions are transitions from S_0 to higher electronic excited states. Instead of HOMO and LUMO orbitals, HOMO–N and LUMO+N orbitals are mainly involved in these major electronic transitions. Unlike other foldamers, for TAm, the first electronic transitions have significant oscillator strengths in addition to other important electronic transitions, and in most of the cases, it is the most important electronic transition. This study suggests that helical π-conjugated heterocyclic oligomers, especially vinylene-linked oligomers, are interesting systems with quite strong CD signals for chiral conjugated materials.

Pyridine–furan/pyrrole/thiophene oligomers: Geometries and optoelectronic properties of helical conformers

This chapter reveals the structural and optoelectronic properties helical conformers of pyridine-furan, pyridine-pyrrole and pyridine-thiophene oligomers. The contents of this chapter are published in the following paper:

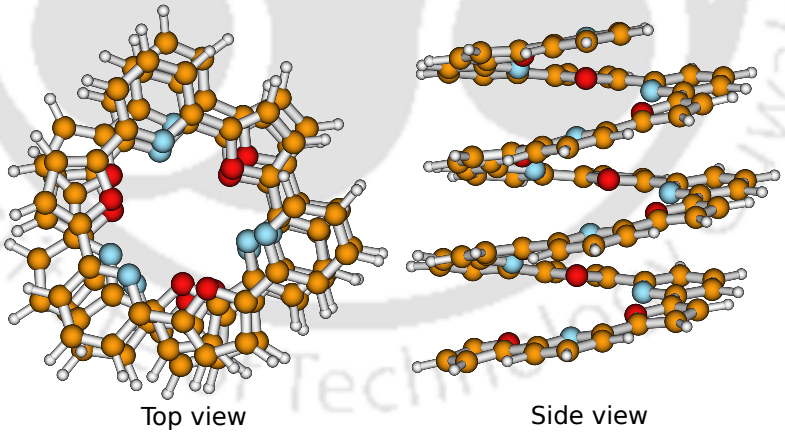

Figure: Helical conformer of pyridine-furan decamer.

- H. Sahu, S. Gupta, P. Gaur and A. N. Panda, *Phys. Chem. Chem. Phys.*, **2015**, 17, 20647.

Copolymers containing alternate electron-deficient pyridine and electron-rich furan or pyrrole or thiophene heterocyclic rings and their derivatives have already been synthesized.[233–240] Some of the synthesized compounds are brightly luminescent, even in the solid state[233,234]. Presence of pyridine in these systems assists in the modulation of optical properties after synthesis.[233,234,241] These type of systems, where a monomer consists of alternating six-membered and five-membered heterocyclic rings connected *via* carbon atoms neighboring the hetero atoms, are expected to form helix/coil-like structures with the increase of chain length.[235,236] Some interesting phenomena are observed for alternated pyridine–ethylenedioxythiophene oligomer.[236] For example, in addition to the bathochromic shift of the lowest energy absorption band, intensities of additional absorption bands at higher energy are found to progressively increase with increasing length. The fluorescence quantum yield was also found to increase with an increase in chain length. This result was suggested to be related to a reduction of torsion in the excited state resulting in a decrease in non-radiative decay. These findings in the case of pyridine–ethylenedioxythiophene indicate that coiled structures of pyridine-furan/pyrrole/thiophene oligomers may also have interesting optoelectronic properties. However, to the best of our knowledge, these types of systems are not yet studied. Keeping this in mind, a systematic conformational analysis was carried out for oligomers of these systems. As non-bonding interactions are important factors for the stabilization of helices, the B3LYP-D3 functional, in addition to B3LYP, has been used for large oligomers. Non-bonding interaction energies are calculated for both the functionals to check the effect of dispersion correction on the structure and stability of these structures. To characterize their geometries, inner and outer diameters, pitch, number of repeating units needed to complete one helical turn, rise per repeating unit and bond length alternation values are calculated. In addition, ground state dipole moments, ionization potentials, excitation energies, oscillator strengths and absorption spectra of these compounds were evaluated to reveal their ground and excited state properties. In section 5.1, computational aspects are briefly discussed. This is followed by results and discussion in section 5.2 and conclusions in 5.3.

5.1 Computational details

All calculations were carried out using the Gaussian 09 package.[242] With the exception of $(PF)_{24}$, ground state geometries of all other studied compounds were fully optimized using B3LYP and B3LYP-D3 functionals combined with the 6-31G(d) basis set. In B3LYP-D3, the original D3 damping function was used with the D3 version of dispersion, as mentioned in subsection 2.2.4. Ground state properties of $(PF)_{24}$ were obtained by carrying out a single point calculation at the B3LYP-D3/6-31G(d) level with the optimized geometry computed at the B3LYP/3-21G level. To check the effects of various functionals and basis sets on the ground state structures and their stabilities, along with the above level of theories, CAM-B3LYP and M06-2X functionals in combination with the 6-31G(d) basis set and the B3LYP functional in combination with the 6-31++G(d,p) basis set were used to optimize ground state structures of monomers and dimers. Harmonic vibrational analysis was performed subsequently on the optimized structures of monomers and dimers to characterize the nature of stationary points. Relaxed torsional potentials were calculated for each monomer as a function of the inter-ring C–C dihedral angle ($\theta = \angle$ 1-2-3-4, see Figure 5.1), which was varied between 0° and 180° in steps of 15°. Vertical excitation energies and oscillator strengths were calculated by performing single point TDDFT studies using the B3LYP-D3 functional with the same basis set that was used to optimize the ground state geometries at B3LYP-D3. Absorption and CD spectra are obtained from these TDDFT studies.

5.2 Results and discussion

A representative structure of repeating units of the studied oligomers is shown in Figure 5.1. As shown in the figure, these oligomers consist of alternate pyridine and 5-membered heterocyclic rings connected through carbon atoms neighboring the hetero atoms of these rings. Pyridine-furan, pyridine-pyrrole and pyridine-thiophene oligomers are denoted by PF, PP and PT, respectively. Our studied oligomers are represented by the following

abbreviation: conformation-(PF/PP/PT)$_n$. Here, n is the number of repeating units. Different conformations of our studied oligomers are discussed below.

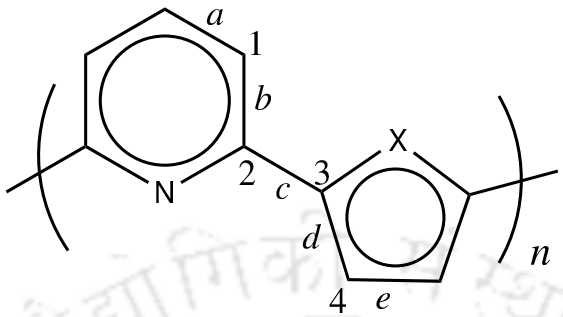

compounds	PF	PP	PT
X	O	NH	S

FIGURE 5.1: A representative structure of repeating units of the studied molecules, where $n = 1, 2, \ldots$. $\angle$ 1-2-3-4 is the inter-ring C–C dihedral angle (denoted as θ). a, b, c d and e are alternate C–C and C=C bonds.

5.2.1 Effect of functionals on the geometries and their stabilities

In monomers, two heterocyclic rings are connected by a single bond. So, there are two possible structures for each monomer: hetero atoms of two heterocyclic rings are located either on opposite sides (denoted as ***i***) or on same sides (denoted as ***ii***). Optimized structures of two conformers for (PF)$_1$ calculated at the B3LYP-D3/6-31G(d) level are shown in Figure 5.2. To check the stability of these isomers, B3LYP, CAM-B3LYP, B3LYP-D3 and M06-2X functionals combined with the 6-31G(d) basis set were used to optimize their ground state structures. Optimized structures of all monomers are planar. Absence of imaginary frequency shows that all are stable ground state structures. Differences in energies between the two isomers are plotted in Figure 5.3. As shown in the figure, all the functionals produce similar results. Conformer ***i*** of (PF)$_1$, and ***ii*** of (PP)$_1$ and (PT)$_1$ are comparatively more stable than the other possible conformer in each case. Differences in energies between two isomers are the largest and the smallest for (PP)$_1$ and (PT)$_1$, respectively. Furthermore, these differences are nearly the same

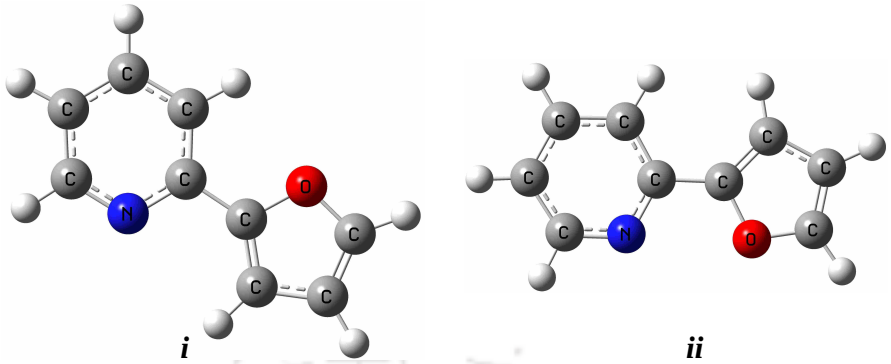

FIGURE 5.2: Optimized structures of two conformers of $(PF)_1$ obtained at the B3LYP-D3/6-31G(d) level.

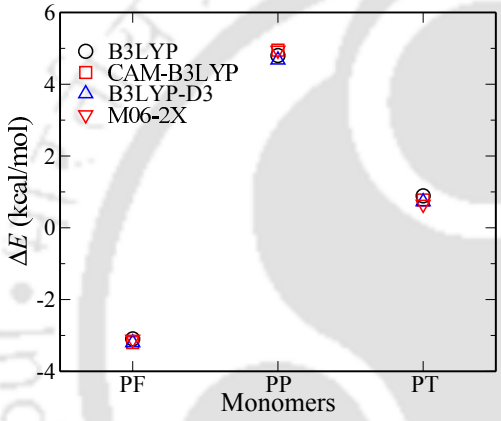

	PF	PP	PT
B3LYP	-3.1	4.8	0.9
CAM-B3LYP	-3.2	5	0.8
B3LYP-D3	-3.2	4.7	0.7
M06-2X	-3.1	5	0.7

FIGURE 5.3: Differences in energies (ΔE) between the two possible conformations (i.e., $E_{\boldsymbol{i}} - E_{\boldsymbol{ii}}$) of monomers calculated using B3LYP, CAM-B3LYP, B3LYP-D3 and M06-2X functionals in combination with the 6-31G(d) basis set. Structures of conformations ***i*** and ***ii*** for $(PF)_1$ are shown in Figure 5.2. Calculated values are tabulated on the right hand side of the figure and all are in kcal/mol.

for all the functionals. Ground state structures of monomers were also optimized at the B3LYP/6-31++G(d,p) level and results are found to be similar to those at the B3LYP/6-31G(d) level.

For each monomer, torsional potentials were calculated with respect to inter-ring C–C dihedral angle ($\theta = \angle$ 1-2-3-4, see Figure 5.1) varying between 0° to 180° with a step of 15°. B3LYP, CAM-B3LYP, B3LYP-D3 and M06-2X functionals combined with the 6-31G(d) basis set, and the B3LYP functional with the 6-31G++(d,p) basis set are the level of theories used for the above calculations. Relaxed torsional profiles of $(PF)_1$, $(PP)_1$ and $(PT)_1$ are shown in Figure 5.4. The figure shows that the torsional profiles

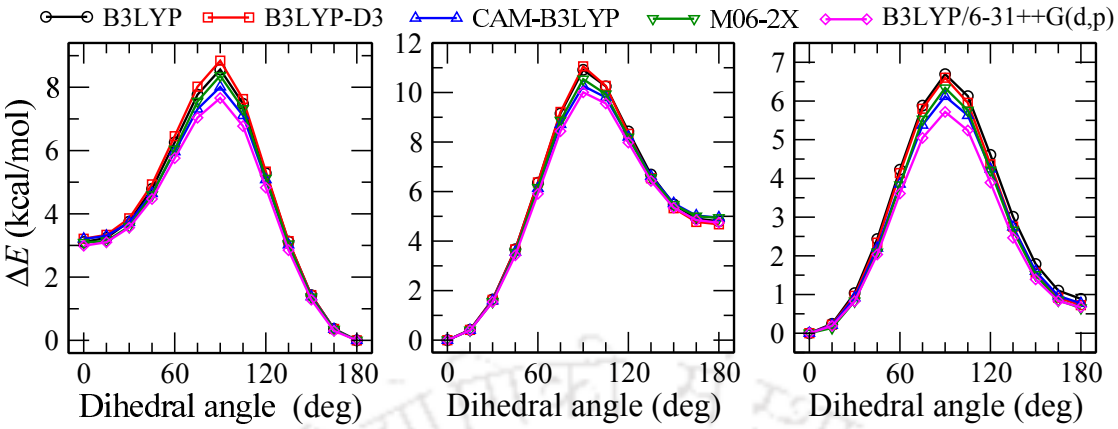

FIGURE 5.4: Relaxed potential energy curves along ∠ 1-2-3-4, for $(PF)_1$ (a), $(PP)_1$ (b) and $(PT)_1$ (c). Energies are relative to the energy of the most stable structure in each case.

of each monomer obtained by these four functionals are similar. The barrier height is the largest for $(PP)_1$ and is the smallest for $(PT)_1$. The figure also shows that the B3LYP/6-31++G(d,p) level of theory predicts similar potential energy curves to those at the B3LYP/6-31G(d) level but with a slightly shorter barrier height. These results highlight the fact that functionals and basis sets have insignificant effects on the ground state structures obtained for the monomers.

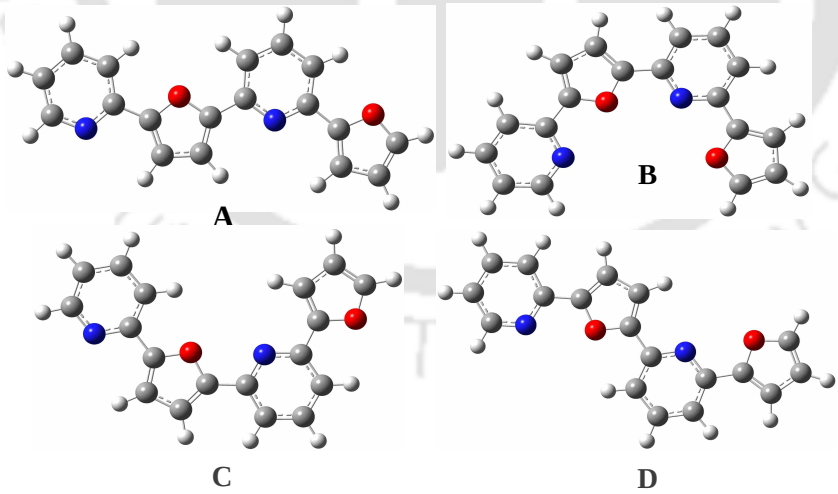

FIGURE 5.5: Optimized structures of four conformers of $(PF)_2$ obtained at the B3LYP-D3/6-31G(d) level.

For each conformer of a monomer, there are two possible geometries of dimers. Thus, four different conformations are possible for a dimer. These four possible structures are

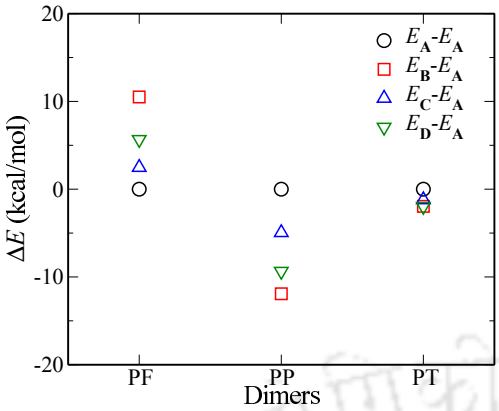

	E_B-E_A	E_C-E_A	E_D-E_A
PF	10.5	2.5	5.7
PP	-11.9	-5.0	-9.4
PT	-2.0	-1.2	-2.0

FIGURE 5.6: Energies of different conformations of $(PF)_2$, $(PP)_2$ and $(PT)_2$ with respect to that of **A** calculated at the B3LYP-D3/6-31G(d) level. These calculated values are also tabulated and all are in kcal/mole.

denoted as **A**, **B**, **C** and **D**. For $(PF)_2$, optimized structures obtained at the B3LYP-D3/6-31G(d) level for these four conformers are shown in Figure 5.5. Absence of any imaginary frequency in each case indicates that all are stable ground state structures. The energies of various conformers with respect to the energy of conformer **A** calculated at the B3LYP-D3/6-31G(d) level of theory are plotted in Figure 5.6. It is observed that conformers **A**, **B** and **D** are the most stable geometries for $(PF)_2$, $(PP)_2$ and $(PT)_2$, respectively. However, for $(PT)_2$, the difference in energies between **B** and **D** conformers is very small ($\sim$ 0.004 kcal/mol) and from trimer onwards, conformer **B** is the most stable structure (not shown). As conformers **C** and **D** are less stable than **A** and/or **B**, and both **A** and **B** are expected to form helix like structures, our study focuses on the **A** and **B** conformers of the oligomers only. Although not shown, results obtained at B3LYP/6-31G(d), M06-2X/6-31G(d), CAM-B3LYP/6-31G(d) and B3LYP/6-31++G(d,p) levels of theories are similar to those for the B3LYP-D3/6-31G(d) level. Hence, from dimer onwards, B3LYP and B3LYP-D3 functionals in combination with the 6-31G(d) basis set were chosen to optimize the ground state structures. These two functionals are selected to reveal the effect of dispersion correction on the geometries and stabilities of ground state structures of long oligomers.

Ground state structures of oligomers having less number of repeating units than required to complete one helical turn obtained by B3LYP and B3LYP-D3 functionals

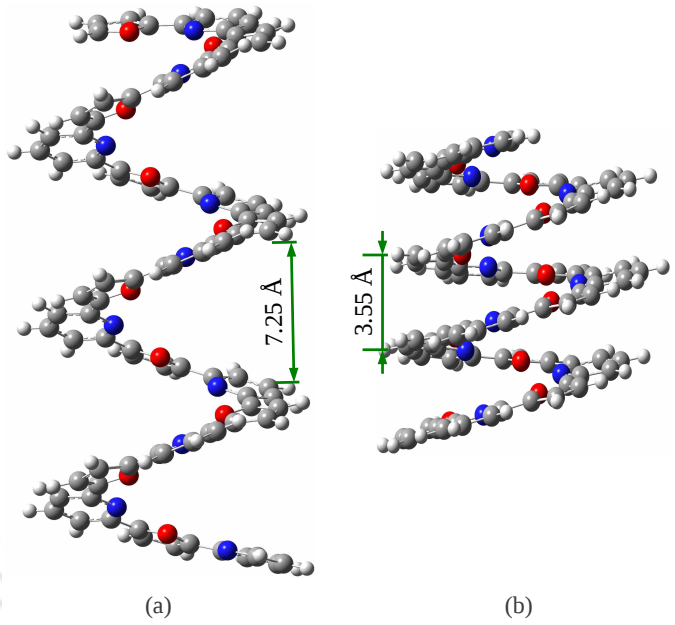

FIGURE 5.7: Optimized structures of **B**-$(PF)_{10}$ obtained by B3LYP (a) and B3LYP-D3 (b) functionals in combination with the 6-31G(d) basis set.

are similar, for both the conformers. However, for larger oligomers, distances between adjacent helical turns (i.e., pitch) obtained by the B3LYP functional are comparatively larger than those for the B3LYP-D3 functional. Optimized structures of **B**-$(PF)_{10}$ obtained by these two functionals are shown in Figure 5.7. As can be seen, for B3LYP and B3LYP-D3, pitches of **B**-$(PF)_{10}$ are 7.25 and 3.55 Å, respectively. Although not shown, similar differences in the results of these two functionals are obtained for other helical oligomers.

For B3LYP and B3LYP-D3 functionals, differences in energies between conformers **A** and **B** (i.e., $E_{\mathbf{A}} - E_{\mathbf{B}}$) were calculated and plotted *versus* n in Figure 5.8. As shown in the figure, for PF, the B3LYP functional estimates that the stability of conformer **A** increases with the increase in chain length. Results of B3LYP-D3 are similar to the results of B3LYP up to trimer. Upon further addition of repeating units, the stability of conformer **B** gradually increases from tetramer to decamer. So, for longer oligomers, it is expected that conformer **B** will be the most stable structure. For PP, conformation **B** is more stable than **A** for both the functionals. However, from trimer onwards, there are noticeable differences between the stabilization energies: for $n > 3$, the stabilization

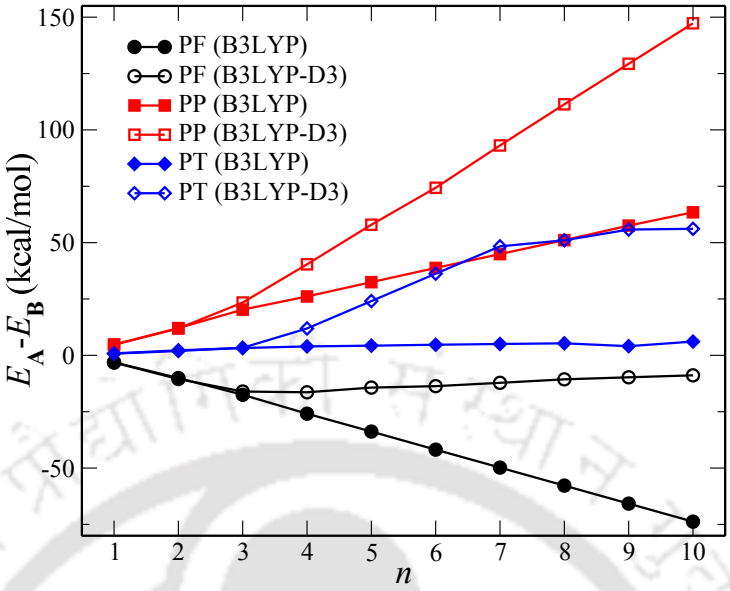

FIGURE 5.8: Energy differences between the two conformers ($E_{\mathbf{A}} - E_{\mathbf{B}}$) of each oligomer. Results are shown for B3LYP and B3LYP-D3 functionals.

energy obtained using B3LYP-D3 is comparatively larger than that obtained using the B3LYP functional. For decamer, B3LYP-D3 results show that conformer **B** is more stable than conformer **A** by 147.3 kcal/mol, while for B3LYP the difference is only 63.5 kcal/mol. In the case of PT, B3LYP results show that energies of two conformers for $n \leq 3$ are nearly the same: $E_{\mathbf{A}} - E_{\mathbf{B}}$ is $\sim$ 4-6 kcal/mol. From tetramer onwards, the results of B3LYP-D3 differ from the results of B3LYP. From $(PT)_4$ to $(PT)_7$, the stability of conformer **B** gradually increases compared to that of **A**. However, for $(PT)_{8-10}$, the energy gap between two conformers remains nearly the same. For $(PT)_{10}$, this gap is 56.1 kcal/mol. Thus, for the studied systems, B3LYP and B3LYP-D3 functionals produce different results for long oligomers. In these type of systems, π–π like non-covalent interactions between adjacent helical turns of a helix play a major role in their stabilities[50,85] and hence, use of functionals like B3LYP-D3 which include these small interactions is essential for their structural analysis[50,94,96]. The increased stability observed with the use of B3LYP-D3 confirms this in our case.

To gain an understanding of this interaction energy, values of $S_{\mathrm{nb}} = [E_n - n \times E_1] - [(n-1)(E_2 - 2 \times E_1)]$ and $s_{\mathrm{nb}} = (E_n - E_{n-1}) - (E_2 - E_1)$ are calculated. The first term is

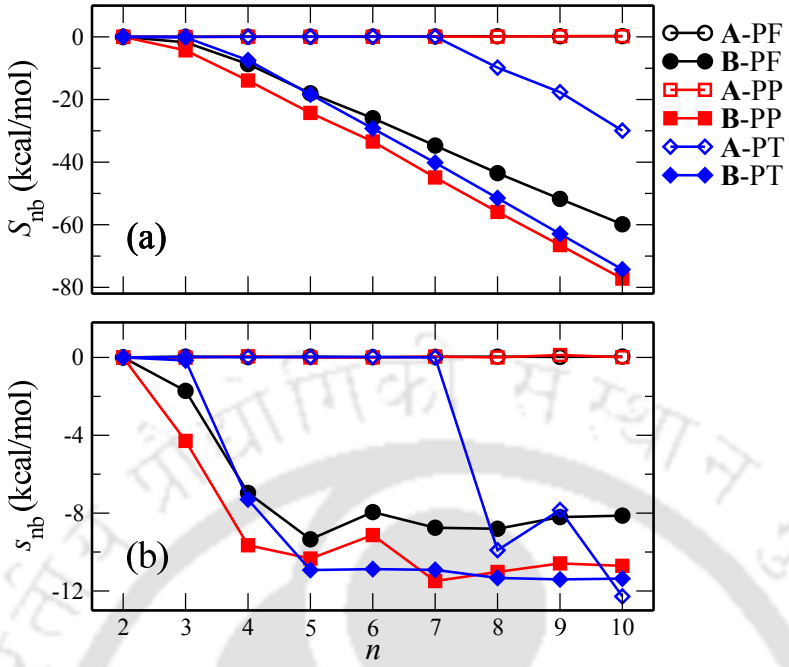

FIGURE 5.9: Values of $S_{\rm nb} = [E_n - n \times E_1] - [(n-1)(E_2 - 2 \times E_1)]$ (a) and $s_{\rm nb} = (E_n - E_{n-1}) - (E_2 - E_1)$ (b) are plotted *versus* n. Here, n and E_n are the number of repeating units and ground state energy of an oligomer having n number of repeating units, respectively.

the total stabilization energy gained as a consequence of non-bonding interaction present in a helix. $s_{\rm nb}$ is the amount of stabilization energy gained per addition of repeating unit. Positive and negative values of $S_{\rm nb}$ and $s_{\rm nb}$ indicate decrease and increase in the stabilization energies, respectively. Plots of $S_{\rm nb}$ and $s_{\rm nb}$ *versus* n are shown in Figures 5.9 and 5.10 for B3LYP-D3 and B3LYP functionals, respectively. In Figure 5.9, it can be seen that $S_{\rm nb}$ and $s_{\rm nb}$ values are ~ 0 kcal/mol for oligomers with $n <$ the number of repeating units needed to complete one helical turn. However, noticeable $S_{\rm nb}$ and $s_{\rm nb}$ values are obtained for **B**-$(PF)_3$, **B**-$(PP)_3$, **B**-$(PT)_4$ and **A**-$(PT)_8$. It is to be mentioned here that for **B**-(PF), **B**-(PP), **B**-(PT) and **A**-(PT), formation of the helical form starts at $n = 3$, 3, 4 and 8, respectively. The $S_{\rm nb}$ value decreases with a further increase of n for these oligomers indicating that this interaction energy coming from the π–π interaction between adjacent helical turns becomes more stronger. It is also noticed that types of 5-membered heterocyclic rings attached to pyridine affect the $s_{\rm nb}$ value added to an oligomer, and therefore the $S_{\rm nb}$ value are different for PF, PP and PT helices. The

trends observed in the variation of $s_{\rm nb}$ *versus* n for **B** conformers show that there is partial overlap of the newly added repeating unit with the existing part of the oligomer in the case of $(PF)_3$, $(PP)_3$ and $(PT)_4$. Further addition of repeating units results in a large decrease in the value of $s_{\rm nb}$ and for $n > 6$, the values are much smaller than those for **B** conformers of $(PF)_3$, $(PP)_3$ and $(PT)_4$. Also, for $n > 6$, $s_{\rm nb}$ values of **B** conformers varies with in a small range. Figure 5.9(b) shows that $s_{\rm nb}$ is $\sim$ 8 kcal/mol for furan containing oligomers and $\sim$ 11 kcal/mol for pyrrole and thiophene containing oligomers, for $n > 6$. However, in the case of B3LYP results shown in Figure 5.10 (a) and (b), positive values of $S_{\rm nb}$ indicate absence of the $\pi - \pi$ interaction energy, except for **B**-$(PP)_3$ and **A**-$(PT)_9$. Thus, the B3LYP-D3 functional is suitable for our studied systems and from now onwards, the results obtained using this functional are discussed.

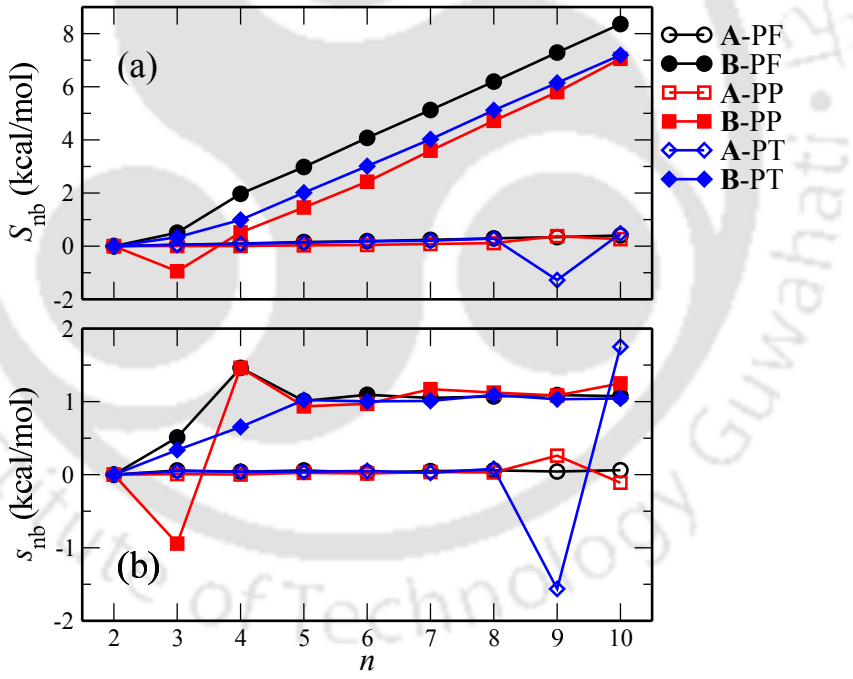

FIGURE 5.10: Stabilization energies of the studied compounds at the B3LYP/6-31G(d) level. $S_{\rm nb} = [E_n - n \times E_1] - [(n-1)(E_2 - 2 \times E_1)]$ (a) and $s_{\rm nb} = (E_n - E_{n-1}) - (E_2 - E_1)$ (b) are plotted versus $n > 1$. Here, n and E_n are the number of repeating units and ground state energy of an oligomer having n number of repeating units, respectively.

5.2.2 Ground state geometries, IPs and dipole moments

TABLE 5.1: Geometrical parameters of largest helical oligomers. D_{inner} and D_{outer} denote diameters of inner and outer of a helix, respectively. p, u and d represent pitch, number of repeating units per turn and rise per repeating unit, respectively.

helices	D_{inner} (Å)	D_{outer} (Å)	p (Å)	u	$d = (p/u)$
A-$(PF)_{24}$	45.60	57.32	4.0	23	0.18
B-$(PF)_{10}$	5.56	11.89	3.6	3	1.18
A-$(PP)_{16}$	28.14	38.85	3.7	15	0.25
B-$(PP)_{10}$	4.66	11.91	3.5	3	1.17
A-$(PT)_{10}$	13.25	23.83	3.5	8	0.47
B-$(PT)_{10}$	7.18	13.12	3.6	4	1.03

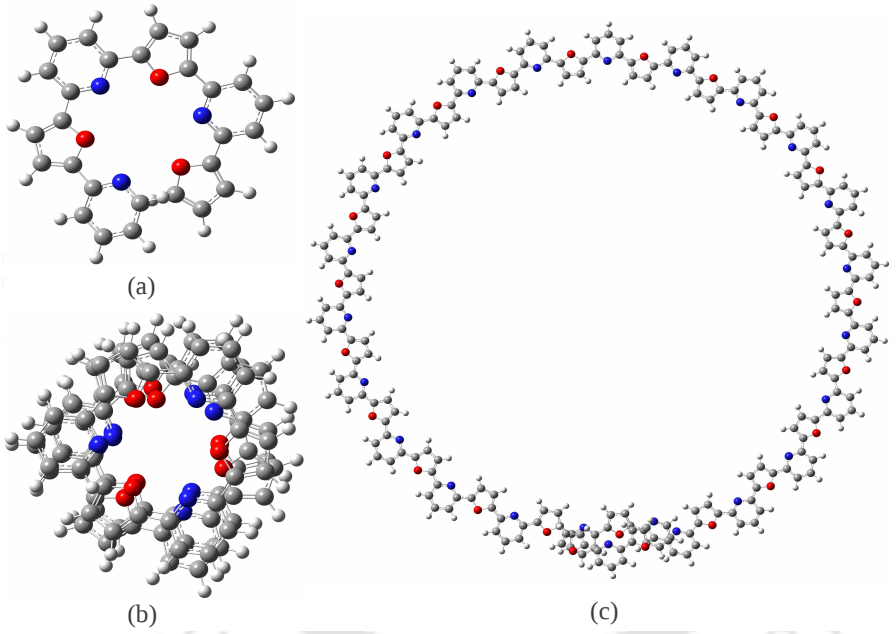

FIGURE 5.11: Optimized structures of **B**-$(PF)_3$ (a), **B**-$(PF)_{10}$ (b) and **A**-$(PF)_{24}$ (c) obtained at the B3LYP-D3/6-31G(d) level.

The geometrical parameters of the largest oligomers for conformers **A** and **B** in each case are listed in Table 5.1. The inner diameter, outer diameter, pitch, number of repeating units needed to complete one helical turn and rise per repeating unit are denoted as D_{inner}, D_{outer}, p, u and d, respectively. For easy understanding of diameters and u of the studied oligomers, top views of **A**-$(PF)_{24}$ and **B**-$(PF)_{n=3,10}$ are shown

in Figure 5.11. Similarly, few selected PP (**A**-$(PP)_{16}$ and **B**-$(PP)_{n=3,10}$) and PT (**A**-$(PT)_{10}$ and **B**-$(PT)_{n=4,10}$) oligomers are shown in Figures A3 and A4, respectively (see Appendix III). As observed from the table and can also be seen in the figures, D_{inner} and D_{outer} values of **A** conformer are larger than those for the **B** conformer, in each case. $D_{\text{inner}}/D_{\text{outer}}$ values of **A**-$(PF)_{24}$, **A**-$(PP)_{16}$ and **A**-$(PT)_{10}$ are 45.60/57.32, 28.14/38.85 and 13.25/23.83 Å, respectively. In comparison, D_{inner} and D_{outer} of **B** conformers are within 4.6-7.2 Å and 11.8-13.2 Å, respectively. Values of D_{inner} and D_{outer} are directly proportional to u and hence, while the u values for conformer **A** of PF, PP and PT oligomers are 23, 15 and 8, respectively, the values are much smaller for **B** oligomers (u values are 3, 3 and 4 for PF, PP and PT oligomers, respectively). **A**-$(PF)_{24}$ has the largest p value. This structure was optimized at the B3LYP/3-21G level only as it was difficult to converge the optimization at the B3LYP-D3 level and the absence of the dispersion interaction term in the functional may be the reason for this result. p of other oligomers varies between 3.5 and 3.7 Å. As the p values of the studied oligomers are nearly the same, d mainly depends on the u. For each oligomer, **A** conformer has a larger u value than that for **B**. As a result, in the case of each oligomer, the d value of **A** conformer is smaller than that for **B**. As **A**-$(PF)_{24}$ has the largest u value, it has the smallest d value. In Figures 5.11 and A3, for **B**-PF and **B**-PP oligomers, it can also be observed that π-stacking occurs between the same heterocyclic rings of adjacent helical turns. However, in the case of other helical oligomers, the presence of different heterocyclic rings is seen along the stacking direction.

Characterization of the optimized geometries was also carried out by computing the Δr values of all the studied oligomers using the following formula:[243]

$$\Delta \mathrm{r} = \left(\frac{r_a + r_c + r_e}{3} - \frac{r_b + r_d}{2} \right) / n. \tag{5.1}$$

Here, r_x indicates bond length of the bond x, where $x = a$, b, c, d and e. A representative structure in Figure 5.1 shows these bonds of a repeating unit. As shown in Figure 5.12,

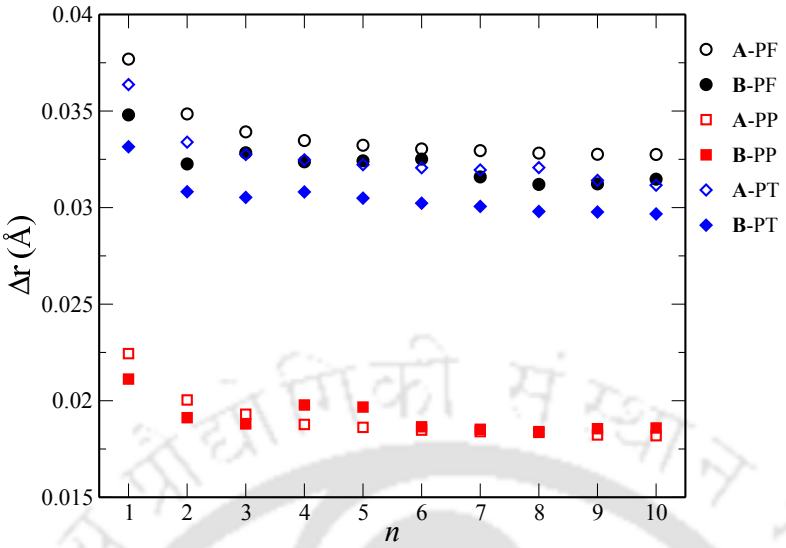

FIGURE 5.12: Δr values of the studied oligomers. The equation used to calculate the Δr is mentioned in the text below.

A conformers of $(PF)_{n=3-10}$ and $(PT)_{n=3-10}$ have slightly larger Δr values (∼ 0.001-0.002 Å) than those for the **B** conformers of these compounds. For example, Δr values for **A**-$(PF)_{10}$, **B**-$(PF)_{10}$, **A**-$(PT)_{10}$ and **B**-$(PT)_{10}$ are 0.033, 0.032, 0.031 and 0.030 Å, respectively. However, for PP, two conformers have nearly the same Δr values (∼ 0.018 Å for $(PP)_{6-10}$). Comparing PF, PP and PT oligomers studied, it is clear that PP oligomers have smaller Δr values than those for PF and PT. It is also worth mentioning that Δr values of **A**-$(PF)_{16}$ and **A**-$(PP)_{16}$ do not differ much (only by ∼ 0.0004 Å) from the respective decamer values exhibiting a convergence pattern. Hence, it is expected that Δr values of other oligomers with $n > 10$ may also not change significantly from the values for their respective decamers.

In Figure 5.13, the IP(v) values of all the oligomers are plotted *versus* n. This figure shows that the IP(v) values, for all the systems, decrease with an increase in n. The IP(v) values for the largest oligomers of **A**-PF, **A**-PP and **A**-PT are 5.61, 5.35 and 5.99 eV, respectively. As can be seen, for the same chain length, PP oligomers have comparatively smaller IP(v)s than the values obtained for PF and PT oligomers. **A** conformers of PF and PT oligomers have comparatively larger IP(v) values than the values for **B** conformers. For example, IP(v)s of **A**-$(PF)_{10}$ and **A**-$(PT)_{10}$ are ∼ 0.27

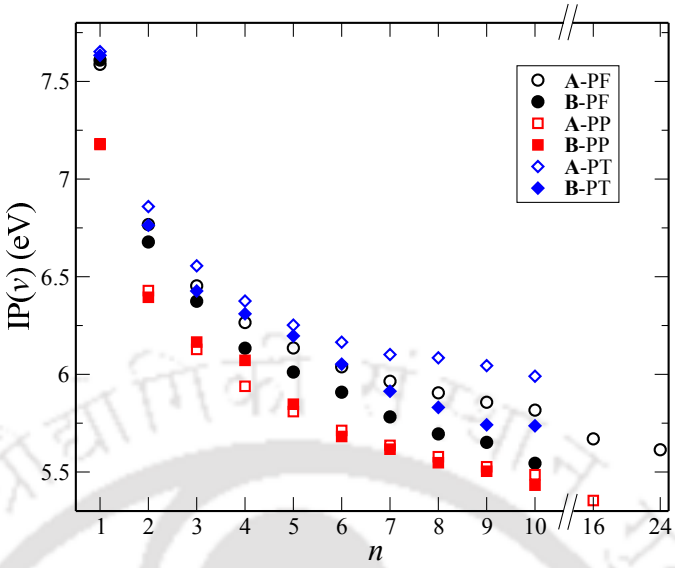

FIGURE 5.13: IP(v)s of the studied oligomers calculated at the B3LYP-D3/6-31G(d) level.

and 0.25 eV larger than that for their respective **B** conformers. However, results of PP oligomers are different from those for PF and PT oligomers. In the case of PP, similar IP values are found for both the conformers. For example, **A**-$(PP)_{10}$ and **B**-$(PP)_{10}$ have 5.49 and 5.43 eV of IP(v) values, respectively.

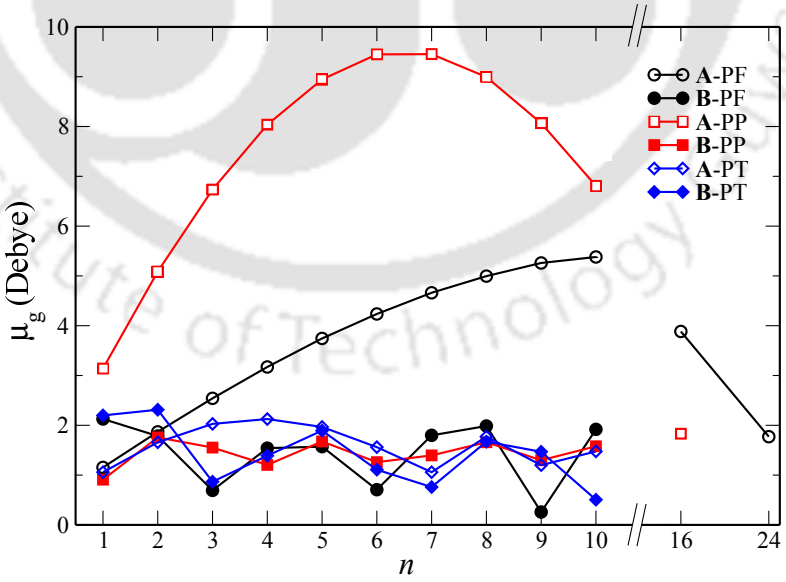

FIGURE 5.14: μ_g values of the studied oligomers calculated at the B3LYP-D3/6-31G(d) level. u values of **A**-PF, **B**-PF, **A**-PP, **B**-PP, **A**-PT and **B**-PT oligomers are 23, 3, 15, 3, 8 and 4, respectively.

μ_g values of all the studied molecules were calculated at the B3LYP-D3/6-31G(d) level and the results are plotted in Figure 5.14. Usually, the μ_g value increases with the increase of chain length as the number of polar atoms increases. However, for our studied systems, it can be seen in Figure 5.14 that initially μ_g increases up to $u/2$ and then starts to decrease gradually up to u. Each time a new helical turn is added to a helix, this process occurs and thus, the μ_g value of each oligomer fluctuates between a certain range. The reason for the above result can be explained in terms of n and u of a helix. For these helical structures, addition of repeating units after completion of half of a helical turn leads to cancellation of the oppositely oriented bond dipole moments, and this results in a decrease in total μ_g value. After completion of one helical turn, the μ_g value again increases with the increase of n as the number of polar atom increases. However, the above trend is interrupted in the case of **A**-$(PT)_8$, and its μ_g value is 0.72 Debye larger than that for **A**-$(PT)_7$. This may be related to the ground state structure of **A**-$(PT)_8$, shown in Figure 5.15, which is distorted due to strong $\pi - \pi$ interaction between the two terminal units. Thus, as in the case of chemical structures and conformations, μ_g of these helical oligomers strongly depends on n and u of a helix.

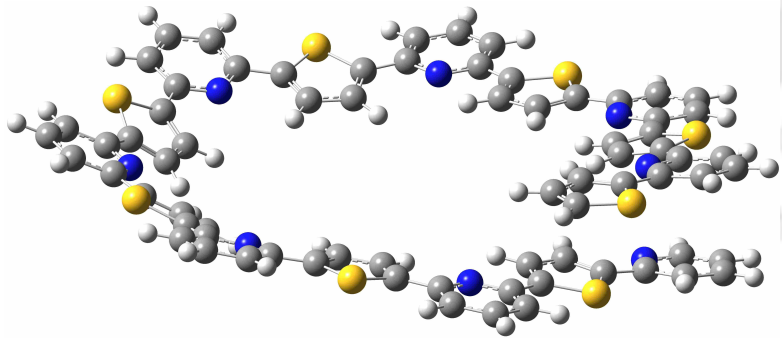

FIGURE 5.15: Optimized structures of **A**-$(PT)_8$ obtained at the B3LYP-D3/6-31G(d) level.

5.2.3 Electronic properties, absorption spectra and frontier molecular orbitals

Pictures of FMOs and the differences in their energies provide knowledge about the length of conjugation and correlation of the optical gap with the polymer chain length. Energies of FMOs of each compound are plotted in Figure 5.16. In cases of **A** conformers,

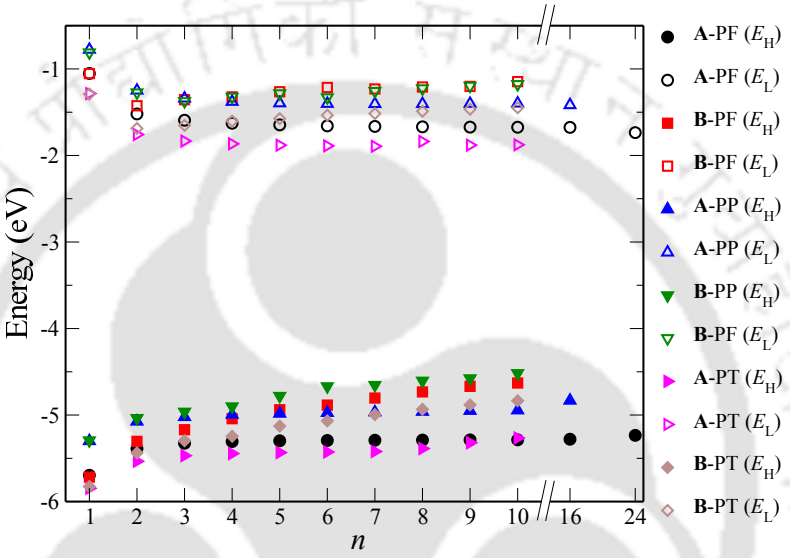

FIGURE 5.16: E_H and E_L for all the studied compounds calculated at the B3LYP-D3/6-31G(d) level. u values of **A**-PF, **B**-PF, **A**-PP, **B**-PP, **A**-PT and **B**-PT oligomers are 23, 3, 15, 3, 8 and 4, respectively.

for $n < u$, initially E_Hs and E_Ls rapidly increase and decrease with the increase of n, respectively. In this regime, after a certain value of n, small increases and decreases in E_H and E_L are found, respectively. However, for $n \geq u$, large changes in E_H and E_L values are noticed. While E_H increases for all oligomers, E_L does not follow a particular trend in this region of n. In the case of **B** conformers, u values are very small (3 or 4 only) and hence, large changes in E_H and E_L values are seen with the increase of n from 1 to 10. For oligomers with $n > u$, E_H and E_L values do not vary in a particular order, making it difficult to extrapolate to infinite chain length.

In Figure 5.17, E_g^{hl} and E_g^{opt} of oligomers are plotted *versus* $1/n$. As can be seen, for each of the studied oligomers, the E_g^{hl} value is larger than E_g^{opt}. However, both

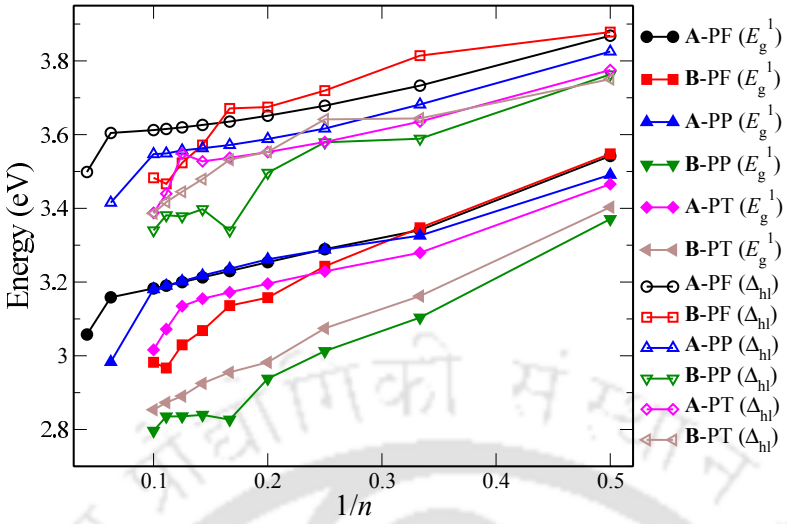

FIGURE 5.17: E_g^{hl} and E_g^{opt} of oligomers calculated at the B3LYP-D3/6-31G(d) level. u values of **A**-PF, **B**-PF, **A**-PP, **B**-PP, **A**-PT and **B**-PT oligomers are 23, 3, 15, 3, 8 and 4, respectively.

have the same decreasing trend for each compound, except for **A**-$(PT)_8$. The E_g^{hl} value of **A**-$(PT)_8$ is 0.02 eV larger than the value obtained for **A**-$(PT)_7$, while the reverse happens for the E_g^{opt}. For all oligomers, in the case of $n < u$, E_g^{hl} and E_g^{opt} decrease in a regular manner with increasing chain length. However, beyond $n = u$, E_g^{hl} and E_g^{opt} decrease sharply in the case of most of the studied oligomers. Deviations in the above mentioned trend occur for **B**-$(PF)_{10}$ and **B**-$(PP)_{n=7-10}$. **B**-$(PF)_{10}$ has larger E_g^{hl} and E_g^{opt} values than that for **B**-$(PF)_9$. In the case of **B**-PP, slopes of E_g^{hl} and E_g^{opt} are more steeper from tetramer to hexamer than those from dimer to trimer. However, **B**-$(PP)_7$ has larger E_g^{hl} and E_g^{opt} values than the values for **B**-$(PP)_6$. For **B**-$(PP)_{n=8-10}$, E_g^{hl} and E_g^{opt} are close to those for **B**-$(PP)_7$.

Details of electronic transitions, including E_gs, f_{osc}s and dominant configurations involved in the first and other major electronic transitions for $(PF)_n$, $(PP)_n$ and $(PT)_n$ are presented in Tables 5.2, A12 and A13, respectively. For compounds other than decamers, the first 45 lowest electronic transitions are considered. For decamers, the first 150 lowest electronic transitions were calculated. As reported in Table 5.2, the first electronic transitions of **A**-$(PF)_{n=1-10}$ have the largest f_{osc} values. HOMO→LUMO excitations

TABLE 5.2: Electronic transition data obtained by the TDDFT method for **A**-$(PF)_n$ and **B**-$(PF)_n$ at the B3LYP-D3/6-31G(d) level. E_g, f_{osc}, H and L denote excitation energy, oscillator strength, HOMO and LUMO, respectively. Electronic transitions are from S_0 to S_m. E_gs are in eV.

n (**A**)	m	E_g	f_{osc}	configurations	n (**B**)	m	E_g	f_{osc}	configurations
1	1	4.36	0.32	H → L (75%)	1	1	4.44	0.40	H → L (79%)
2	1	3.54	0.63	H → L (76%)	2	1	3.55	0.50	H → L (81%)
3	1	3.34	0.72	H → L+1 (92%)		8	4.58	0.44	H-1 → L+1 (82%)
4	1	3.29	1.54	H → L+2 (82%)	3	1	3.35	0.15	H → L+1 (87%)
5	1	3.25	2.28	H → L+3 (67%)		8	4.18	0.52	H-1 → L+2 (59%)
6	1	3.23	2.93	H → L+4 (56%)	4	1	3.24	0.06	H → L+1 (52%)
7	1	3.21	3.48	H → L+5 (47%)		15	4.25	0.35	H-2 → L+3 (54%)
8	1	3.20	3.92	H → L+6 (40%)	5	1	3.16	0.06	H → L (47%)
9	1	3.19	4.26	H → L+7 (35%)		22	4.11	0.48	H-4 → L+2 (21%)
10	1	3.18	4.46	H → L+8 (30%)					H-4 → L+1 (15%)
	2	3.26	1.77	H → L+7 (25%)	6	1	3.14	0.02	H → L+1 (41%)
16	1	3.16	3.56	H → L+14 (15%)		35	4.21	0.29	H-1 → L+6 (28%)
				H-2 → L+12 (12%)		39	4.24	0.29	H-1 → L+6 (37%)
				H-1 → L+13 (12%)	7	1	3.07	0.01	H → L (43%)
	2	3.21	6.35	H-1 → L+14 (11%)		43	4.12	0.31	H-5 → L+5 (24%)
24	1	3.06	0.23	H-1 → L+20 (14%)	8	1	3.03	0.00	H → L (74%)
				H-2 → L+19 (11%)		37	3.72	0.16	H-4 → L+3 (19%)
	2	3.10	8.39	H-1 → L+19 (11%)	9	1	2.97	0.00	H → L (78%)
	3	3.11	7.75	H-2 → L+17 (6%)	10	1	2.98	0.00	H → L (76%)
				H-1 → L+18 (6%)		94	4.14	0.25	H-9 → L+1 (11%)
				H-1 → L+20 (6%)					H-9 → L+4 (11%)
						111	4.25	0.29	H → L+16 (15%)

dominate the $S_0 \rightarrow S_1$ transition for **A**-$(PF)_{n=1-2}$. However, for **A**-$(PF)_{n=3-10}$, excitations from HOMO to an unoccupied orbital other than LUMO dominate the $S_0 \rightarrow S_1$ transition. In these cases, with the increase of n, N of the unoccupied orbital (LUMO+N) predominantly involved with the $S_0 \rightarrow S_1$ transition also increases. In the case of **A**-$(PF)_{n=16,24}$, $S_0 \rightarrow S_2$ has the largest oscillator strength. For **A**-$(PF)_{24}$, along with the $S_0 \rightarrow S_2$, $S_0 \rightarrow S_3$ transition also has significant f_{osc}. In these electronic transitions, HOMO$-N$ and LUMO$+N$ are mainly involved. Additionally, it is worth mentioning that $S_0 \rightarrow S_1$ transition of **A**-$(PF)_{24}$ has a negligible f_{osc} of 0.229.

In the case of **B**-$(PF)_{n=1-2}$, the first electronic transitions have the largest oscillator strengths. These transitions are mainly assigned to HOMO→LUMO excitations. For **B**-$(PF)_{n=3-10}$, transitions from S_0 to higher excited states ($S_{m>1}$) are prominent transitions. It is apparent from the table that m of S_m in the major electronic transition increases with the increase in n. For example, $S_0 \rightarrow S_8$, $S_0 \rightarrow S_{15}$ and $S_0 \rightarrow S_{22}$ are the dominant transitions for **B**-$(PF)_3$, **B**-$(PF)_4$ and **B**-$(PF)_5$, respectively. In the case of

B-$(PF)_{10}$, transitions from S_0 to S_{94} and S_{111} are major electronic transitions. In these cases, contributions of HOMO/HOMO$-N$ to LUMO$+N$ excitations dominate major electronic transitions.

TDDFT results of PP and PT oligomers are reported in Tables A12 and A13, respectively (see Appendix III). For **A**-$(PP)_{n=1-3}$, $S_0 \rightarrow S_2$ transitions have the largest f_{osc} values, although $S_0 \rightarrow S_1$ transitions have significant f_{osc}s. However, the first electronic transitions are with the largest oscillator strengths for **A**-$(PP)_{n=4-9}$. In the case of **A**-$(PP)_{10}$ and **A**-$(PP)_{16}$, $S_0 \rightarrow S_2$ and $S_0 \rightarrow S_{m=5,6}$ are dominant transitions, respectively. Transitions from S_0 to S_1, S_2, S_6 and $S_{m=8,11}$ are prominent transitions for **A**-$(PT)_{n=2-6}$, **A**-$(PT)_{n=7-8}$, **A**-$(PT)_9$ and **A**-$(PT)_{10}$, respectively. Similar to **B**-PF oligomers, transitions from S_0 to S_8, S_{14} and S_{21} are the major electronic transitions for **B**-$(PP)_3$, **B**-$(PP)_4$ and **B**-$(PP)_5$, respectively. Similarly, for **B**-$(PT)_{n=3-5}$, electronic transitions from the ground state to S_4, S_5 and S_{24} are major transitions for n = 3, 4, 5, respectively. In the case of **B**-$(PP)_{10}$, $S_0 \rightarrow S_{114}$ and $S_0 \rightarrow S_{117}$ are important electronic transitions. Like **B**-$(PP)_{10}$, excitations to S_{52}, S_{54} and S_{108} are main electronic transitions for **B**-$(PT)_{10}$. From the above results, in the case of $n \geq u$, it may be concluded that 'm' of S_m in the major electronic transitions, $(S_0 \rightarrow S_m)$, increases with the increase in n. Furthermore, HOMO$+N$ and LUMO$-N$ orbitals are significantly involved in these transitions, for our studied systems.

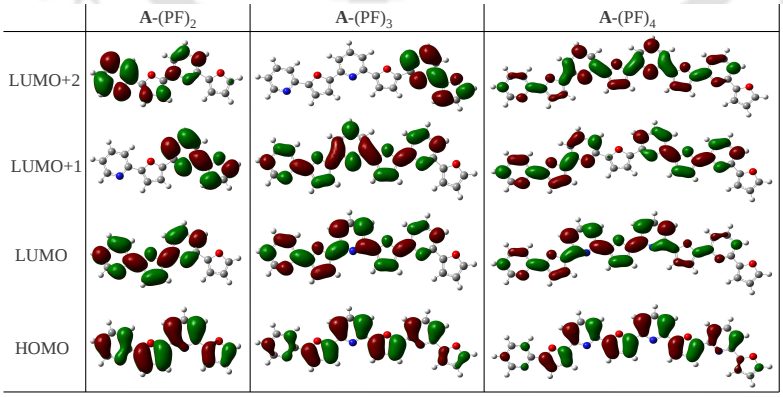

FIGURE 5.18: HOMO, LUMO, LUMO+1 and LUMO+2 of **A**-$(PF)_{n=2-4}$ at an isosurface value of 0.02.

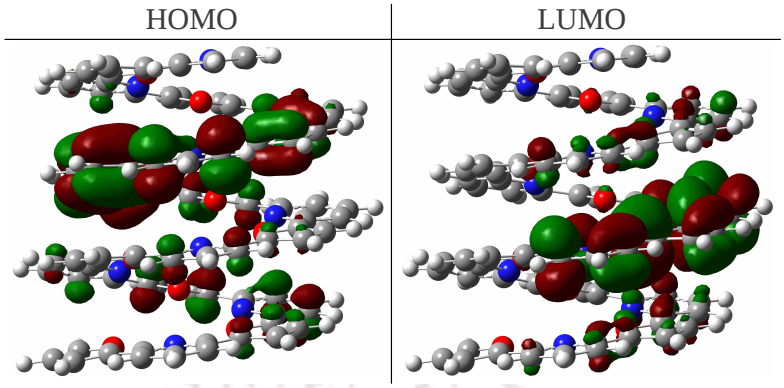

FIGURE 5.19: HOMO and LUMO of **B**-$(PF)_{10}$ at an isosurface value of 0.02.

To gain insights into the variations of f_{osc}s with n, various molecular orbitals are plotted in Figures 5.18, 5.19 and A5, for few selected oligomers. It is apparent from Figure 5.18 that degrees of overlap of HOMO with LUMO, LUMO+1 and LUMO+2 are the largest compared to other possible combinations for **A**-$(PF)_2$, **A**-$(PF)_3$ and **A**-$(PF)_4$, respectively. This may be a reason for the increase of N of LUMO+N in the dominating configuration with the increase of n in the case of **A**-PF. For **B**-$(PF)_{10}$, frontier molecular orbitals are shown in Figure 5.19. As can be seen, the electron densities of HOMO and LUMO of **B**-$(PF)_{10}$ do not overlap. Frontier molecular orbitals for **A**-$(PP)_{16}$, **B**-$(PP)_{10}$ and $(PT)_{10}$ are shown in Figure A5. Similar to **B**-$(PF)_{10}$, small overlap of electron densities of HOMO and LUMO is found for these oligomers. As discussed in previous paragraphs, in these systems excitations involving molecular orbitals other than FMOs dominate major electronic transitions.

Absorption spectra based on the lowest 150 singlet energies for decamers of both conformers **A** and **B** are shown in Figure 5.20. Half-width at half-maximum height of each spectrum is 1500 cm^{-1}. Absorption spectra of **B** conformers are both hypsochromically and hypochromically shifted compared to those of **A** conformers, for each oligomer. This result may be explained by the fact that u of **B** conformer is smaller than that for **A**. Therefore, as discussed in the previous paragraph, in the case of conformer **B**, the major electronic transition is from S_0 to a higher excited state compared to that in the case of **A**. Among the decamers shown, **A**-PP has the largest intensity with an absorption

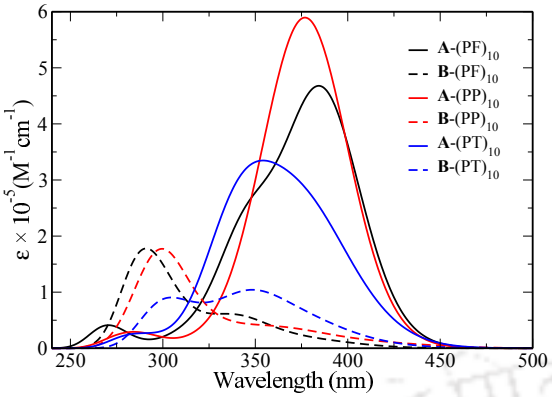

FIGURE 5.20: Absorption spectra of decamers calculated at the TDDFT/B3LYP-D3/6-31G(d) level. Half-width at half-maximum height is 1500 cm^{-1}.

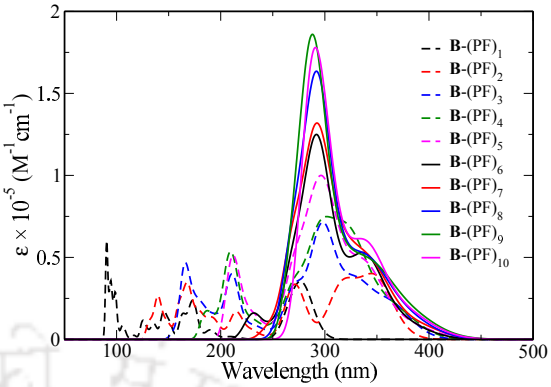

FIGURE 5.21: Absorption spectra of **B**-$(PF)_{n=1-10}$ calculated at the TDDFT/B3LYP-D3/6-31G(d) level.

maximum $\sim$ 379 nm (f_{osc} = 3.48). Compared to other oligomers, the absorption spectrum of **A**-$(PF)_{10}$ is shifted to the red end of the spectrum having maximum absorption at 390 nm (f_{osc} = 4.46) in the UV-Vis spectra. For **B**-$(PF)_{10}$ and **B**-$(PT)_{10}$, absorption spectra have the largest hypsochromic and hypochromic shifts, respectively. In Figure 5.21, absorption spectra of B-PF oligomers *versus* n are plotted. As shown in the figure, for **B**-$(PF)_{3-10}$ oligomers, the main absorption peaks of are located at $\sim$ 300 nm. It is worth mentioning that **B**-PF oligomers start to form helix-like structures at $n = 3$, and with further increase in chain length, the position of the main absorption peak does not change much.

To investigate the chiroptical nature of our studied oligomers, CD spectra are simulated at the TDDFT/B3LYP-D3/6-31G(d) level based on the optimized geometries obtained at the B3LYP-D3/6-31G(d) level, except **A**-$(PF)_{24}$. As mentioned already, **A**-$(PF)_{24}$ was optimized at the B3LYP/3-21G level. Figure 5.22 depicts the CD spectra of the largest helical oligomers of all the studied compounds. As can be seen, all these helical oligomers are CD active and the CD curves are bisignate in nature. But there are distinct differences in the nature of CD curves between the two conformers of an oligomer. For **A**-$(PT)_{10}$, a positive signal at 330 nm and a negative signal at 420 nm are observed. In comparison, for **B** conformer of the same compound, the positive signal is

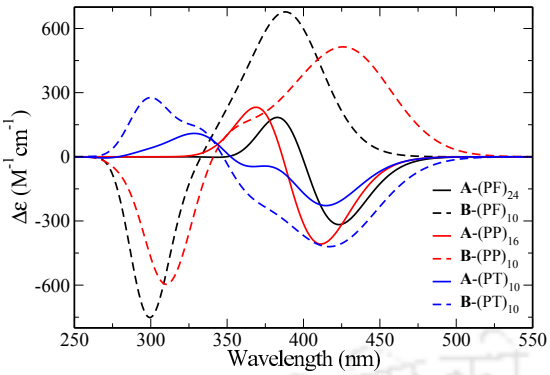

FIGURE 5.22: CD spectra of the largest oligomers of conformers **A** (solid line) and **B** (dashed line) for PF, PP and PT compounds.

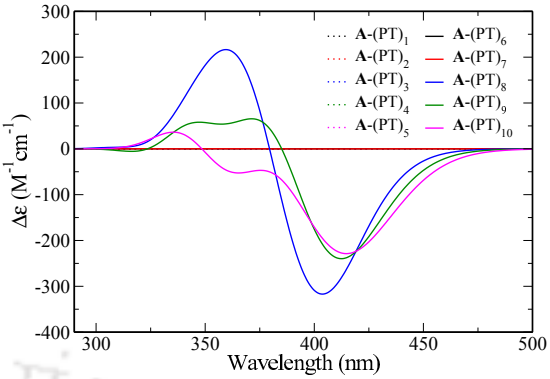

FIGURE 5.23: CD spectra of **A**-(PT)$_{n=1-10}$ calculated at the TDDFT/B3LYP-D3/6-31G(d) level.

shifted to a smaller wavelength ($\sim$ 300 nm) while the negative signal is almost at the same position as that in **A** but is much broader. Similarly, the positive band in the case of **B**-PP is much broader and the negative band is blue shifted in comparison to the bands in **A**-PP. In Figure 5.23, the CD spectra for the oligomers of **A**-(PT) are shown. As seen, all the oligomers are CD inactive until n is equal to u. As soon as helix is formed, the system becomes CD active. Similar observations are made for other systems.

5.3 Salient findings

In this chapter, computational studies on the structural and optoelectronic properties of pyridine-furan, pyridine-pyrrole and pyridine-thiophene oligomers are carried out at B3LYP/6-31G(d) and B3LYP-D3/6-31G(d) levels. Our results reveal that dispersion corrected functionals like B3LYP-D3 are essential in the theoretical studies of these systems where there are possibilities of helical structures. Two of the possible helical conformations for each oligomer, having hetero atoms of 5-membered and 6-membered heterocyclic rings on different sides (conformer **A**) or on the same side (conformer **B**), are considered. Values of stabilization energies indicate that stabilities of helical oligomers increase with the increase of n owing to the increase of the non-bonding interaction

energy between adjacent helical turns. Our results show that **B** is the most stable conformer for PP and PT oligomers, while **A** is the most stable in the case of PF. However, compared to **A**-PF, the stability of **B**-PF gradually increases with the increase in n, indicating that like PP and PT, conformer **B** of PF may become more stable for larger oligomers. In the case of each oligomer, u of the conformer **A** is larger than that for **B**. While u values for the **B** conformers are 3, 3 and 4 for PF, PP and PT systems, respectively, the values are 23, 15 and 8 for **A** conformers. μ_g values of these helical oligomers fluctuate between a certain range and this fluctuation range for conformer **A** is larger than that for **B**. For each oligomer, the μ_g value depends on the n and u of a helix. TDDFT results conclude that for oligomers with $n > u$, m of the most important electronic transition ($S_0 \rightarrow S_m$) increases with an increase in n. In accordance with u values, the absorption spectra for **B** conformers are blue shifted compared to those for **A**, for decamers. Multiple electronic transitions other than the first excitation are significantly involved in an absorption spectrum of a helical oligomer. These major electronic transitions are dominated by HOMO–N $\rightarrow$ LUMO+N excitations. All the helical structures are found to be CD active.

Pyridine-pyrrole based cross-conjugated oligomers: Effects of insertion of π-spacers in the main chain on the electronic and optical properties

This chapter reveals the effects of insertion of vinylene-, azomethine-, azo π-spacers in the main chain of *N*-methylpyrrole–pyridine–*N*-methylpyrrole (D–A–D) cross-conjugated oligomers on the structural, electronic and optical properties. The contents of this chapter are submitted to the *Polymer* journal.

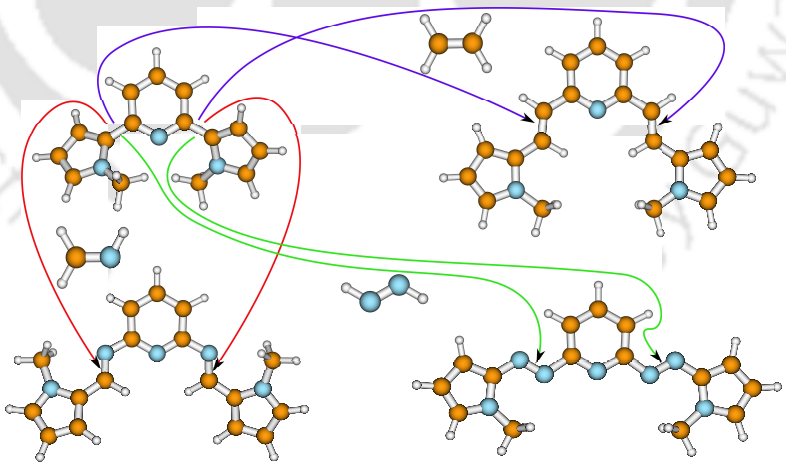

Figure: Monomers of four different oligomers.

In comparison to through-conjugated systems, studies on cross-conjugated systems are rare in the literature, and tuning of their electronic and optical properties remains a very challenging task to date.[51,98–100] In contrast, a large number of informations are available for tuning these properties of through-conjugated systems. One of the strategies to reduce the band gap is to have the system made up of alternating donor (D) and acceptor (A) units.[146,244–249] D-A polymers are known to have narrow band gaps as a result of mixing of orbitals of the donor and acceptor units.[20] However, the presence of very strong electron donating and accepting groups in D-A polymers leads to localization of electron density on a specific part of the chain, which may hinder the electron mobility.[30] Thus, choosing proper D/A units is vital in designing D-A polymers. In this scenario, moderately donating pyrrole and accepting groups like pyridine may be suitable for this purpose. Further, postsynthetic modulation of optoelectronic properties of pyridine containing oligomers is also possible *via* protonation or interaction with Lewis acids due to the presence of nitrogen atoms of pyridine rings.[233,234,241] Apart from the D-A approach, optoelectronic properties of an oligomer can also be tuned by inserting π-spacers like vinylene, azomethine and azo-linkages in the main chain of the oligomers.[17,64,65] These linkages reduce torsional strain in the main chain and enhance π electron delocalization along the backbone resulting in reduced band gap.

Considering the above mentioned strategies for tuning the optoelectronic properties of cross-conjugated polymers, the objective of this chapter is to study the effect of insertion of π-spacers between donor and acceptor units in a donor-acceptor-donor (D-A-D) type oligomer. Four types of oligomers are taken into consideration, namely, a D-A-D and three D-π-A-π-D types, where *N*-methylpyrrole and pyridine rings are donor and acceptor units, respectively. Figure 6.1 shows the repeating units of the four systems, denoted as PP, PCCP, PCNP and PNNP. In PP, the electron deficient central pyridine ring is 2,6-substituted by two electron-rich *N*-methylpyrrole rings making it a D-A-D type system. Replacing the single bond between the donors and the acceptors in PP by vinylene, azomethine and azo linkages, D-π-A-π-D type systems are obtained named as PCCP, PCNP and PNNP, respectively. In these repeating units, substitutions at the

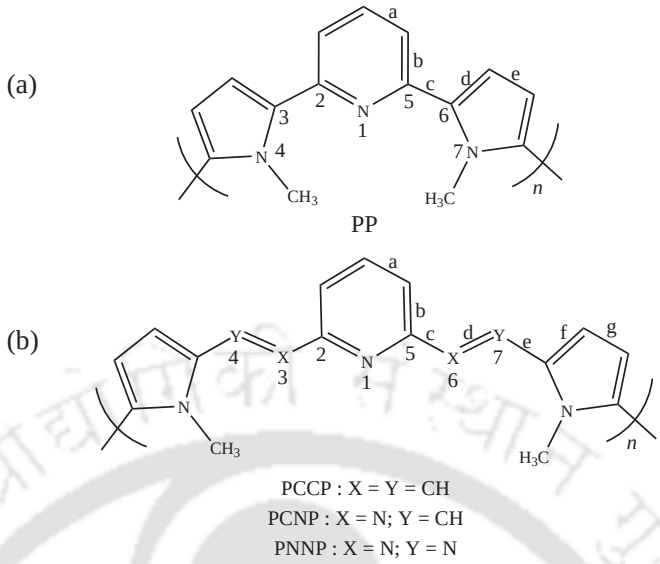

FIGURE 6.1: Sketch map representations of repeating units of the oligomers considered in this chapter. Here, $n = 1$, 2, 3 and 4. Two important dihedral angles, $\angle$ 1-2-3-4 and $\angle$ 1-5-6-7, in the nth repeating unit are denoted as d_n^{a} and d_n^{b}, respectively. Few bonds marked as *a*, *b*, *c*, *d*, *e*, *f* and *g* are also shown in the figure and discussed in the text.

2 and 6-positions of a pyridine ring by two D/D-π units result in conjugation between these two units and the pyridine ring, but these two are not conjugated to each other, leading to cross-conjugation in the backbone chain.[22,250] PP, PCCP and few similar D-π-A-π-D systems are already synthesized.[250–252] Experimental absorption spectra of PCCP[250] and 2,6-Py-V-EDOT[252] shows that the most intense bands of these spectra are assigned to other than the first excitation with a shoulder at low energy region. However, TDDFT study of 2,6-Py-V-EDOT[252] does not report the full absorption spectrum. With this additional curiosity to reveal the missing information, this chapter begins with an arduous conformational search of the all studied monomers. Our study focuses on properties such as ionization potential, electron affinity, excitation energies and their corresponding oscillator strengths, changes in dipole moment upon electron excitation, fundamental and optical gaps and hole-electron binding energy. In section 6.1, computational aspects are briefly discussed. This is followed by results and discussion in section 6.2 and conclusions in 6.3.

6.1 Computational details

All the electronic structure calculations were carried out using the Gaussian 09 package.[242] Ground state geometries for all the studied oligomers were optimized at B3LYP/6-31G(d,p) and CAM-B3LYP/6-31G(d,p) levels of theories without any constraint. These were followed by frequency calculations for all the studied molecules to ensure that the structures are minima. Ground state properties of the systems are studied at the B3LYP/6-31++G(d,p)//B3LYP/6-31G(d,p) level of theory. For monomers, excitation energies and oscillator strengths were obtained by TDDFT single point calculations at different levels of theory. For oligomers, excitation calculations were performed at the TDDFT/B3LYP/6-31++G(d,p) level for the optimized geometries obtained by the B3LYP/6-31G(d,p) level. First 25 excitations were considered in these calculations. Absorption spectrum for each molecule was obtained by using the standard formula

$$\epsilon(\nu') = \frac{2.175 \times 10^8}{\Delta_{1/2}\nu'} f \times \exp\left[-2.772\left(\frac{\nu' - \nu'_{i\to f}}{\Delta_{1/2}\nu'}\right)^2\right], \tag{6.1}$$

as implemented in GaussSum.[253] Here, $\Delta_{1/2}\nu'$, $\nu'_{i\to f}$ and f are the full-width half-maximum, electronic transition energy and oscillator strength of the respective transition, respectively. IP(v) and EA(v) values were calculated by equations 1.3 and 1.3, respectively, at the B3LYP/6-31++G(d,p)//B3LYP/6-31G(d,p) level.

6.2 Results and discussion

In subsection 6.2.1, the various possible conformers for each monomer are discussed and then, for the most stable geometry, a combination of a functional and basis set is chosen which produces the results best in comparison with the available experimental results for $(PP)_1$ and $(PCCP)_1$. While a crystal structure is available for $(PP)_1$,[251] the absorption spectrum is reported for $(PCCP)_1$[250]. In the second subsection, the structures and

properties of oligomers like dipole moments, IPs, EAs, band gaps, hole-electron binding energies and absorption spectra are discussed.

6.2.1 Conformations of monomers, choice of functionals and basis sets

Various possible conformers of the monomers were optimized in the ground state using B3LYP and CAM-B3LYP functionals in combination with the 6-31G(d,p) basis set. Most stable structures of the studied molecules are shown in Figure 6.2. Geometries of all the studied conformers and energies of these conformers with respect to the most stable conformers of $(PP)_1$, $(PCCP)_1$, $(PCNP)_1$ and $(PNNP)_1$ are shown in Figures A6, A7, A8 and A9, respectively (see Appendix IV). As can be seen, both functionals

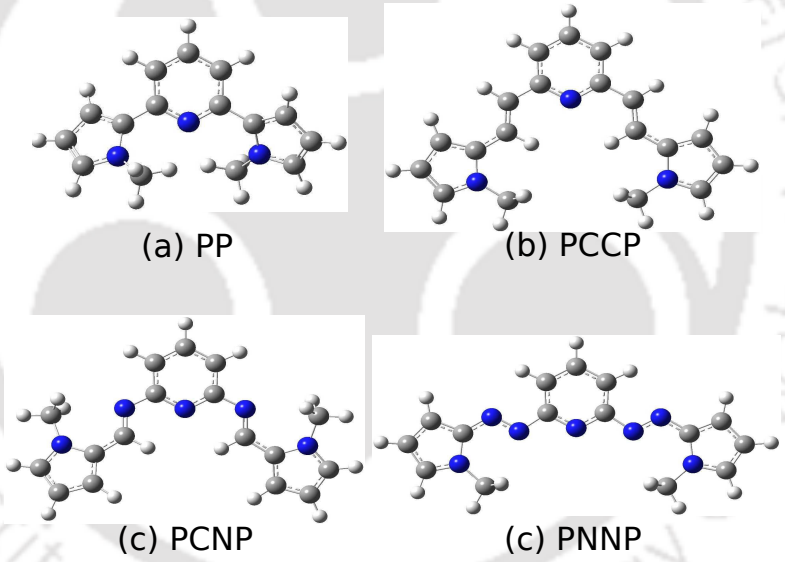

FIGURE 6.2: Structures of the most stable conformers of $(PP)_1$ (a), $(PCCP)_1$ (b), $(PCNP)_1$ (c) and $(PNNP)_1$ (d) obtained at the B3LYP/6-31G(d,p) level.

show similar results. For $(PCCP)_1$, single point calculations were carried out using 6-31++G(d,p) basis set for the B3LYP/6-31G(d,p) optimized geometries and as Figure A7 shows, conformer 1 remains the most stable structure. In addition, for $(PCCP)_1$, optimizations were also carried out at the MP2/6-31G(d,p) level for all the 10 conformers and results obtained are similar to those for B3LYP and CAM-B3LYP functionals as observed in Figure A7. Most stable structures for monomers of PP and PCNP are not

TABLE 6.1: Selected dihedral angles of the studied molecules. Intraunit and interunit dihedral angles are represented in Figures 6.1 and 6.5, respectively. All values are in degree. Results listed outside and inside parentheses are obtained at B3LYP/6-31G(d,p) and CAM-B3LYP/6-31G(d,p) levels, respectively.

molecules	d_1^a	d_1^b	d_2^a	d_2^b	d_3^a	d_3^b	d_4^a	d_4^b	d_i	d_j	d_k
$(PP)_1$	30.7(31.9)	30.6(31.9)									
$(PP)_2$	29.9	29.3	29.3	29.9					–43.5		
$(PP)_3$	28.7	31.8	30.1	30.6	29.8	30.3			–43.6	–42.6	
$(PP)_4$	28.3	31.5	29.6	29.2	29.2	29.6	31.5	28.3	–43.5	–44.5	–43.6
$(PCCP)_1$	0.0(0.0)	0.0(0.0)									
$(PCCP)_2$	–1.1	–1.1	–1.1	–1.1					45.7		
$(PCCP)_3$	–1.5	–1.6	–1.3	–1.3	–1.6	–1.5			46.9	46.9	
$(PCCP)_4$	–1.2	–1.4	–2.7	–1.7	–1.7	–2.7	–1.4	–1.2	45.4	47.3	45.5
$(PCNP)_1$	13.3(16.9)	13.3(17.0)									
$(PCNP)_2$	14.7	13.2	13.2	14.7					–45.1		
$(PCNP)_3$	13.7	12.3	13.5	13.5	12.3	13.7			–44.8	–45.0	
$(PCNP)_4$	14.7	13.5	15.8	13.2	13.2	15.8	13.5	14.7	–45.3	–44.7	–45.5
$(PNNP)_1$	180.0(180.0)	180.0(180.0)									
$(PNNP)_2$	179.8	–179.5	–179.5	179.8					44.6		
$(PNNP)_3$	178.1	178.6	178.9	179.9	–178.0	–179.6			44.2	45.2	
$(PNNP)_4$	179.6	180.0	179.5	–178.2	–178.2	179.5	180.0	179.6	44.6	45.3	44.6

planar, while all three heterocyclic rings of $(PCCP)_1$ and $(PNNP)_1$ are in the same plane. Few selected intraunit dihedral angles (d_1^a and d_1^b) are reported in Table 6.1. A representative structure of these dihedral angles is shown in Figure 6.1. As reported in the table, both functionals produce similar results. Values of d_1^a and d_1^b for $(PP)_1$ and $(PCNP)_1$ obtained at the CAM-B3LYP/6-31G(d,p) level are slightly larger than the values obtained at the other level of theory. As already noted, a crystal structure of $(PP)_1$ is available.[251] The most stable structure from our computational studies matches with the crystal structure. Differences between the bond lengths of calculated and experimental structures are less than 0.025 Å and 0.019 Å for B3LYP and CAM-B3LYP functionals, respectively. Dihedral angles between two adjacent heterocyclic rings in B3LYP and CAM-B3LYP optimized structures are around 3.6° and 2.4° smaller than those for the crystal structure, respectively.

As discussed before, another confirmation regarding the use of a particular functional and basis set is achieved by comparing the absorption spectra of $(PCCP)_1$ with

the available experimental data. Absorption spectra of the most stable conformer of $(PCCP)_1$ calculated at different levels of theory are depicted in Figure 6.3. As can be seen in 6.3(a), in each spectrum, the major electronic transition is associated with a shoulder at a lower energy, similar to the experimental absorption spectrum[250]. The major peak is due to the $S_0 \rightarrow S_4$ transition and the shoulder is because of the $S_0 \rightarrow S_3$ excitation. In addition to these two, the first excitation also has significant oscillator strength, in each case. However, peaks of the absorption spectrum calculated at the B3LYP/6-31G(d,p) level over the optimized structure obtained at the same level of theory are shifted towards the blue end compared to the experimentally observed peaks. Calculated values for $S_0 \rightarrow S_1$ and $S_0 \rightarrow S_4$ transitions are 404.57 and 320.10 nm, while experimental values are 435.0 and 340.0 nm, respectively[250]. 6-31++G(d,p) basis set significantly improves the results by having differences of only 8.9 and 3.9 nms from the above mentioned experimental values. No further improvement in results is observed with increase of basis set size to 6-311++G(d,p). Furthermore, a similar absorption spectrum is obtained at the TDDFT/B3LYP/6-31++G(d,p) level for the ground state geometry optimized at the B3LYP/6-31G(d,p) level, as is shown in the same figure. It is important to note that solvent and other environmental effects are not considered during the absorption spectrum calculation, and small differences between experimental and theoretical results may be due to these approximations.

It is worth to clarify that the experimental absorption spectrum of $(PCCP)_1$ is broad and featureless. However, Abbotto et al.[250] used the low energetic edge (at 435.00 nm) as the first excitation energy to obtain the band gap of this molecule. Therefore, our computed value of 425.68 nm corresponding to $S_0 \rightarrow S_1$ transition is compared with the same low-energetic edge at 435.0 nm. This transition is mainly dominated by the HOMO-LUMO excitation, and as shown in Figure A10, electron density in the frontier molecular orbitals is spread over the entire chain length, ruling out the possibility of a charge-transfer type excitation.[230]

The CAM-B3LYP functional is known to be a suitable functional for the prediction of charge-transfer excitations, while common functionals such as B3LYP often fail.[230] To

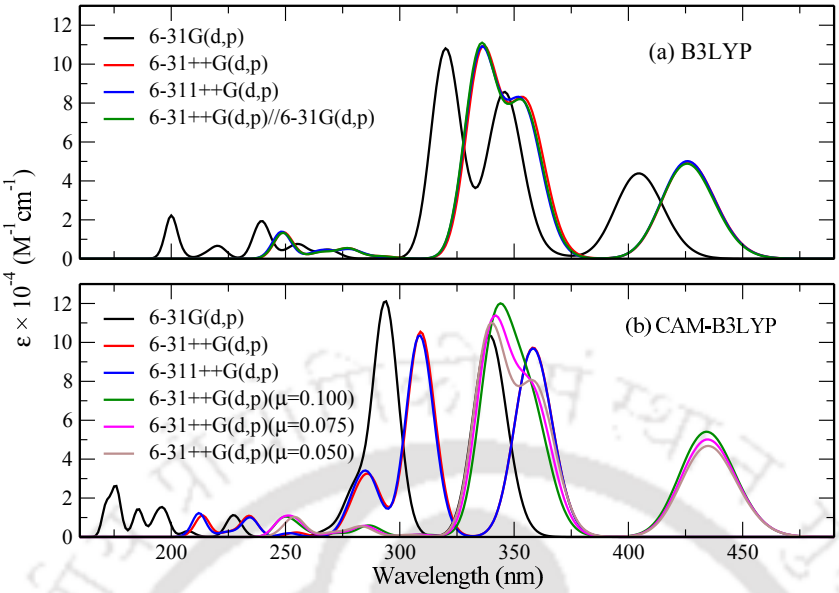

FIGURE 6.3: Absorption spectra of $(PCCP)_1$ using B3LYP (a) and CAM-B3LYP (b) functionals. For B3LYP, the effect of different basis sets is shown. For CAM-B3LYP, in addition to showing the effect of basis sets, the performance of CAM-B3LYP with respect to variation of set of parameters (μ, α, β) = (0.100,0.0693,0.9307), (0.075,0.1257,0.8743) and (0.050,0.1625,0.8375) is also shown. It is to be mentioned that the experimental peak appears at 340.00 nm, with a shoulder at larger wavelength and the low energetic edge at 435.00 nm.[250]

check the effect of long-range correction, absorption spectra of $(PCCP)_1$ were also calculated using this functional in combination with different basis sets. As can be seen in Figure 6.3, similar to B3LYP results, addition of diffuse functions in the basis set improves the quality of results. However, as default parameters of the CAM-B3LYP functional are not suitable for conjugated molecules, especially for TDDFT calculations[254,255], absorption spectra obtained using this functional differ too much from the experimental results. Therefore, parameters in CAM-B3LYP, i.e., μ, α and β, are tuned in combination with the 6-31++G(d,p) basis set using the procedure described by Okuno et al.[255] The sets of tuned values obtained are (μ, α, β) = (0.100,0.0693,0.9307),(0.075,0.1257,0.8743) and (0.050,0.1625,0.8375). Absorption spectra obtained at these levels are also shown in Figure 6.3(b). As can be seen, peaks are very close to the experimental values, in these three cases. Comparing the differences between the calculated and experimental peak values, and the intensity ratios between two major electronic transitions (i.e., $S_0 \rightarrow S_3$ and $S_0 \rightarrow S_4$), the set of parameters (μ, α, β) = (0.050,0.1625,0.8375) is found to be

the most suitable. However, lack of experimental data for other studied molecules and comparatively large computational cost to obtain tuned parameters are the obstacles for using the CAM-B3LYP functional. Further, tuned parameters for monomers may not produce satisfactory results for large oligomers at the same level of accuracy as those for monomers. As the absorption spectrum obtained at the TDDFT/B3LYP/6-31++G(d,p) level over the optimized geometry obtained at the B3LYP/6-31G(d,p) level of theory is comparable to the spectrum obtained at the tuned CAM-B3LYP/6-31++(d,p) level and the method is cheaper than other methods, this combination is chosen for further studies.

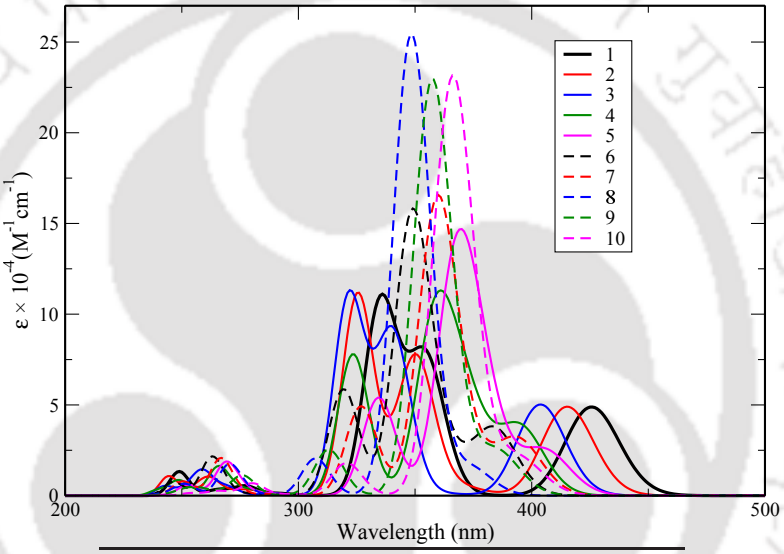

conformers	$S_0 \rightarrow S_1$	$S_0 \rightarrow S_3$	$S_0 \rightarrow S_4$
1	425.7	354.5	335.3
2	415.2	350.2	325.5
3	403.8	340.4	321.7
4	395.1	358.9	323.5
5	405.6	368.2	334.5
6	384.1	348.9	319.4
7	394.1	359.7	326.9
8	373.8	348.5	307.4
9	385.7	357.4	313.0
10	395.7	366.3	320.7
exp[250]	435.0		340.0

FIGURE 6.4: Absorption spectra of different conformers of $(PCCP)_1$. A full-width at half-maximum value of 1500 cm^{-1} is used while computing the spectra. Calculated and experimental transition energies (in nm) from ground state to different excited states are also tabulated.

It is noticed that differences in energies between different conformers are very small ($<$ 5 kcal/mol for $(PCCP)_1$). Therefore, it is worth discussing the dependency of opto-electronic properties with the change of conformation. Absorption spectra of different conformers of $(PCCP)_1$ are calculated and plotted in Figure 6.4. It is clear that the important peaks of the conformer 1 are closer to the experimental peaks than the results for other conformers. These results further justify the chosen level of theory used for these calculations.

6.2.2 Oligomers: Structures, dipole moments, band gaps and absorption spectra

6.2.2.1 Structures and BLA

Important dihedral angles of all the studied oligomers are reported in Table 6.1. $d_n^{a,b}$s are the intraunit dihedral angles located in the nth repeating unit of an oligomer and $d_{i,j,k}$ are the interunit dihedral angles. Representative structures of intraunit and interunit dihedral angles are shown in Figures 6.1 and 6.5, respectively. Results show that $d_n^{a,b}$s do

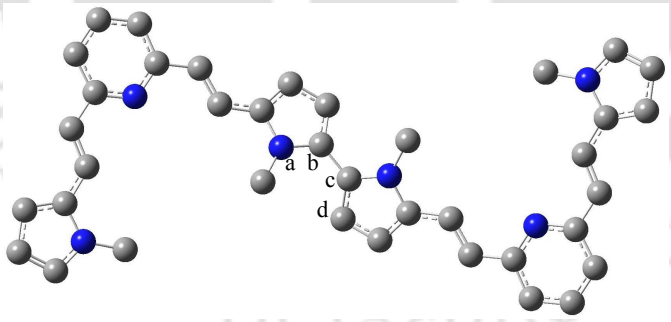

FIGURE 6.5: Ground state structure of $(PCCP)_2$ showing the interunit dihedral angle $d_i = \angle$ a-b-c-d. Hydrogen atoms are not shown for clarity.

not change much ($<$ 3°) with n. For example, repeating units of $(PCCP)_4$ and $(PNNP)_4$ are nearly planar, and differences between their $d_n^{a,b}$s and those for their respective monomers are less than 2.7°. It is also found that $d_{i,j,k}$ values of all the studied oligomers

are quite large (> 42.0°). These large dihedral angles may largely affect their π electron delocalization across the chain.

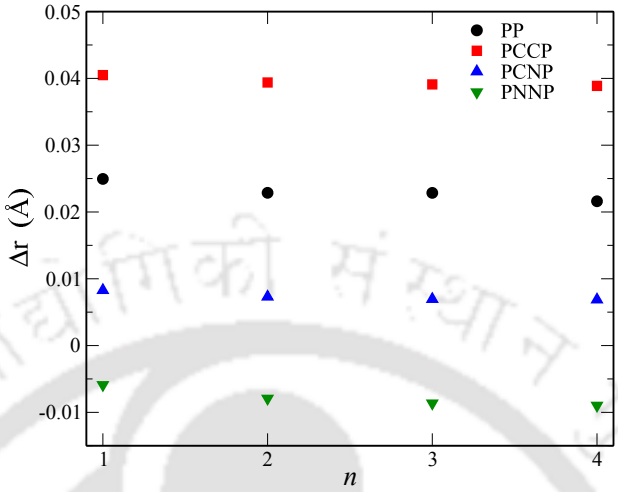

FIGURE 6.6: Δr values of the studied molecules. Two different equations are used to calculate Δr for PP and other three π-spaced oligomers, and details of these calculations are mentioned in the text below.

Δr values obtained for the studied molecules are shown in Figure 6.6. Δr values are calculated as the difference between the average lengths of single bonds and double bonds using the following equation for PP oligomers, $\Delta r = \frac{r_a s + r_c s + r_e s}{3n} - \frac{r_b s + r_d s}{2n}$, while the equation $\Delta r = \frac{r_a s + r_c s + r_e s + r_g s}{4n} - \frac{r_b s + r_d s + r_f s}{3n}$ is used in cases of PCCP, PCNP and PNNP oligomers.[243] Here, r_x is the bond length of the "x" bond, which is shown in Figure 6.1. In cases of PCNP and PNNP oligomers, bonds associated with N-atoms are not considered during the calculation.[192] As shown in Figure 6.6, the variation in BLA values with the increase of chain length is negligible. Differences between BLAs of two successive oligomers are $\leq$ 0.002 Å. Cross-conjugation in the main chain[256] and large interunit dihedral angles may be the possible reasons for the above result. It is important to mention that large differences seen in Δr values between PCCP and PCNP/PNNP oligomers are because of exclusion of -C=N- and -C–N- bonds in the Δr calculation for PCNP and PNNP oligomers. For effective comparison, if the bonds similar to N-atom containing bonds in $(PCNP)_4$ and $(PNNP)_4$ are excluded in $(PCCP)_4$, the Δrs of $(PCCP)_4$ become 0.009 and -0.005 Å, respectively, much closer to the Δrs of $(PCNP)_4$ and $(PNNP)_4$. Thus, smaller Δr values in cases of PCNP/PNNP oligomers than those

for PCCP oligomers does not imply that former oligomers are more conjugated than the latter ones.

6.2.2.2 Dipole Moment

μ_g and μ_e values are obtained from SCF and TDDFT CI densities, respectively, and $\Delta\mu_{ge}$ was calculated from the relationship: $\Delta\mu_{ge} = [(\mu_{gx} - \mu_{ex})^2 + (\mu_{gy} - \mu_{ey})^2 + (\mu_{gz} - \mu_{ez})^2]^{1/2}$.[37,257] μ_g, μ_e and $\Delta\mu_{ge}$ of the studied molecules are plotted in Figure 6.7, and reported in Table A14. In the case of PP, μ_g value for the dimer is 0.19 Debye smaller than that for the monomer as a result of cancellation of bond dipole moments. However, from dimer onwards, the μ_g gradually increases with the increase in

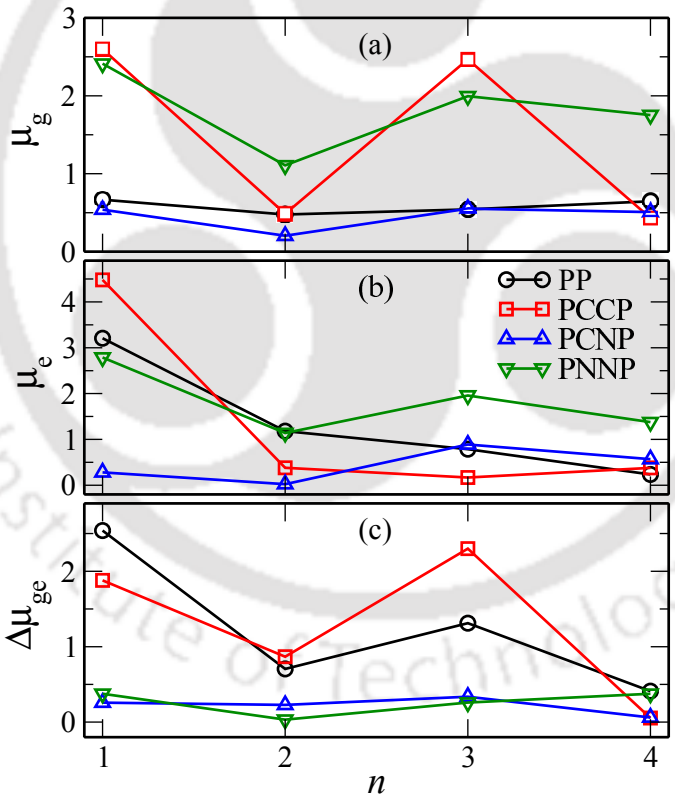

FIGURE 6.7: Dipole moments of the studied molecules in ground states, denoted as μ_g (a) and excited states, denoted as μ_e (b). In (c), $\Delta\mu_{ge}$, i.e., change in dipole moment upon excitation is depicted. $\Delta\mu_{ge}$, the absolute difference in dipole moments between the ground and vertical excited states of the studied molecules is calculated as $\Delta\mu_{ge} = [(\mu_{gx} - \mu_{ex})^2 + (\mu_{gy} - \mu_{ey})^2 + (\mu_{gz} - \mu_{ez})^2]^{1/2}$. Here, ($\mu_{gx}$, μ_{gy}, μ_{gz}) and (μ_{ex}, μ_{ey}, μ_{ez}) are the x, y and z-components of the ground state and the vertical excited state dipole moments, respectively. All the dipole moment values are in Debye.

n, although the increment is very small ($\approx$ 0.1 Debye). In cases of D-π-A-π-D molecules, oligomers having odd number of repeating units have larger μ_g values than those for one unit smaller and larger oligomers. This is clearly seen in the case of PCCP oligomers as fluctuation range is the largest in this case. As monomer of PCCP is planar having hetero atoms only at heterocyclic rings, the opposite orientation of these heterocyclic rings in the case of even n oligomers leads to cancellation of bond dipole moments. However, the situation is different in the case of PCNP and PNNP oligomers. The presence of -C=N- and -C–N- bonds leads to improper cancellation of bond dipole moments, and μ_g of tetramers are comparatively lager than those for their respective dimers, in the cases of PCNP and PNNP systems. Figure 6.7(b) shows that monomers of PP, PCCP and PNNP and trimer of PCNP have the largest μ_e, respectively. For PP, μ_e decreases with increasing n. In the case of PCCP, dimer has a smaller μ_e than that for the monomer and from dimer onwards, the value remains almost constant. For PCNP and PNNP, oligomers having odd n have larger μ_e values compared to oligomers having n–1 and n+1 repeating units. It is also noticed that PNNP oligomers have comparatively larger μ_e than those for PCNP oligomers. As can be seen in Figure 6.7(c), for PP and PCCP, oligomers having odd n have larger $\Delta\mu_{ge}$ than those for oligomers having one unit smaller and/or larger chain length. For both the cases, significant change in $\Delta\mu_{ge}$ value is seen with the increase of n. However, PCNP and PNNP have similar $\Delta\mu_{ge}$ values which do not vary significantly with the increase in chain length.

6.2.2.3 IPs and EAs

IP(v)s and EA(v)s of the studied systems are shown in Figure 6.8, and reported in Table A15. IP(v) and EA(v) values decrease and increase, respectively, with increase in chain length. For monomers, the order of IP(v) is PCCP < PCNP < PP < PNNP. From dimer onwards, the order changes to PCCP < PP < PCNP < PNNP. However, unlike IP(v), the order of EA(v) does not get disrupted with the increase in chain length and it remains as PP < PCCP < PCNP < PNNP. IP(v) and EA(v) values are often calculated by $-E_H$ and $-E_L$, respectively.[29,145,258] For comparison purpose, E_H and E_L

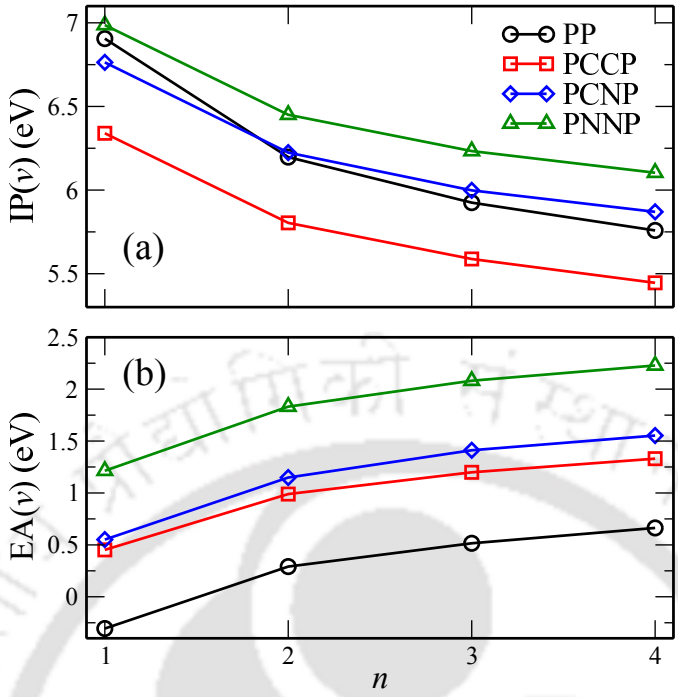

FIGURE 6.8: Vertical IP(v)s (a) and EA(v)s (b) of the studied molecules obtained at the B3LYP/6-31++G(d,p)//B3LYP/6-31G(d,p) level.

are also reported in Table A15 and plotted in Figure 6.9. As expected, E_{H} and E_{L} values gradually increase and decrease, respectively, with the increase in n. For each n, the orders of E_{H} and E_{L} are PNNP < PCNP < PP < PCCP and PNNP < PCNP < PCCP < PP, respectively. Also it is clear that for each oligomer, the orders of IP(v) and EA(v) are the same to those of $-E_{\mathrm{H}}$ and $-E_{\mathrm{L}}$, respectively. However, IP(v) and EA(v) values are larger and smaller by 0.61-1.45 eV than $-E_{\mathrm{H}}$ and $-E_{\mathrm{L}}$, respectively, and these differences decrease with increase in chain length.

6.2.2.4 Energy Gaps and Binding Energy

Variation of fundamental and optical band gaps with respect to $1/n$ are shown in Figure 6.10. These values are reported in Table A15 (see Appendix IV). Results show that both $E_{\mathrm{g}}^{\mathrm{fund}}$ and $E_{\mathrm{g}}^{\mathrm{hl}}$ decrease with the increase in n, and the orders of variation for each n among the four sets of studied systems remains the same for both the cases. However, values of $E_{\mathrm{g}}^{\mathrm{fund}}$ are 1.25 - 2.88 eV larger than the corresponding $E_{\mathrm{g}}^{\mathrm{hl}}$ values. It

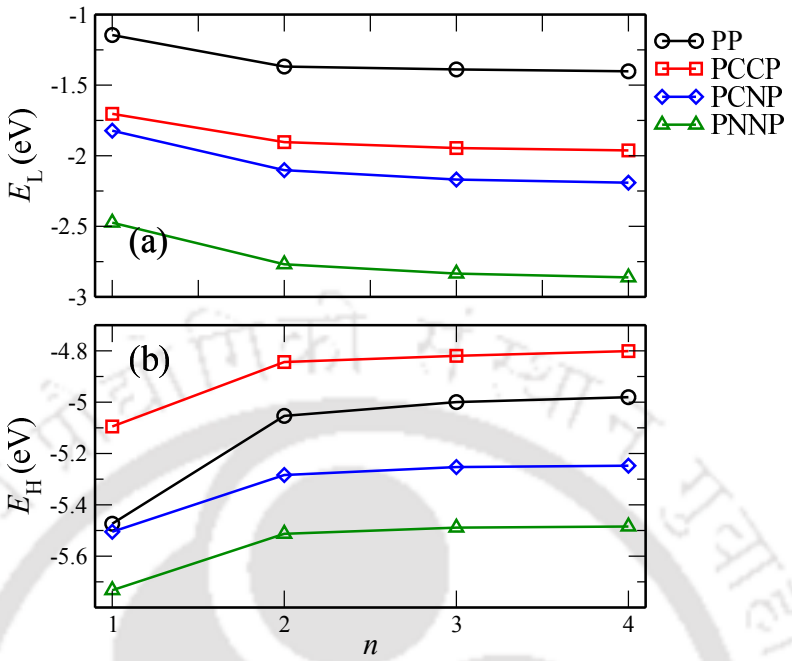

FIGURE 6.9: Energies of HOMOs (E_H) and LUMOs (E_L) of the studied molecules calculated at the B3LYP/6-31++G(d,p)//B3LYP/6-31G(d,p) level.

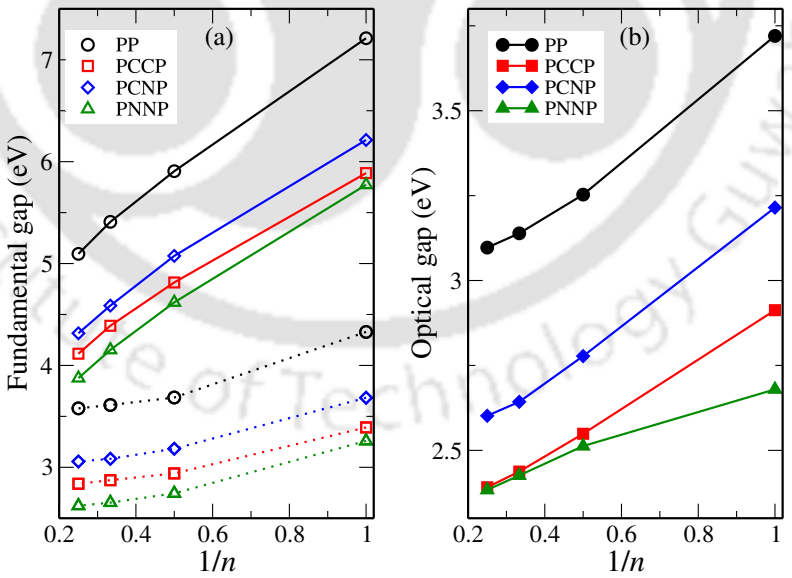

FIGURE 6.10: Fundamental (a) and optical (b) band gaps of the studied molecules. Fundamental gap is calculated in two different ways; 1. as E_H - E_L denoted as E_g^{hl} in text and 2. as IP - EA denoted as E_g^{fund} in text. In (a), dotted and solid lines represent the E_g^{hl} and E_g^{fund} values, respectively.

is worth mentioning that differences between E_g^{fund} and E_g^{hl} decrease with the increase of chain length, and these two may meet at the infinite chain length, similar to previous works.[31,259]

For the studied systems, E_g^{opt} *versus* $1/n$ is plotted in Figure 6.10 (b). Similar to E_g^{fund}, E_g^{opt} decreases with the increase in n and the order of its variation for each n among the studied systems is the same as E_g^{fund}. However, E_g^{opt} values are always much smaller than E_g^{fund} values. As expected, the presence of vinylene-, azomethine- and azo-linkages between heterocyclic rings effectively reduces both E_g^{fund} and E_g^{opt} values compared to PP oligomers. In chapter 4, it is reported that linear conformers of azomethine-linked oligomers have smaller E_g^{hl} and E_g^{opt} values compared to those for their vinylene counterparts. However, in the present case, planar repeating units of PCCP oligomers result in smaller E_g^{hl} and E_g^{opt} compared to PCNP oligomers having non-planar repeating units. It is also noticed that the slope of the line connecting E_g^{opt} of PNNP oligomers is different from those for other systems, and values of E_g^{opt} of $(PNNP)_{3-4}$ are very close to the respective PCCP oligomers of the same chain length.

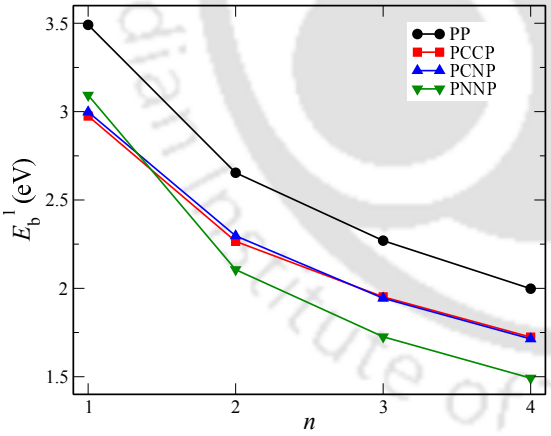

FIGURE 6.11: Binding energies (E_b^1) of the hole-electron pair in studied molecules calculated as $E_b^1 = E_g^{fund} - E_g^{opt}$. Here, E_g^{fund} = IP - EA and E_g^{opt} is the first excitation energy of a molecule.

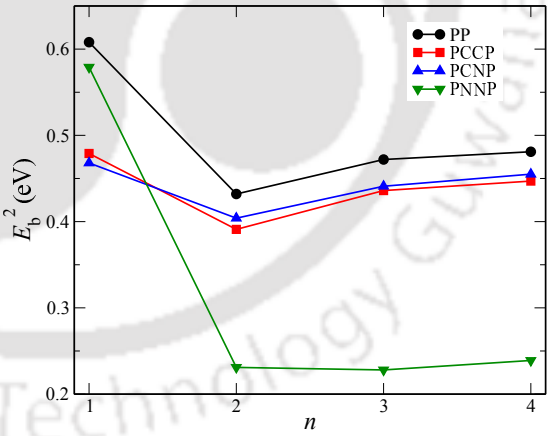

FIGURE 6.12: Binding energies (E_b^2) of the hole-electron pair in studied molecules, calculated as: $E_b^2 = E_g^{hl} - E_g^{opt}$. Here, $E_g^{hl} = E_L$-E_H, and E_g^{opt} is the first excitation energy of a molecule.

Here, binding energies are calculated in two different ways: $E_b^1 = E_g^{fund} - E_g^{opt}$ and $E_b^2 = E_g^{hl} - E_g^{opt}$. E_b^1 and E_b^2 are plotted in Figures 6.11 and 6.12, respectively,

and listed in Table A15. As can be seen in Figure 6.11, E_b^1 decreases with increasing chain length as the exciton gets extra space to span over the oligomer chain.[31] It is interesting to note that the presence of vinylene-, azomethine- and azo-linkages in the repeating unit helps to reduce the binding energy by enhancing the π conjugation in the backbone chain, which may help in the separation of electron-hole pair. For each n, E_b^1 values of PCCP and PCNP oligomers are similar and these two have nearly 0.27-0.39 eV smaller E_b^1 values compared to corresponding PP oligomers. PNNP oligomers have the smallest E_b^1 values and these values are $\sim$ 0.5 eV smaller than the PP oligomers. As shown in Figure 6.12, compared to E_b^1, values E_b^2 are quite smaller and the order is completely different, i.e., the E_b^2 does not decrease with the increase of n. Thus, for our studied systems, approximating the fundamental band gap as the HOMO-LUMO energy difference results in incorrect binding energy.

6.2.2.5 Absorption Spectra

Absorption spectra of the studied molecules are shown in Figure 6.13. As can be seen, for all the cases, major absorption bands get red shifted with the increase in chain length. Absorption spectra of PCCP are broader compared to other oligomers. Important electronic transitions, their oscillator strengths and major molecular orbitals involved in these transitions are reported in Table 6.2. In the case of monomers, transitions from ground state to an excited state other than S_1 are the most prominent transitions, and these transitions are mainly dominated by excitation from occupied orbitals other than HOMO to unoccupied orbitals other than LUMO. From dimer onwards, first excitations are the most important transitions and their oscillator strengths increase with the increase in chain length. In cases of PCCP and PCNP, HOMO $\rightarrow$ LUMO transition dominate the first excitation. Similar results are obtained for $(PP)_2$ and $(PNNP)_2$. However, for $(PP)_{3-4}$ and $(PNNP)_{3-4}$, $S_0 \rightarrow S_1$ is dominated by HOMO to LUMO+N, where N is 1 and 2 for trimer and tetramer, respectively. Although $S_0 \rightarrow S_1$ is the major electronic transition for PCCP oligomers, other electronic transitions also have significant oscillator strengths which makes their spectra broad. For example, in the

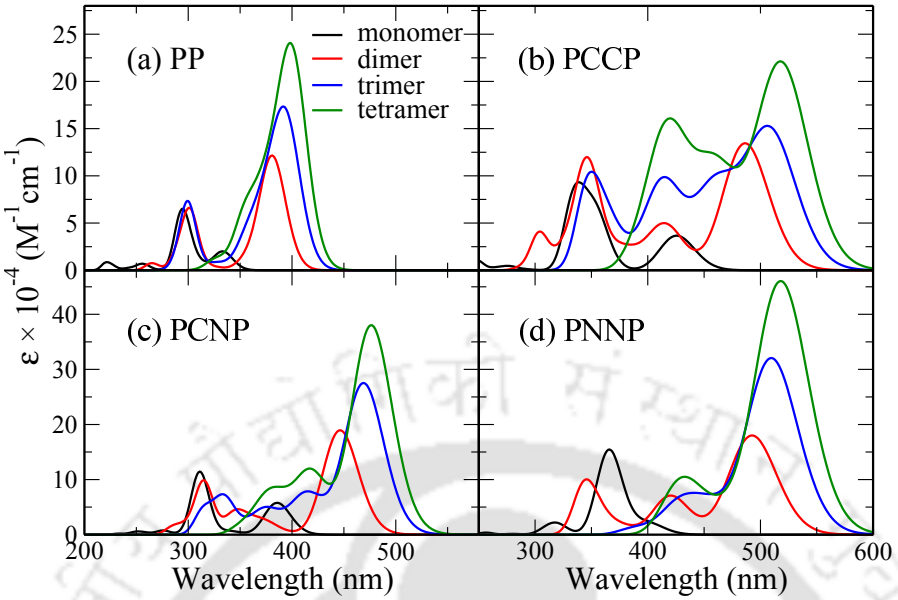

FIGURE 6.13: Absorption spectra of the studied molecules. Full width at half maximum of each spectrum is 2000 cm^{-1}.

TABLE 6.2: Electronic transition data obtained by the TDDFT/B3LYP/6-31++G(d,p) level over the optimized geometries obtained at the B3LYP/6-31G(d,p) level of theory.

compounds	m	E_g(eV)	f_{osc}	configurations	compounds	m	E_g(eV)	f_{osc}	Configurations
$(PP)_1$	1	3.72	0.18	H→L(93%)	$(PCCP)_1$	1	2.91	0.34	H→L(97%)
	3	4.20	0.46	H−1→L+1(93%)		3	3.50	0.53	H−1→L+1(97%)
$(PP)_2$	1	3.25	1.10	H→L(88%)		4	3.70	0.74	H→L+1(66%)
$(PP)_3$	1	3.14	1.36	H→L+1(80%)					H−1→L(33%)
$(PP)_4$	1	3.10	2.04	H→L+2(61%)	$(PCCP)_2$	1	2.55	1.24	H→L(92%)
					$(PCCP)_3$	1	2.44	1.34	H→L(88%)
					$(PCCP)_4$	1	2.39	2.01	H→L(73%)
$(PCNP)_1$	1	3.22	0.531	H→L(98%)	$(PNNP)_1$	1	2.68	0.00	H−2→L(70%)
	3	3.96	0.55	H−1→L+1(97%)		5	3.39	1.42	H−1→L(70%)
	4	4.00	0.50	H−1→L(58%)	$(PNNP)_2$	1	2.51	1.57	H→L(90%)
				H→L+1(32%)	$(PNNP)_3$	1	2.43	2.68	H→L+1(57%)
$(PCNP)_2$	1	2.78	1.74	H→L(94%)	$(PNNP)_4$	1	2.38	3.77	H→L+2(39%)
$(PCNP)_3$	1	2.64	2.52	H→L(87%)					H−1→L+1(28%)
$(PCNP)_4$	1	2.60	3.49	H→L(75%)					

case of $(PCCP)_4$, in addition to first electronic transition, $S_0 \rightarrow S_4$ (463.69 nm, f_{osc} = 0.80), $S_0 \rightarrow S_{11}$ (423.45 nm, $f_{osc} = 0.72$) and $S_0 \rightarrow S_{15}$ (409.61 nm, $f_{osc} = 0.56$) transitions significantly contribute to the absorption spectrum, as shown in Figure 6.13(b). As can be seen, the extension of π conjugation by inserting π spacers between heterocyclic rings in PP oligomers leads to red-shift in absorption spectra. As an example, maximum absorption peak of $(PCCP)_4$ is at 518.47 nm compared to 400.35 nm of $(PP)_4$.

6.3 Salient findings

This chapter reports the change of optical and electronic properties of a cross-conjugated molecule upon increase in conjugation length of its two conjugated branches. Four types of cross-conjugated systems are chosen for this study, namely PP, PCCP, PCNP and PNNP, where PP is a D-A-D type and other three are D-π-A-π-D types. Here, *N*-methylpyrrole and pyridine rings are D and A units, respectively, and vinylene, azomethine and azo linkages are used as π spacers. For both B3LYP and CAM-B3LYP functionals, conformation search of monomers shows that geometries of the most stable structures of four different systems are distinctly different. To obtain absorption spectra, TDDFT/B3LYP/6-31++G(d,p) level over the optimized structures obtained at the B3LYP/6-31G(d,p) level is found to be a suitable method of choice in terms of both accuracy and computational cost. Our results also show that for conjugated systems, CAM-B3LYP functional with default μ, α and β parameters are not reliable for the TDDFT calculation.

Fundamental and optical gaps of D-π-A-π-D types oligomers are smaller than those for PP oligomers, for the same chain length. In addition, the major absorption peaks get shifted towards longer wavelengths after insertion of π linkers, in comparison to the D-A-D system. As insertion of π spacers increases conjugation length of the system, an exciton gets extra space to span over the main chain in cases of D-π-A-π-D types oligomers, resulting reduction in binding energy of a hole-electron pair. Similarly, properties like IP, EA, μ_g, μ_e and $\Delta\mu_{ge}$ are altered significantly for D-π-A-π-D type oligomers compared to the same chain length of PP oligomers.

Summary and conclusions

In this dissertation, structural, optical and electronic properties of heterocyclic through– and cross–conjugated oligomers are studied using DFT and TDDFT methods. In addition to linearly conjugated systems, secondary structures such as foldamers are also taken into consideration. Our studies unearthed important structure-property and conformer-property relationships, which will assist in tuning geometries and properties of organic materials.

In *chapter 3*, structural and optoelectronic properties of fifteen thiophene–azomethine–pyrrole-based systems are studied. It is observed that these properties can be tuned by the steric and electronic effects of substituents. In the case of two of the studied oligomers, the O$\cdots$S interaction helps in planarizing the main chain, and this enhances the π-electron delocalization across the chain, resulting in an optical gap of $\sim$1.75 eV. Optoelectronic properties of few of the studied azomethines are found to be suitable for the absorption layer of an organic solar cell. To study the charge injection and transport properties, eight are carefully chosen out of fifteen azomethines. Few of these azomethines have large hole and electron mobilities. However, these azomethines are only suitable for the hole injection process, as barrier height is larger than 1 eV for the electron injection process. Further, anion of these materials are not stable enough due to small EA values ($<$ 3 eV). Consequently, these oligomers are not appropriate materials for the ETL. However, small hole injection barrier and large hole mobilities of few of these heterocyclic-azomethines indicate their suitability for the HTL.

In *chapter 4*, structural and optoelectronic properties of helical and nonhelical conformers of vinylene- and azomethine-linked heterocyclic oligomers are studied. For each oligomer, three different conformations are considered: one foldamer and two linear conformers. Out of six foldamers, furan-azomethine and pyrrole-azomethine oligomers are irregular foldamers, while

other four oligomers form helix-like structures. Dispersion correction term in the B3LYP-D3 functional results in drastic change in the ground state geometries of foldamers, compared to those obtained by the B3LYP functional, except in the case of thiophene-azomethine oligomers. Calculation of the interaction energy between two adjacent turns of a helix indicates that the B3LYP-D3 functional is suitable for these types of foldamers, where the π-π interaction plays an important role in the determination of ground state geometries. It is observed that for all the studied vinylene-linked oligomers, stabilities of conformers change with the increase of chain length. In these cases, while a linear conformer is the most stable for $n < u$, a helical conformer becomes the most stable for $n \geq u$. Optical and electronic properties of foldamers are quite different than those of their respective linearly conjugated conformers. In the case of foldamers, more than one electronic transitions contribute significantly to their absorption spectra. All these important transitions are dominated by transitions other than the HOMO to LUMO excitations. Except thiophene-azomethines, first excitations of all these foldamers have negligible f_{osc}s. However, in the case of linearly conjugated oligomers, the first excitation is the most important electronic transition, which is mainly dominated by the HOMO→LUMO excitation. In the case of few linear azomethine-linked oligomers, the $S_0 \rightarrow S_2$ transition has also significant f_{osc} value. Unlike other helical oligomers, in the case of thiophene-azomethines, in addition to other electronic transitions, first excitations also have significant f_{osc}s.

In *chapter 5*, structural and optoelectronic properties of helical conformers of pyridine-furan, pyridine-pyrrole and pyridine-thiophene based oligomers are studied in detail. Here, the B3LYP-D3 is again found to be a suitable functional to obtain ground state geometries of helical oligomers. For these oligomers, the HOMO–LUMO gap and the first excitation energy vary irregularly with the increase of chain length, making it impossible to extrapolate for polymer value. μ_{g} of these helices fluctuate between a certain range, and for a particular oligomer, it depends upon its conformation, n and u. In cases of all the studied oligomers, for $n < u$, the first electronic transitions have significant f_{osc}s, while the same has negligible f_{osc}s for $n \geq u$. For helical oligomers, more than one electronic transitions have sufficiently large f_{osc}s, and these transitions are mainly dominated by other than FMOs.

In *chapter 6*, structural, electronic and optical properties of pyridine-pyrrole based cross-conjugated oligomers are studied. This chapter reveals that these properties of a neutral cross-conjugated oligomers can be effectively tuned by the insertion of π-spacers, such as vinylene-, azomethine- and azo linkages in the main chain. The main peak of absorption spectrum is shifted

towards the red end upon extending the conjugation of two conjugated fragments of the cross-conjugated repeating unit. Similarly, properties like IP, EA, E_g^{opt}, E_g^{hl}, E_g^{fund}, dipole moments are altered significantly for π-spaced systems compared to the primary pyridine-pyrrole-based oligomer of the same chain length. In addition, it is noticed that default parameters (α, β and μ) of the CAM-B3LYP functional are not suitable for conjugated systems, especially for the TDDFT calculations. Results can be improved by tuning these parameters, and in our case, tuned parameters for the vinylene-linked system are (μ, α, β) = (0.050, 0.1625, 0.8375).

Bibliography

[1] H. Shirakawa, E. J. Louis, A. G. MacDiarmid, C. K. Chiang, and A. J. Heeger, *Synthesis of electrically conducting organic polymers: Halogen derivatives of polyacetylene, $(CH)_x$*, J. C. S. Chem. Comm. 578 (1977).

[2] H. Shirakawa, A. G. McDiarmid, and A. J. Heeger, *Twenty-five years of conducting polymers*, Chem. Commun. 1 (2003).

[3] A. C. Grimsdale, K. Leok Chan, R. E. Martin, P. G. Jokisz, and A. B. Holmes, *Synthesis of light-emitting conjugated polymers for applications in electroluminescent devices*, Chem. Rev. **109**, 897 (2009).

[4] Y.-J. Cheng, S.-H. Yang, and C.-S. Hsu, *Synthesis of conjugated polymers for organic solar cell applications*, Chem. Rev. **109**, 5868 (2009).

[5] I. Etxebarria, J. Ajuria, and R. Pacios, *Solution-processable polymeric solar cells: A review on materials, strategies and cell architectures to overcome 10%*, Org. Electron. **19**, 34 (2015).

[6] C. Wang, H. Dong, W. Hu, Y. Liu, and D. Zhu, *Semiconducting π-conjugated systems in field-effect transistors: A material odyssey of organic electronics*, Chem. Rev. **112**, 2208 (2012).

[7] F. C. Krebs, N. Espinosa, M. Hösel, R. R. Søndergaard, and M. Jørgensen, *25th anniversary article: Rise to power–OPV-based solar parks*, Adv. Mater. **26**, 29 (2014).

[8] M. Kuik, G.-J. A. H. Wetzelaer, H. T. Nicolai, N. I. Craciun, D. M. De Leeuw, and P. W. M. Blom, *25th anniversary article: Charge transport and recombination in polymer light-emitting diodes*, Adv. Mater. **26**, 512 (2014).

[9] H. Sirringhaus, *25th anniversary article: Organic field-effect transistors: The path beyond amorphous silicon*, Adv. Mater. **26**, 1319 (2014).

[10] H. Dong, X. Fu, J. Liu, Z. Wang, and W. Hu, *25th anniversary article: Key points for high-mobility organic field-effect transistors*, Adv. Mater. **25**, 6158 (2013).

[11] L. Dou, J. You, Z. Hong, Z. Xu, G. Li, R. A. Street, and Y. Yang, *25th anniversary article: A decade of organic/polymeric photovoltaic research*, Adv. Mater. **25**, 6642 (2013).

[12] J. Liu, X. Wu, X. Shi, J. Wang, Z. Min, Y. Wang, M. Yang, and G. He, *Highly efficient and stable electron injection layer for inverted organic light-emitting diodes*, ACS Appl. Mater. Interfaces **7**, 6438 (2015).

[13] L. Xiao, Z. Chen, B. Qu, J. Luo, S. Kong, Q. Gong, and J. Kido, *Recent progresses on materials for electrophosphorescent organic light-emitting devices*, Adv. Mater. **23**, 926 (2011).

[14] C. L. Chochos and S. A. Choulis, *How the structural deviations on the backbone of conjugated polymers influence their optoelectronic properties and photovoltaic performance*, Prog. Polym. Sci. **36**, 1326 (2011).

[15] L.-H. Xie, C.-R. Yin, W.-Y. Lai, Q.-L. Fan, and W. Huang, *Polyfluorene-based semiconductors combined with various periodic table elements for organic electronics*, Prog. Polym. Sci. **37**, 1192 (2012).

[16] W. Wu, Y. Liu, and D. Zhu, *π-conjugated molecules with fused rings for organic field-effect transistors: design, synthesis and applications*, Chem. Soc. Rev. **39**, 1489 (2010).

[17] A. Bolduc, C. Mallet, and W. G. Skene, *Survey of recent advances of in the field of π-conjugated heterocyclic azomethines as materials with tuneable properties*, Sci. China: Chem. **56**, 3 (2013).

[18] B. M. Wong and J. G. Cordaro, *Electronic properties of vinylene-linked heterocyclic conducting polymers: Predictive design and rational guidance from DFT calculations*, J. Phys. Chem. C **115**, 18333 (2011).

[19] F.-C. Tsai, C.-C. Chang, C.-L. Liu, W.-C. Chen, and S. A. Jenekhe, *New thiophene-linked conjugated poly(azomethine)s: Theoretical electronic structure, synthesis, and properties*, Macromolecules **38**, 1958 (2005).

[20] R. S. Kularatne, H. D. Magurudeniya, P. Sista, M. C. Biewer, and M. C. Stefan, *Donor–acceptor semiconducting polymers for organic solar cells*, J. Polym. Sci. Part A, Polym. Chem. **51**, 743 (2013).

[21] L. Pandey, C. Risko, J. E. Norton, and J.-L. Brédas, *Donor–acceptor copolymers of relevance for organic photovoltaics: A theoretical investigation of the impact of chemical structure modifications on the electronic and optical properties*, Macromolecules **45**, 6405 (2012).

[22] N. F. Phelan and M. Orchin, *Cross conjugation*, J. Chem. Educ. **45**, 633 (1968).

[23] C. Castiglioni, G. Zerbi, and M. Gussoni, *Peierls distortion in trans polyacetylene: Evidence from infrared intensities*, Solid State Commun. **56**, 863 (1985).

[24] D. Jacquemin and C. Adamo, *Bond length alternation of conjugated oligomers: Wave function and DFT benchmarks*, J. Chem. Theory Comput. **7**, 369 (2011).

[25] W. Kuhn, *Über das absorptionsspektrum der polyene*, Helv. Chim. Acta **31**, 1780 (1948).

[26] S. S. Zade, N. Zamoshchik, and M. Bendikov, *From short conjugated oligomers to conjugated polymers. Lessons from studies on long conjugated oligomers*, Acc. Chem. Res. **44**, 14 (2011).

[27] S. S. Zade and M. Bendikov, *From oligomers to polymer: Convergence in the HOMO-LUMO gaps of conjugated oligomers*, Org. Lett. **8**, 5243 (2006).

[28] J. Gierschner, J. Cornil, and H.-J. Egelhaaf, *Optical bandgaps of π-conjugated organic materials at the polymer limit: Experiment and theory*, Adv. Mater. **19**, 173 (2007).

[29] J.-L. Brédas, *Mind the gap!*, Mater. Horiz. **1**, 17 (2014).

[30] U. Salzner, *Electronic structure of conducting organic polymers: insights from time-dependent density functional theory*, WIREs Comput. Mol. Sci. **4**, 601 (2014).

[31] R. S. Bhatta and M. Tsige, *Chain length and torsional dependence of exciton binding energies in P3HT and PTB7 conjugated polymers: A first-principles study*, Polymer **55**, 2667 (2014).

[32] B. Semire and O. A. Odunola, *Semiempirical and density functional thoery study on structure of fluoromethylfuran oligomers.*, Aust. J. Basic & Appl. Sci. **5**, 354 (2011).

[33] R.-F. Chen, L.-Y. Liu, H. Fu, C. Zheng, H. Xu, Q.-L. Fan, and W. Huang, *The influence of the linkage pattern on the optoelectronic properties of polysilafluorenes: A theoretical study*, J. Phys. Chem. B **115**, 242 (2011).

[34] J. Xu, L. Wen, W. Zhou, J. Lv, Y. Guo, M. Zhu, H. Liu, Y. Li, and L. Jiang, *Asymmetric and symmetric dipole–dipole interactions drive distinct aggregation and emission behavior of intramolecular charge-transfer molecules*, J. Phys. Chem. C **113**, 5924 (2009).

[35] Y.-L. Liu, J.-K. Feng, and A.-M. Ren, *Theoretical study on photophysical properties of bis-dipolar diphenylamino-endcapped oligoarylfluorenes as light-emitting materials*, J. Phys. Chem. A **112**, 3157 (2008).

[36] B. Carsten, J. M. Szarko, L. Lu, H. J. Son, F. He, Y. Y. Botros, L. X. Chen, and L. Yu, *Mediating solar cell performance by controlling the internal dipole change in organic photovoltaic polymers*, Macromolecules **45**, 6390 (2012).

[37] P. D. Homyak, J. Tinkham, P. M. Lahti, and E. B. Coughlin, *Thieno[3,4-b]thiophene acceptors with alkyl, aryl, perfluoroalkyl, and perfluorophenyl pendants for donor–acceptor low bandgap polymers*, Macromolecules **46**, 8873 (2013).

[38] B. Carsten, J. M. Szarko, H. J. Son, W. Wang, L. Lu, F. He, B. S. Rolczynski, S. J. Lou, L. X. Chen, and L. Yu, *Examining the effect of the dipole moment on charge separation in donor−acceptor polymers for organic photovoltaic applications*, J. Am. Chem. Soc. **133**, 20468 (2011).

[39] T. Xu, L. Lu, T. Zheng, J. M. Szarko, A. Schneider, L. X. Chen, and L. Yu, *Tuning the polarizability in donor polymers with a thiophenesaccharin unit for organic photovoltaic applications*, Adv. Funct. Mater. **24**, 3432 (2014).

[40] B. Valeur, *Molecular Fluorescence: Principles and Applications* (Wiley, 2001).

[41] B. Qi and J. Wang, *Fill factor in organic solar cells*, Phys. Chem. Chem. Phys. **15**, 8972 (2013).

[42] Y. Shen, A. R. Hosseini, M. H. Wong, and G. G. Malliaras, *How to make ohmic contacts to organic semiconductors*, ChemPhysChem **5**, 16 (2004).

[43] R. A. Nawrocki, E. Pavlica, N. Ćelić, D. Orlov, M. Valant, D. Mihailović, and G. Bratina, *Fabrication of poly(3-hexylthiophene) nanowires for high-mobility transistors*, Org. Electron. **30**, 92 (2016).

[44] Y.-K. Lan, C. H. Yang, and H.-C. Yang, *Theoretical investigations of electronic structure and charge transport properties in polythiophene-based organic field-effect transistors*, Polym. Int. **59**, 16 (2010).

[45] Y. Wen and Y. Liu, *Recent progress in n-channel organic thin-film transistors*, Adv. Mater. **22**, 1331 (2010).

[46] A. Zhugayevych and S. Tretiak, *Theoretical description of structural and electronic properties of organic photovoltaic materials*, Annu. Rev. Phys. Chem. **66**, 305 (2015).

[47] K. Watanabe and K. Akagi, *Helically assembled π-conjugated polymers with circularly polarized luminescence*, Sci. Technol. Adv. Mater. **15**, 044203 (2014).

[48] S. Tang and J. Zhang, *First principles investigation on the key factors of broad absorption spectra and electronic properties for oligothiophene and its derivatives for solar cells*, Int. J. Quantum Chem. **111**, 2089 (2011).

[49] J. D. Ripoll, A. Serna, D. Guerra, and A. Restrepo, *Electronic structure calculations on helical conducting polymers*, J. Phys. Chem. A **114**, 10917 (2010).

[50] R. D. Parra, *Folding oligomers of difluorinated thienylfurans: a DFT study*, Phys. Chem. Chem. Phys. **12**, 523 (2010).

[51] P. A. Limacher and H. P. Lüthi, *Cross-conjugation*, WIREs Comput. Mol. Sci. **1**, 477 (2011).

[52] R. S. Ashraf, I. Meager, M. Nikolka, M. Kirkus, M. Planells, B. C. Schroeder, S. Holliday, M. Hurhangee, C. B. Nielsen, H. Sirringhaus, et al., *Chalcogenophene comonomer comparison in small band gap diketopyrrolopyrrole-based conjugated polymers for high-performing field-effect transistors and organic solar cells*, J. Am. Chem. Soc. **137**, 1314 (2015).

[53] M. Nakano, I. Osaka, and K. Takimiya, *Naphthodithiophene diimide (NDTI)-based semiconducting copolymers: From ambipolar to unipolar n-type polymers*, Macromolecules **48**, 576 (2015).

[54] R. Chen, Y. Wang, T. Chen, H. Li, C. Zheng, K. Yuan, Z. Wang, Y. Tao, C. Zheng, and W. Huang, *Heteroatom-bridged benzothiazolyls for organic solar cells: A theoretical study*, J. Phys. Chem. B **119**, 583 (2015).

[55] S. Sharma, N. Zamoshchik, and M. Bendikov, *Polyfurans: A computational study*, Isr. J. Chem. **54**, 712 (2014).

[56] N. Zamoshchik, Y. Sheynin, and M. Bendikov, *Toward the rational design of conjugated oligomers and polymers: Systematic study of the substituent effect in oligothiophenes*, Isr. J. Chem. **54**, 723 (2014).

[57] O. Gidron and M. Bendikov, *α-oligofurans: An emerging class of conjugated oligomers for organic electronics*, Angew. Chem. Int. Ed. **53**, 2546 (2014).

[58] H. Huang, N. Zhou, R. P. Ortiz, Z. Chen, S. Loser, S. Zhang, X. Guo, J. Casado, J. T. López Navarrete, X. Yu, et al., *Alkoxy-functionalized thienyl-vinylene polymers for field-effect transistors and all-polymer solar cells*, Adv. Funct. Mater. **24**, 2782 (2014).

[59] F. D. Maria, M. Gazzano, A. Zanelli, G. Gigli, A. Loiudice, A. Rizzo, M. Biasiucci, E. Salatelli, P. D' Angelo, and G. Barbarella, *Synthesis and photovoltaic properties of regioregular head-to-head substituted thiophene hexadecamers*, Macromolecules **45**, 8284 (2012).

[60] A. S. Özen, C. Atilgan, and G. Sonmez, *Noncovalent intramolecular interactions in the monomers and oligomers of the acceptor and donor type of low band gap conducting polymers*, J. Phys. Chem. C **111**, 16362 (2007).

[61] G. R. Hutchison, M. A. Ratner, and T. J. Marks, *Electronic structure and band gaps in cationic heterocyclic oligomers. Multidimensional analysis of the interplay of heteroatoms, substituents, molecular length, and charge on redox and transparency characteristics*, J. Phys. Chem. B **109**, 3126 (2005).

[62] A. Mishra, C.-Q. Ma, and P. Bäuerle, *Functional oligothiophenes: Molecular design for multidimensional nanoarchitectures and their applications*, Chem. Rev. **109**, 1141 (2009).

[63] S. Tang and J. Zhang, *Design of donors with broad absorption regions and suitable frontier molecular orbitals to match typical acceptors via substitution on oligo(thienylenevinylene) toward solar cells*, J. Comput. Chem. **33**, 1353 (2012).

[64] S. Ko, R. Mondal, C. Risko, J. K. Lee, S. Hong, M. D. McGehee, J.-L. Brédas, and Z. Bao, *Tuning the optoelectronic properties of vinylene-linked donor–acceptor copolymers for organic photovoltaics*, Macromolecules **43**, 6685 (2010).

[65] Y. Wang, J. Ma, and Y. Jiang, *Tuning of electronic structures of poly(p-phenylenevinylene) analogues of phenyl, thienyl, furyl, and pyrrolyl by double-bond linkages of group 14 and 15 elements*, J. Phys. Chem. A **109**, 7197 (2005).

[66] Y. Fu, H. Cheng, and R. L. Elsenbaumer, *Electron-rich thienylene–vinylene low bandgap polymers*, Chem. Mater. **9**, 1720 (1997).

[67] M. Turbiez, P. Frère, and J. Roncali, *Oligothienylenevinylenes incorporating 3,4-ethylenedioxythiophene (EDOT) units*, Tetrahedron **61**, 3045 (2005).

[68] P. Frère, J.-M. Raimundo, P. Blanchard, J. Delaunay, P. Richomme, J.-L. Sauvajol, J. Orduna, J. Garin, and J. Roncali, *Effect of local molecular structure on the chain-length dependence of the electronic properties of thiophene-based π-conjugated systems*, J. Org. Chem. **68**, 7254 (2003).

[69] A. Bolduc, A. Al Ouahabi, C. Mallet, and W. G. Skene, *Insight into the isoelectronic character of azomethines and vinylenes using representative models: A spectroscopic and electrochemical study*, J. Org. Chem. **78**, 9258 (2013).

[70] D. Işik, C. Santato, S. Barik, and W. G. Skene, *Charge-carrier transport in thin films of π-conjugated thiopheno-azomethines*, Org. Electron. **13**, 3022 (2012).

[71] S. Radhakrishnan, R. Parthasarathi, V. Subramanian, and N. Somanathan, *Quantum chemical studies on polythiophenes containing heterocyclic substituents: Effect of structure on the band gap*, J. Chem. Phys. **123**, 164905 (2005).

[72] H. H. Nguyen, J. H. McAliley, W. R. Batson, and D. A. Bruce, *Molecular design of functionalized m-poly(phenylene ethynylene) foldamers: from simulation to synthesis*, Macromolecules **43**, 5932 (2010).

[73] E. Yashima, K. Maeda, H. Iida, Y. Furusho, and K. Nagai, *Helical polymers: Synthesis, structures, and functions*, Chem. Rev. **109**, 6102 (2009).

[74] J. Park, T. Yu, T. Inagaki, and K. Akagi, *Helical network polymers exhibiting circularly polarized luminescence with thermal stability. Synthesis via photo-cross-link polymerizations of methacrylate derivatives in a chiral nematic liquid crystal*, Macromolecules **48**, 1930 (2015).

[75] E. M. Sánchez-Carnerero, F. Moreno, B. L. Maroto, A. R. Agarrabeitia, M. J. Ortiz, B. G. Vo, G. Muller, and S. de la Moya, *Circularly polarized luminescence by visible-light absorption in a chiral O-BODIPY dye: Unprecedented design of CPL organic molecules from achiral chromophores*, J. Am. Chem. Soc. **136**, 3346 (2014).

[76] Sudha, D. Kumar, and M. Iwamoto, *Investigation of the chiroptical behavior of optically active polyaniline synthesized from naturally occurring amino acids*, Polym. J. **45**, 160 (2013).

[77] J. E. Field, G. Muller, J. P. Riehl, and D. Venkataraman, *Circularly polarized luminescence from bridged triarylamine helicenes*, J. Am. Chem. Soc. **125**, 11808 (2003).

[78] H. Goto, E. Yashima, and Y. Okamoto, *Unusual solvent effects on chiroptical properties of an optically active regioregular polythiophene in solution*, Chirality **12**, 396 (2000).

[79] K. Watanabe, K. Suda, and K. Akagi, *Hierarchically self-assembled helical aromatic conjugated polymers*, J. Mater. Chem. C **1**, 2797 (2013).

[80] D. T. McQuade, A. E. Pullen, and T. M. Swager, *Conjugated polymer-based chemical sensors*, Chem. Rev. **100**, 2537 (2000).

[81] K. Akagi, *Helical polyacetylene: Asymmetric polymerization in a chiral liquid-crystal field*, Chem. Rev. **109**, 5354 (2009).

[82] J. Torras, O. Bertran, and C. Alemán, *Structural and electronic properties of poly(thiaheterohelicene)s*, J. Phys. Chem. B **113**, 15196 (2009).

[83] K. Tagami, M. Tsukada, Y. Wada, T. Iwasaki, and H. Nishide, *Electronic transport of benzothiophene-based chiral molecular solenoids studied by theoretical simulations*, J. Chem. Phys. **119**, 7491 (2003).

[84] S. Mathew, L. A. Crandall, C. J. Ziegler, and C. S. Hartley, *Enhanced helical folding of ortho-phenylenes through the control of aromatic stacking interactions*, J. Am. Chem. Soc. **136**, 16666 (2014).

[85] S. M. Mathew, J. T. Engle, C. J. Ziegler, and C. S. Hartley, *The role of arene–arene interactions in the folding of ortho-phenylenes*, J. Am. Chem. Soc. **135**, 6714 (2013).

[86] K. P. Divya, S. Sreejith, C. H. Suresh, D. S. Philips, and A. Ajayaghosh, *Chain folding controlled by an isomeric repeat unit: Helix formation versus random aggregation in acetylene-bridged carbazole–bipyridine co-oligomers*, Chem. Asian J. **8**, 1579 (2013).

[87] R. Liu, M. Shiotsuki, T. Masuda, and F. Sanda, *Synthesis and chiroptical properties of hydroxyphenylglycine-based poly(m-phenyleneethynylene-p-phenyleneethynylene)s*, Macromolecules **42**, 6115 (2009).

[88] N. Kiriy, E. Jähne, H.-J. Adler, M. Schneider, A. Kiriy, G. Gorodyska, S. Minko, D. Jehnichen, P. Simon, A. A. Fokin, et al., *One-dimensional aggregation of regioregular polyalkylthiophenes*, Nano Lett. **3**, 707 (2003).

[89] S. Dubus, V. Marceau, and M. Leclerc, *Helical conjugated polymers by design*, Macromolecules **35**, 9296 (2002).

[90] C. S. Hartley, *Excited-state behavior of ortho-phenylenes*, J. Org. Chem. **76**, 9188 (2011).

[91] O. Bertran, J. Torras, and C. Alemán, *Modeling the structural and electronic properties of an optically active regioregular polythiophene*, J. Phys. Chem. C **114**, 11074 (2010).

[92] R. Méreau, F. Castet, E. Botek, and B. Champagne, *Effect of the dynamical disorder on the second-order nonlinear optical responses of helicity-encoded polymer strands*, J. Phys. Chem. A **113**, 6552 (2009).

[93] E. Botek, F. Castet, and B. Champagne, *Theoretical investigation of the second-order nonlinear optical properties of helical pyridine–pyrimidine oligomers*, Chem. Eur. J. **12**, 8687 (2006).

[94] K. S. Thanthiriwatte, E. G. Hohenstein, L. A. Burns, and C. D. Sherrill, *Assessment of the performance of DFT and DFT-D methods for describing distance dependence of hydrogen-bonded interactions*, J. Chem. Theory Comput. **7**, 88 (2011).

[95] S. Grimme, J. Antony, S. Ehrlich, and H. Krieg, *A consistent and accurate ab initio parametrization of density functional dispersion correction (DFT-D) for the 94 elements H-Pu*, J. Chem. Phys. **132**, 154104 (2010).

[96] J. P. McNamara and I. H. Hillier, *Semi-empirical molecular orbital methods including dispersion corrections for the accurate prediction of the full range of intermolecular interactions in biomolecules*, Phys. Chem. Chem. Phys. **9**, 2362 (2007).

[97] Y. Zhao and D. G. Truhlar, *Hybrid meta density functional theory methods for thermochemistry, thermochemical kinetics, and noncovalent interactions: The MPW1B95 and MPWB1K models and comparative assessments for hydrogen bonding and van der Waals interactions*, J. Phys. Chem. A **108**, 6908 (2004).

[98] Z.-L. Gong, Y.-W. Zhong, and J. Yao, *Conformation-determined through-bond versus through-space electronic communication in mixed-valence systems with a cross-conjugated urea bridge*, Chem. Eur. J. **21**, 1554 (2015).

[99] N. M. Dickson-Karn, C. M. Olson, W. C. W. Leu, and C. S. Hartley, *Intramolecular charge transfer in donor-bridge-acceptor compounds with paired linearly conjugated or cross-conjugated pathways*, J. Phys. Org. Chem. **27**, 661 (2014).

[100] M. Gholami and R. R. Tykwinski, *Oligomeric and polymeric systems with a cross-conjugated π-framework*, Chem. Rev. **106**, 4997 (2006).

[101] P. Guiglion and M. A. Zwijnenburg, *Contrasting the optical properties of the different isomers of oligophenylene*, Phys. Chem. Chem. Phys. **17**, 17854 (2015).

[102] G. W. P. van Pruissen, J. Brebels, K. H. Hendriks, M. M. Wienk, and R. A. J. Janssen, *Effects of cross-conjugation on the optical absorption and frontier orbital levels of donor–acceptor polymers*, Macromolecules **48**, 2435 (2015).

[103] M. A. Christensen, E. A. Della Pia, J. Houmøller, S. Thomsen, M. Wanko, A. D. Bond, A. Rubio, S. Brøndsted Nielsen, and M. Brøndsted Nielsen, *Cross-conjugation vs. linear conjugation in donor–bridge–acceptor nitrophenol chromophores*, Eur. J. Org. Chem. **2014**, 2044 (2014).

[104] M. E. Cinar and T. Ozturk, *Thienothiophenes, dithienothiophenes, and thienoacenes: Syntheses, oligomers, polymers, and properties*, Chem. Rev. **115**, 3036 (2015).

[105] M. Heeney, C. Bailey, K. Genevicius, M. Shkunov, D. Sparrowe, S. Tierney, and I. McCulloch, *Stable polythiophene semiconductors incorporating thieno[2,3-b]thiophene*, J. Am. Chem. Soc. **127**, 1078 (2005).

[106] T. P. Voortman, D. Bartesaghi, L. J. A. Koster, and R. C. Chiechi, *Cross-conjugated n-dopable aromatic polyketone*, Macromolecules **48**, 7007 (2015).

[107] J. Song, T. Wu, X. Zhao, Y. Kan, and H. Wang, *Synthesis and molecular properties of butterfly-shaped tetrathiophene derivatives*, Tetrahedron **71**, 1838 (2015).

[108] T. Inouchi, T. Nakashima, and T. Kawai, *Charge transfer emission of T-shaped π-conjugated molecules: Impact of quinoid character on the excited state properties*, J. Phys. Chem. A **118**, 2591 (2014).

[109] S. B. Nielsen, M. B. Nielsen, and A. Rubio, *Spectroscopy of nitrophenolates in vacuo: Effect of spacer, configuration, and microsolvation on the charge-transfer excitation energy*, Acc. Chem. Res. **47**, 1417 (2014).

[110] E. Maggio, G. C. Solomon, and A. Troisi, *Exploiting quantum interference in dye sensitized solar cells*, ACS Nano **8**, 409 (2014).

[111] V. Martínez-Martínez, J. Lim, J. Bañuelos, I. López-Arbeloa, and O. Š. Miljanić, *Strong intramolecular charge transfer emission in benzobisoxazole cruciforms: solvatochromic dyes as polarity indicators*, Phys. Chem. Chem. Phys. **15**, 18023 (2013).

[112] G. C. Solomon, D. Q. Andrews, R. H. Goldsmith, T. Hansen, M. R. Wasielewski, R. P. V. Duyne, and M. A. Ratner, *Quantum interference in acyclic systems: Conductance of cross-conjugated molecules*, J. Am. Chem. Soc. **130**, 17301 (2008).

[113] S. A. Mewes, J.-M. Mewes, A. Dreuw, and F. Plasser, *Excitons in poly(para phenylene vinylene): A quantum-chemical perspective based on high-level ab initio calculations*, Phys. Chem. Chem. Phys. **18**, 2548 (2016).

[114] T. M. Cardozo, A. J. A. Aquino, M. Barbatti, I. Borges, Jr., and H. Lischka, *Absorption and fluorescence spectra of poly(p-phenylenevinylene) (PPV) oligomers: An ab Initio simulation*, J. Phys. Chem. A **119**, 1787 (2015).

[115] A. N. Panda, F. Plasser, A. J. A. Aquino, I. Burghardt, and H. Lischka, *Electronically excited states in poly(p-phenylenevinylene): Vertical excitations and torsional potentials from high-level ab initio calculations*, J. Phys. Chem. A **117**, 2181 (2013).

[116] N. E. Jackson, B. M. Savoie, K. L. Kohlstedt, M. O. de la Cruz, G. C. Schatz, L. X. Chen, and M. A. Ratner, *Controlling conformations of conjugated polymers and small molecules: The role of nonbonding interactions*, J. Am. Chem. Soc. **135**, 10475 (2013).

[117] J. S. Sears, R. R. Chance, and J.-L. Brédas, *Torsion potential in polydiacetylene: Accurate computations on oligomers extrapolated to the polymer limit*, J. Am. Chem. Soc. **132**, 13313 (2010).

[118] V. Lukeš, A. Aquino, , and H. Lischka, *Theoretical study of vibrational and optical spectra of methylene-bridged oligofluorenes*, J. Phys. Chem. A **109**, 10232 (2005).

[119] B. G. Sumpter and V. Meunier, *Can computational approaches aid in untangling the inherent complexity of practical organic photovoltaic systems?*, J. Polym. Sci. Part B: Polym. Phys. **50**, 1071 (2012).

[120] P. Hohenberg and W. Kohn, *Inhomogeneous electron gas*, Phys. Rev. **136**, B864 (1964).

[121] W. Kohn and L. J. Sham, *Self-consistent equations including exchange and correlation effects*, Phys. Rev. **140**, A1133 (1965).

[122] P. J. Stephens, F. J. Devlin, C. F. Chabalowski, and M. J. Frisch, *Ab initio calculation of vibrational absorption and circular dichroism spectra using density functional force fields*, J. Phys. Chem. **98**, 11623 (1994).

[123] C. Adamo and V. Barone, *Toward reliable density functional methods without adjustable parameters: The PBE0 model*, J. Chem. Phys. **110**, 6158 (1999).

[124] J. P. Perdew, M. Ernzerhof, and K. Burke, *Rationale for mixing exact exchange with density functional approximations*, J. Chem. Phys. **105**, 9982 (1996).

[125] Y. Zhao and D. G. Truhlar, *The M06 suite of density functionals for main group thermochemistry, thermochemical kinetics, noncovalent interactions, excited states, and transition elements: two new functionals and systematic testing of four M06-class functionals and 12 other functionals*, Theor. Chem. Acc. **120**, 215 (2008).

[126] Y. Zhao and D. G. Truhlar, *Design of density functionals that are broadly accurate for thermochemistry, thermochemical kinetics, and nonbonded interactions*, J. Phys. Chem. A **109**, 5656 (2005).

[127] S. Grimme, *Semiempirical hybrid density functional with perturbative second-order correlation*, J. Chem. Phys. **124**, 34108 (2006).

[128] L. Goerigk and S. Grimme, *Efficient and accurate double-hybrid-meta-GGA density functionals–evaluation with the extended GMTKN30 database for general main group thermochemistry, kinetics, and noncovalent interactions*, J. Chem. Theory Comput. **7**, 291 (2011).

[129] Y. Tawada, T. Tsuneda, S. Yanagisawa, T. Yanai, and K. Hirao, *A long-range-corrected time-dependent density functional theory*, J. Chem. Phys. **120**, 8425 (2004).

[130] T. Yanai, D. P. Tew, and N. C. Handy, *A new hybrid exchange–correlation functional using the coulomb-attenuating method (CAM-B3LYP)*, Chem. Phys. Lett. **393**, 51 (2004).

[131] S. Grimme, *Density functional theory with london dispersion corrections*, WIREs Comput. Mol. Sci. **1**, 211 (2011).

[132] J.-D. Chai and M. Head-Gordon, *Long-range corrected hybrid density functionals with damped atom-atom dispersion corrections*, Phys. Chem. Chem. Phys. **10**, 6615 (2008).

[133] S. Grimme, *Accurate description of van der Waals complexes by density functional theory including empirical corrections*, J. Comput. Chem. **25**, 1463 (2004).

[134] S. Grimme, *Semiempirical GGA-type density functional constructed with a long-range dispersion correction*, J. Comput. Chem. **27**, 1787 (2006).

[135] S. Grimme, S. Ehrlich, and L. Goerigk, *Effect of the damping function in dispersion corrected density functional theory*, J. Comput. Chem. **32**, 1456 (2011).

[136] E. Runge and E. K. U. Gross, *Density-functional theory for time-dependent systems*, Phys. Rev. Lett. **52**, 997 (1984).

[137] C. A. Ullrich, *Time-Dependent Density-Functional Theory: Concepts and Applications* (OUP Oxford, 2011).

[138] T. Körzdörfer and J.-L. Brédas, *Organic electronic materials: Recent advances in the DFT description of the ground and excited states using tuned range-separated hybrid functionals*, Acc. Chem. Res. **47**, 3284 (2014).

[139] R. S. Bhatta and M. Tsige, *Understanding the effect of heteroatoms on structural and electronic properties of conjugated polymers*, Polymer **56**, 293 (2015).

[140] I. T. Lima, C. Risko, S. G. Aziz, D. A. da Silva Filho, and J.-L. Brédas, *Interplay of alternative conjugated pathways and steric interactions on the electronic and optical properties of donor-acceptor conjugated polymers*, J. Mater. Chem. C **2**, 8873 (2014).

[141] L. Wang, B. Xu, J. Zhang, Y. Dong, S. Wen, H. Zhang, and W. Tian, *Theoretical investigation of electronic structure and charge transport property of 9,10-distyrylanthracene (DSA) derivatives with high solid-state luminescent efficiency*, Phys. Chem. Chem. Phys. **15**, 2449 (2013).

[142] S.-F. Zhang, X.-K. Chen, J.-X. Fan, and A.-M. Ren, *Charge transport properties in a series of five-ring-fused thienoacenes: A quantum chemistry and molecular mechanic study*, Org. Electron. **14**, 607 (2013).

[143] J. Brèdas and S. Marder, *Wspc Reference on Organic Electronics, The: Organic Semiconductors Volume I* (WORLD SCIENTIFIC Publishing Company Incorporated, 2015).

[144] J. Lu, Y. Yao, P. M. Shenai, L. Chen, and Y. Zhao, *Elucidating the enhancement in optical properties of low band gap polymers by tuning the structure of alkyl side chains*, Phys. Chem. Chem. Phys. **17**, 9541 (2015).

[145] D. Gajalakshmi, R. V. Solomon, V. Tamilmani, M. Boobalan, and P. Venuvanalingam, *A DFT/TDDFT mission to probe push-pull vinyl coupled thiophene oligomers for optoelectronic applications*, RSC Adv. **5**, 50353 (2015).

[146] M. Yu, L. Zhang, Q. Peng, H. Zhao, and J. Gao, *Narrow-band gap benzodipyrrolidone (BDPD) based donor conjugated polymer: A theoretical investigation*, Comput. Theor. Chem. **1055**, 88 (2015).

[147] O. V. Gritsenko and E. Jan Baerends, *Double excitation effect in non-adiabatic time-dependent density functional theory with an analytic construction of the exchange-correlation kernel in the common energy denominator approximation*, Phys. Chem. Chem. Phys. **11**, 4640 (2009).

[148] N. T. Maitra, F. Zhang, R. J. Cave, and K. Burke, *Double excitations within time-dependent density functional theory linear response*, J. Chem. Phys. **120**, 5932 (2004).

[149] A. Zabulica, M. Balan, D. Belei, M. Sava, B. C. Simionescu, and L. Marin, *Novel luminescent phenothiazine-based Schiff bases with tuned morphology. Synthesis, structure, photophysical and thermotropic characterization*, Dyes Pigm. **96**, 686 (2013).

[150] L. Marin, E. Perju, and M. D. Damaceanu, *Designing thermotropic liquid crystalline polyazomethines based on fluorene and/or oxadiazole chromophores*, Eur. Polym. J. **47**, 1284 (2011).

[151] C. I. Simionescu, M. Grigoras, I. Cianga, and N. Olaru, *Synthesis of new conjugated polymers with Schiff base structure containing pyrrolyl and naphthalene moieties and HMO study of the monomers reactivity*, Eur. Polym. J. **34**, 891 (1998).

[152] J. A. Puértolas, E. Carod, R. Díaz-Calleja, P. Cerrada, L. Oriol, M. Piñol, and J. L. Serrano, *Influence of the metal cross-linking on the dielectric, mechanical, and thermal properties of a liquid crystalline polyazomethine*, Macromolecules **30**, 773 (1997).

[153] S. Barik, S. Bishop, and W. G. Skene, *Spectroelectrochemical and electrochemical investigation of a highly conjugated all-thiophene polyazomethine*, Mater. Chem. Phys. **129**, 529 (2011).

[154] S. Barik and W. G. Skene, *Selective chain-end postpolymerization reactions and property tuning of a highly conjugated and all-thiophene polyazomethine*, Macromolecules **43**, 10435 (2010).

[155] S. Barik, T. Bletzacker, and W. G. Skene, *π-conjugated fluorescent azomethine copolymers: Opto-electronic, halochromic, and doping properties*, Macromolecules **45**, 1165 (2012).

[156] S. Barik and W. G. Skene, *A fluorescent all-fluorene polyazomethine-towards soluble conjugated polymers exhibiting high fluorescence and electrochromic properties*, Polym. Chem. **2**, 1091 (2011).

[157] S. Dufresne and W. G. Skene, *Unsymmetric pyrrole, thiophene, and furan-conjugated comonomers prepared using azomethine connections: Potential new monomers for alternating homocoupled products*, J. Org. Chem. **73**, 3859 (2008).

[158] M. Bourgeaux and W. G. Skene, *A highly conjugated p- and n-type polythiophenoazomethine: Synthesis, spectroscopic, and electrochemical investigation*, Macromolecules **40**, 1792 (2007).

[159] T. Nishinaga, T. Miyata, M. Tateno, M. Koizumi, M. Takase, M. Iyoda, N. Kobayashi, and Y. Kunugi, *Synthesis and structural, electronic, optical and FET properties of thiophene-pyrrole mixed hexamers end-capped with phenyl and pentafluorophenyl groups*, J. Mater. Chem. **21**, 14959 (2011).

[160] M. M. Oliva, T. M. Pappenfus, J. H. Melby, K. M. Schwaderer, J. C. Johnson, K. A. McGee, D. A. da Silva Filho, J.-L. Brédas, J. Casado, and J. T. López Navarrete, *Comparison of thiophene–pyrrole oligomers with oligothiophenes: A joint experimental and theoretical investigation of their structural and spectroscopic properties*, Chem. Eur. J. **16**, 6866 (2010).

[161] M. Fujii, T. Nishinaga, and M. Iyoda, *Synthesis of thiophene–pyrrole mixed oligomers end-capped with hexyl group for field-effect transistors*, Tetrahedron Lett. **50**, 555 (2009).

[162] J. Cai, H. Niu, C. Wang, L. Ma, X. Bai, and W. Wang, *Tuning the bandgaps of polyazomethines containing triphenylamine by different linkage sites of dialdhyde monomers*, Electrochim. Acta **76**, 229 (2012).

[163] J.-C. Chen, Y.-C. Liu, J.-J. Ju, C.-J. Chiang, and Y.-T. Chern, *Synthesis, characterization and hydrolysis of aromatic polyazomethines containing non-coplanar biphenyl structures*, Polymer **52**, 954 (2011).

[164] M. A. Khalid, A. G. El-Shekeil, and F. A. Al-Yusufy, *A study of a thienylene–phenylene polyazomethine and its copper complex*, Eur. Polym. J. **37**, 1423 (2001).

[165] P. Cerrada, L. Oriol, M. Piñol, and J. L. Serrano, *Copper-containing semiflexible hydroxypolyazomethines: Metallomesogenic units inducing enhanced mechanical properties*, J. Am. Chem. Soc. **119**, 7581 (1997).

[166] G. García, M. Moral, A. Garzón, J. M. Granadino-Roldán, A. Navarro, and M. Fernández-Gómez, *Poly(arylenethynyl-thienoacenes) as candidates for organic semiconducting materials. A DFT insight*, Org. Electron. **13**, 3244 (2012).

[167] Y. Li, L.-Y. Zou, A.-M. Ren, and J.-K. Feng, *Theoretical study on the electronic structures and photophysical properties of a series of dithienylbenzothiazole derivatives*, Comput. Theor. Chem. **981**, 14 (2012).

[168] L. Wang, G. Duan, Y. Ji, and H. Zhang, *Electronic and charge transport properties of perixanthenoxanthene: The effects of heteroatoms and phenyl substitutions*, J. Phys. Chem. C **116**, 22679 (2012).

[169] X.-K. Chen, J.-F. Guo, L.-Y. Zou, A.-M. Ren, and J.-X. Fan, *A promising approach to obtain excellent n-type organic field-effect transistors: Introducing pyrazine ring*, J. Phys. Chem. C **115**, 21416 (2011).

[170] X.-K. Chen, L.-Y. Zou, A.-M. Ren, and J.-X. Fan, *How dual bridging atoms tune structural and optoelectronic properties of ladder-type heterotetracenes?-a theoretical study*, Phys. Chem. Chem. Phys. **13**, 19490 (2011).

[171] G. García, V. Timón, A. Hernández-Laguna, A. Navarro, and M. Fernández-Gómez, *Influence of the alkyl and alkoxy side chains on the electronic structure and charge-transport properties of polythiophene derivatives*, Phys. Chem. Chem. Phys. **13**, 10091 (2011).

[172] X.-F. Ren, A.-M. Ren, L.-Y. Zou, and J.-K. Feng, *Fluorene-based oligomers as red light-emitting materials: A density functional theory study*, Theor. Chem. Acc. **126**, 305 (2010).

[173] X. Yang, L. Wang, C. Wang, W. Long, and Z. Shuai, *Influences of crystal structures and molecular sizes on the charge mobility of organic semiconductors: Oligothiophenes*, Chem. Mater. **20**, 3205 (2008).

[174] V. Coropceanu, J. Cornil, D. A. da Silva Filho, Y. Olivier, R. Silbey, and J.-L. Brédas, *Charge transport in organic semiconductors*, Chem. Rev. **107**, 926 (2007).

[175] M. J. Tauber, R. F. Kelley, J. M. Giaimo, B. Rybtchinski, and M. R. Wasielewski, *Electron hopping in π-stacked covalent and self-assembled perylene diimides observed by ENDOR spectroscopy*, J. Am. Chem. Soc. **128**, 1782 (2006).

[176] Y. Sun, Y. Liu, and D. Zhu, *Advances in organic field-effect transistors*, J. Mater. Chem. **15**, 53 (2005).

[177] J.-L. Brédas, D. Beljonne, V. Coropceanu, and J. Cornil, *Charge-transfer and energy-transfer processes in π-conjugated oligomers and polymers: A molecular picture*, Chem. Rev. **104**, 4971 (2004).

[178] R. A. Marcus, *Electron transfer reactions in chemistry. Theory and experiment*, Rev. Mod. Phys. **65**, 599 (1993).

[179] R. A. Marcus, *On the theory of electron-transfer reactions. VI. Unified treatment for homogeneous and electrode reactions*, J. Chem. Phys. **43**, 679 (1965).

[180] T. Koopmans, *Über die zuordnung von wellenfunktionen und eigenwerten zu den einzelnen elektronen eines atoms*, Physica **1**, 104 (1934).

[181] F. Neese, *ORCA, An ab initio, DFT and semiempirical SCF-MO package* (Max-Planck Institute for Bioinorganic Chemistry, Mülheim a. d. Ruhr, Germany, 2010).

[182] B. P. Karsten, L. Viani, J. Gierschner, J. Cornil, and R. A. J. Janssen, *An oligomer study on small band gap polymers*, J. Phys. Chem. A **112**, 10764 (2008).

[183] J. Torras, J. Casanovas, and C. Alemán, *Reviewing extrapolation procedures of the electronic properties on the π-conjugated polymer limit*, J. Phys. Chem. A **116**, 7571 (2012).

[184] F. Neese, *The ORCA program system*, WIREs Comput. Mol. Sci. **2**, 73 (2012).

[185] L. Pauling, *The Nature of the Chemical Bond, 4th ed.* (Cornell University Press, Ithaca, NY, 1973).

[186] V. I. Minkin and R. M. Minyaev, *Cyclic aromatic systems with hypervalent centers*, Chem. Rev. **101**, 1247 (2001).

[187] H. Huang, Z. Chen, R. P. Ortiz, C. Newman, H. Usta, S. Lou, J. Youn, Y.-Y. Noh, K.-J. Baeg, L. X. Chen, et al., *Combining electron-neutral building blocks with intramolecular "conformational locks" affords stable, high-mobility p- and n-channel polymer semiconductors*, J. Am. Chem. Soc. **134**, 10966 (2012).

[188] M. Vangheluwe, T. Verbiest, and G. Koeckelberghs, *Influence of the substitution pattern on the chiroptical properties of regioregular poly(3-alkoxythiophene)s*, Macromolecules **41**, 1041 (2008).

[189] X. Guo, F. S. Kim, S. A. Jenekhe, and M. D. Watson, *Phthalimide-based polymers for high performance organic thin-film transistors*, J. Am. Chem. Soc. **131**, 7206 (2009).

[190] A. S. Özen, *Peripheral and structural effects on the band gap of acceptor–donor type conducting polymers containing pendant bisfulleroid groups*, J. Phys. Chem. C **115**, 25007 (2011).

[191] J. Roncali, P. Blanchard, and P. Frére, *3,4-ethylenedioxythiophene (EDOT) as a versatile building block for advanced functional π-conjugated systems*, J. Mater. Chem. **15**, 1589 (2005).

[192] Y.-H. Tian and M. Kertesz, *Ladder-type polyenazine based on intramolecular S···N interactions: A theoretical study of a small-bandgap polymer*, Macromolecules **42**, 6123 (2009).

[193] N. Martínez de Baroja, J. Garín, J. Orduna, R. Andreu, M. J. Blesa, B. Villacampa, R. Alicante, and S. Franco, *Synthesis, characterization, and optical properties of 4H-pyran-4-ylidene donor-based chromophores: The relevance of the location of a thiophene ring in the spacer*, J. Org. Chem. **77**, 4634 (2012).

[194] P. M. Oberhumer, Y.-S. Huang, S. Massip, D. T. James, G. Tu, S. Albert-Seifried, D. Beljonne, J. Cornil, J.-S. Kim, W. T. S. Huck, et al., *Tuning the electronic coupling in a low-bandgap donor–acceptor copolymer via the placement of side-chains*, J. Chem. Phys. **134**, 114901 (2011).

[195] L. Yang, Y. Liao, J.-K. Feng, and A.-M. Ren, *Theoretical studies of the modulation of polymer electronic and optical properties through the introduction of the electron-donating 3,4-ethylenedioxythiophene or electron-accepting pyridine and 1,3,4-oxadiazole moieties*, J. Phys. Chem. A **109**, 7764 (2005).

[196] B. D. Koepnick, J. S. Lipscomb, and D. K. Taylor, *Effect of substitution on the optical properties and HOMO–LUMO gap of oligomeric paraphenylenes*, J. Phys. Chem. A **114**, 13228 (2010).

[197] J. L. Brédas, G. B. Street, B. Thémans, and J. M. André, *Organic polymers based on aromatic rings (polyparaphenylene, polypyrrole, polythiophene): Evolution of the electronic properties as a function of the torsion angle between adjacent rings*, J. Chem. Phys. **83**, 1323 (1985).

[198] C. Quattrocchi, R. Lazzaroni, J. L. Brédas, R. Zamboni, and C. Taliani, *Theoretical investigation of the structure and electronic properties of poly(dithieno[3,4-b:3',4'-d]thiophene), a small-band-gap conjugated polymer*, Macromolecules **26**, 1260 (1993).

[199] P.-F. Coheur, J. Cornil, D. A. dos Santos, P. R. Birkett, J. Liévin, J. L. Brédas, D. R. M. Walton, R. Taylor, H. W. Kroto, and R. Colin, *Photophysical properties of multiply phenylated C_{70} derivatives: Spectroscopic and quantum-chemical investigations*, J. Chem. Phys. **112**, 6371 (2000).

[200] D. A. dos Santos, T. Kogej, J. L. Brédas, C. Boutton, E. Hendrickx, S. Houbrechts, K. Clays, A. Persoons, J. X. Xhang, P. Dubois, et al., *Novel functionalized oligovinylthiophene molecules with modulated second-order nonlinear optical response*, J. Mol. Struct. **521**, 221 (2000).

[201] G. R. Hutchison, M. A. Ratner, and T. J. Marks, *Hopping transport in conductive heterocyclic oligomers: Reorganization energies and substituent effects*, J. Am. Chem. Soc. **127**, 2339 (2005).

[202] Y. A. Berlin, G. R. Hutchison, P. Rempala, M. A. Ratner, and J. Michl, *Charge hopping in molecular wires as a sequence of electron-transfer reactions*, J. Phys. Chem. A **107**, 3970 (2003).

[203] J. Fabian and H. Hartmann, *Chromophores of neutral and dicationic thiophene-based oligomers –A study by first-principle methods*, Dyes Pigm. **79**, 126 (2008).

[204] F. Laquai, *Electronic energy transfer processes and charge carrier transport in π-conjugated [pi-conjugated] polymers* (2006).

[205] H. B. Michaelson, *The work function of the elements and its periodicity*, J. Appl. Phys. **48**, 4729 (1977).

[206] S.-W. Rhee and D.-J. Yun, *Metal-semiconductor contact in organic thin film transistors*, J. Mater. Chem. **18**, 5437 (2008).

[207] C. H. Cheung, W. J. Song, and S. K. So, *Role of air exposure in the improvement of injection efficiency of transition metal oxide/organic contact*, Org. Electron. **11**, 89 (2010).

[208] Y.-M. Koo, S.-J. Choi, T.-Y. Chu, O.-K. Song, W.-J. Shin, J.-Y. Lee, J. C. Kim, and T.-H. Yoon, *Ohmic contact probed by dark injection space-charge-limited current measurements*, J. Appl. Phys. **104**, 123707 (2008).

[209] D. Poplavskyy, W. Su, and F. So, *Bipolar charge transport, injection, and trapping studies in a model green-emitting polyfluorene copolymer*, J. Appl. Phys. **98**, 014501 (2005).

[210] A. J. Campbell, D. D. C. Bradley, H. Antoniadis, M. Inbasekaran, W. W. Wu, and E. P. Woo, *Transient and steady-state space-charge-limited currents in polyfluorene copolymer diode structures with ohmic hole injecting contacts*, Appl. Phys. Lett. **76**, 1734 (2000).

[211] M. S. A. Abdou, F. P. Orfino, Y. Son, and S. Holdcroft, *Interaction of oxygen with conjugated polymers: Charge transfer complex formation with poly(3-alkylthiophenes)*, J. Am. Chem. Soc. **119**, 4518 (1997).

[212] H. Nalwa, *Handbook of Advanced Electronic and Photonic Materials and Devices* (Academic Press, 2000).

[213] M. S. Liu, X. Jiang, P. Herguth, and A. K.-Y. Jen, *Efficient cyano-containing electron-transporting polymers for light-emitting diodes*, Chem. Mater. **13**, 3820 (2001).

[214] A. Garzón, J. M. Granadino-Roldán, G. García, M. Moral, and M. Fernández-Gómez, *Crystal structure and charge transport properties of poly(arylene-ethynylene) derivatives: A DFT approach*, J. Chem. Phys. **138**, 154902 (2013).

[215] M. Banno, T. Yamaguchi, K. Nagai, C. Kaiser, S. Hecht, and E. Yashima, *Optically active, amphiphilic poly(meta-phenylene ethynylene)s: Synthesis, hydrogen-bonding enforced helix stability, and direct AFM observation of their helical structures*, J. Am. Chem. Soc. **134**, 8718 (2012).

[216] T. Iwasaki, Y. Kohinata, and H. Nishide, *Poly(thiaheterohelicene): A stiff conjugated helical polymer comprised of fused benzothiophene rings*, Org. Lett. **7**, 755 (2005).

[217] R. Yang, K. M. Dalsin, D. F. Evans, L. Christensen, and W. A. Hendrickson, *Scanning tunneling microscopic imaging of electropolymerized, doped polypyrrole. Visual evidence of semicrystalline and helical nascent polymer growth*, J. Phys. Chem. **93**, 511 (1989).

[218] G. Caple, B. L. Wheeler, R. Swift, T. L. Porter, and S. Jeffers, *Scanning tunneling microscopy of polythiophene, poly(3-methylthiophene), and poly(3-bromothiophene)*, J. Phys. Chem. **94**, 5639 (1990).

[219] R. Yang, D. F. Evans, L. Christensen, and W. A. Hendrickson, *Scanning tunneling microscopy evidence of semicrystalline and helical conducting polymer structures*, J. Phys. Chem. **94**, 6117 (1990).

[220] B. M. W. Langeveld-Voss, M. P. T. Christiaans, R. A. J. Janssen, and E. W. Meijer, *Inversion of optical activity of chiral polythiophene aggregates by a change of solvent*, Macromolecules **31**, 6702 (1998).

[221] B. M. W. Langeveld-Voss, R. J. M. Waterval, R. A. J. Janssen, and E. W. Meijer, *Principles of "majority rules" and "sergeants and soldiers" applied to the aggregation of optically active polythiophenes: Evidence for a multichain phenomenon*, Macromolecules **32**, 227 (1999).

[222] B. M. W. Langeveld-Voss, R. A. J. Janssen, and E. W. Meijer, *On the origin of optical activity in polythiophenes*, J. Mol. Struct. **521**, 285 (2000).

[223] J. R. Matthews, F. Goldoni, A. P. H. J. Schenning, and E. W. Meijer, *Non-ionic polythiophenes: a non-aggregating folded structure in water*, Chem. Commun. 5503 (2005).

[224] K. P. R. Nilsson, J. D. M. Olsson, P. Konradsson, and O. Inganäs, *Enantiomeric substituents determine the chirality of luminescent conjugated polythiophenes*, Macromolecules **37**, 6316 (2004).

[225] C. X. Cui and M. Kertesz, *Two helical conformations of polythiophene, polypyrrole, and their derivatives*, Phys. Rev. B **40**, 9661 (1989).

[226] A. D. Becke and E. R. Johnson, *A density-functional model of the dispersion interaction*, J. Chem. Phys. **123**, 154101 (2005).

[227] L. Goerigk, *How do DFT-DCP, DFT-NL, and DFT-D3 compare for the description of london-dispersion effects in conformers and general thermochemistry?*, J. Chem. Theory Comput. **10**, 968 (2014).

[228] W. Hujo and S. Grimme, *Performance of non-local and atom-pairwise dispersion corrections to DFT for structural parameters of molecules with noncovalent interactions*, J. Chem. Theory Comput. **9**, 308 (2013).

[229] S. Tang and J. Zhang, *Rational design of organic asymmetric donors D1–A –D2 possessing broad absorption regions and suitable frontier molecular orbitals to match typical acceptors toward solar cells*, J. Phys. Chem. A **115**, 5184 (2011).

[230] A. D. Dwyer and D. J. Tozer, *Effect of chemical change on TDDFT accuracy: orbital overlap perspective of the hydrogenation of retinal*, Phys. Chem. Chem. Phys. **12**, 2816 (2010).

[231] B. Pal, W.-C. Yen, J.-S. Yang, C.-Y. Chao, Y.-C. Hung, S.-T. Lin, C.-H. Chuang, C.-W. Chen, and W.-F. Su, *Substituent effect on the optoelectronic properties of alternating fluorene–cyclopentadithiophene copolymers*, Macromolecules **41**, 6664 (2008).

[232] B. Milián-Medina and J. Gierschner, *Computational design of low singlet–triplet gap all-organic molecules for OLED application*, Org. Electron. **13**, 985 (2012).

[233] S. V. Rocha and N. S. Finney, *Systematic evaluation of 2,6-linked pyridine–thiophene oligomers*, J. Org. Chem. **78**, 11255 (2013).

[234] S. V. Rocha and N. S. Finney, *Synthesis and evaluation of 2,5-linked alternating pyridine–thiophene oligomers*, Org. Lett. **12**, 2598 (2010).

[235] A. Tabatchnik-Rebillon, C. Aubé, H. Bakkali, T. Delaunay, G. T. Manh, V. Blot, C. Thobie-Gautier, E. Renault, M. Soulard, A. Planchat, et al., *Electrochemical synthesis and characterisation of alternating tripyridyl–dipyrrole molecular strands with multiple nitrogen-based donor–acceptor binding sites*, Chem. Eur. J. **16**, 11876 (2010).

[236] F. Chevallier, M. Charlot, C. Katan, F. Mongin, and M. Blanchard-Desce, *Novel chromophores from alternated pyridine-ethylenedioxythiophene unit oligomers: dramatic enhancement of photoluminescence properties in elongated derivatives*, Chem. Commun. **6**, 692 (2009).

[237] O. Meth-Cohn and H. Jiang, *Ligands containing alternating 2,6-linked pyridine and 2,5-linked thiophene units*, J. Chem. Soc., Perkin Trans. 1 **22**, 3737 (1998).

[238] R. A. Jones and P. U. Civcir, *Extended heterocyclic systems 2. The synthesis and characterisation of (2-furyl)pyridines, (2-thienyl)pyridines, and furan-pyridine and thiophene-pyridine oligomers*, Tetrahedron **53**, 11529 (1997).

[239] R. A. Jones, M. Karatza, T. N. Voro, P. U. Civeir, A. Franck, O. Ozturk, J. P. Seaman, A. P. Whitmore, and D. J. Williamson, *Extended heterocyclic systems 1. The synthesis and characterisation of pyrrolylpyridines, alternating pyrrole:pyridine oligomers and polymers, and related systems*, Tetrahedron **52**, 8707 (1996).

[240] T. Yamamoto, Z.-h. Zhou, T. Kanbara, M. Shimura, K. Kizu, T. Maruyama, Y. Nakamura, T. Fukuda, B.-L. Lee, N. Ooba, et al., *π-conjugated donor–acceptor copolymers constituted of π-excessive and π-deficient arylene units. Optical and electrochemical properties in relation to CT structure of the polymer*, J. Am. Chem. Soc. **118**, 10389 (1996).

[241] G. C. Welch, R. Coffin, J. Peet, and G. C. Bazan, *Band gap control in conjugated oligomers via lewis acids*, J. Am. Chem. Soc. **131**, 10802 (2009).

[242] M. J. Frisch, G. W. Trucks, H. B. Schlegel, G. E. Scuseria, M. A. Robb, J. R. Cheeseman, G. Scalmani, V. Barone, B. Mennucci, G. A. Petersson, et al., *Gaussian 09 Revision D.01*, gaussian Inc. Wallingford CT 2009.

[243] Z. M. Su, Y. H. Kan, Z. H. Huang, Y. Liao, Y. Q. Qiu, and R. S. Wang, *Theoretical study on excited state structures and charge transfer characteristics of 2,2'-bipyridine, pyridine-imidazole ligands and their complexes*, Synth. Met. **137**, 1095 (2003).

[244] P. Johari and S. P. Singh, *Dependence of the structure and electronic properties of D–A–D based molecules on the D/A ratio and the strength of the acceptor moiety*, J. Phys. Chem. C **119**, 14890 (2015).

[245] S. Ming, S. Zhen, K. Lin, L. Zhao, J. Xu, and B. Lu, *Thiadiazolo[3,4-c]pyridine as an acceptor toward fast-switching green donor–acceptor-type electrochromic polymer with low bandgap*, ACS Appl. Mater. Interfaces **7**, 11089 (2015).

[246] C. Liu, C. Yi, K. Wang, Y. Yang, R. S. Bhatta, M. Tsige, S. Xiao, and X. Gong, *Single-junction polymer solar cells with over 10% efficiency by a novel two-dimensional donor–acceptor conjugated copolymer*, ACS Appl. Mater. Interfaces **7**, 4928 (2015).

[247] S. Wood, J.-H. Kim, D.-H. Hwang, and J.-S. Kim, *Effects of fluorination and side chain branching on molecular conformation and photovoltaic performance of donor–acceptor copolymers*, Chem. Mater. **27**, 4196 (2015).

[248] H. Kayi and A. Elkamel, *A theoretical investigation of 4,7-di(furan-2-yl)benzo[c][1,2,5]selenadiazole-based donor–acceptor type conjugated polymer*, Comput. Theor. Chem. **1054**, 38 (2015).

[249] M. P. Balanay and D. H. Kim, *Molecular engineering of donor–acceptor co-polymers for bulk heterojunction solar cells*, Comput. Theor. Chem. **1055**, 15 (2015).

[250] A. Abbotto, E. H. Calderon, N. Manfredi, C. M. Mari, C. Marinzi, and R. Ruffo, *Vinylene-linked pyridine-pyrrole donor–acceptor conjugated polymers*, Synth. Met. **161**, 763 (2011).

[251] D. E. Lynch and J. Ewington, *The structure/property relationship in a series of pyrrolic polysquaraines*, Synth. Met. **183**, 40 (2013).

[252] A. Abbotto, E. H. Calderon, M. S. Dangate, F. D. Angelis, N. Manfredi, C. M. Mari, C. Marinzi, E. Mosconi, M. Muccini, R. Ruffo, et al., *Pyridine–EDOT heteroarylene–vinylene donor–acceptor polymers*, Macromolecules **43**, 9698 (2010).

[253] N. M. O'boyle, A. L. Tenderholt, and K. M. Langner, *cclib: A library for package-independent computational chemistry algorithms*, J. Comput. Chem. **29**, 839 (2008).

[254] K. Okuno, Y. Shigeta, R. Kishi, and M. Nakano, *Non-empirical tuning of CAM-B3LYP functional in time-dependent density functional theory for excitation energies of diarylethene derivatives*, Chem. Phys. Lett. **585**, 201 (2013).

[255] K. Okuno, Y. Shigeta, R. Kishi, H. Miyasaka, and M. Nakano, *Tuned CAM-B3LYP functional in the time-dependent density functional theory scheme for excitation energies and properties of diarylethene derivatives*, J. Photochem. Photobiol. A: Chem. **235**, 29 (2012).

[256] M. Bruschi, M. G. Giuffreda, and H. P. Lüthi, *Through versus Cross electron delocalization in polytriacetylene oligomers: A computational analysis*, ChemPhysChem **6**, 511 (2005).

[257] H. D. de Gier, B. J. Rietberg, R. Broer, and R. W. A. Havenith, *Influence of push–pull group substitution patterns on excited state properties of donor–acceptor co-monomers and their trimers*, Comput. Theor. Chem. **1040-1041**, 202 (2014).

[258] R. Nithya and K. Senthilkumar, *Theoretical studies on the quinoidal thiophene based dyes for dye sensitized solar cell and NLO applications*, Phys. Chem. Chem. Phys. **16**, 21496 (2014).

[259] M. Dubois, S. Latil, L. Scifo, B. Grévin, and A. Rubio, *Scanning tunneling spectroscopy simulations of poly(3-dodecylthiophene) chains adsorbed on highly oriented pyrolytic graphite*, J. Chem. Phys. **125**, 034708 (2006).

Appendix I

TABLE A1: IPs and EAs for oligomers n=1–4 calculated at the B3LYP/6-31G(d,p) level of theory. Values for pentamers are listed in Table 3.7. All energies are in eV.

		1	**7**	**8**	**9**	**11**	**12**	**14**	**15**
IP(a)	1	6.62	6.32	6.52	6.95	7.19	6.21	6.47	5.92
	2	5.74	5.63	5.62	6.16	6.46	5.31	5.43	4.98
	3	5.37	5.37	5.24	5.84	6.18	4.95	5.05	4.59
	4	5.18	5.25	5.06	5.69	6.04	4.71	4.81	4.37
IP(v)	1	6.82	6.52	6.71	7.18	7.41	6.45	6.67	6.15
	2	5.90	5.88	5.79	6.36	6.65	5.57	5.58	5.15
	3	5.52	5.61	5.40	6.02	6.33	5.17	5.18	4.73
	4	5.31	5.47	5.20	5.83	6.16	4.96	4.93	4.50
EA(a)	1	0.06	0.05	0.05	0.42	0.78	0.02	0.10	−0.05
	2	1.03	0.82	0.99	1.38	1.73	0.96	0.99	0.76
	3	1.44	1.13	1.41	1.76	2.10	1.39	1.37	1.11
	4	1.66	1.30	1.62	1.97	2.29	1.65	1.58	1.30
EA(v)	1	−0.12	−0.13	−0.12	0.23	0.61	−0.18	−0.09	−0.28
	2	0.88	0.62	0.85	1.20	1.57	0.80	0.85	0.60
	3	1.32	0.95	1.26	1.62	1.96	1.21	1.26	0.97
	4	1.56	1.13	1.50	1.85	2.18	1.45	1.48	1.18

Appendix II

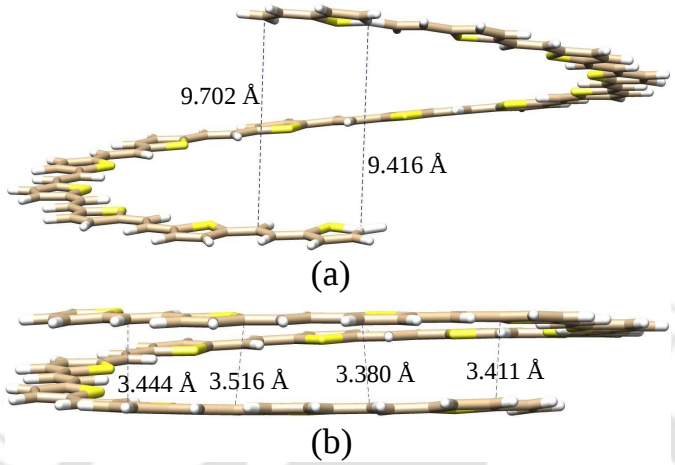

FIGURE A1: Ground-state structures of **A**-$(TV)_{14}$ optimized at B3LYP/6-31G(d,p) (a) and B3LYP-D3/6-31G(d,p) (b) levels. Distances between the atoms of two adjacent helical turns of conformer **A** are given in Å.

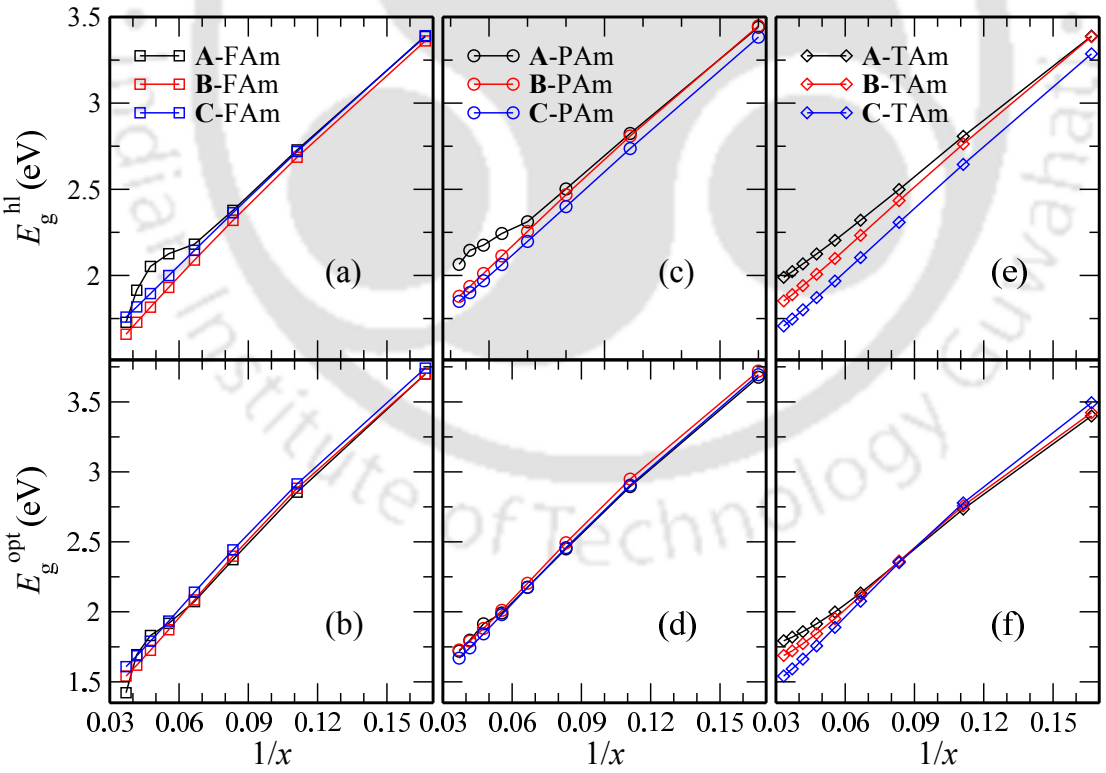

FIGURE A2: E_g^{hl} and E_g^{opt} of azomethine-linked oligomers as function of the reciprocal number of the double bonds (x) in oligomers.

TABLE A2: Electronic transition data obtained by the TDDFT method for **B** and **C** conformers of FV, PV and TV oligomers at the B3LYP/6-31G(d,p) level. The HOMO and LUMO are indicated by H and L, respectively. All electronic transitions are from S_0 to S_1.

B-(FV)$_n$	E_g	f_{osc}	configurations	**C**-(FV)$_n$	E_g	f_{osc}	configurations
2	3.70	1.97	H→L(97%)	2	3.68	1.38	H→L(97%)
3	2.96	2.95	H→L(98%)	3	2.92	1.91	H→L(98%)
4	2.52	3.77	H→L(98%)	4	2.49	2.49	H→L(98%)
5	2.25	4.44	H→L(98%)	5	2.22	2.95	H→L(98%)
6	2.07	5.04	H→L(98%)	6	2.05	3.38	H→L(98%)
7	1.94	5.60	H→L(98%)	7	1.92	3.77	H→L(98%)
8	1.85	6.15	H→L(97%)	8	1.83	4.15	H→L(97%)
B-(PV)$_n$	E_g	f_{osc}	configurations	**C**-(PV)$_n$	E_g	f_{osc}	configurations
2	3.73	1.97	H→L(96%)	2	3.69	1.51	H→L(96%)
3	3.01	2.98	H→L(97%)	3	2.95	2.15	H→L(98%)
4	2.59	3.79	H→L(98%)	4	2.53	2.78	H→L(98%)
5	2.33	4.46	H→L(98%)	5	2.27	3.29	H→L(98%)
6	2.16	5.08	H→L(98%)	6	2.10	3.76	H→L(98%)
7	2.05	5.67	H→L(98%)	7	1.98	4.21	H→L(98%)
8	1.96	6.26	H→L(97%)	8	1.90	4.65	H→L(97%)
B-(TV)$_n$	E_g	f_{osc}	configurations	**C**-(TV)$_n$	E_g	f_{osc}	configurations
2	3.52	1.84	H→L(97%)	2	3.47	1.48	H→L(96%)
3	2.81	2.95	H→L(98%)	3	2.77	2.35	H→L(98%)
4	2.41	3.84	H→L(98%)	4	2.38	3.12	H→L(98%)
5	2.16	4.58	H→L(98%)	5	2.12	3.75	H→L(98%)
6	1.98	5.24	H→L(98%)	6	1.95	4.31	H→L(98%)
7	1.87	5.84	H→L(98%)	7	1.84	4.82	H→L(98%)
8	1.78	6.44	H→L(97%)	8	1.75	5.32	H→L(97%)
9	1.72	7.03	H→L(96%)	9	1.69	5.81	H→L(96%)
10	1.67	7.63	H→L(95%)	10	1.64	6.31	H→L(95%)
11	1.63	8.24	H→L(94%)	11	1.60	6.82	H→L(94%)
12	1.60	8.87	H→L(92%)	12	1.57	7.34	H→L(93%)
13	1.58	9.51	H→L(91%)	13	1.55	7.87	H→L(91%)

TABLE A3: Electronic transition data obtained by the TDDFT method for **A**-FV oligomers at the B3LYP/6-31G(d,p) level. The HOMO and LUMO are indicated by H and L, respectively. Electronic transitions are from S_0 to S_m.

A-$(FV)_n$	m	E_g (eV)	f_{osc}	configurations
2	1	3.70	1.67	H → L(97%)
3	1	2.93	2.03	H → L(97%)
	5	4.39	1.00	H-1 → L(47%), H → L+1(44%)
6	1	2.01	0.58	H → L(96%)
	5	2.92	2.39	H-1 → L(43%), H → L+1(41%)
	8	3.43	1.86	H-3 → L(31%), H-2 → L+1(26%)
7	1	1.70	0.05	H → L(98%)
	5	2.63	1.24	H → L+1(39%), H-1 → L(38%)
	8	3.07	1.03	H-1 → L+2(36%)
	16	3.69	1.87	H-4 → L(24%)
8	1	1.77	0.13	H → L(90%)
	15	3.37	2.82	H-2 → L+2(19%), H-4 → L(18%)
	17	3.48	1.49	H-3 → L(21%), H → L+3(19%)

TABLE A4: Electronic transition data obtained by the TDDFT method for **A**-PV oligomers at the B3LYP/6-31G(d,p) level. The HOMO and LUMO are indicated by H and L, respectively. Electronic transitions are from S_0 to S_m.

A-$(PV)_n$	m	E_g (eV)	f_{osc}	configurations
2	1	3.72	1.78	H → L(97%)
3	1	2.97	2.35	H → L(98%)
4	1	2.54	2.44	H → L(98%)
	5	3.74	1.33	H-1 → L(43%), H → L+1(38%)
7	1	1.96	1.29	H → L(98%)
	5	2.73	2.84	H-1 → L(37%), H → L+1(34%)
	8	3.19	1.35	H-3 → L(38%), H-2 → L+1(36%)
8	1	1.88	0.95	H → L(97%)
	5	2.55	2.32	H → L+1(27%), H-1 → L(28%)
	8	2.95	1.32	H-3 → L(37%), H-2 → L+1(34%)
	9	3.06	1.01	H-2 → L(25%), H → L+2(25%)
	13	3.44	1.35	H-4 → L(31%), H-3 → L+1(24%)

TABLE A5: Electronic transition data obtained by the TDDFT method for **A**-TV oligomers at the B3LYP/6-31G(d,p) level. The HOMO and LUMO are indicated by H and L, respectively. Electronic transitions are from S_0 to S_m.

A-$(TV)_n$	m	E_g (eV)	f_{osc}	configurations
2	1	3.48	1.62	H → L(96%)
3	1	2.78	2.46	H → L(97%)
4	1	2.38	2.95	H → L(97%)
5	1	2.12	3.16	H → L(97%)
	5	3.09	1.15	H → L+1(41%), H-1 → L(39%)
6	1	1.95	3.17	H → L(98%)
	5	2.78	1.70	H → L+1(39%), H-1 → L(37%)
7	1	1.83	3.03	H → L(98%)
	5	2.55	2.20	H → L+1(35%), H-1 → L(33%)
9	1	1.68	2.44	H → L(96%)
	3	2.17	1.52	H → L+1(27%), H-1 → L(25%)
	5	2.25	2.49	H-2 → L(26%), H → L+2(26%)
	8	2.59	1.44	H-2 → L+1(32%), H-1 → L+2(29%)
10	1	1.64	2.07	H → L(95%)
	3	2.07	2.41	H → L+1(36%), H-1 → L(32%)
	5	2.14	2.16	H → L+2(33%), H-2 → L(33%)
	8	2.45	1.56	H-2 → L+1(32%), H-1 → L+2(30%)
11	1	1.60	1.64	H → L(93%)
	3	1.99	3.30	H → L+1(42%), H-1 → L(38%)
	5	2.06	1.67	H → L+2(39%), H-2 → L(39%)
	8	2.33	1.61	H-2 → L+1(32%), H-1 → L+2(31%)
	9	2.42	1.05	H → L+3(29%), H-2 → L(27%)
12	1	1.58	1.60	H → L(91%)
	3	1.93	3.79	H → L+1(49%), H-1 → L(41%)
	8	2.24	1.25	H-1 → L+2(32%), H-2 → L+1(32%)
	9	2.32	1.60	H → L+2(29%), H-2 → L(26%)
	13	2.55	1.39	H-3 → L+1(21%), H-4 → L(21%)

TABLE A6: Electronic transition data obtained by the TDDFT method for **A**-FAm oligomers at the B3LYP/6-31G(d,p) level. The HOMO and LUMO are indicated by H and L, respectively. Electronic transitions are from S_0 to S_m.

A-$(FAm)_n$	m	E_g (eV)	f_{osc}	configurations
2	1	3.70	1.44	H → L(96%)
3	1	2.86	1.53	H → L(91%)
6	1	1.92	0.60	H → L(97%)
	5	3.01	2.69	H-1 → L(38%), H → L+1(37%)
	8	3.42	1.53	H-3 → L(36%), H-2 → L+1(28%)
7	1	1.83	0.68	H → L(96%)
	5	2.75	2.51	H-1 → L(29%), H → L+1(29%)
	8	3.10	1.57	H-3 → L(32%)
	13	3.58	1.11	H-4 → L(30%)
8	1	1.69	0.42	H → L(99%)
	5	2.61	2.02	H → L+2(48%)
	13	3.24	1.98	H-3 → L(15%), H → L+3(16%)

TABLE A7: Electronic transition data obtained by the TDDFT method for **B** and **C** conformers of FAm oligomers at the B3LYP/6-31G(d,p) level. The HOMO and LUMO are indicated by H and L, respectively. Electronic transitions are from S_0 to S_m.

B-$(FAm)_n$	m	E_g (eV)	f_{osc}	configurations
2	1	3.70	1.65	H → L(96%)
3	1	2.88	2.19	H → L(92%)
6	1	1.87	2.84	H → L(96%)
	2	2.24	2.77	H → L+1(52%), H-1 → L(43%)
7	1	1.73	2.92	H → L(98%)
	2	2.07	3.41	H → L+1(52%), H-1 → L(43%)
8	1	1.62	2.99	H → L(99%)
	2	1.94	3.99	H → L+1(53%), H-1 → L(43%)
C-$(FAm)_n$	m	E_g (eV)	f_{osc}	configurations
2	1	3.74	1.42	H → L(97%)
3	1	2.91	1.86	H → L(96%)
6	1	1.93	2.89	H → L(97%)
	2	2.23	1.02	H → L+1(48%), H-1 → L(48%)
7	1	1.79	3.15	H → L(98%)
	2	2.07	1.27	H → L+1(49%), H-1 → L(48%)
8	1	1.69	3.43	H → L(98%)
	2	1.95	1.51	H → L+1(49%), H-1 → L(48%)

TABLE A8: Electronic transition data obtained by the TDDFT method for **A**-PAm oligomers at the B3LYP/6-31G(d,p) level. The HOMO and LUMO are indicated by H and L, respectively. Electronic transitions are from S_0 to S_m.

A-$(PAm)_n$	m	E_g (eV)	f_{osc}	configurations
2	1	3.68	1.43	H → L(95%)
3	1	2.90	1.65	H → L(94%)
6	1	1.99	0.57	H → L(97%)
	5	2.98	2.49	H-1 → L(45%), H → L+1(37%)
	8	3.47	1.14	H-3 → L(45%), H-2 → L+1(32%)
7	1	1.91	0.65	H → L(96%)
	5	2.74	2.27	H-1 → L(37%)
	8	3.18	1.46	H-3 → L(40%)
8	1	1.80	0.20	H → L(92%)
	5	2.61	1.02	H → L+2(32%)
	8	2.92	1.36	H-3 → L(27%), H-1 → L+2(27%)
	10	3.10	1.90	H-2 → L(23%)

TABLE A9: Electronic transition data obtained by the TDDFT method for **B** and **C** conformers of PAm oligomers at the B3LYP/6-31G(d,p) level. The HOMO and LUMO are indicated by H and L, respectively. Electronic transitions are from S_0 to S_m.

B-$(PAm)_n$	m	E_g (eV)	f_{osc}	configurations
2	1	3.72	1.65	H → L(96%)
3	1	2.95	2.35	H → L(94%)
6	1	2.01	3.31	H → L(98%)
	2	2.38	2.26	H → L+1(56%), H-1 → L(41%)
7	1	1.88	3.51	H → L(98%)
	2	2.22	2.78	H → L+1(56%), H-1 → L(41%)
8	1	1.79	3.74	H → L(98%)
	2	2.09	3.22	H → L+1(56%), H-1 → L(40%)
C-$(PAm)_n$	m	E_g (eV)	f_{osc}	configurations
2	1	3.69	1.53	H → L(97%)
3	1	2.91	2.10	H → L(98%)
6	1	1.98	3.64	H → L(98%)
7	1	1.84	4.04	H → L(98%)
8	1	1.74	4.44	H → L(97%)

TABLE A10: Electronic transition data obtained by the TDDFT method for **A**-TAm oligomers at the B3LYP/6-31G(d,p) level. The HOMO and LUMO are indicated by H and L, respectively. Electronic transitions are from S_0 to S_m.

A-$(TAm)_n$	m	E_g (eV)	f_{osc}	configurations
2	1	3.40	0.93	H → L(88%)
3	1	2.73	1.36	H → L(93%)
6	1	2.00	1.53	H → L(98%)
	2	2.37	1.48	H-1 → L(48%) H → L+1(49%)
	5	3.00	1.18	H-2 → L(43%) H → L+2(33%)
7	1	1.91	1.52	H → L(96%)
	2	2.23	1.50	H-1 → L(46%) H → L+1(47%)
	5	2.77	1.47	H-2 → L(46%) H → L+2(37%)
8	1	1.86	1.54	H → L(92%)
	2	2.12	1.45	H-1 → L(43%) H → L+1(46%)
	5	2.60	1.58	H-2 → L(49%) H → L+2(40%)
9	1	1.82	1.60	H → L(86%)
	2	2.04	1.39	H-1 → L(38%) H → L+1(42%)
	5	2.46	1.51	H-2 → L(51%) H → L+2(43%)

TABLE A11: Electronic transition data obtained by the TDDFT method for **B** and **C** conformers of TAm oligomers at the B3LYP/6-31G(d,p) level. The HOMO and LUMO are indicated by H and L, respectively. Electronic transitions are from S_0 to S_m.

B-$(TAm)_n$	m	E_g (eV)	f_{osc}	configurations
2	1	3.42	1.02	H → L(86%)
3	1	2.76	1.76	H → L(92%)
6	1	1.95	2.78	H → L(98%)
	2	2.31	2.21	H → L+1(50%) H-1 → L(46%)
7	1	1.84	3.02	H → L(98%)
	2	2.16	2.62	H → L+1(50%) H-1 → L(46%)
8	1	1.77	3.28	H → L(96%)
	2	2.05	2.94	H → L+1(48%) H-1 → L(44%)
9	1	1.72	3.59	H → L(92%)
	2	1.96	3.16	H → L+1(46%) H-1 → L(41%)
C-$(TAm)_n$	m	E_g (eV)	f_{osc}	configurations
2	1	3.49	1.29	H → L(94%)
3	1	2.78	2.14	H → L(96%)
6	1	1.89	3.62	H → L(98%)
7	1	1.76	3.99	H → L(98%)
	2	2.03	1.19	H-1 → L(50%) H → L+1(47%)
8	1	1.66	4.37	H → L(98%)
	2	1.92	1.42	H-1 → L(49%) H → L+1(47%)
9	1	1.59	4.77	H → L(96%)
	2	1.83	1.61	H-1 → L(48%) H → L+1(46%)

Appendix III

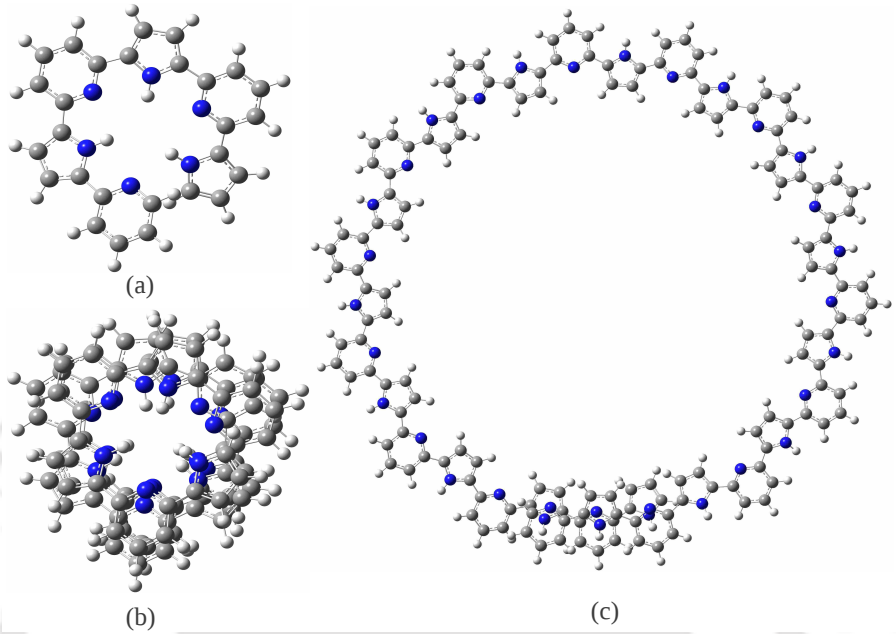

FIGURE A3: Optimized structures of **B**-$(PP)_3$ (a), **B**-$(PP)_{10}$ (b) and **A**-$(PP)_{16}$ (c) obtained at the B3LYP-D3/6-31G(d) level.

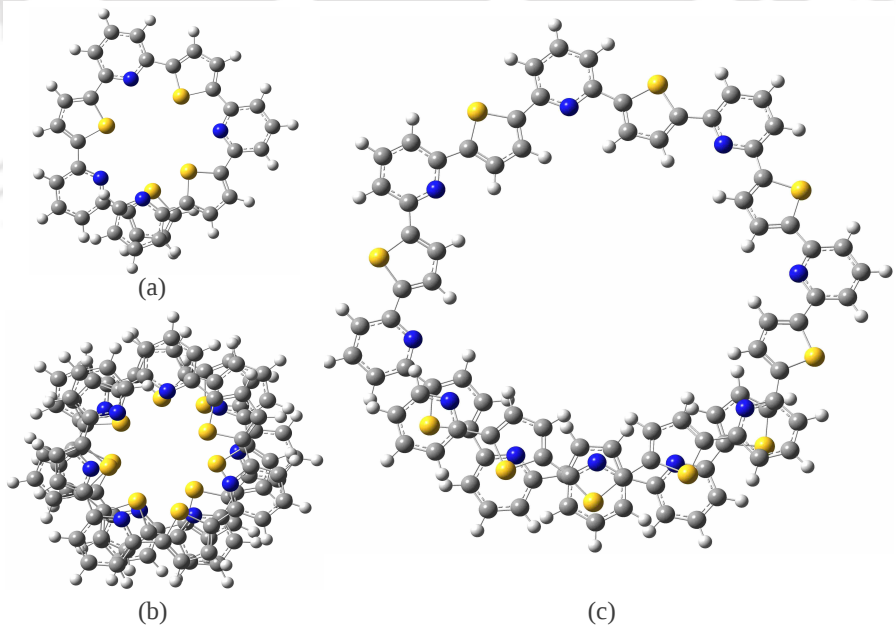

FIGURE A4: Optimized structures of **B**-$(PT)_4$ (a), **B**-$(PT)_{10}$ (b) and **A**-$(PT)_{10}$ (c) obtained at the B3LYP-D3/6-31G(d) level.

TABLE A12: Electronic transition data obtained by TDDFT method for **A**-$(PP)_n$ and **B**-$(PP)_n$ at B3LYP-D3/6-31G(d) level. E_g, f_{osc}, H and L denote excitation energy, oscillator strength, HOMO and LUMO, respectively. Electronic transitions are from S_0 to S_m. E_gs are in eV.

n (**A**)	m	E_g	f_{osc}	configurations	n (**B**)	m	E_g	f_{osc}	configurations
1	1	4.13	0.15	H → L (55%)	1	1	4.12	0.17	H → L (62%)
				H → L+1 (42%)		14	7.51	0.41	H-4 → L+1 (40%)
	2	4.49	0.43	H → L (44%)	2	1	3.37	0.39	H → L (86%)
				H → L+1 (54%)		2	3.79	0.34	H-1 → L (88%)
2	1	3.49	0.42	H → L (63%)	3	1	3.10	0.09	H → L (86%)
	2	3.70	0.57	H-1 → L (38%)		8	3.97	0.60	H-2 → L+1 (34%)
				H → L (31%)	4	1	3.01	0.03	H-1 → L (45%)
3	1	3.33	0.25	H → L+1 (74%)					H → L+1 (33%)
	2	3.41	0.91	H → L (46%)		14	3.98	0.37	H-3 → L (20%)
4	1	3.29	0.87	H → L+2 (54%)					H → L+4 (25%)
5	1	3.26	2.41	H → L+3 (55%)	5	1	2.94	0.03	H → L+1 (64%)
6	1	3.24	3.02	H → L+4 (43%)		21	3.93	0.40	H-4 → L+3 (23%)
7	1	3.22	3.34	H → L+5 (33%)	6	1	2.83	0.02	H → L (86%)
				H-1 → L-4 (22%)		37	4.06	0.62	H-5 → L+3 (18%)
8	1	3.20	3.40	H → L+6 (27%)	7	1	2.84	0.02	H → L (46%)
				H-1 → L+5 (20%)	8	1	2.84	0.01	H → L (46%)
9	1	3.19	3.21	H → L+7 (21%)	9	1	2.84	0.02	H-1 → L+1 (32%)
				H-1 → L+6 (19%)	10	1	2.80	0.00	H → L (75%)
10	1	3.18	2.89	H → L+8 (19%)		114	4.15	0.24	H-2 → L+13 (14%)
				H-1 → L+7 (17%)					H → L+18 (12%)
	2	3.27	3.48	H → L+7 (14%)		117	4.18	0.31	H-9 → L+7 (13%)
				H → L+8 (12%)					H-2 → L+15 (15%)
16	1	2.98	0.07	H → L (47%)					
	5	3.21	3.60	H → L+14 (12%)					
	6	3.23	3.56	H → L (6%)					
				H → L+4 (6%)					

TABLE A13: Electronic transition data obtained by TDDFT method for **A**-$(PT)_n$ and **B**-$(PT)_n$ at B3LYP-D3/6-31G(d) level. E_g, f_{osc}, H and L denote excitation energy, oscillator strength, HOMO and LUMO, respectively. Electronic transitions are from S_0 to S_m. E_gs are in eV.

n (**A**)	m	E_g	f_{osc}	configurations	n (**B**)	m	E_g	f_{osc}	configurations
1	1	4.30	0.42	H → L (90%)	1	1	4.26	0.40	H → L (92%)
	18	7.26	0.44	H-4 → L+1 (47%)		16	7.23	0.51	H-4 → L+1 (39%)
2	1	3.47	0.69	H → L (82%)	2	1	3.40	0.56	H → L (85%)
3	1	3.28	0.73	H → L+1 (94%)	3	1	3.16	0.31	H → L (82%)
4	1	3.23	1.28	H → L+2 (77%)		4	3.62	0.42	H-1 → L (61%)
5	1	3.20	1.50	H → L+3 (63%)	4	1	3.07	0.05	H-1 → L (40%)
6	1	3.17	1.41	H → L+4 (53%)					H → L+1 (42%)
7	1	3.15	1.12	H → L+5 (45%)		5	3.43	0.46	H-1 → L+2 (72%)
	2	3.25	1.59	H → L+4 (42%)	5	1	2.98	0.02	H → L (56%)
8	1	3.13	0.02	H → L+4 (13%)		24	4.02	0.39	H-4 → L+3 (60%)
	2	3.23	0.65	H-1 → L+4 (21%)	6	1	2.96	0.02	H → L+1 (56%)
				H → L+1 (30%)		17	3.48	0.26	H-2 → L+3 (23%)
9	1	3.07	0.07	H → L+5 (35%)	7	1	2.93	0.01	H-1 → L+1 (20%)
	6	3.21	0.64	H → L+7 (28%)					H → L (23%)
				H-1 → L+5 (17%)		28	3.61	0.36	H-3 → L+5 (44%)
10	1	3.02	0.25	H → L+3 (54%)	8	1	2.89	0.01	H → L (48%)
	8	3.21	0.50	H → L (30%)		35	3.56	0.30	H-5 → L (26%)
	11	3.27	0.43	H-2 → L+2 (18%)	9	1	2.87	0.01	H-1 → L (26%)
				H-2 → L+4 (12%)					H → L+1 (31%)
						45	3.56	0.15	H-6 → L+1 (23%)
					10	1	2.85	0.01	H → L (49%)
						52	3.52	0.16	H-5 → L+5 (21%)
						54	3.54	0.14	H-4 → L+8 (26%)
						108	4.08	0.16	H → L+10 (19%)

Oligomers	HOMO	LUMO
A-$(PP)_{16}$	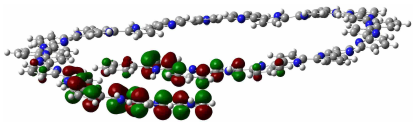	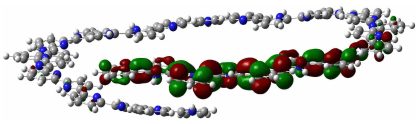
B-$(PP)_{10}$	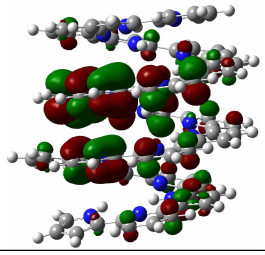	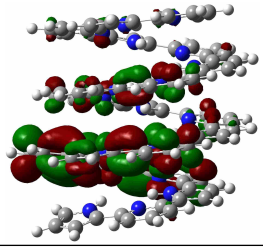
A-$(PT)_{10}$	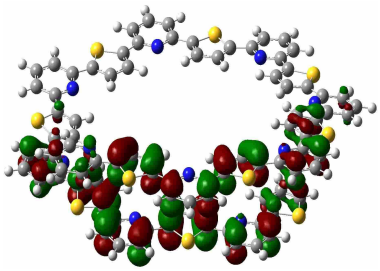	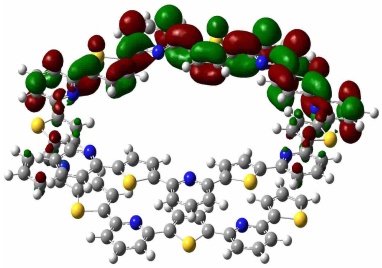
B-$(PT)_{10}$	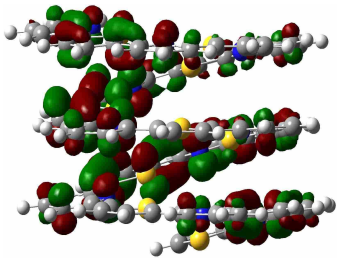	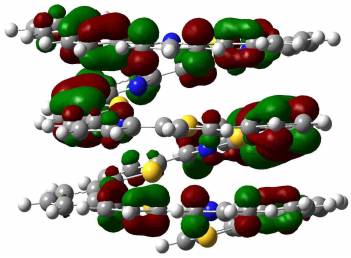

FIGURE A5: Frontier molecular orbitals of **A**-$(PP)_{16}$, **B**-$(PP)_{10}$, **A**-$(PT)_{10}$ and **B**-$(PT)_{10}$ at an isosurface value of 0.02.

Appendix IV

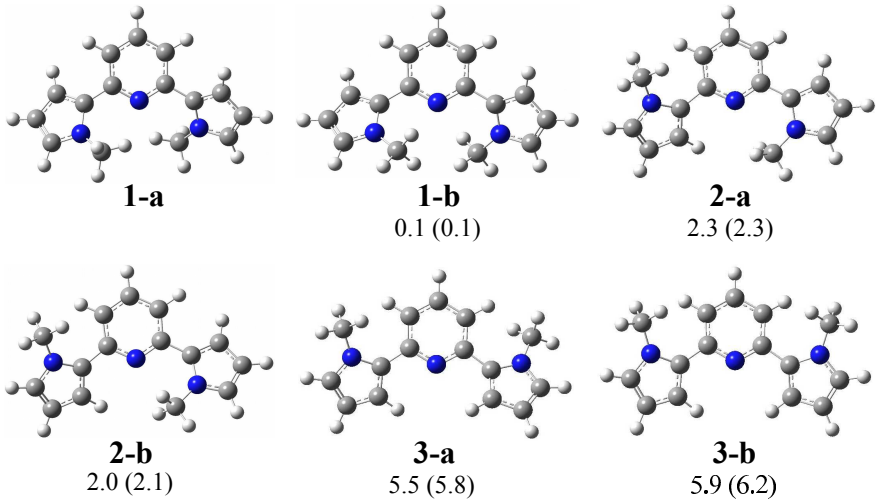

FIGURE A6: Optimized structures of different conformers of $(PP)_1$ obtained at the B3LYP/6-31G(d,p) level. Name of conformers are designated as **x-a**/**b**, where '**x**' is an integer denoting the conformer number. '**a**' and '**b**' denote the two different starting geometries for optimization in which the two pyrrole rings are on the same and opposite sides, respectively. **1-a** is the most stable structure. Stability of other conformers with respect to the most stable conformer (i.e., $E_{\mathbf{x-a/b}}$ - $E_{\mathbf{1-a}}$) obtained at B3LYP/6-31G(d,p) and CAM-B3LYP/6-31G(d,p) levels are written outside and inside parentheses, respectively. All values are in kcal/mol.

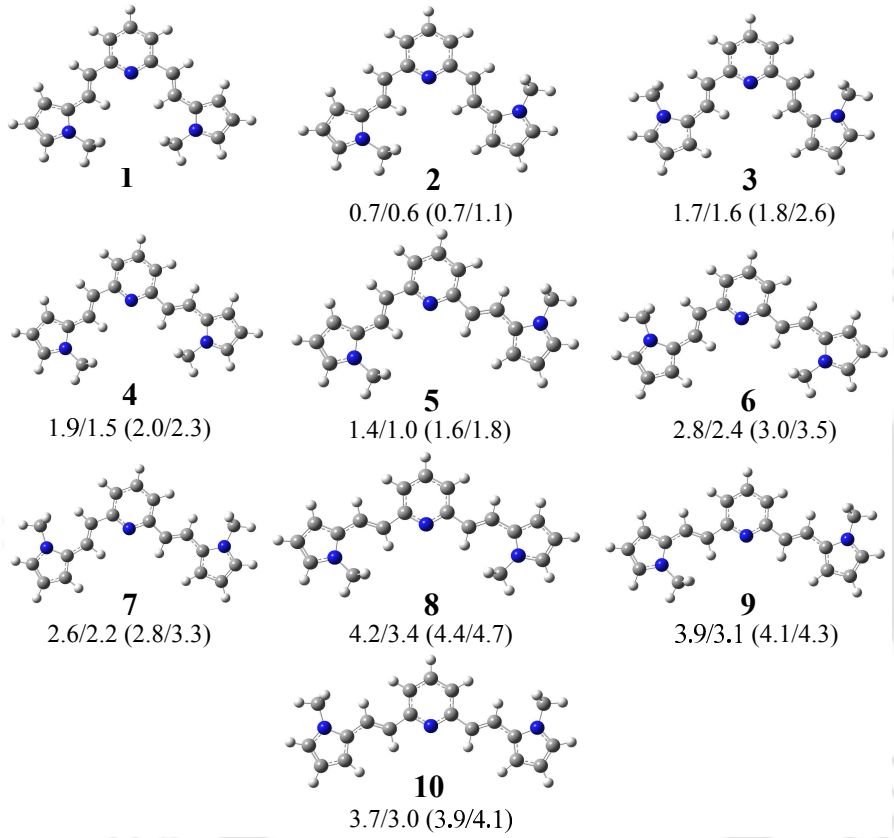

FIGURE A7: Optimized structures of different conformers of $(PCCP)_1$ obtained at the B3LYP/6-31G(d,p) level. Stabilities of other conformers with respect to the most stable conformer **1** obtained at B3LYP/6-31G(d,p) and B3LYP/6-31++G(d,p)//B3LYP/6-31G(d,p) levels are written outside parentheses, and results obtained at the CAM-B3LYP/6-31G(d,p) and MP2/6-31G(d,p) levels are mentioned inside parentheses, respectively. All values are in kcal/mol.

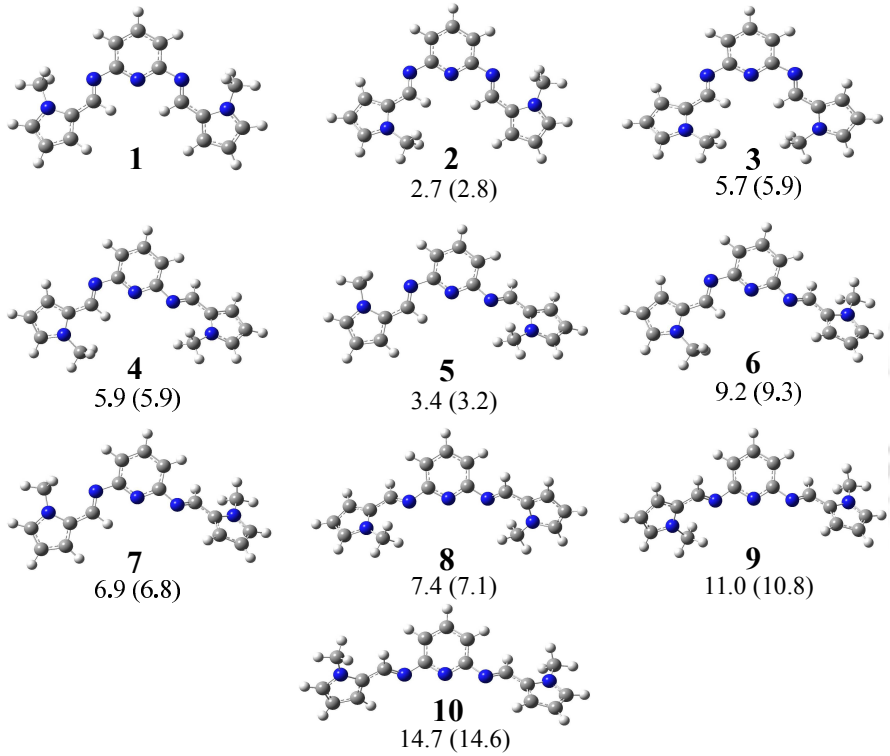

FIGURE A8: Optimized structures of different conformers of $(PCNP)_1$ obtained at the B3LYP/6-31G(d,p) level. Stability of other conformers with respect to the most stable conformer **1** obtained at B3LYP/6-31G(d,p) and CAM-B3LYP/6-31G(d,p) levels are written outside and inside parentheses, respectively. All values are in kcal/mol.

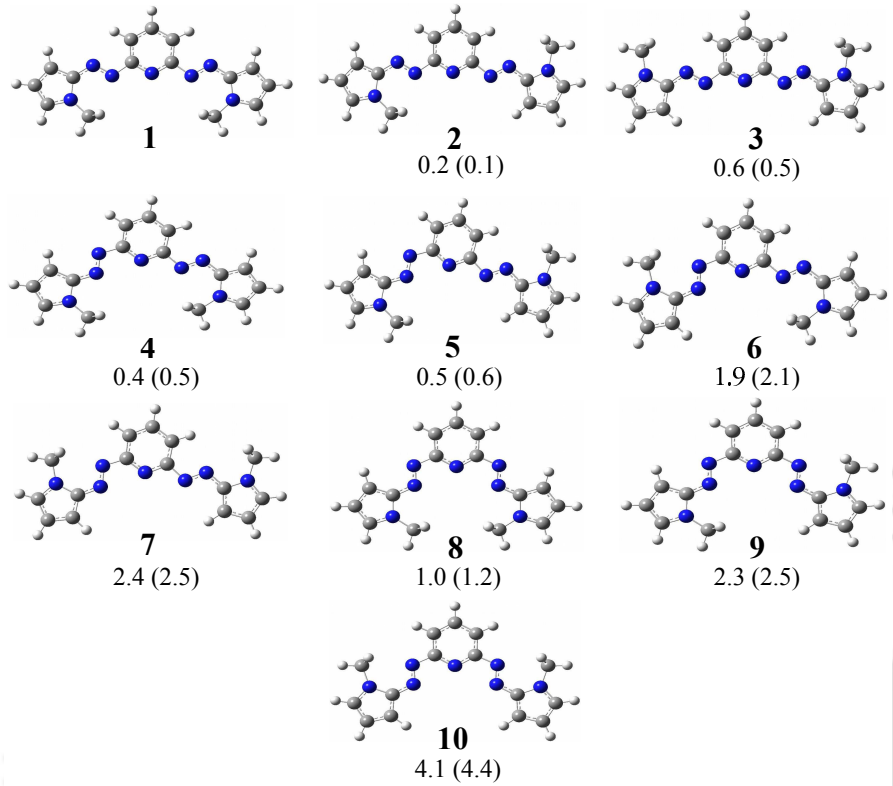

FIGURE A9: Optimized structures of different conformers of $(PNNP)_1$ obtained at the B3LYP/6-31G(d,p) level. Stability of other conformers with respect to the most stable conformer **1** obtained at B3LYP/6-31G(d,p) and CAM-B3LYP/6-31G(d,p) levels are written outside and inside parentheses, respectively. All values are in kcal/mol.

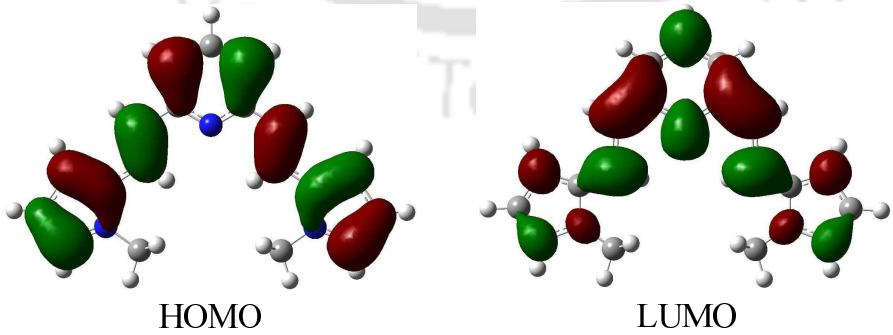

FIGURE A10: HOMO and LUMO of $(PCCP)_1$ at an isosurface value of 0.02.

TABLE A14: Calculated Dipole moments of ground (μ_g) and first excited states (μ_e), and their differences ($\Delta\mu_{ge}$) for the studied molecules.

$(PP)_n$	μ_g	μ_e	$\Delta\mu_{ge}$	$(PCCP)_n$	μ_g	μ_e	$\Delta\mu_{ge}$
$(PP)_1$	0.67	3.21	2.54	$(PCCP)_1$	2.60	4.48	1.88
$(PP)_2$	0.48	1.18	0.71	$(PCCP)_2$	0.49	0.38	0.87
$(PP)_3$	0.54	0.79	1.31	$(PCCP)_3$	2.47	0.17	2.30
$(PP)_4$	0.65	0.24	0.41	$(PCCP)_4$	0.43	0.38	0.05
$(PCNP)_n$	μ_g	μ_e	$\Delta\mu_{ge}$	$(PNNP)_n$	μ_g	μ_e	$\Delta\mu_{ge}$
$(PCNP)_1$	0.54	0.28	0.26	$(PNNP)_1$	2.41	2.79	0.38
$(PCNP)_2$	0.20	0.02	0.23	$(PNNP)_2$	1.11	1.14	0.03
$(PCNP)_3$	0.55	0.89	0.34	$(PNNP)_3$	2.00	1.96	0.26
$(PCNP)_4$	0.51	0.57	0.06	$(PNNP)_4$	1.75	1.38	0.38

TABLE A15: E_H, E_L, IP(v), EA(v), E_g^{hl}, E_g^{fund} and E_g^{opt} calculated at the B3LYP/6-31++G(d,p)//B3LYP/6-31G(d,p) level for all the studied molecules. Hole-electron binding energies E_b^1 and E_b^2 are also reported. All values are in eV.

compounds	E_H	E_L	IP	EA	E_g^{hl}	E_g^{fund}	E_g^{opt}	$E_b^1(E_b^2)$
$(PP)_1$	−5.47	−1.15	6.91	−0.31	4.33	7.21	3.72	3.49(0.61)
$(PP)_2$	−5.05	−1.37	6.20	0.29	3.69	5.91	3.25	2.65(0.43)
$(PP)_3$	−5.00	−1.39	5.93	0.52	3.61	5.41	3.14	2.27(0.47)
$(PP)_4$	−4.98	−1.40	5.76	0.66	3.58	5.10	3.10	2.00(0.48)
$(PCCP)_1$	−5.10	−1.70	6.34	0.45	3.39	5.89	2.91	2.98(0.48)
$(PCCP)_2$	−4.84	−1.90	5.80	0.99	2.94	4.82	2.55	2.27(0.39)
$(PCCP)_3$	−4.82	−1.95	5.59	1.20	2.87	4.39	2.44	1.95(0.44)
$(PCCP)_4$	−4.80	−1.96	5.45	1.33	2.84	4.12	2.39	1.72(0.45)
$(PCNP)_1$	−5.51	−1.82	6.76	0.55	3.68	6.21	3.22	3.00(0.47)
$(PCNP)_2$	−5.28	−2.10	6.22	1.15	3.18	5.08	2.78	2.30(0.40)
$(PCNP)_3$	−5.25	−2.17	6.00	1.41	3.08	4.59	2.64	1.94(0.44)
$(PCNP)_4$	−5.25	−2.19	5.87	1.55	3.06	4.32	2.60	1.71(0.46)
$(PNNP)_1$	−5.73	−2.47	6.99	1.21	3.26	5.77	2.68	3.09(0.58)
$(PNNP)_2$	−5.51	−2.77	6.45	1.83	2.74	4.62	2.51	2.11(0.23)
$(PNNP)_3$	−5.49	−2.84	6.23	2.08	2.65	4.15	2.43	1.73(0.23)
$(PNNP)_4$	−5.48	−2.86	6.10	2.23	2.62	3.88	2.38	1.49(0.24)

List of articles published/submitted

1. Harikrishna Sahu, Swaraj Rashmi Pradhan and Aditya N. Panda, Tuning the properties of pyridine-pyrrole based cross-conjugated oligomers by the insertion of π-spacers in the main chain: A DFT study, submitted.

2. Harikrishna Sahu, Shashwat Gupta, Priyank Gaur and Aditya N. Panda, Structure and optoelectronic properties of helical pyridine–furan, pyridine–pyrrole and pyridine–thiophene oligomers, *Phys. Chem. Chem. Phys.*, **2015**, 17, 20647–20657.

3. Harikrishna Sahu and Aditya N. Panda, Helical and nonhelical structures of vinylene- and azomethine- linked heterocyclic oligomers: A computational study of conformation-dependent optoelectronic properties, *J. Phys. Chem. C*, **2015**, 119, 22855–22865.

4. Harikrishna Sahu and Aditya N. Panda, Computational investigation of charge injection, and transport properties of a series of thiophene–pyrrole-based oligo-azomethines, *Phys. Chem. Chem. Phys.*, **2014**, 16, 8563–8574.

5. Harikrishna Sahu and Aditya N. Panda, Computational study on the effect of substituents on the structural and electronic properties of thiophene–pyrrole- based π-conjugated oligomers, *Macromolecules*, **2013**, 46, 844–855.

Oral presentation

1. **2015** Research Conclave, Hosted by Indian Institute of Technology Guwahati, presented an oral titled "*Linear and folding conformers of vinylene-, azomethine-, and azo-linked heterocyclic oligomers: Stabilities and optoelectronic properties*".

Poster presentations

1. **2015** ChemConvene, Hosted by Department of chemistry, IIT Guwahati, presented a poster titled "*Structural and optoelectronic properties of pyridine-furan, pyridine-pyrrole and pyridine-thiophene helices: A DFT study*".
2. **2014** Theoretical Chemistry Symposium (TCS), Hosted by NCL, Pune, presented a poster titled "*Structural and optoelectronic properties of linearly and helically conjugated vinylene-linked heterocyclic oligomers: A DFT study*".
3. **2014** Chemistry with Computers (CWC), Hosted by IIIT and IICT, Hyderabad, presented a poster titled "*Thiophene-pyrrole-based oligo-azomethines for optoelectronic applications: A Computational Study*"
4. **2013** Current Trends in Theoretical Chemistry (CTTC), Hosted by Bhabha Atomic Research Centre, Mumbai, presented a poster titled "*Detailed investigation on charge injection and transport properties of a series of thiophene-pyrrole-based oligo-azomethines*"
5. **2012** Theoretical chemistry symposium (TCS), Hosted by Indian Institute of Technology Guwahati, presented a poster titled "*Electronic structures of thiophene-pyrrole based oligomers in neutral and charged states: A computational study*"
6. **2012** Frontiers in Chemical Sciences (FICS), Hosted by Indian Institute of Technology Guwahati, presented a poster titled "*Structural, optical and electronic properties of thiophene and pyrrole based oligomers: A computational study*"